# Contents

# Preface



The proceedings at hand are the result from the Bauhaus Summer School Course: Forecast Engineering held at the Bauhaus-Universität Weimar, 2015 & 2016. It summarizes the results of the conducted project work, provides the abstracts of the contributions by the participants, as well as impressions from the accompanying programme and organized cultural activities of the DAAD supported Summer School.

Each Summer, the Faculty of Civil Engineering of the Bauhaus-Universität Weimar makes its experience and expertise in teaching and research available under the organizational leadership of the Institute of Structural Engineering (IKI). The extraordinary format of the interdisciplinary Summer School provides the opportunity for foreign and local students to study advanced levels of recent developments of numerical methods and sophisticated modelling in different disciplines of civil engineering far beyond traditional graduate courses. In addition, results of ongoing research and projects at the involved partner universities of the Bauhaus-Universität Weimar as well as topics from neighbouring disciplines affecting and describing the demands on civil engineer structures are presented by invited guest lectures.

In August 2015 about 45 students and 10 guest lecturers from 22 countries and in August 2016 again about 37 Students and 7 guest lecturers from 21 countries have participated at the Technical Summer Course "Forecast Engineering: From Past Design to Future Decision" and contributed to the international atmosphere, to the scientific and the intercultural exchange of experience and ideas which were noticeably appreciated by the guests and organizers.

*Group Picture of the Summer Course Participants 2015 (Photo: B. Proschak)*



*Group Picture of the Summer Course Participants 2016 (Photo: B. Proschak)*

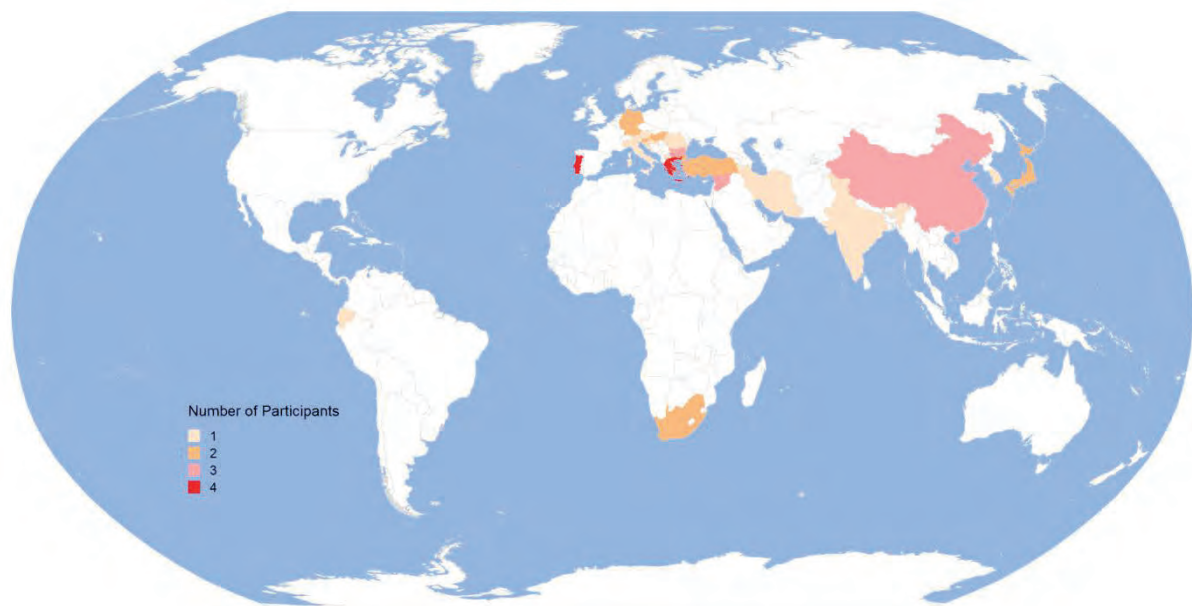# Bauhaus Summer School – Forecast Engineering 2015
From Past Design to Future Decision

*ABRAHAMCZYK Lars, SCHWARZ Jochen*
*Earthquake Damage Analysis Center, Bauhaus-Universität Weimar, Germany*

## Targets and objectives

Planning of a civil engineering structure is based on static calculations today as well as in the past. With the development of construction methods and new usage requirements, the consideration of uncertainties in model quality is gaining more and more importance. In addition to the traditional force-based approaches, the experience and observations on the deformation behavior of components or the entire structure under different conditions of influence enable the introduction of novel detection and evaluation criteria. The special character of this course lies in the combination of fundamental disciplines of civil engineering with applied research projects in the areas of steel and reinforced concrete structures, earthquake and wind engineering as well as in building informatics and their combination with mathematical methods and modern tools of visualization. Keynote speeches by international experts from partner universities and recognized research institutes also provide insights into current research projects and international development trends. The broad spectrum of civil engineering in the field of modeling and simulation is highlighted. In addition, all participants the course offers the opportunity to exchange ideas, to work in an international environment and to improve personal transversal as well as language skills.



**Figure 1.** Home Countries of the Participants attending the Summer School "Forecast Engineering" 2015.

# Participants

The course targets post-graduate students, i.e., second (M.Sc.) and third cycle (Ph.D.) from different institutions and countries to enable knowledge transfer between the participants. By providing students with advanced, scientifically-based interdisciplinary knowledge, skills and methods, they are trained to react to demanding engineering tasks in the areas of planning, construction and realization of structures under specific site, action and loading conditions. In addition the soft skills of each participant (like team working and task sharing) will be trained in internationally composed project groups. Students from nearly all over the world attended the summer course, which leads to a very intercultural exchange of ideas, thinking and life styles (cf. Figure 1).

# Course topics

The summer course is divided into three parts: lectures, project work, and presentation by the participants. This time sharing ensures theoretical and practical oriented work under holistic aspects and the use of modern analyses methods and tools for numerical simulation in structural and mechanical engineering. The young scientists get experience and modern scientific knowledge under realistic training settings. The offered formats and forms of training can be summarized as follows:

▪ **Lectures:** The necessary theoretical basics, the current state of research (in project targeting fields) as well as special topics are presented by lecturers, leading scientists from the partner institution, and invited guest speakers (cf. Guest lecturers and invited speakers).

▪ **Project Work** (including presentation and submission of final results): The course offers the possibility to work in interdisciplinary teams on different projects. The participants could choose between six offered projects dealing with advanced current engineering research topics:

Project 1 | Implementation and Validation of Wireless Structural Health Monitoring Systems
*Chair of Computing in Civil Engineering*

Project 2 | Image Analysis for Change Detection
*Chair of Computer Vision in Engineering*

Project 3 | Evaluation of Existing Masonry Structures under Multiple Extreme Load Impacts
*Earthquake Damage Analysis Center*

Project 4 | Numerical Analysis of Steel Frames
*Chair of Steel and Hybrid Structures*

Project 5 | Selected Topics of Optimisation in Civil Engineering
*Junior Chair of Optimization and Stochastics*

Project 6 | Wind-induced Vibrations of Long-span Bridges
*Chair of Modelling and Simulation of Structures*

The project work was conducted in small groups and intensively supervised. The outcome – presented by the herein compiled reports – reaches an impressive level of results and graphical elaboration (cf. Project Reports).

- **Presentation by the Participants** (workshop character): Participating students were requested to present their work in special sessions and to defend their results in front of a broad scientific audience. Therefore each participant had to submit a short abstract together with his/her application. On the basis of these abstracts 15 titles were elected as presentation by the participants, which also shall honor the effort and work of the participant (cf. Papers Contributed by the Participants).

The summer school combines theory and practice on the basis of advanced research and tool development. The modular structure of the programme allows the participants to address current and trendsetting problems and research topics.

# Guest lecturers and invited speakers

In 2015 again nationally and internationally well-known and high-ranked scientist could be welcomed as guest speakers at the engineering summer course at Bauhaus-Universität Weimar. The current state of research at the project partner's universities as well as lecturers from other disciplines highlighted the future demands on engineers to overcome future requirements on engineered structures.

- Stability and Design of Lattice Steel Structures | *Prof. M. Kraus (BUW)*
- Design assisted by testing of Cold-formed Steel Structures | *Dr. A. Crisan (University of Timosora)*
- Basic tools for forecasting in Bridge Aerodynamics: Numerical simulations and wind tunnel tests | *A.S. Corriols*
- Analytic methods in fracture mechanics | *Prof. K. Gürlebeck (BUW)*
- Bridges in Thuringia | *W. König (TLBV, Germany)*
- Fusing Big City Data with Civil Engineering Design Ideas | *Prof. T. Hartmann (University of Twente)*
- How to deal with climate change impacts on transport infrastructure? | *Prof. I. Stipanovic (University of Twente)*
- Inelastic behavior of structures under earthquake loading: analysis, design and assessment | *Prof. A. Sextos (AUTH)*
- From the real construction to the experimental set | *Prof. P. Pavlov (UACEG, Sofia)*
- Recent advances in the seismic analysis and design of connections in precast RC structures | *Prof. T. Isakovic (University of Ljubljana)*
- Numerical modelling of structures under fire conditions | *Prof. N. Lopes (Aveiro, Portugal)*
- Natural Hazards & Climate Change: Future challenges for insurers and engineers | *Dr. T. Bistry (Deutsche Rück, Germany)*
- Evaluating Statistical and Machine Learning Techniques for Landslide Susceptibility Modelling | *Prof. A. Brenning (University Jena, Germany)*

Federal Ministry
of Education
and Research

**DAAD** Deutscher Akademischer Austausch Dienst
German Academic Exchange Service

*Participants at guest lecture class (Photo: B. Proschak)*



*Participants at project work (Photo: B. Proschak)*

# Time Schedule

| | Monday 17 August | Tuesday 18 August | Wednesday 19 August | Thursday 20 August | Friday 21 August | Saturday 22 August |
|---|---|---|---|---|---|---|
| **09:00 - 10:30** | Opening 2015 Presentation of the Staff and Projects 1-4 (30min per Project) | Dr. A. Crisan (University of Timosora) *Lecture Hall 6* | Presentation by Participants *Lecture Hall 6* | Project work | W. König (TLBV) Presentation by Participants *Lecture Hall 6* | 08:00 - 17:00 Excursion: Bridges in Thuringia |
| **11:00 - 12:30** | *Lecture Hall 6* | A.S. Corriols *Lecture Hall 6* | Prof. K. Gürlebeck (BUW) *Lecture Hall 6* | *will be announced* | Prof. T. Hartmann (University of Twente) *Lecture Hall 6* | |
| | Lunch | | | | | |
| **13:30 - 15:00** | Presentation of the Staff and Projects 5 & 6 (30min per Project) | Project work | Interdisciplinary experience exchange with specialised courses of Bauhaus Summer School **14:00 - 17:00** | Project work | Prof. I.Stipanovic (University of Twente) *Lecture Hall 6* | |
| **15:30 - 17:00** | Prof. M. Kraus (BUW) *Lecture Hall 6* | *will be announced* | | *will be announced* | Presentation by Participants *Lecture Hall 6* | |
| **17:30 - 19:00** | Icebreaker Party **17:30** | | Team Building (Sport challenges) *"Falkenburg"* | | Sightseeing Weimar *meeting point* | |
| | Cultural events as part of the Bauhaus Summer School 2015 | | | | | |

| | Monday 24 August | Tuesday 25 August | Wednesday 26 August | Thursday 27 August | Friday 28 August | Saturday 29 August |
|---|---|---|---|---|---|---|
| **09:00 - 10:30** | Prof. A. Sextos (AUTH) *Lecture Hall 6* | Prof. T. Isakovic (University of Ljubljana) *Lecture Hall 6* | Dr. T. Bistry (Deutsche Rück) *Lecture Hall 6* | Project work | Presentation of project works | 05:00 - 10:00 Departure |
| **11:00 - 12:30** | Prof. P. Pavlov (UACEG, Sofia) *Lecture Hall 6* | Prof. N. Lopes (Aveiro, Portugal) *Lecture Hall 6* | Prof. A. Brenning (Uni Jena) *Lecture Hall 6* | *will be announced* | Closure *Lecture Hall 6* | |
| | Lunch | | | | | |
| **13:30 - 15:00** | Project work | Project work | Interdisciplinary experience exchange with specialised courses of Bauhaus Summer School **14:00 - 17:00** | Preparing of presentation | Preparation of final report | |
| **15:30 - 17:00** | | | | | | |
| | | | | *will be announced* | *will be announced* | |
| **17:30 - 19:00** | *will be announced* | *will be announced* | | Food evening *M18* | Farewell Party **18:00** *Mensa* | |
| | Cultural events as part of the Bauhaus Summer School 2015 | | | | | |

# Excursion

A special highlight of the Engineering Course at the Bauhaus Summer School is the annual excursion to current construction sites or already finished outstanding engineering projects in Thuringia. The participants became the once-only chance to visit modern bridge structures designed with different and sometimes unique super-structures not only from outside. The excursion was guided inside of the super-structures to highlight and impart knowledge about the special construction of engineering art in bridge design.

The excursion programm introduced bridges with:

| | |
|---|---|
| Overall length: | 280 to 845 m |
| Height over ground: | 35 to 110 m |

and including the highest arch bridge in Germany. All bridges are built as composite structures made of steel and concrete, whereas different techniques were applied (e.g. Pre-stressed concrete; external tendons steel).



*Impressions from the Excursion to bridge structures in Thuringia, Germany* (Photos: J. Rautenberg)

# Project reports 2015

# A wireless structural health monitoring system for automated, decentralized modal analysis

ZOUBEK Blaz[a], MANOJLOVSKI Filip[b], ZHELYAZKOV Aleksandar[c], NAEIMI Negar[d], NISHINO Hiromichi[e], ABDOLLAHI Hossein[f]

[a] *Faculty of Civil and Geodetic Engineering, University of Ljubljana, Slovenia*

[b] *Institute of Earthquake Engineering and Engineering Seismology, Skopje, F.Y.R. of Macedonia*

[c] *Risk Engineering Ltd, Sofia, Bulgaria*

[d] *Isfahan University of Technology, Iran*

[e] *Kyoto University, Japan*

[f] *Daneshpajoohan Higher Education Institute, Iran*

DRAGOS Kosmas, TAUSCHER Eike, SMARSLY Kay
*Chair of Computing in Civil Engineering, Bauhaus University Weimar, Germany*

## Abstract

Wireless sensor networks have proven to be cost-effective tools for structural health monitoring (SHM). The elimination of long cables has rendered wireless sensor nodes an attractive alternative to conventional cable-based systems. Embedded computing is an integral aspect of wireless SHM systems, and many algorithms have been proposed for on-board processing of data in an attempt to reduce wireless data traffic. This paper highlights the advantages of embedded computing in wireless structural health monitoring systems. A wireless SHM system is proposed, able to perform automated modal analyses in a decentralized fashion. The wireless SHM system is composed of sensor nodes with embedded algorithms able to perform on-board fast Fourier transforms of collected acceleration response data in order to identify the natural frequencies of the monitored structure. The proposed wireless SHM system is validated through laboratory experiments on a scaled model of an existing suspension bridge. The consistency of the results is corroborated through multiple repetitions of the experiment. Finally, conclusions are drawn on both the dynamic characteristics of the bridge model and the performance of the proposed wireless structural health monitoring system. This research has been conducted within the 2015 Bauhaus Summer School at Bauhaus University Weimar, Germany.

## Introduction

Structural health monitoring (SHM) has become a vital part of infrastructure maintenance and asset management. Wireless structural health monitoring has been drawing increasing research interest due to the advantages of wireless sensor networks in terms of cost and installation effort. The coexistence of processing power with sensing boards enables wireless sensor nodes to autonomously perform monitoring tasks such as data acquisition, data processing, and data analysis. Embedded computing is used to execute the monitoring tasks directly on-board the sensor nodes. Thus, several research approaches have been dealing with embedded computing for wireless SHM systems aiming to limit data transmission and to enhance the autonomy of wireless sensor nodes. On the other hand, the

complexity of embedded computing approaches needs to be kept as low as possible in order to preserve the inherently low power resources of sensor nodes.

An early approach towards wireless SHM systems with embedded computing capabilities was proposed by Lynch et al. (2004), by introducing an SHM system performing damage detection using embedded algorithms for autoregressive modelling with exogenous inputs (AR-ARX). A wireless SHM system with embedded system identification algorithms was proposed by Zimmerman et al. (2008). Cho et al. (2008) presented the wireless tension force estimation system to estimate cable forces in cable-stayed bridges. The benefits of using embedded computing in wireless SHM systems in terms of power reduction were highlighted by Lei et al. (2010). Smarsly and Law (2013) presented an SHM system with embedded software to perform detection and analysis of potential anomalies on demand based on a migration-based approach, i.e. using software agents that assemble in real time and migrate to the sensor node where the anomaly is detected (Smarsly et al., 2011). Dragos and Smarsly (2015) proposed an embedded computing approach to perform on-board condition assessment of structures based on system identification and structural dynamics. Further examples include the utilization of artificial intelligence approaches (Smarsly and Law, 2014); embedding artificial intelligence techniques into wireless sensor nodes was largely inspired by research efforts on cable-based SHM systems at the beginning of this century. Specifically, multi-agent technology has been proven an efficient means to increase the reliability and performance of SHM systems, as presented in a number of practical applications, such as bridge or wind turbine monitoring (Smarsly and Hartmann, 2009a, b).

This paper presents an SHM system with embedded algorithms to enable automated, decentralized identification of natural frequencies of structures. The embedded algorithms perform fast Fourier transform on collected acceleration data directly on the sensor nodes. Validation tests of the proposed SHM system are conducted on a scaled model of a suspension bridge. In the first section of the paper, a general overview of wireless structural health monitoring concepts is given. Section 2 presents the embedded algorithms of the wireless SHM system, including the mathematical background and the implementation process. Section 3 describes the experimental tests conducted on the bridge model, including a description of the bridge and discussion on the results. Finally, conclusions of this work are drawn and an outlook on future work is provided.

## Wireless structural health monitoring

The rapid developments in computer sciences and sensor technologies facilitate the implementation of reliable systems for the acquisition of real-time response data from structures. Particularly with the development of wireless communication technology, costly wired SHM systems used in the field of structural health monitoring are gradually substituted by cost-effective wireless systems. Typically, wired systems comprise wired sensors connected to a central server through coaxial cables; the sensors collect response data, which is transferred to a data acquisition unit and then stored on a computer. In order to assess the condition of the structure, data processing is performed either in real time or offline.

A typical wireless SHM architecture, on the other hand, comprises wireless sensor nodes and a base station connected to a computer. Data collected by the wireless sensor nodes is sent to a computer terminal, which communicates with the network via a gateway (base station). Then, the processed data is sent to different servers or to the "cloud" enabling remote access. Since wireless sensor nodes

essentially represent integrated platforms combining processing units with sensing modules, on-board data processing prior to wireless communication is possible.

Two primary challenges of wireless sensor networks can be identified; these are (i) limited power resources and (ii) possible data loss affecting the reliability of wireless communication among the sensor nodes. Wireless communication has proven to be particularly power consuming, while the communication range also becomes an issue in larger wireless sensor networks in urban or industrial areas, due to the density of the building stock comprising buildings with dimensions of hundreds of meters (Swartz and Lynch, 2009). Therefore, the wireless SHM system proposed in this paper is equipped with embedded algorithms that enable on-board data processing prior to transmission, thus considerably reducing the amount of data to be wirelessly communicated.

## Identification of natural frequencies

The embedded algorithms of the proposed wireless SHM system are related to system identification and data processing. More precisely, the collected data sets are automatically transformed into the frequency domain directly on the sensor nodes prior to being wirelessly transmitted to the server. The following subsections cover the mathematical background of the data transformation from the time domain into the frequency domain as well as the implementation of the embedded algorithms into the wireless SHM system.

### Mathematical background

*The Fast Fourier Transform (FFT)*

In SHM applications, signal processing is used for identifying dynamic characteristics of structures, such as natural frequencies and mode shapes. The Fourier transform is an essential algorithm for gaining insights into the dynamic properties of the monitored structure. According to the theory of the Fourier transform, time domain signals or functions can be analyzed to a sum of harmonic sinusoidal component functions. The Fourier amplitude *F(ω)* represents the range of each component function at frequency *ω*, while the plot of all amplitudes versus frequencies is called "frequency spectrum". According to the theory of structural dynamics, peaks in the frequency spectrum of experimental response data correspond to resonant responses of the structure, and the respective frequencies at these peaks reflect the natural frequencies of the structure. Considering a continuous function of time *f(t)*, the Fourier transform is defined as in Eq. 1.

$$F(\omega) = \int f(t) \cdot e^{2\pi i \omega t} dt \tag{1}$$

In practice, Eq.1 cannot be used for analysis of measured data; due to the analog-to-digital conversion that takes place in data acquisition units, the data is obtained in discrete time steps constituting a discontinuous time function. Instead, the discrete Fourier transform (DFT) is used and each Fourier amplitude $F_k$ is obtained from Eq. 2.

$$F_k = \sum_{n=0}^{N-1} f_n \cdot e^{-2\pi i k \frac{n}{N}} \qquad k \in [0, N) \qquad N \in Z \qquad \omega = \frac{k}{N} \tag{2}$$

where $f_n$ is the discrete function $f(t)$ and $N$ is the length of the discrete time series. The Fourier amplitude $F_k$ is a complex number and each sinusoid's frequency is described as $k$ cycles per $N$ samples. It is clear that the DFT algorithm needs $N^2$ calculations because the equation produces $N$ outputs of $F_k$ and each output is obtained as a sum of $N$ terms. In an attempt to reduce the computational effort of the DFT algorithm, Cooley and Tukey (1965) proposed the fast Fourier transform (FFT) reducing the number of calculations to $N \cdot logN$ calculations. FFT is a "divide and conquer" algorithm. By dividing DFT of an arbitrary composite size $N = N_1 N_2$ into smaller DFTs of sizes $N_1$ and $N_2$ recursively, FFT leads to fewer calculations. In the Cooley-Tukey algorithm, a radix-2 decimation-in-time FFT is a most common form where a DFT of size $N$ is divided into two DFTs (even part and odd part) of size $N/2$ with each recursive stage, as shown in Eq. 3 and Eq. 4.

$$F_k = \sum_{n=0}^{N/2-1} f_n \cdot e^{-2\pi i k \cdot \frac{n}{N}} + \sum_{n=0}^{N/2-1} f_{n+1} \cdot e^{-2\pi i k \cdot \frac{n+1}{N}} = \sum_{n=0}^{N/2-1} f_n \cdot e^{-2\pi i k \cdot \frac{n}{N}} + e^{-\frac{2\pi i k}{N}} \cdot \sum_{n=0}^{N/2-1} f_{n+1} \cdot e^{-2\pi i k \cdot \frac{n}{N}} \tag{3}$$

From the identity $e^{2\pi i n} = 1$ ($n \in \mathbf{Z}$):

$$F_{N+k} = \sum_{n=0}^{N-1} f_n \cdot e^{-2\pi i (N+k) \cdot \frac{n}{N}} = \sum_{n=0}^{N-1} f_n \cdot e^{-2\pi i k \cdot \frac{n}{N}} \cdot e^{-2\pi i n} = \sum_{n=0}^{N-1} f_n \cdot e^{-2\pi i k \cdot \frac{n}{N}} \tag{4}$$

## Implementation of the wireless SHM

*Wireless sensor node platform*

In this study, the Oracle SunSPOTs (Small Programmable Object Technology) (Oracle Corp., 2007) wireless sensor nodes are used, shown in Figure 1. The sensor node features a powerful 32-bit ARM 920T microcontroller at 400 MHz speed, with 4MB flash memory and 512 kB RAM. The operating system of the sensor node is the Java Squawk Virtual Machine (Shaylor et al., 2003). For acceleration measurements, an 8-bit MMA7455L microelectromechanical system (MEMS) accelerometer is embedded into the sensor node platform, with three measurement range options ±2g, ±6g, or ±8g. The maximum sampling rate of the accelerometer is 125 Hz.



**Figure 1.** The Oracle SunSPOT sensor node

*Embedded software*

To autonomously perform the monitoring tasks, the process described in the previous section is implemented into a wireless SHM system using Java programming language. The embedded software designed for the proposed SHM system needs to perform calculation, communication, and storage tasks. To this end, two applications are developed; a "host application" launched on the server to

manage establishing communication links, receiving and plotting data, and an "on-board application" executed directly on the sensor nodes for data acquisition and transformation of the acceleration response data from the time domain into the frequency domain.

When starting system operation, the SHM system is initialized by the host application, which communicates with the sensor nodes via another node, the "base station". First, the wireless communication links between the base station and the sensor nodes are established by the host application. Second, the on-board application handles the calibration of the sensor nodes, which involves estimating the noise level of the system by collecting and averaging a predefined number of acceleration measurements at rest. Third, the sensor nodes switch to standby mode and start collecting acceleration response data once a predefined acceleration threshold is exceeded. Once the acceleration has dropped below the predefined threshold, acceleration stops and the collected response data is transformed on-board into the frequency domain using the FFT algorithm. Finally, the transformed data is wirelessly communicated to the server via the base station where the host application handles the graphical visualization of the frequency spectra.

## Experimental tests

The performance of the automated, decentralized wireless SHM system presented in the previous section is validated on a down-scaled model of an existing suspension bridge. The wireless SHM system is used to identify the natural frequencies of the model. In the following subsection, structural details about the bridge are provided, and the experimental setups as well as the performed tests are described. Finally, the obtained frequency spectra are presented and discussed.

### The New Little Belt suspension bridge

The New Little Belt (Lillebælt) suspension bridge was built in the 1970s to connect the island of Jutland with Funen Peninsula in Denmark. The elevation view of the bridge is shown in Figure 2a. The central span is 600 m long, while the side spans and the prestressed concrete approach viaducts are 250 m and 31 m long, respectively (Ostenfeld et al., 1970). The total length of the bridge is 1700 m. A simplified schematic of the deck section of the bridge is shown in Figure 2b. The width and the thickness of the deck are 33 m and 2.85 m, respectively. The mass of the deck is equal to 11 667 kg/m, while the suspension cables are spaced at 12 m intervals. The two main cables are made of 61 prefabricated strands and are 1500 m long (Dragos et al. 2015).
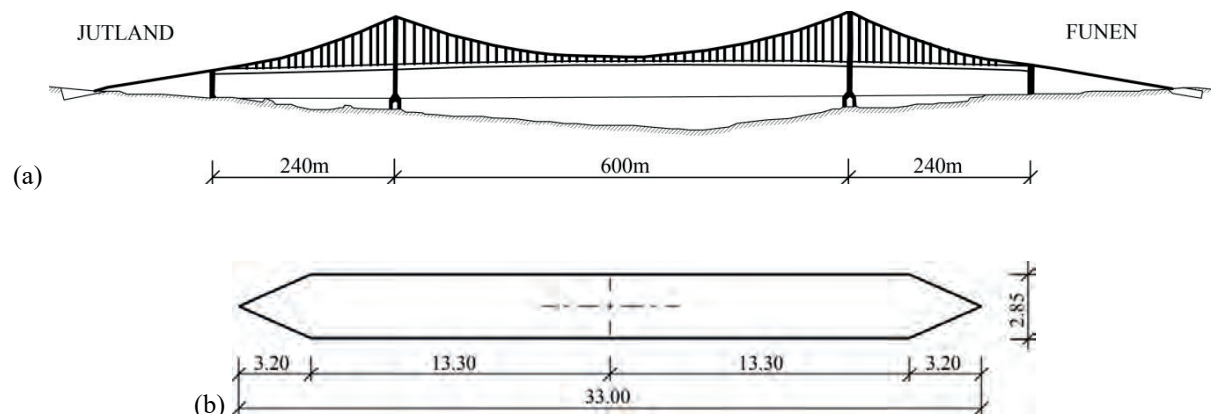


**Figure 2.** (a) Elevation view; (b) and schematic of the deck of the Lillebælt suspension bridge (Abbas and Morgenthal, 2014)

**Figure 3.** (a) Laboratory model of the New Little Belt suspension bridge (scale of 1:200) and (b) a mounted SunSPOT node
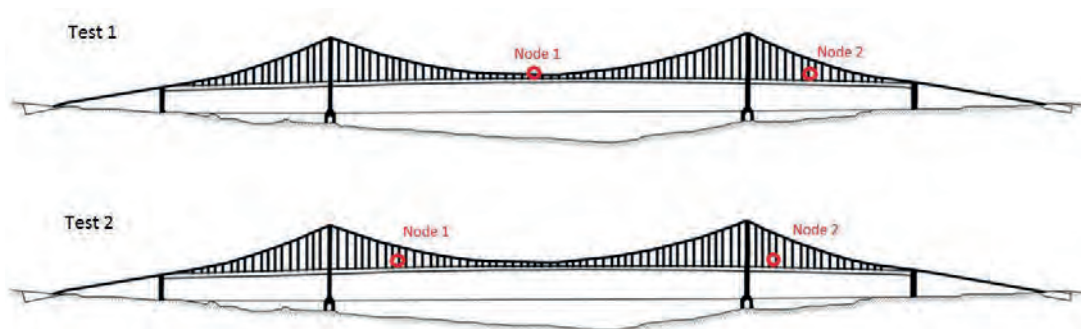


**Figure 4.** Sensor node locations in the tests 1 and 2

## Experimental setup and description of the performance tests

In Figure 3a, the down-scaled model (scale 1:200) of the suspension bridge is shown. The wireless SHM system proposed in this paper is installed on the bridge model, as shown in Figure 3b. Two sensor nodes (node 1 and node 2), wirelessly communicating with a computer through one base station, are attached to the bridge deck. The nodes are tasked to collect accelerations, calculate the frequency spectra and send the spectrum data to the computer, where the frequency spectra are plotted.

Six tests are performed in total, employing different sensor node placement, excitation intensity, and excitation direction. In the following, the two tests with excitations in the vertical direction, referred to as test 1 and test 2 (Figure 4), are discussed. In test 1, node 1 is placed at the middle of the central (longest) span and node 2 is placed at the middle of one of the side (shorter) spans. In test 2, node 1 is placed at ¼ of the length of the central span and node 2 at ¼ of the length of the side span.

## Discussion of experimental results

Figure 5 and Figure 6 illustrate the frequency spectra obtained from test 1 and test 2. For each of the two tests, the frequency spectra calculated by node 1 and node 2 are given. In general, the proximity between the results of both tests validates the applicability of the proposed wireless SHM system. It can be seen from the frequency spectra of test 1 that the first peak is observed at a frequency of approximately 3.1 Hz. The recurrence of this peak on both sensor nodes leads to the conclusion that this peak corresponds to the first eigenfrequency in the vertical direction. The second peak is also well distinguishable in both frequency spectra; however, the frequency corresponding to the second peak of node 1 does not coincide with the frequency of the second peak of node 2 and cannot be identified as an eigenfrequency of the structure. In test 2, however, both peaks in both frequency spectra occur at

almost the same frequencies. As can be seen in Figure 6, the frequencies of the second peak are 4.7 Hz and 5.4 Hz for node 1 and node 2, respectively. The difference between the frequencies in both sensor nodes at the second peak is considered negligible; hence, this frequency can be identified as an eigenfrequency of the structure. Similar to test 1, the first peak in test 2 occurs at a frequency of approximately 3.1 Hz. An interesting feature of the frequency spectrum obtained from node 2 in test 2 is the lack of symmetry of the plot about the Nyquist frequency, which in this study is 12.5 Hz. This lack of symmetry is attributed to data loss during the wireless communication of the results and is indicative of how could unreliable communication compromise the accuracy of the results. Judging from the shape of the spectrum above the Nyquist frequency and the symmetry property of the FFT, it is concluded that information concerning a peak at 3.1 Hz has been lost, which is very important in experimental modal identification.
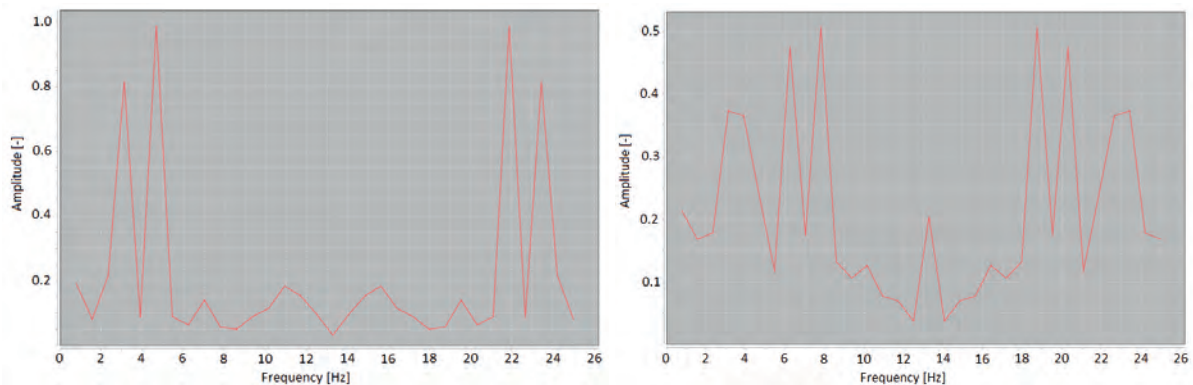


**Figure 5.** Frequency spectra of node 1 (left) and node 2 (right) obtained from the test 1
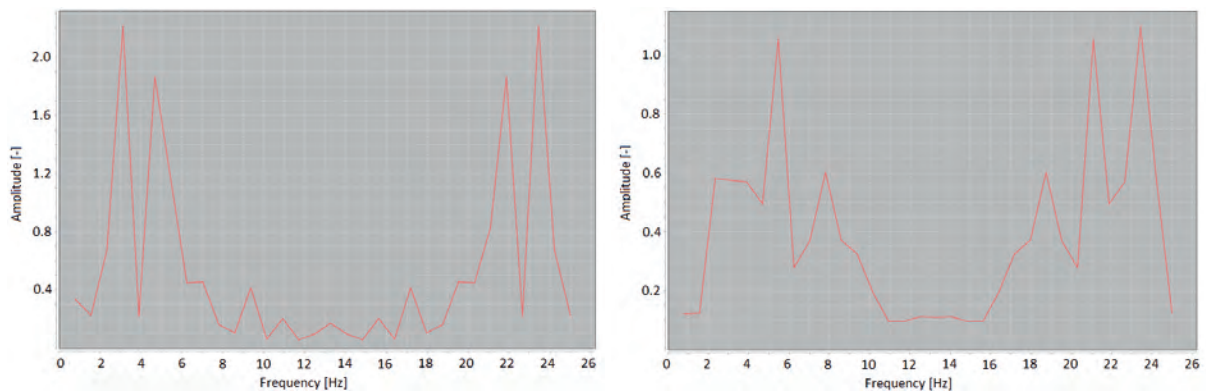


**Figure 6.** Frequency spectra of node 1 (left) and node 2 (right) obtained from the test 2

## Summary and conclusions

In recent years, the deterioration of structures due to ageing has stimulated a growing trend towards the use of structural health monitoring systems. Wireless structural health monitoring systems have drawn significant attention due to the merits of wireless sensing technologies compared to conventional wired structural health monitoring systems. Typical wireless systems for structural health monitoring comprise a network of smart wireless sensor nodes able to perform a broad wealth of monitoring tasks.

In this paper, an automated, decentralized wireless structural health monitoring (SHM) system has been developed for the identification of natural frequencies of structures. The proposed wireless SHM

system has been equipped with embedded algorithms, written in Java programming language, to manage the monitoring tasks both on-board the sensor nodes and at the server. More specifically, the embedded algorithms perform the collection of acceleration response data and the transformation of the collected data into the frequency domain using the fast Fourier transform. Then, the frequency spectrum data is wirelessly transmitted to the server, where the frequency spectra are plotted using a graphical visualization algorithm. The proposed SHM system has been validated through experimental tests on a model of an existing suspension bridge. Two different tests have been carried out to examine the efficiency of system, using two sensor nodes placed at two different locations of the model. In the first test, one of the sensor nodes has been placed at the middle of the central span of the bridge and the other sensor node is placed at the middle of one adjacent span. In the second test, both sensor nodes have been kept on the same spans as they had originally been placed, but moved to a distance of ¼ of the span length. The results from the second test have indicated that two peaks identified in the frequency spectra of both nodes can be attributed to eigenfrequencies of the structure. However, in the second peak of the first test, a discrepancy between the spectral frequencies has been observed. Finally, the lack of symmetry in the frequency spectrum of the second node in test 2 has been indicative of data loss, which in this case has caused the loss of valuable information regarding the first peak of the spectrum, as deduced from the spectrum plot above the Nyquist frequency.

Further tests could be conducted to optimize the positioning of the sensor nodes in order to identify the structural characteristics more accurately and efficiently. Furthermore, different types of structures could be tested in order to examine the robustness of the proposed SHM system.

## Acknowledgments

## References

Abbas, T. and Morgenthal, G. (2014). Numerical models for flutter analysis. In: *Proc. of the 6th International Symposium on Computational Wind Engineering (CWE2014)*; Hamburg, Germany, 08/06/2014.

Cho, S., Yun, C. B., Lynch, J. P., Zimmerman, A., Spencer Jr., B. and Nagayama, T. (2008). Smart wireless sensor technology for structural health monitoring. *Steel Structures* **8**(4): 267-275.

Cooley, J. W. and Tukey, J. W. (1965). An algorithm for the machine calculation of complex Fourier series. *Mathematics of Computation* **19**(90): 297-301.

Dragos, K. & Smarsly, K. (2015). Embedding numerical models into wireless sensor nodes for structural health monitoring. In: *Proc. of the 10th International Workshop on Structural Health Monitoring*; Stanford, CA, USA, 01/09/2015.

Dragos, K., Thessmann, G., Fathy, M., Wang, S., Liang, Y., Tauscher, E. and Smarsly, K., (2015). An embedded computing approach for modular wireless structural health monitoring systems. In: Abrahamczyk, L. & Schwarz, J. (eds.). *Forecast Engineering: Global Climate change and the challenges for built environment*; Weimar, Germany, 17/08/2015. Paper No. 1, 13 pp. Bauhaus University Weimar, Faculty of Civil Engineering, Institute of Structural Engineering, 2015.

Lei, Y., Shen, W. A., Song, Y. and Wang, Y. (2010). Intelligent wireless sensors with application to the identification of structural modal parameters and steel cable forces: from the lab to the field. *Advances in Civil Engineering* **2010:** 1-10.

Lynch, J. P., Sundararajan, A., Law, K. H., Sohn, H. and Farrar, C. R. (2004). Design of a wireless active sensing unit for structural health monitoring. In: *Proc. of SPIE's 11th Annual International Symposium on Smart Structures and Materials*; San Diego, CA, USA, 14/03/2004.

Oracle Corporation (2007). *Sun Small Programmable Object Technology datasheet*. Redwood Shores, CA, USA, 2007.

Ostenfeld, C., Haas, G. and Frandsen, A. G. (1970). Motorway bridge across Lillebælt: Model tests for the superstructure of the suspension bridge. *Bygningsstatiske Meddeleser* **41**(2): 99-112.

Shaylor, N., Simon, D. N. and Bush, W. R. (2003). A Java virtual machine architecture for very small devices. In: *Proc. of the 2003 Conference on Languages, Compilers, and Tools for Embedded Systems (LCTES 03)*; San Diego, CA, USA, 11/07/2003.

Smarsly, K. and Hartmann, D. (2009a). AMBOS – A self-managing system for monitoring civil engineering structures. In: *Proc. of the XVI Workshop on Intelligent Computing in Engineering (EG-ICE)*; Berlin, Germany, 07/15/2009.

Smarsly, K. and Hartmann, D. (2009b). Real-time monitoring of wind energy converters based on software agents. In: *Proc. of the 18th International Conference on the Applications of Computer Science and Mathematics in Architecture and Civil Engineering (IKM)*; Weimar, Germany, 07/07/2009.

Smarsly, K. and Law, K. H. (2013). A migration-based approach towards resource-efficient wireless structural health monitoring. *Advanced Engineering Informatics* **27**(4): 625-635.

Smarsly, K. and Law, K. H. (2014). Decentralized Fault Detection and Isolation in Wireless Structural Health Monitoring Systems using Analytical Redundancy. *Advances in Engineering Software* **73** (2014): 1-10.

Smarsly, K., Law, K. H. and König, M. (2011). Autonomous Structural Condition Monitoring based on Dynamic Code Migration and Cooperative Information Processing in Wireless Sensor Networks. In: *Proc. of the 8th International Workshop on Structural Health Monitoring (IWSHM)*; Stanford, CA, USA, 09/13/2011.

Swartz, R. A. and Lynch, J. P. (2009). Wireless sensor and networks for structural health monitoring of civil infrastructure systems. In: Karbhari, V. M. and Ansari, F. (eds.). *Structural health monitoring of civil infrastructure systems*; Woodhead Publishing Ltd: Cambridge, UK, 2009.

Zimmerman, A., Shiraishi, M., Schwartz, A. and Lynch, J. P. (2008). Automated modal parameter estimation by parallel processing within wireless monitoring systems. *ASCE Journal of Infrastructure Systems* **14**(1): 102-113.

# Evaluation of Change Detection Techniques using Very High Resolution Optical Satellite Imagery

*CEROVECKI Adriana [a], GHARAHJEH Siamak [b], HARIRCHIAN Ehsan [c], ILIN Dmitry [d], OKHOTNIKOVA Kristina [d]*

*[a] University J.J. Strossmayer, Osijek*

*[b] Middle East Technical University*

*[c] University Technology of Malaysia (UTM)*

*[d] Moscow State University of Civil Engineering*


*KERSTEN Jens*

*Chair of Computer Vision in Engineering, Bauhaus-University Weimar, Germany*

## Abstract

Remotely sensed imagery is a rich source of information and can contribute to various applications, for example land cover classification as well as rapid mapping for disaster and crisis-management support. A central issue is the reliable detection of relevant changes based on images from two or more dates.

The present paper offers a report over the changes detected based on very high resolution (VHR) optical satellite imagery after the heavy earthquake in L'Aquila, Italy on April 06, 2009. Well known pixel-based techniques are considered for the detection of desired changes. For comparing and verifying purposes, two different methods, namely post classification comparison (PCC) and multi date direct comparison (MDC), were deployed. The results of the analysis show that the majority of the changes are correctly identified over the region of interest. In spite of a general agreement between the results of PCC and MDC, it seems like that the MDC is predicting more promising results in terms of locating the severely changed spots. In the end, accuracy assessment was performed for the obtained analysis. The results show that the accuracy is in an acceptable range.

## Introduction

Remote sensing means the ability to detect change on the earth's surface through space-borne sensors (Ramachandra and Kumar 2004). The repetitive coverage of satellite images and the improvement of image quality can provide valuable assistance in the identification of changes (Jensen 1983).

Change detection (CD) is the process of identifying differences in the state of an object or phenomenon by observing it at different times (Singh 1989). The time and accuracy of change detection on the earth's surface can provide a better understanding of the relationships and interactions between human and natural phenomena and can provide guidance in the management of the use of resources. Temporal and spatial resolutions allow scientists to monitor and detect changes over a broad scale and help planners to obtain or maintain information on various phenomena, such as shifting agricultural patterns, crop stress, disaster monitoring, land use and land cover changes (Rogan and Chen 2004).

A geographic information system (GIS) is a useful tool for measuring the change between two or more time periods. It has the ability to incorporate multi-sources of data into a change detection platform (Lu et al. 2004). For example, the use of multiple layers, such as classified images, topographical maps, soil maps and hydrological maps, provides a greater ability to extract useful information about the changes over a particular area. Moreover, GIS can measure the trends in these changes by modeling the available data and using statistical and analytical functions. The benefit of GIS is the provision of different outputs in different formats (e.g. maps or tables), which allows users to select the appropriate output for extracting the desired information.

Remotely sensed data and GIS are widely used for detecting land use and land cover changes. Many studies have attempted to use remotely sensed data and GIS to address land use change detection e.g. (Brondizio et al. 1994, Kuemmerle et al. 2006, Pelorosso et al. 2009, Thapa and Murayama 2009). A variety of procedures or methods of remote sensing technologies are used to detect land use and land cover changes. Some studies have actually utilized remote sensing techniques, others have integrated remotely sensed data with GIS data e.g. (Michalak 1993, Weng 2001, Rogan et al. 2007). In addition, many studies have reviewed and summarized the various change detection techniques (Singh 1989, Rogan and Chen 2004, Mouat et al. 1993, Deer 1995, Jensen 1993).

As for CD-techniques from remotely sensed images, different techniques have been developed which each comes in handy depending on the requirements and conditions. However, the selection of the most suitable method or algorithm for CD is not easy in practice (Lu et al. 2004). Researchers have made enormous efforts in developing various CD methodologies including both the traditional pixel-based (Mas 1999) and more recently, the object-based (Araya and Hergarten 2008) approach.

In this work two traditional pixel-based approaches are utilized in order to detect destroyed houses based on two QuickBird satellite images, a pre-disaster scene from 2006 and a scene covering the same region acquired immediately after an earthquake in April 2009.

## Pixel- vs. Object-Based Analysis

Among a number of various CD strategies, two pixel-based approaches were employed for comparing purposes. Even though object- or segment-based approaches tend to be more suitable for the analysis and classification of VHR satellite data, traditional pixel-based techniques are applied here because of the following reasons. (1) The first step in segment-based analysis is image segmentation, i.e., the partition of an image into non-overlapping sets of pixels according to a defined criterion, for example the homogeneity of neighboring pixel intensities. The choice of a suitable segmentation approach from various available methods as well as the definition of required parameters (e.g. homogeneity thresholds) is difficult and requires expert knowledge. (2) Object-based image analysis software like Trimble's eCognition (Trimble 2015) supports various classification approaches like fuzzy logic and context-driven analysis, which in turn require expert knowledge and are therefore not applicable here. (3) The application of pixel-based approaches on VHR data is known to produce very noisy classification results due to high intra- and low inter-class variations. In order to reduce this effect, Haralick texture features (Haralick, 1979) are used in order to incorporate information from a local neighborhood of each image pixel.

**Figure 1.** Input pre-disaster QuickBird scene (DigitalGlobe 2006)**.**

The post classification comparison (PCC) and multi date direct comparison (MDC) are two major sub-components of the classification based change detection methods. In post classification comparison method the pre- and post-image is separately classified and then are compared at once in search of relevant changes. In PCC method the effect of atmospheric factors are minimized, yet the accuracy of the final results depend on classification accuracy of each individual image. On the other hand, in MDC method only one classification for stacked data is required, however there can be confusion over labeling the change classes. More relevant literature work can be found in (Hussain et al. 2013).

## Dataset and Software

Two QuickBird scenes covering the city of L'Aquila, Italy, acquired on September 04, 2006 (Figure 1) and April 08, 2009 (DigitalGlobe 2009) are used in this study. The pan-sharpened scenes have a ground sampling distance of 0.6 m, cover an area of 25 km² and consist of four spectral bands (red, green, blue and near-infrared).

In order to detect the changes in the available images QGIS software (QGIS 2015) was used. This software is previously known as "Quantum GIS". QGIS is a cross-platform free and open-source desktop GIS application that provides data viewing, editing, and analysis capabilities. QGIS is a software that allows creating maps with many layers using different map projections. All crated maps can be composed in different formats and for different users. Different kinds of raster formats are supported and the software can perform georeferencing of images (Treglia 2015).

# Change Detection Workflows

As stated above, two different pixel-based approaches were used in this study. The CD methods PCC and MDC consist of the following main steps: Pre-processing, image classification, change detection and post-processing. Whereas in PCC the image classification is done for each image individually, the changes of interest are directly classified based on a stacked image in MDC.

## Pre-processing

The topographical variations in the surface of the earth and the tilt of the satellite sensor affect the distance with which features on the satellite image are displayed. The more topographically diverse the landscape, the more distortion inherent to the image. Hence, first of all the steps is orthorectification - the process of removing perspective distortionsfor each image pixel individually (GIS dictionary 2015). Based on elevation data (Figure **2**, 1), the exterior orientation of the sensor (Figure **2**, 2) and the pixel intensities (Figure **2**, 1) the new pixel locations with respect to a parallel projection (Figure **2**, 1) as well as the corresponding intensities can be computed. In this study, the ASTER global digital elevation model (GDEM) V2 available at (ASTER 2015) with a ground sampling distance of 30 m was used.
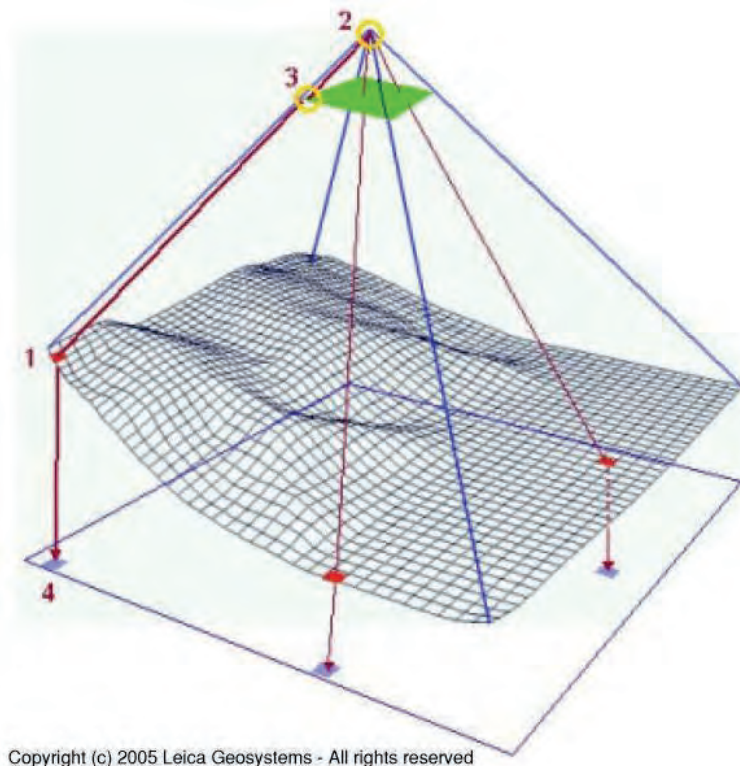
**Figure 2.** Orthorectification process (Image courtesy of Satellite Imaging Corporation).

In order to reduce the computational loads and the complexity of CD, a region of interest (ROI) is defined and used for all further processing steps (Figure 3).
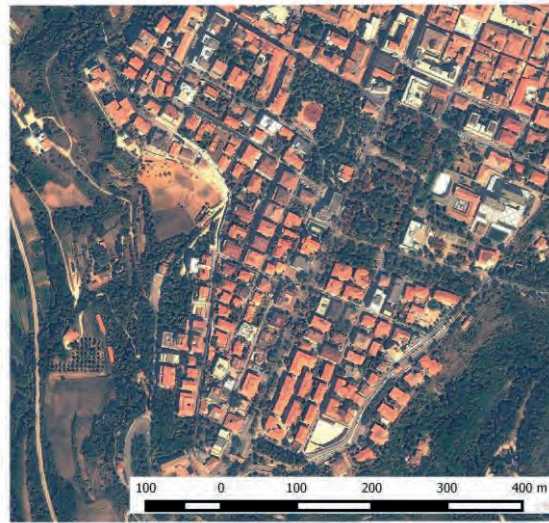
**Figure 3.** Defined ROI.

Whereas pixel displacements due to sensor orientation and topography are removed by the orthorectification step, it is still possible that the two scenes do not exhibit perfect overlay. Therefore, a further image-to-image registration is required. This step has a crucial value since the change detection results immediately depend on this registration. A four parameter 2D-Helmert transformation is usually used for this step, where at least two corresponding points have to be identified manually in the pre- and post-scene to estimate the transformation parameters (two translations, one rotation and a scale factor). The best accuracy will be given by providing a higher number of corresponding points covering the entire image area. A Helmert transformation in QGIS software can be applied with the „Georeferencer" plugin.

Orthorectification removes the influence of topography using a DEM. Since no detailed information regarding the objects on top of the earth's surface, for example houses, are incorporated, the rooftops and other objects usually still are displaced in the images according the sensor pose and the height of the building. Hence, it is crucial to use corresponding points located on the ground for the registration.

In order to enable a pixel-wise analysis, the spatially transformed image is resampled with respect to the reference image using a nearest neighbor interpolation. After this step both scenes have the same spatial resolution and pixel positions.

Based on the available spectral information, i.e., the red, green, blue and near infrared channel, several further features can be computed in order to achieve a better separability of the classes in the feature space domain. In this work the normalized differenced vegetation index (NDVI),

$$NDVI = \frac{NIR - RED}{NIR + RED} \tag{1}$$

the HSV (hue, saturation and value) cylindrical-coordinate color transform (Gozales and Woods 2006) as well as 8 different Haralick texture features (Haralick, 1979) are used. The texture features are computed from so-called gray level co-occurrence histograms obtained from a local neighborhood of each pixel. Even though the classification approach itself is pixel-based, local contextual information is incorporated into the classification process by using these features.

As a result of pre-processing 17 channels for each scene are available for the classification: 4 images with red, green, blue and near infrared information, 3 images with hue saturation and value channels, 8 images with texture layers, a single grayscale image as well as the NDVI channel.

## Image Classification

In both methods, PCC as well as MDC, the individual classification of each image pixel into defined thematical classes is required. Whereas in PCC a landcover classification of each image is done, the changes are directly classified in MDC.

In this study the Maximum-Likelihood (ML) approach for image classification is used. According to the image content, the image analyst has to define different thematic classes (e.g. buildings, vegetation, etc.) as well as to provide representative training data for each class. In QGIS this is realized by defining regions of interest for each class using shapefiles. Based on $N$ provided training pixels, the mean value $\mu_c$ in each channel as well as the covariance matrix $\Sigma_c$ can be computed for each class $c$ according to

$$\mu_c = \frac{1}{N}\sum_{i=1}^{N} X_i \text{ and } \Sigma_c = \frac{1}{N-1}\sum_{i=1}^{N}\left(X_i - \mu_c\right)\cdot\left(X_i - \mu_c\right)^{T}, \tag{2}$$

where $X_i$ are the 17-dimensional feature vectors and $\Sigma_c$ is a $17\times17$ matrix. A pixel is classified according the maximum log-likelihood criterion

$$\log\left[p\left(X_i \mid \mu_c, \Sigma_c\right)\right] = -\frac{1}{2}\left[\log\left(\left|\Sigma_c\right|\right) + \left(X_i - \mu_c\right)^{T}\Sigma_c^{-1}\left(X_i - \mu_c\right)\right]. \tag{3}$$

The main difficulty of this approach is that the quality of the classification result depends on the definition of thematic classes and the fact that thematic classes usually consist of many spectral classes. A training region may intuitively be defined according to Figure 4.

The visualization of the corresponding scatter plots clarifies the problem (Figure 5): Even though a rooftop represents a single thematic class, it consists of two spectral classes, since we can observe differences in illumination due to different main rooftop orientations.



**Figure 4.** Example training ROI for the thematic class building.

The mean value for the two plots will obviously lie between the two cluster centers which results in a wrong model and bad classification results. Hence, the thematic classes usually have to be subdivided into many different spectral classes corresponding to single clusters in the feature space domain. Furthermore, all occurring classes have to be modeled in order to ensure good results. A representative parametrization is ensured when a number of $1000 \cdot N_{\text{dim}}$ pixels are provided for each class.
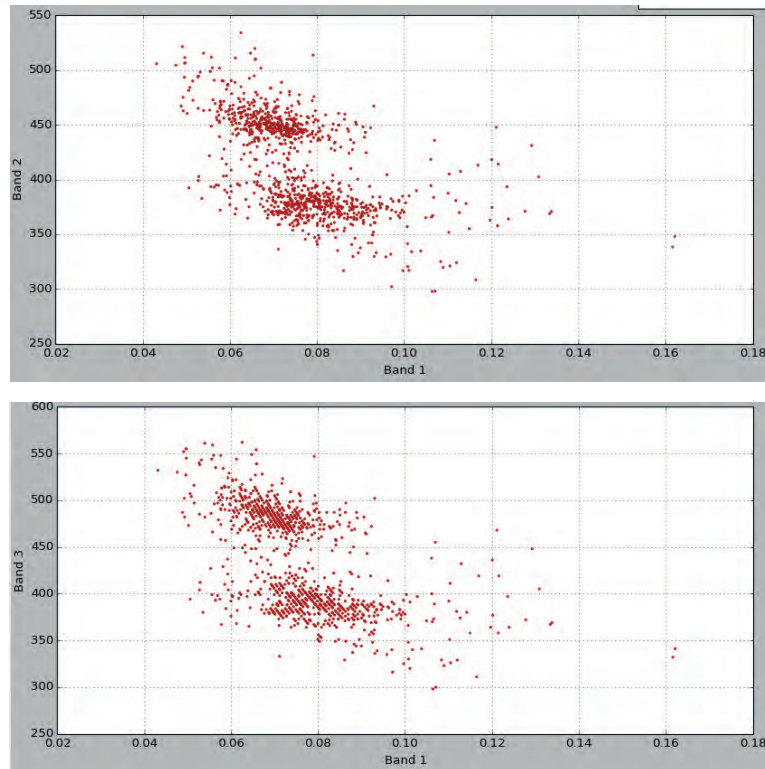


**Figure 5.** Scatter plots of the training region shown in Figure **4**. Upper : NDVI (band 1) and grayscale channel (band 2). Lower : NDVI (band 1) and red channel (band 2).
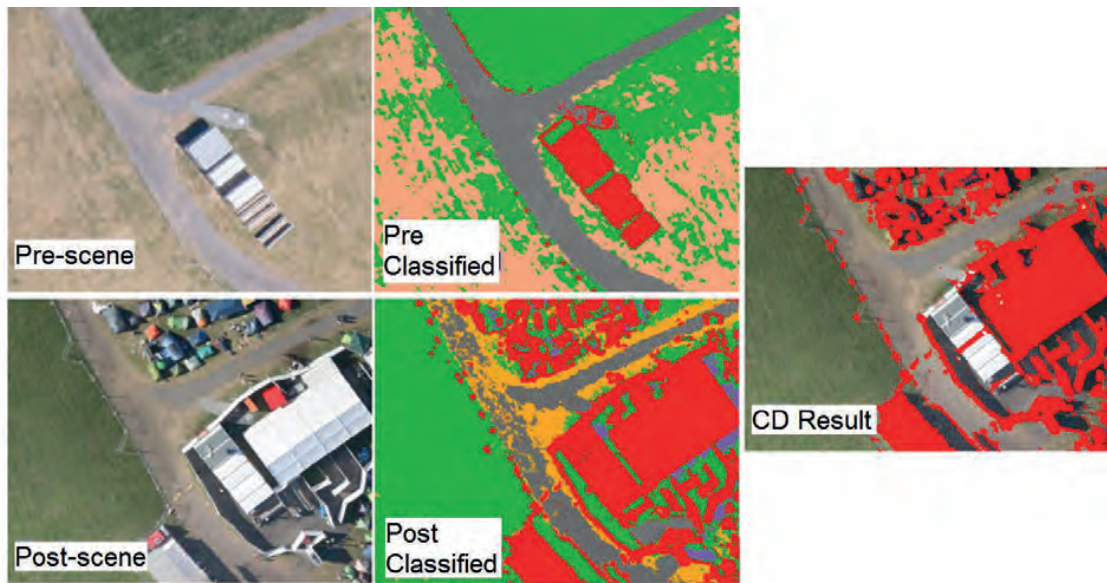
## Change Detection

After the single images are classified individually according to the defined classes, the changes of interest can easily be obtained by simply searching for the corresponding changes of the thematic classes (PCC). In Figure 6 exemplary results of PCC are shown.

In the pre-scene a container is present and in the post-scene more artificial objects are present (Figure 6, left and center). All changes from non-artificial classes to artificial objects are marked in red in the CD result (Figure 6, right). Since the container was already present in the pre scene, it is not detected as change. The quality of CD for PCC obviously depends on the quality of the classification results.

In MDC the changes of interest are directly classified in MDC by training a classifier using a stack of the two images (34 channels). Even though only one classification is done here, the definition of appropriate training regions and classes is much more complex.

## Post-Processing

Since the image pixels are classified individually, the classification results are usually affected by salt-and-pepper noise. These artifacts can easily be removed or reduced using a majority filter or morphological filters like opening and closing (Efford 2000).

**Figure 6.** Detection of changes in PCC : Artificial structures in the pre and post scenes (red) and the corresponding changes wrt this class (right image, red).

# Results and Discussion

In this study, PCC and MDC is applied in order to detect destroyed houses after the earthquake in L'Aquila, Italy, on April 06, 2009. Due to the simple pixel-based analysis, the long period of time between the acquisition of the images as well as the different sensor configurations, missclassifications are likely. Hence, the aim was to identify regions in the image where several neighboring pixels support the hypothesis of an destroyed house instead of robustly localizing the damages. The CD results presented here may therefore serve as a support for the identification and localization of destroyed infrastructure in large satellite images by visual analysts.

PRE-SCENE          POST-SCENE
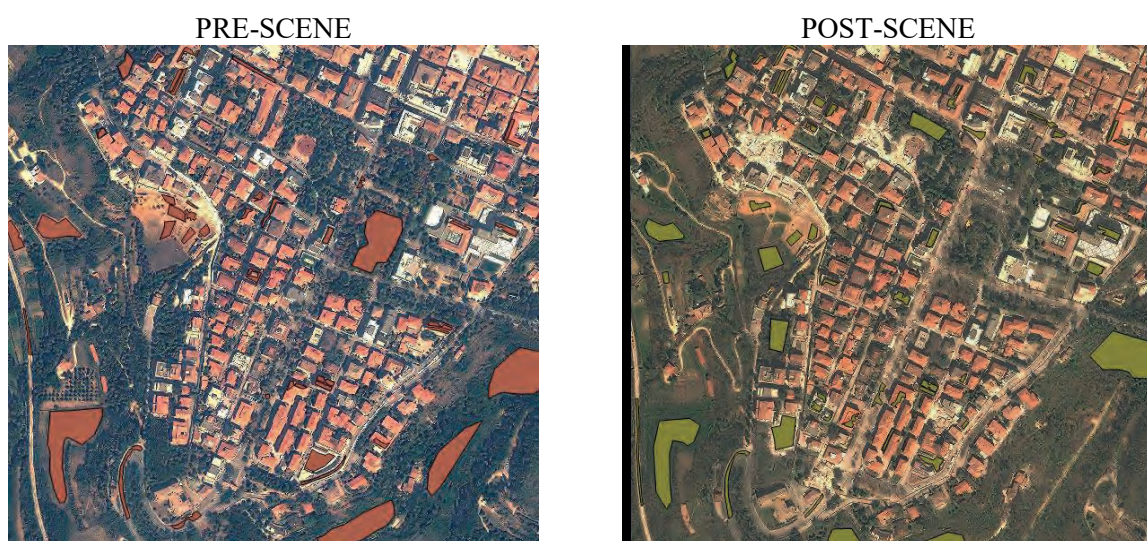


**Figure 7.** View of the pre- and post-scene training areas.

## Post Classification Comparison

Figure 7 shows the training shapefiles for each scene. There are some similar areas on each image used for classification but since post-scene also contains damaged buildings there was a need of changing some areas used for classification.

The ML-classification results were filtered using a majority filter with the purpose of reducing the salt and pepper noise (Figure 8). This step has a crucial value since it considers every pixel and his neighbourhood and changes the classification if the many pixels nearby are classified as a different class.

Comparing the two images we find similar shapes where the non-damaged buildings are found. Looking at the legend, classification for damaged buildings was not possible due to spectral similarities to other classes. In order to get the best divergence between different classes it was best to leave the destroyed building as a road or soil in the end. Destroyed buildings had similar colors as soil or roads and therefore the misclassification appeared in this area. Since the problem is related to changes from building to any other class it is not important whether the changed building is soil, road or something else.

PRE-SCENE                    POST-SCENE
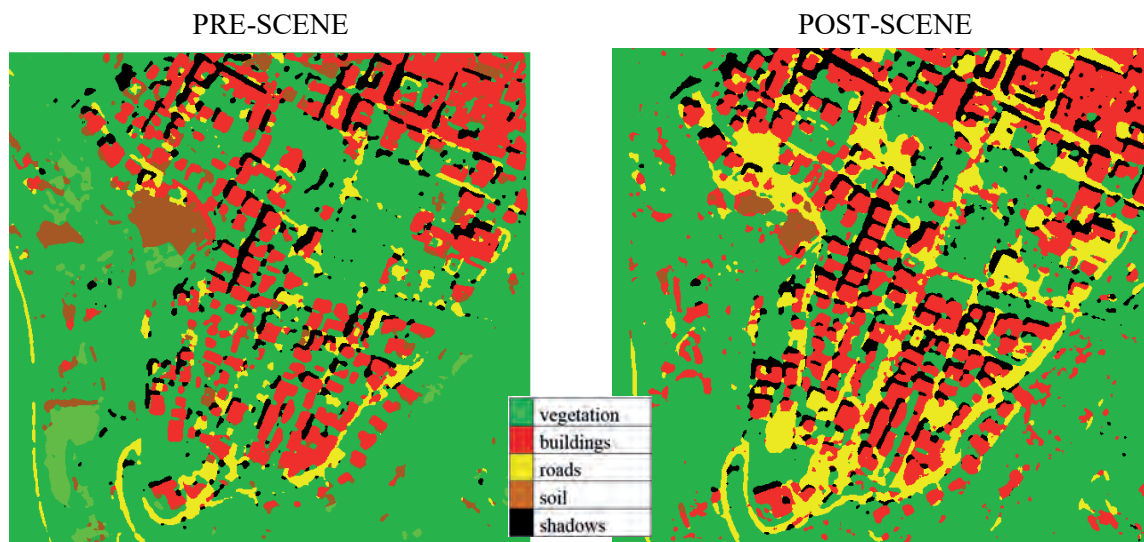


**Figure 8.** Majority filtered ML-classification results.

After applying the filter to the images, accuracy assessment (AA) was performed for each scene based on test regions defined in a shapefile. In order to get reliable results, these regions should not be used for the training procedure and an equal number of pixels for each class has to be used. Hence, new regions had to be defined for AA.

The confusion matrix is a square table which contains information about actual and predicted classifications of the test pixels. Usually, the rows of this matrix represent the true test instances, wheras the columns are related to the predicted classes using a classifier. A perfect classifier would result in a diagonal confusion matrix. The more missclassifications we can observe, the more and higher off-diagonal elements can be observed. From this matrix three different values can be computed. The overall accuracy can be derived by counting all correctly classified reference pixels and dividing this by the total number of all reference pixels. In order to get more detailed class-related information, the user and producer accuracy can be computed for each class. The producer's accuracy refers to the probability that a certain land-cover of an area on the ground is classified as such, while

the user's accuracy refers to the probability that a pixel labeled as a certain land-cover class in the map is really this class. AA of the pre-scene for filtered image shows overall accuracy of 97.75 %.

**Table 1.** Accuracy assessment results of the pre-scene.

| Class | Producer's Accuracy [%] | User's Accuracy [%] |
|---|---|---|
| Vegetation | 99.68 | 96.35 |
| Meadow | 97.44 | 100.00 |
| Soil | 86.96 | 99.46 |
| Buildings | 99.28 | 100.00 |
| Shadow | 99.44 | 95.77 |
| Roads | 99.91 | 97.63 |

The results in Table 1 show that the classification results are very good. The relatively low producer's accuracy shows that the classifier had problems in classifying soil pixels correctly. Nonetheless, by visual inspection of the classification results (Figure 8) we can easily detect areas which are obviously misclassified, for example roads. This intends that more test regions are required in order to obtain a statistically reliable information.

Further, same procedure was performed on the post-scene. AA showed 92,86 % of overall accuracy. The low user's accuracy and the high producer's accuracy of roads (Table 1Table 2) indicates that several pixels from other classes were incorrectly classified as roads whereas nearly all pixels from roads were classified correctly as roads. Because of this we can see more pixels classified as roads in the result of the post-scene (Figure 8, right, yellow).

**Table 2.** Accuracy assessment results of the post-scene.

| Class | Producer's Accuracy [%] | User's Accuracy [%] |
|---|---|---|
| Vegetation | 98.19 | 99.89 |
| Soil | 99.65 | 99.95 |
| Buildings | 94.48 | 93.99 |
| Shadow | 99.11 | 99.76 |
| Roads | 98.83 | 55.88 |



**Figure 9.** Changes detected using PCC method.

CD was performed with the help of a MATLAB script, which identifies the changes of interest based on the classified maps. The changes from pixels of the class "Buildings" in the pre-scene to any other class in the post-scene are shown in Figure 9 (marked in red).

Changes detected are matching areas that had damaged and collapsed buildings. Due to spectral similarities there are some misclassifications in areas which changed over time but were not damaged. Another source for confusions is the shift of the rooftop positions due to different sensor poses also depending on the position of the buildings as well as their height. The overall accuracy of the detected changes is 94,20 %.

**Table 3.** PCC accuracy assessment results.

| Class | Producer's Accuracy [%] | User's Accuracy [%] |
|---|---|---|
| Changed/Destroyed | 61.54 | 67.53 |
| Unchanged | 97.24 | 96.44 |

The results in Table 3 show that only 61.54 % of all reference pixels could correctly be detected as changed and only 67.53 % of all reference pixels classified as changed were reference pixels from that class. Nonetheless, the visual inspection of the result (Figure 9) indicates, that this method is suitable to highlight potential destroyed areas which could be used in the context of decision support workflows.

## Multi Date Direct Comparison

With regard to the MDC attempt, the general trend is to specify couple of training areas over the ROI associated with desired changes and unchanged features of the land (shown in Figure 10). The minimum distance classification algorithm (Richards and Jia 2006) produced the best results compared other methods like ML. The reason for this is that some features of the training regions, for example the Haralick texture features, were constant for all pixels. Hence, it was not possible to compute a covariance matrix in these cases and a ML-classification was not possible.



**Figure 10.** Training areas for changed and unchanged spots.

**Figure 11.** Detected changes (red) using MDC.

Instead of the log-Likelihood (3) the Euclidean distance in the 34-dimensional feature space is used as the classification criterion. The majority-filtered result of CD within pre- and post-scenes are visualized in Figure 11.

As seen in Figure 9, the red areas are indicating the changed fields in the post-scene. Some inaccuracies can be observed in certain areas due to confusing factors such as differences in lighting conditions and tilted view of some of tall structures. The AA for the mentioned case is shown in Table 4. The overall accuracy for this method is 96.57 %.

**Table 4.** MDC accuracy assessment results.

| Class | Producer's Accuracy [%] | User's Accuracy [%] |
|---|---|---|
| Changed/Destroyed | 63.96 | 93.77 |
| Unchanged | 99.60 | 96.74 |

Especially the user's accuracy for the changed class is significantly higher than using PCC, which indicates that the probability that a pixel labeled as changed in the map is really this class.

By comparing the CD results for two different methods, the MDC classification approach yields relatively better results. Although there are some inaccurate areas identified as changed in north eastern corner of the map by MDC method, the prominent destructions are well-observed by the used approach. Possible reasons for this could be the lack of precise and complete training data and the spectral similarity of thematic classes.

## Conclusion and Outlook

In this study two different change detection approaches are examined in order to detect destroyed houses in very high resolution satellite images. Even though object-based techniques in general are known to be more suitable for the analysis of very high resolution satellite imagery, traditional pixel-

based methods are used here. A reason for this is the lack of experiences in obtaining an appropriate image segmentation as well as in using expert software systems for an object-based image analysis. Nonetheless, the used Maximum-Likelihood (ML) classification approach can also be used for an object-based analysis.

The results of the accuracy assessment indicate that the multi date direct comparison (MDC) produces better results than the post classification comparison (PCC) for the used dataset. Whereas in MDC no landcover classification of the pre- and post-scene is required, the identification and definition of the occurring spectral classes is much more difficult than in PCC.

Minor shortcomings were faced in classification phase in PCC method, yet the results and accuracy of the analysis are relatively acceptable and a visual inspection of the analyzed images in a smaller scale can reveal the potentially damaged buldings.

For the MDC, minimum distance method was chosen most accurate among others only after careful investigation of the various results. The main reason for the fail of the ML-approach was the homogeneity of some spectral features within defined training areas which lead to zero standard deviations. A ML-classification in QGIS fails in this case.

Overall, it can be concluded that although the change detection by both methods might sometimes fail to give the exact result as expected, it gives a general picture of the most likely areas suspicious of experiencing change. While it can be quite tedious to identify such changes free of any digital image processings, the result of analysis narrows this quest down to a practical level.

In further works, different object-based methods could be tested and compared to the used pixel-based approaches.

# References

Araya, Y.H., Hergarten, C., (2008). A comparison of pixel and object-based land cover classification: a case study of the Asmara region, Eritrea. In: *WIT Transactions on the Built Environment, Geo-Environment and Landscape Evolution III 100*.

ASTER (2015). http://gdem.ersdac.jspacesystems.or.jp/, accessed at August 10, 2015.

Brondizio, E. (1994). Land Use Change in the Amazon Estuary: Patterns of Caboclo Settlement and Landscape Management. *Human Ecology*, **22** (3): 249-278.

Deer, P. (1995). Digital Change Detection Techniques in Remote Sensing. *DTIC Document, Technical Report*.

DigitalGlobe (2006). QuickBird scene 054594261010_01_P001, Level S2AS, DigitalGlobe, Longmont, Colorado, 09/04/2006.

DigitalGlobe (2009). QuickBird scene 054594261020_01_P001, Level S2AS, DigitalGlobe, Longmont, Colorado, 04/08/2009.

GISdictionary (2015).http://support.esri.com/en/knowledgebase/GISDictionary/term/orthorectification accessed at August 28, 2015.

Gonzalez, R. C., Woods, R. E. (2006). *Digital Image Processing (3rd Edition)*. Prentice-Hall, Inc., Upper Saddle River, NJ, USA.

Efford, N. (2000). *Digital Image Processing: A Practical Introduction Using Java$^{TM}$*. Pearson Education.

Haralick, R. M. (1979). Statistical and structural approaches to texture. *Proc. IEEE*, **67** (5): 786-804.

Jensen, J. R. E. (1983). Urban/Suburban Land Use Analysis. *American Society of Photogrammetry*, Falls Church, Virginia, **2**: 1571-1666.

Jensen, J. R., Lulla, K. (1987). Introductory digital image processing: a remote sensing perspective. *Taylor and Francis*.

Kuemmerle, T. (2006). Cross-Border Comparison of Land Cover and Landscape Pattern in Eastern Europe Using a Hybrid Classification Technique. *Remote Sensing of Environment*, **103** (4): 449-464.

Lu, D. (2004). Change Detection Techniques. *International Journal of Remote Sensing*, **25** (12): 2365-2401.

Mas, J.F., (1999). Monitoring land-cover changes: a comparison of change detection techniques. *International Journal of Remote Sensing* **20**: 139–152.

Hussain, M., Chen, D., Cheng, A., Wie, H., Stanley, D. (2013). Change detection from remotely sensed images: From pixel-based to object-based approaches. *ISPRS Journal of Photogrammetry and Remote Sensing,* **80**: 91–106.

Michalak, W. Z. (1993). GIS in Land Use Change Analysis: Integration of Remotely Sensed Data into GIS. *Applied Geography*, **13** (1): 28-44.

Mouat, D. A. (1993). Remote Sensing Techniques in the Analysis of Change Detection. *Geocarto International*, Vol. 8, No. 2, 1993, pp. 39-50. DOI: 10.1080/10106049309354407

Pelorosso, R. (2009). Land Cover and Land Use Change in the Italian Central Apennines: A Comparison of Assessment Methods. *Applied Geography*, **29** (1):35-48.

QGIS (2015). http://www.qgis.org/en/site/, accessed at October 1, 2015.

Ramachandra, T., Kumar, U. (2004). Geographic Resources Decision Support System for Land Use, Land Cover Dynamics Analysis. *Proceedings of the FOSS/GRASS Users Conference*, Bangkok, Thailand.

Richards, J. A., Jia, X. (2006). *Remote Sensing Digital Image Analysis: An Introduction* (4th ed.). Springer-Verlag Berlin, Heidelberg, Germany.

Rogan, J. (2004). Remote Sensing Technology for Mapping and Monitoring Land-Cover and Land-Use Change. *Progress in Planning*, **61** (4): 301-325.

Rogan, J. (2007). Integrating GIS and Remotely Sensed Data for Mapping Forest Disturbance and Change. In*: M. A. Wulder and S. E. Franklin, Eds., Understanding Forest Disturbance and Spatial Pattern: Remote Sensing and GIS Approaches*, pp. 133-171.

Singh, A. (1989). Review Article Digital Change Detection Techniques Using Remotely-Sensed Data. *International Journal of Remote Sensing* **10 (**6): 989- 1003.

Thapa, R. B. (2009). Urban Mapping, Accuracy, & Image Classification: A Comparison of Multiple Approaches in Tsukuba City, Japan. *Applied Geography*, **29** (1): 135-144.

Treglia, M. L. (2015). An Introduction to GIS using QGIS (v. 2.6.1). http://mltconsecol.github.io/QGIS-Tutorial/QGIS-Tutorial/Treglia_OSOS%20Notes_V1.01.pdf, accessed at August 28, 2015.

Trimble (2015). http://www.ecognition.com/suite, Accessed at October 1, 2015.

Weng, Q. (2001). A Remote Sensing GIS Evaluation of Urban Expansion and Its Impact on Surface Temperature in the Zhujiang Delta, China. *International Journal of  Remote Sensing*, **22** (10): 1999-2014.

# Evaluation of Existing Masonry Structures under Multiple Extreme Impacts

PETRUS Cristian [a], MARIC Dario [b], THOMAIDIS Ioannis [c], THOMAIDIS Ioannis – Prodromos [c], PIOMBO Silvia [d], SCAGLIOTTI Giulia [e], DIMITRENKO Evgeniy [f], TIRADO Rodolfo Javier [g], KAHSAY HAGOS Simon [h]

[a] Politehnica University of Timisoara, Faculty of Civil Engineering, Romania

[b] University Josip Juraj Strossmayer Osijek, Faculty of Civil Engineering, Croatia

[c] Aristotle University of Thessaloniki, Faculty of Civil Engineering, Greece

[d] Universita degli Studi di Genova, Scuola Politecnica, Department of Civil Engineering, Italy

[e] Universita degli Studi di Pavia, Faculty of Civil Engineering and Architecture, Italy

[f] National Aviation University, Institute of Airports, Department of Computer Technologies in Constructions, Kiev, Ukraine

[g] Universidad Industrial de Santander, Faculty of Civil Engineering, Bucaramanga, Colombia

[h] Bauhaus-Universität Weimar, Faculty of Civil Engineering, Germany


ABRAHAMCZYK Lars, SCHWARZ Jochen

Earthquake Damage Analysis Center, Bauhaus-University Weimar, Germany

## Abstract

In close collaboration with local partners, Earthquake Damage Analysis Centre (EDAC) of Bauhaus University Weimar initiated a Turkish-German joint research project on Seismic Risk Assessment and Mitigation in the Antakya-Maraş-Region (SERAMAR). In this context, the instrumental investigation of buildings being representative for the study area becomes an essential part of the project to calibrate the models and to predict reliable capacity curves as well as scenario-dependent damage pattern or failure modes. A number of masonry buildings have been chosen and could be temporarily and permanently equipped with modern Seismic Building Monitoring Systems (BMS).

In this paper, one of the temporarily instrumented masonry buildings will be investigated in detail to evaluate the dynamic response and horizontal load bearing capacity under seismic action. The available response measurements are elaborated and the real response characteristic of the study object determined as input parameters for the model calibration and validation. The capacity of the study building is determined for different model assumptions to consider the model uncertainties in the damage prognosis. Therefore, a 3D numerical model is created using the computer software SAP2000, whereas the masonry walls are represented by piers and spandrels following the equivalent frame approach. The nonlinear behavior of the elements is described by non-linear hinges following a set of different available formulas and approaches.

Finally, an experimental testing on small scale approximation of the real structure could be conducted in part of the project. The Experiment pointed out the vulnerable character of the structure when it is subjected to an earthquake after earthquake scenario.
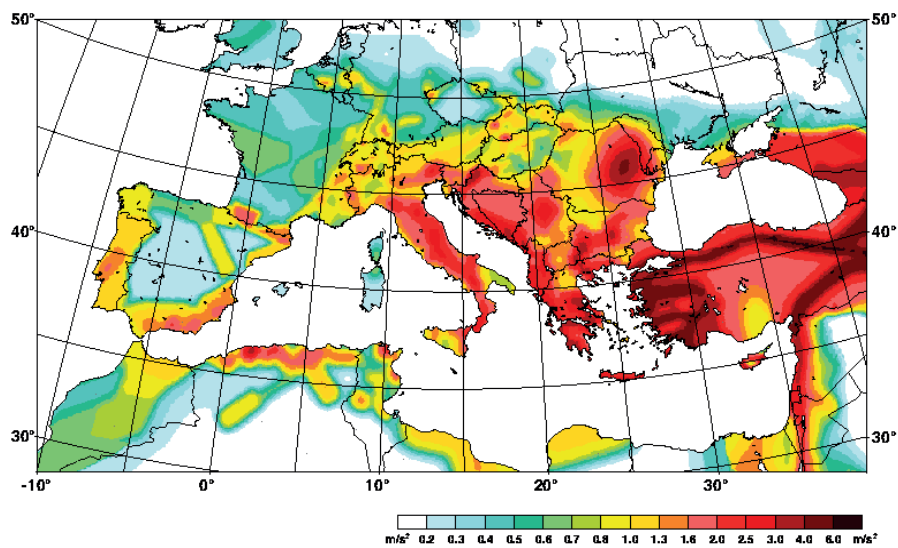
**Figure 1.** Seismic zonation map of Europe [1]

# Introduction

History as well as recent recordings has shown us that earthquakes impact our daily lives in such a way that the engineers and architects try to build a risk free and healthy environment for the community. Due to the variable nature of ground motion, such a task is rarely achieved. Earthquakes occur all over the world and are a result of a sudden release of energy from the Earth's crust. This affects all surrounding regions in a manner influenced by soil factors, wave propagation and intensity of the seismic wave. Almost half of the European continent is affected by seismic activity, as it can be seen in Figure 1.

Earthquakes are a present hazard which were also mentioned in ancient times by historians and scribes, which recorded in writing the damages and effects of the extreme events in a subjective manner. In present times, more objective technologies and techniques are used to evaluate the magnitude of an earthquake. Since all of Turkey is vulnerable to seismic activities, in Figure 2 it can be observed a history of the seismic events which occurred on the current territory of the country.

Recent events, such as the one from the Van province from 2011 having a magnitude of 7.1 on the Richter scale, reminded us of the destructive force of the ground motion, as it can be seen in Figure 3.



**Figure 2.** History of earthquakes in Turkey

*[https://en.wikipedia.org/wiki/List_of_earthquakes_in_Turkey]*

**Figure 3.** Damages of buildings after the Van earthquake, 2011

*[http://www.eqclearinghouse.org/2011-10-23-eastern-turkey/2011/10/31/photos-of-earthquake-damage/, photos from I. Bedirhanoglu]*

## Case study

The proposed structure to be analysed is a real structure from the city of Antakya, situated in the South-eastern part of Turkey near the East Anatolian seismic fault [2 - 4]. The building is made of masonry and has 4 stories and a length of 22.7m by 11.2m with a storey height of 2.8m. The initial plans of the building showed 4 storeys on one side and 3 storeys on the other. Due to recent interventions, there was constructed an additional level on one side of the building, and modified the sensitivity to torsional effects. From the provided architecture plans, an area of 14.53m$^2$ was observed for the longitudinal walls and 9.52m$^2$ for the transversal walls. An overview of the building and the floor plan can be taken from Figure 4.
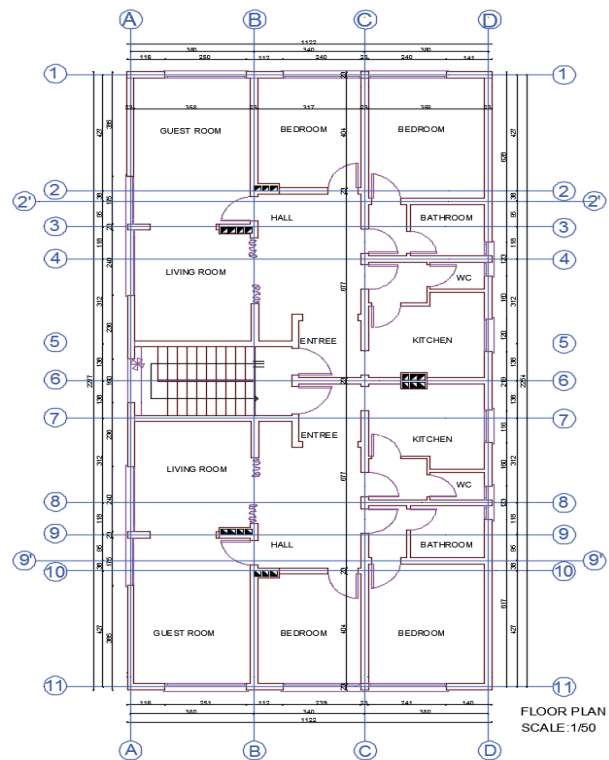


**Figure 4.** View of the existing building and floor plan (Source: EDAC)
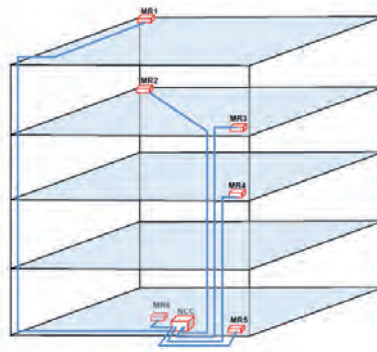
**Figure 5.** Location of the sensors

## Dynamic characteristics of the existing structure

In order to calibrate the finite element model of the building to correspond with the real behavior of the existing building, six sensors were placed on different floors recording and transmitting ambient noise data. The sensors were recording the micro-vibrations in terms of velocity (mm/sec) in three axes (X, Y, Z).

Each sensor was active for around 25 minutes and the data was separated into 25 files of 1 minute each. The sampling rate of the sensors was 100 Hz. The divided files were subsequently combined into one master file for each axis, showing the velocity time history of each sensor due to ambient noise. In order to correct the error of the sensors, which has displaced the neutral axis from zero, baseline correction was applied by subtracting the mean value from each measurement.
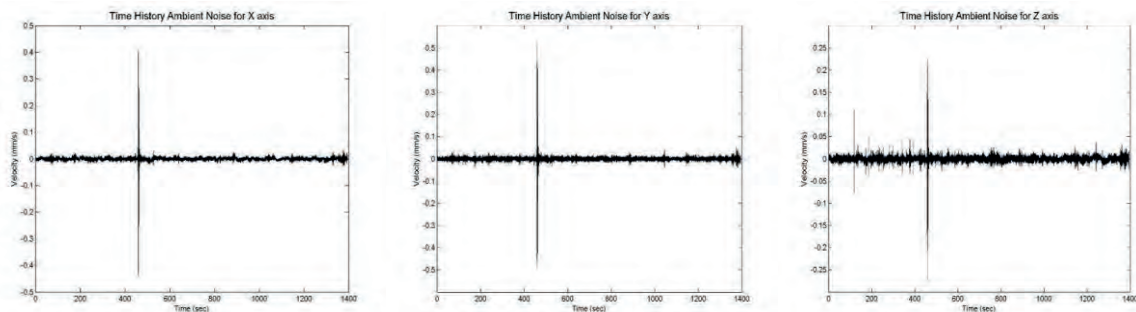


**Figure 6.** Time histories of sensor MR1 for axes X, Y, Z
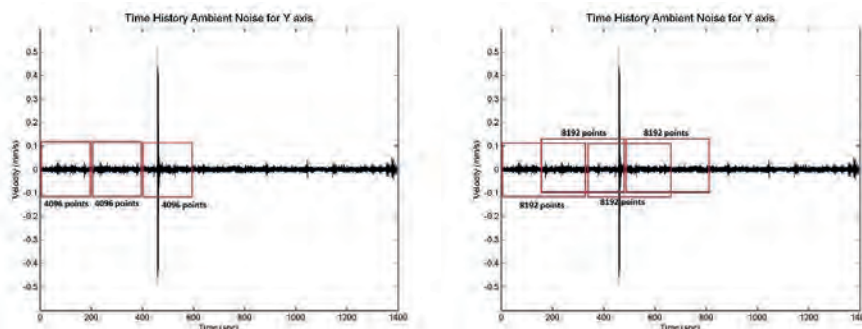


**Figure 7.** Parallel segments (4096 points) and overlapping segments (8192 points)

The purpose of this procedure is to identify the dynamic characteristics of the existing structure, explicitly the Eigen frequencies. To achieve this, it is required to translate the data from the time domain to the frequency domain by using the Fast Fourier Transformation and produce Fourier Spectrums. With a view to accomplish a better accuracy, the segmentation of the time histories was determined to by using two different methods. In the first one, it was decided to pick in succession segments of 4096 points each, while in the second one overlapping segments of 8192 points each.

The procedure was implemented to every segment of each axis of all sensors. In total, for each time history, there were 34 segments for the first method and 33 for the second one and the Fourier Spectrums were calculated for all of them. Consequently, it was calculated the mean and the standard deviation of all the processed data for every sensor. Comparing the diagrams between the two different methods, it is concluded that there is high convergence of the amplified frequencies.

Although it is already possible to reach a conclusion for the frequencies from the previous diagrams, in order to pinpoint the Eigen frequencies of the existing structure, it is essential to exclude any outside influences (moving cars, footsteps etc.) from the Fourier Spectrums. This is feasible by calculating the Spectrum ratios between the sensors which are located to the top floors and those on the base. The most representative result is given by the ratio of the top floor (4th) to the base of the building (MR1/MR6) but the same result was achieved by other ratios as well (MR2/MR6). The results from the ratios of sensors MR3 and MR4 were discarded because of the low amplification and the difficulty to determine the Eigen frequencies.

The peak amplification for both methods is concentrated around the frequencies 6.15 Hz for the X axis and 4.67 Hz for the Y axis.
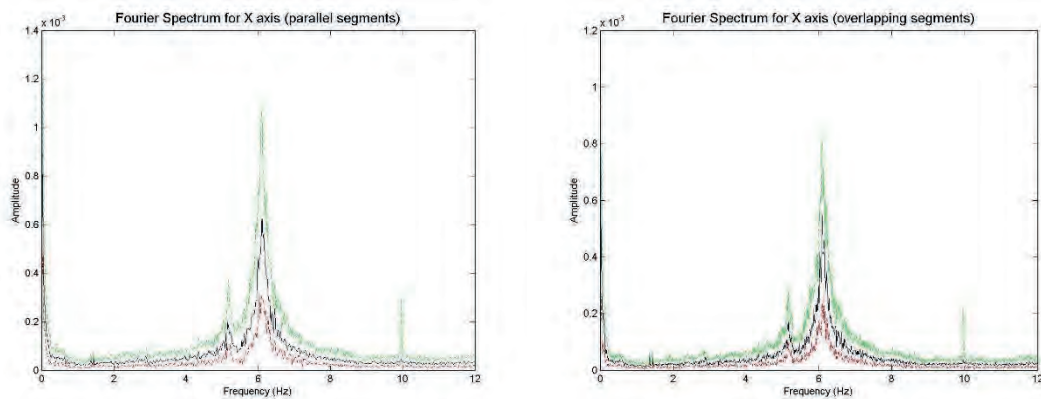


**Figure 8.** Fourier Spectrums of 16th percentile, mean and 84th percentile for the two methods
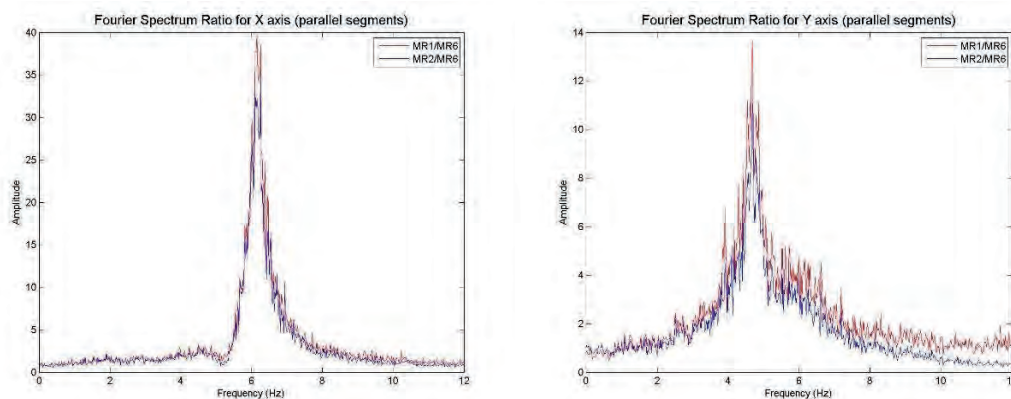


**Figure 9.** Fourier spectrum ratios between MR1 to MR6 for X and Y axis

**Table 1.** Measured Eigen frequencies and Periods of the structure

|  | X axis | Y axis |
| --- | --- | --- |
| Frequency (Hz) | 6,15 | 4,67 |
| Period (sec) | 0,163 | 0,214 |

# Equivalent Frame Model

Simplified Analysis Method (SAM), developed since 1996 by *Magenes and Calvi*, and then modified by *Magenes and Della Fontana*. The SAM, considers that spandrel as deformable; furthermore it can move horizontally and can rotate. In the SAM, the wall is schematized with an equivalent frame composed by: column elements representing the piers; beam elements representing the spandrels; rigid offsets describing the joint panel. The joint is considered infinitely rigid because generally (but not always) this area is not cracked.

Both the pier and the spandrel have an elastic-plastic behaviour with a deformation limit; in particular, the element is considered elastic until it reaches the threshold of a failure criterion (rocking, diagonal shear and sliding shear for pier; rocking and shear for spandrel); once the threshold is exceeded, a plastic hinge is activated. The nonlinearity of the material is taken into account through the use of plastic hinges. Three types of plastic hinges are used: shear hinges (V type), bending hinges (M type) and rocking hinges (PM type).

➢ For the piers are used V and PM hinges. The V hinges are placed in the middle of the deformable part of the piers, the PM hinges at the end of it.

➢ For the spandrels are used V hinges in the middle of the spandrel, and M hinges at the end of it.
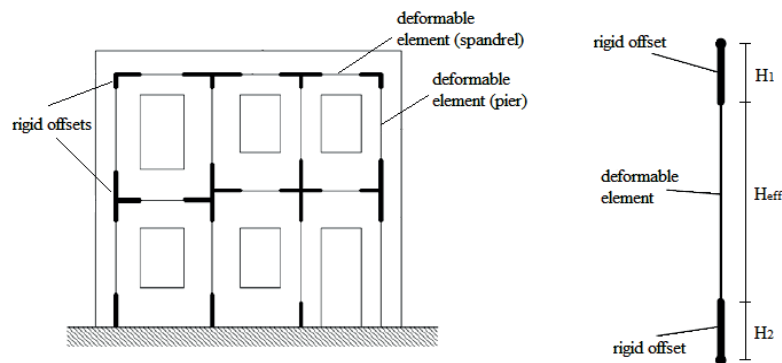


**Figure 10.** Equivalent frame wall using rigid offsets
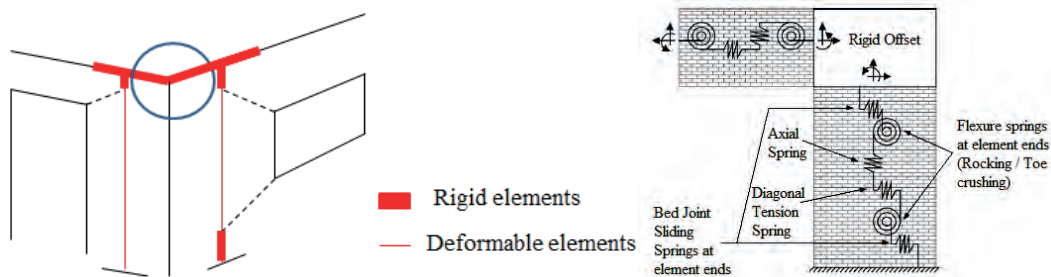


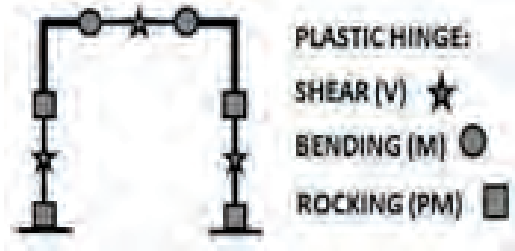**Figure 11.** Rigid Offset (stiff behaviour) and Deformable Element (elastic to plastic behaviour)

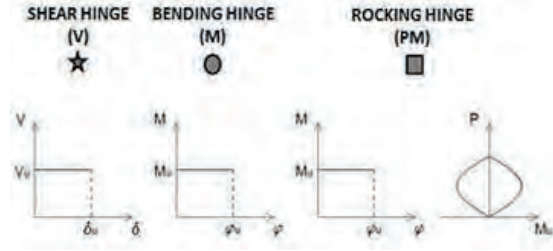**Figure 12.** Location and type of plastic hinges



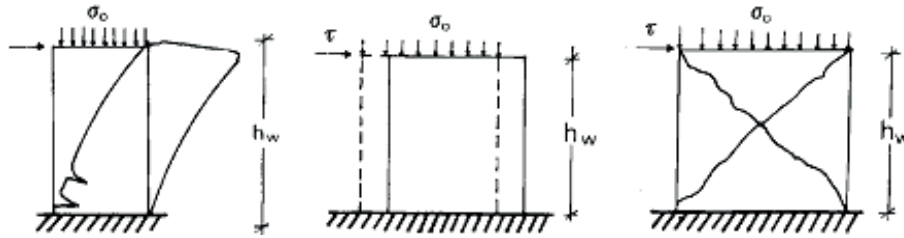**Figure 13.** Behaviour of the different plastic hinges



**Figure 14.** In-plane failure modes of masonry walls a) rocking; b) sliding; c) diagonal cracking

The behaviour that has been assigned to the various hinges is shown in Figure 13: the V hinges take into account the relationship between the ultimate displacement of the panel $\delta_u$ and the limit shear $V_u$, and the M hinges between the moment $M_u$ and ultimate rotation $\varphi_u$; on the other hand, the PM hinges consider the interaction between the normal stress $P$ and the ultimate moment $M_u$.

## Proposal of different nonlinear hinge definitions

According to *Pasticier et al.* [5] the strength in terms of ultimate moment $M_u$ is defined by Equation (1). As far as the shear strength is concerned, according to the experimental test outcomes [7], authors of [1] decided to consider two strength criteria. The first criterion (Eq. 2) is recommended in [6] for existing buildings.

This criterion, which refers to shear failure with diagonal cracking, was originally proposed by *Turnsek and Cacovic* [8] and later modified by *Turnsek and Sheppard* [9]. The second criterion (Eq. 3) refers to shear failure with sliding and is recommended in [6] for new buildings. Although formulated differently, such a criterion is also recommended by the Eurocode 8 [10].

$$M_u = \frac{\sigma_0 D^2 t}{2}\left(1 - \frac{\sigma_0}{k f_d}\right) \tag{1}$$

$$V_u^f = \frac{1.5 f_{v0d} D t}{\xi}\sqrt{1 + \frac{\sigma_0}{1.5 f_{v0d}}} \tag{2}$$

$$V_u^s = \frac{\dfrac{3}{2} f_{v0d} + \mu \dfrac{\sigma_0}{\gamma_m}}{1 + \dfrac{3 H_0}{D \sigma_0} f_{v0d}} D t \tag{3}$$

where $\sigma_0$ is the mean vertical stress, $D$ the pier width, $t$ the pier thickness, $k$ the coefficient taking into account the vertical stress distribution at the compressed toe, $f_d$ the design compression strength, $f_{v0d}$ the design shear strength with no axial force; $\mu$ (friction coefficient) = 0.4, the coefficient related to the pier geometrical ratio, $H_0$ the effective pier height, and $\gamma_m$ the safety factor.

For the rocking hinges the strength is given by Equation (1), and the ultimate rotation $\phi_u$ corresponds to an ultimate lateral deflection $\delta_u$ equal to 0.8% of the deformable height of the pier, minus the elastic lateral deflection, as recommended in [6]. For the shear hinge, the strength is given by the minimum value resulting from Equations (2) and (3). The ultimate shear displacement $\delta_u$ was assumed to be equal to 0.4% of the deformable height of the pier, minus the elastic lateral deflection, as recommended in [6].

As far as the modelling of the spandrel beams is concerned, assuming the presence of a lintel properly restrained at both supports, only one 'shear hinge' was introduced at mid-span (Figure 3a), with the shear strength $V_u$ given by

$$V_u = htf_{v0d} \tag{4}$$

where $h$ is the spandrel depth, $t$ the spandrel thickness, and $f_{v0d}$ the design shear strength with no axial force.

According to *Bal et al.* [11] three different types of failure modes have been considered for the piers like in work [5]: flexural (rocking) (see Eq. 5), diagonal shear (see Eq. 6) and sliding shear (see Eq. 7).

$$M_u = \frac{pD^2 t}{2}\left(1 - \frac{p}{kf_u}\right) \tag{5}$$

$$V_y^d = \frac{f_{tu}Dt}{b}\sqrt{1 + \frac{p}{f_{tu}}} \tag{6}$$

$$V_y^s = \frac{f_{tu} + \mu\dfrac{p}{\gamma_m}}{1 + \dfrac{2H_0}{Dp}f_{tu}} \tag{7}$$

where $f_{tu}$ represents the conventional tensile strength of masonry (not the tensile strength of the bed joints), $b$ is a parameter which is assumed to be dependent on the $H/D$ aspect ratio of the pier (like $\xi$ at *Pasticier et al.* [5]), $p$ is the mean vertical stress on the pier, $f_u$ is the compressive strength of masonry.

*Bal et al.* [11] propose two failure modes for the spandrels: flexural (see Eq. 8) and shear. The ultimate shear capacity is given as $V_u = f_{v0d}ht$ as well as *Pasticier et al.* [5].

$$M_u = \frac{H_p h}{2}\left(1 - \frac{H_p}{kf_{hd}ht}\right) \tag{8}$$

where $H_p$ is the minimum of the horizontal shear resistance of the element or the value $0.4f_{hd}ht$, $f_{hd}$ is the compressive strength of the masonry in the horizontal direction in plan of the wall.

According to *Diogo et al.* [12] Equations (9), (10), (11) define the failure modes for piers:

$$M_u = \frac{\sigma_0 D^2 t}{2}\left(1 - \frac{\sigma_0}{kf_d}\right) \text{ - rocking} \tag{9}$$

$$V_{rd} = \frac{1.5 C_u Dt}{\xi}\sqrt{1 + \frac{\sigma_0}{1.5 \cdot C_u}} \text{ - diagonal cracking} \tag{10}$$

$$V_{rd} = \frac{1.5 C_u + \sigma_0 \tan\varphi}{1 + \frac{3 \cdot H_0}{\sigma_0 D} C_u} Dt \text{ - sliding} \tag{11}$$

where, $C_u$ is the cohesion; $\varphi$ is the friction internal angle; $H_0$ is the distance from zero moment section to control section.

*Diogo et al.* [12] argue that in spandrels the rupture is usually due to shear and its resistance is often regarded as being owed to material cohesion (see Eq. 12).

$$V_{rd} = htC_u \tag{12}$$

According to *Bucchi et al.* [13] following equations (13), (14), (15) define the failure modes for piers:

$$M_u = \frac{\sigma_0 D^2 t}{2}\left(1 - \frac{\sigma_0}{kf_d}\right) \text{ - rocking} \tag{13}$$

$$V_{uf} = \frac{f_{td} Dt}{\xi}\sqrt{1 + \frac{\sigma_0}{f_{td}}} \text{ - diagonal cracking} \tag{14}$$

$$V_{us} = l' t f_{vd} \text{ - sliding} \tag{15}$$

where $f_{td}$ – diagonal shear strength, $f_{vd}$ - sliding shear strength in absence of normal stress, $f_{hd}$ - compression strength in horizontal direction; l' – length of compressed part of pier.

For definition of spandrels strength criteria authors of [13] use Equations (16), (17):

$$M_u = \frac{H_p h}{2}\left(1 - \frac{H_p}{kf_{hd} ht}\right) \text{ - rocking} \tag{16}$$

$$V_{rd} = ht f_{vd} \text{ - sliding} \tag{17}$$

And finally, according to *Lagomarsino et al.* [14] strength criteria of piers are defining by Equations (18), (19), (20):

$$M_u = \frac{N \cdot l}{2}\left(1 - \frac{N}{kf_m lt}\right) \text{ - rocking} \tag{18}$$

$$V_{uf} = \frac{\tau_0 Dt}{\xi}\sqrt{1 + \frac{N}{1.5 \cdot \tau_0 lt}} \text{ - diagonal cracking} \tag{19}$$

$$V_{us} = l' t C_u + \mu N \text{ - sliding} \tag{20}$$

where $N$ – axial load; $f_m$ – compression strength; $\tau_0$ – diagonal shear strength; $C_u$ – cohesion; $f_{hd}$ – compression strength in horizontal direction.

For spandrels authors of [14] consider 2 strength criteria – rocking and sliding (see Eq. 21, 22):

$$M_u = \frac{H_p h}{2}(1 - \frac{H_p}{kf_{hd}ht}) \text{ - rocking} \tag{21}$$

$$V_{rd} = htC_u \text{ - sliding} \tag{22}$$

As we can see from the above works, there are substantial differences in the formulas of the strength criteria of nonlinear elements frame hinges simulating the work of masonry walls under seismic load. A comparison of the hinge definition results obtained by previous researchers is presented in the following figures.

Material and mechanical parameters involved in hinge definitions leads to under or over prediction of the actual strength of the structure. It is difficult to single out an accurate hinge definition without model validation, due to strong variability in results.


## Numerical modelling

According to the provided architecture plans, the equivalent frame was created in SAP2000®. A new model was set by using the *3D Frames* command. Joint restraints were assigned at the base of the building in order to constrain the grades of freedom (rotation and translation in the three directions). The material characteristics used for masonry were: density of 11 kg/m$^3$, modulus of elasticity 3600 N/mm$^2$ and Poisson's ratio of 0.25. For each frame, in X and Y direction, there were assigned sections for the piers, spandrels and also there was defined the rigid offsets in order to obtain the equivalent frame.
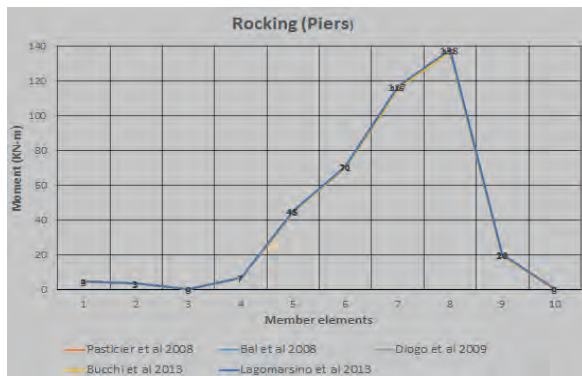


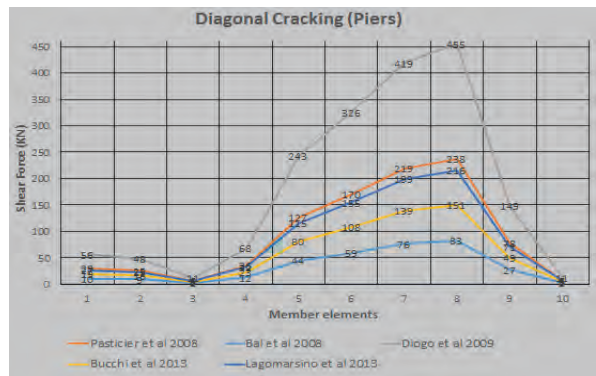**Figure 15.** Rocking plots for piers
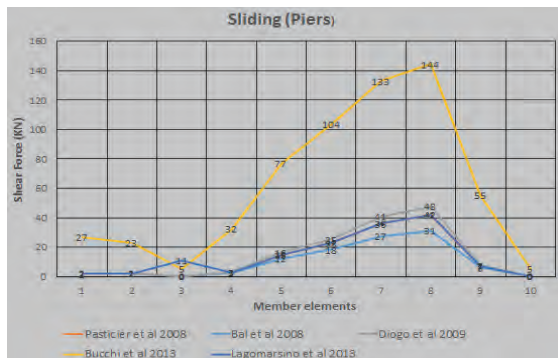


**Figure 16.** Diagonal plots for shear in piers



**Figure 17.** Sliding plots for shear in piers



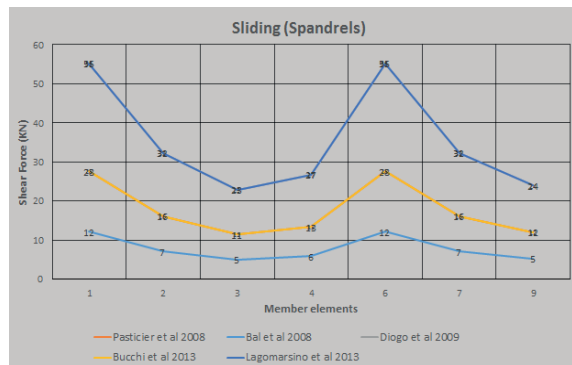**Figure 18.** Sliding plots for shear in spandrels

The dead load for the slabs was considered 6 kN/m$^2$ and the live load 2 kN/m$^2$ in accordance to Eurocode 0. For the mass source, the dead load was taken with a coefficient of 1.0 and the live load with 0.3, according to Eurocode 8: The behaviour of the plastic hinges were defined in terms of moments-rotations and forces-displacements and the following four criteria were chosen: Pasticier, Bucchi, Bal and Lagomarsino. Different hinge parameters were set for all the piers and spandrels for each one of the previous four criteria. In order to simplify the model, same parameters were assigned to the groups of similar piers and spandrels. These parameters were calculated at the average of the actual values of all elements of each group. The following acceptance limits were fixed at 100%, 60% and 30% of the rotation capacity for collapse prevention, life safety and immediate occupancy. For this model, a linear variation of the rotation of the plastic hinge was implemented. Using modal analysis, the period of vibration of the structure was verified and, there were obtained similar results to the period measured by the sensors, both in X and Y direction.

## Nonlinear pushover analysis

In order to obtain the pushover curves, two load distributions having linear and constant variation were used, for both X and Y directions. The plastic hinge positions can be observed in the following figure, in which the collapse state hinge is shown in red.
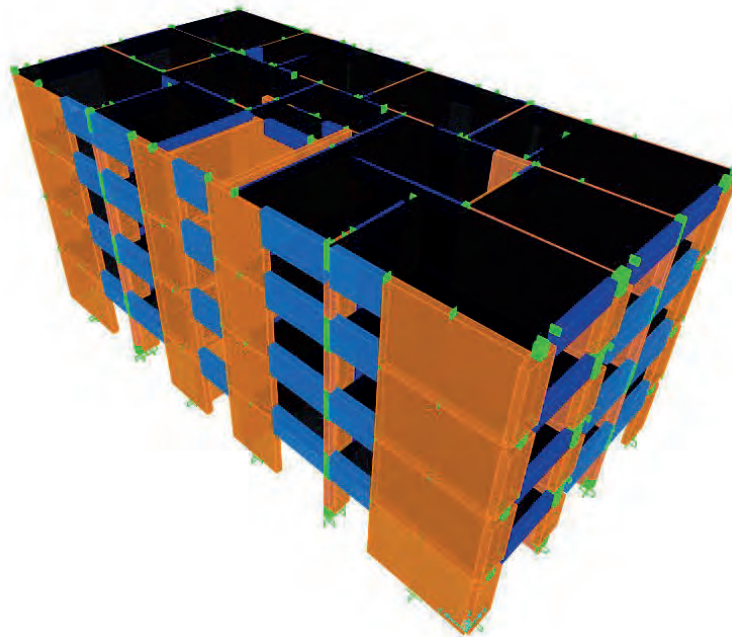


**Figure 19.** Equivalent 3D frame model in SAP2000

**Table 2.** Eigen frequencies and Periods of the structure.

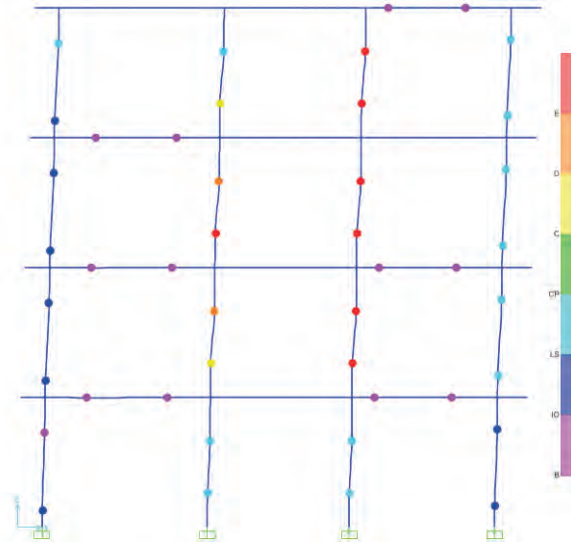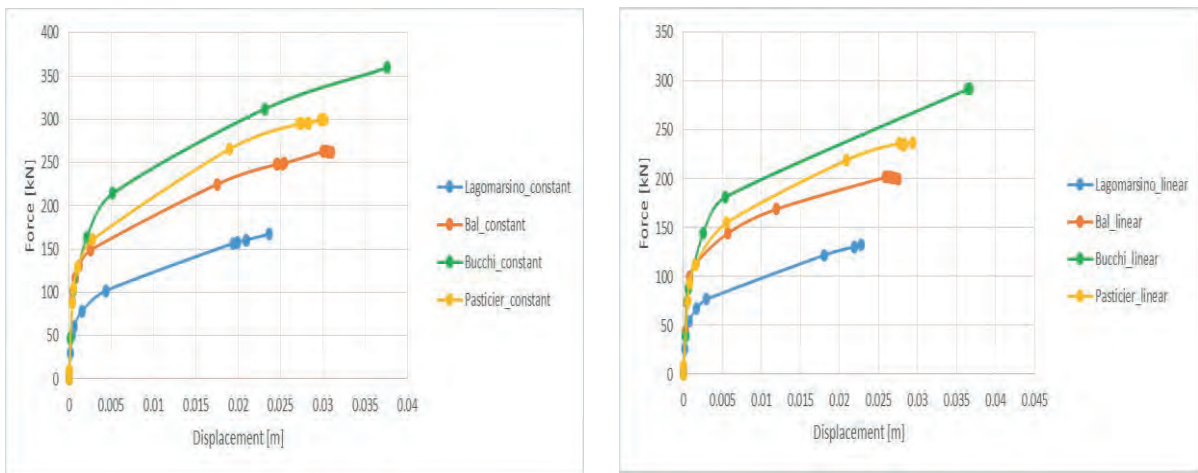| | Measured | | Calculated | |
|---|---|---|---|---|
| | Frequency [Hz] | Period [sec] | Frequency SAP2000 [Hz] | Period SAP2000 [sec] |
| X axis | 6,15 | 0,16 | 6,81 | 0,14 |
| Y axis | 4,67 | 0,21 | 8,34 | 0,13 |

**Figure 20.** Image of hinge collapsing



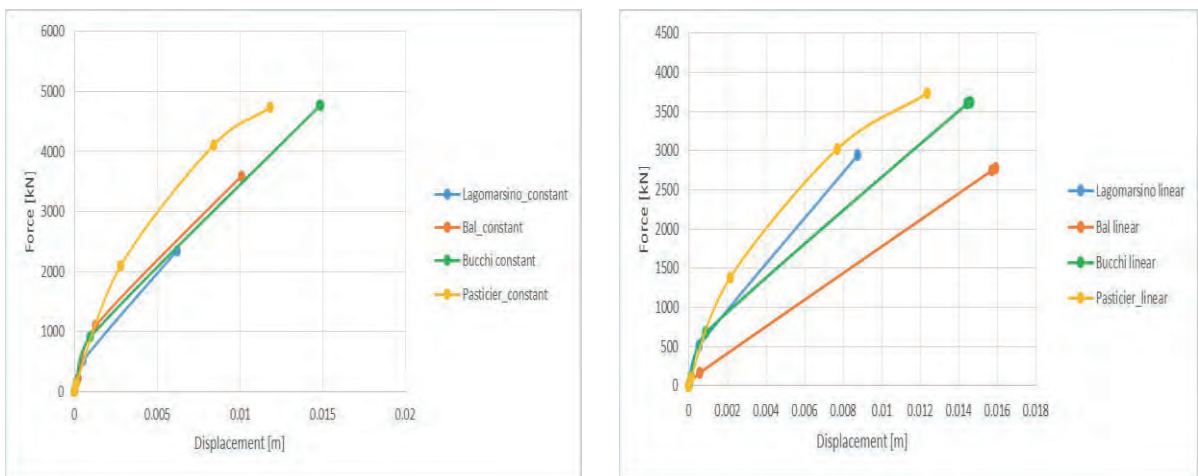**Figure 21.** Pushover curves comparison for costant and linear load, X direction



**Figure 22.** Pushover curves comparison for costant and linear load, Y direction

The values from the pushover curves for the four criteria of plastic hinge definitions are presented in Figures 21 and 22 for each loading type (constant and linear).

From the presented graphs it can be observed that the structure has more resistance on Y transversal direction than on longitudinal X direction.

In addition to pushover curves, there was also calculated the perfomance point for the structure, which represents the state of maximum inelastic capacity of the structure, found by crossing the point of the capacity spectrum and demand spectrum for a given damping ratio. This point was evaluated at a displacement of 1.2cm at a base shear force of 125kN.
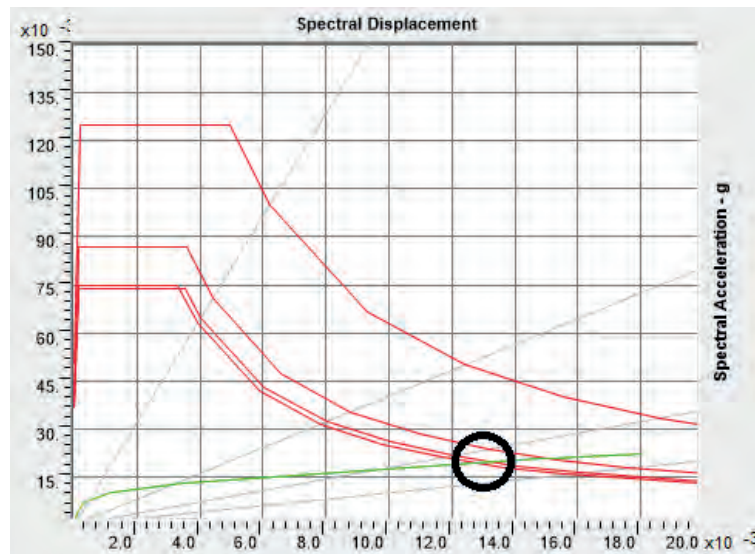


**Figure 23.** Performance point of the structure

# Experimental Testing

There was constructed an experimental model of the building, at a scale of 1:50, which was tested on a shaking table at Bauhaus University from Weimar. The model was built using brick-like elements and wooden pieces in order to simulate the reinforced concrete slabs. This structure was used in order to validate the analytical reasoning of the building model.
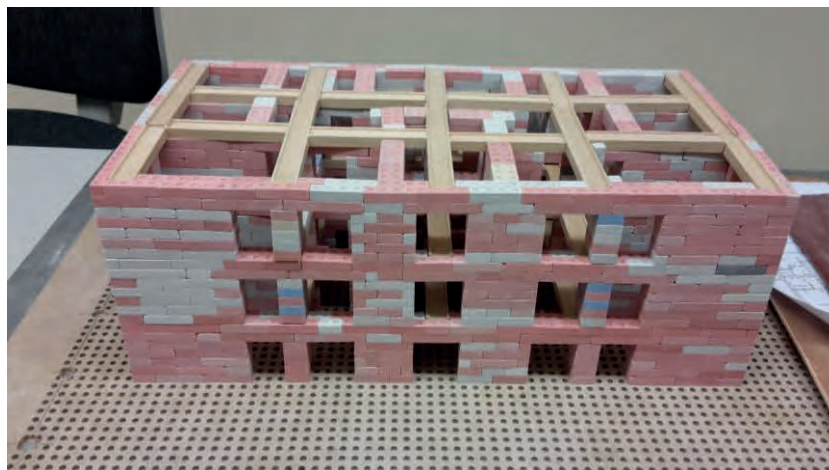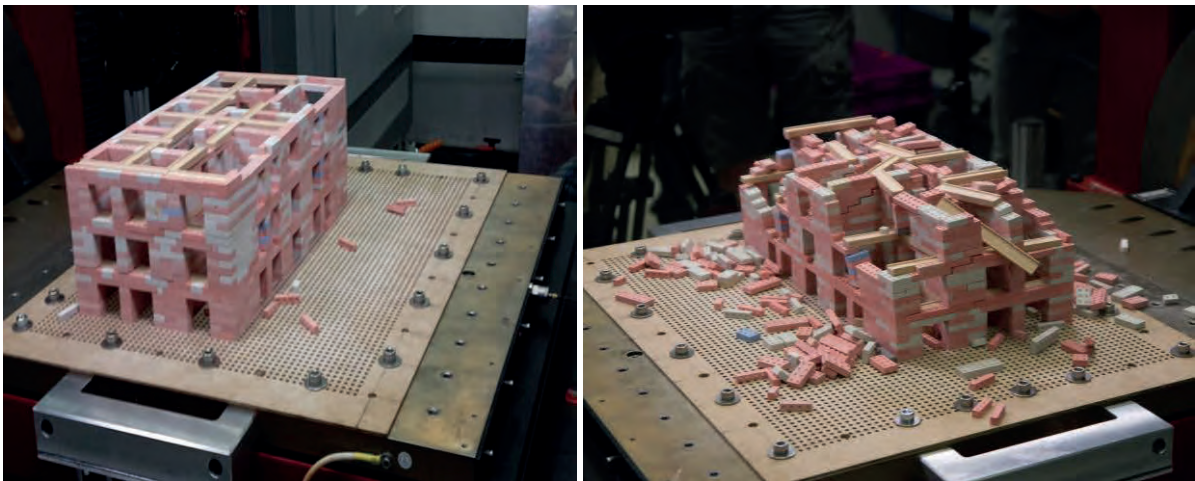


**Figure 24.** Building model, scale 1:50
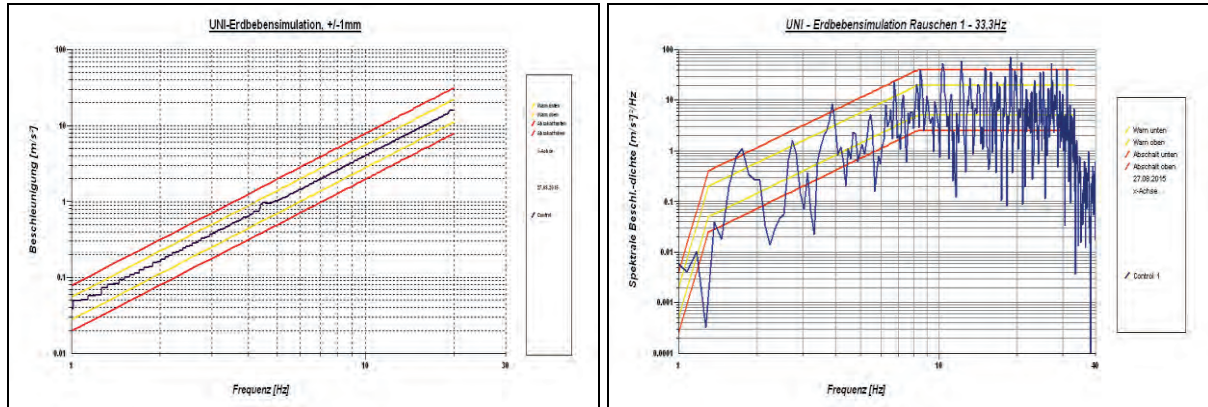
**Figure 25.** Simulation of seismic loading a) pre-shock; b) main shock



**Figure 26.** Consequences of seismic loading a) before; b) after main shock

The structure has been tested by a simulation of two real earthquake with different intensities. The first one (pre-shock) produced only a few damages on the top part of the model, while the second one (main-shock), characterized by a frequency of 33.3 Hz produced the collapse of the entire structure.

## Conclusions

Extreme events, such as earthquakes, influence our daily lives and the way in which we build secure buildings. There has been performed a 3D nonlinear analysis on a model of an existing building from Turkey. Several proposals for the hinge definitions were studied, each having a similar approach but with different results. Pushover analysis confirms the importance of hinge definitions in order to obtain reliable results. Further investigations must be carried out in order to obtain accurate results in the nonlinear domain of masonry structures. Small scale experimental testing revealed that it is important to consider the earthquake-after-earthquake scenario in the current design and construction trends.

# References

[1] Grünthal, G., Bosse, Ch., Sellami, S., Mayer-Rosa, D., Giardini, D. (1999): Compilation of the GSHAP regional seismic hazard for Europe, Africa and the Middle East. *Annals of Geophysics*, **Vol. 42, No. 6.**

[2] Abrahamczyk, L., Schwarz, J., Langhammer, T., Genes, M.C., Bikce, M., Kacin, S. and Gülkan, P. (2013): Seismic Risk Assessment and Mitigation in the Antakya-Maras Region (SERAMAR): Empirical Studies on the basis of EMS-98. *Earthquake Spectra* **Vol. 29 (3)**, 683-704.

[3] Abrahamczyk, L., Schwarz, J., Langhammer, T., Genes, M.C., Bikçe, M., Kaçin, S., Yakut, A., Erberik, A.M., Gülkan, P. (2012): Empirical and Analytical Vulnerability Assessment of the Masonry Building Stock in Antakya (Hatay/ Turkey). In Proceedings *15th World Conference Earthquake Engineering*, Lisboa, Paper 1081.

[4] Genes, M.C., Erberik, A.M., Abrahamczyk, L., Gülkan, P., Bikçe, M., Kaçin, S., Yakut, A., Schwarz, J. (2012): Vulnerability assessment of two instrumented masonry buildings in Antakya (Hatay, Turkey). In Proceedings: *10th International Congress on Advances in Civil Engineering ACE2012*, Middle East Technical University, Cultural and Convention Center, Ankara Turkey, 17-19 October 2012, Paper 1019.

[5] Pasticier, L., Amadio, C., Fragiacomo, M. (2008): Non-linear seismic analysis and vulnerability evaluation of a masonry building by means of the SAP2000 V.10 code. *Earthquake Engineering and Structural Dynamics*: **Vol. 37**: 467–485.

[6] Decree of the cabinet president No. 3274. Annex 2: Provisions for design, seismic evaluation and retrofit of buildings. Appendix No. 72 to The Italian Official Gazette, vol. 105, 20 March 2003 (in Italian).

[7] Magenes, G., Calvi, GM. (1997): In-plane seismic response of brick masonry walls. *Earthquake Engineering and Structural Dynamics*, Vol. 26(11):1091–1112.

[8] Turnsek, V., Cacovic, F. (1971): Some experimental results on the strength of brick masonry walls. Proceedings: *2nd International Brick Masonry Conference*, Stoke-on-Trent, 149–156.

[9] Turnsek, V., Sheppard, P. (1980): The shear and flexural resistance of masonry walls. Proceedings: *International Research Conference on Earthquake Engineering*, Skopje, 517–573.

[10] CEN. Eurocode 8 (2004): Design of Structures for Earthquake Resistance. Part 3: Assessment and Retrofitting of Buildings. DRAFT No. 7. Stage 49. June 2004.

[11] Bal, I.E., Crowley, H., Pinho, R. (2008): Displacement based earthquake loss assessment of Turkish masonry structures. Proceedings: *14th World Conference on Earthquake Engineering*, Beijing, China.

[12] Diogo, F. (2009): Nonlinear seismic analysis of ancient buildings – structural characterization for successful seismic retrofit. *Master Thesis*. Department of Civil Engineering. Universidade Technica de Lisboa.

[13] Bucchi, F., Arangio, S., Bontempi, F. (2013): Seismic assessment of an historical masonry building using nonlinear static analysis. Proceedings: *14th International Conference on Civil Engineering*, Scotland.

[14] Lagomarsino, S., Penna, A., Galasco, A., Cattari, S. (2013): TREMURI program: An equivalent frame model for the nonlinear seismic analysis of masonry buildings. *Engineering Structures*, **Vol. 56**, pp. 87 – 99.

# Numerical evaluation of short coupling beams for moment-resisting steel frames in seismic areas

*ABERLE Marcus [a], ABU SHAMMA Amr [b], GAÁL Betti [c], KOZMA András [d], LAJKOVIC Grega [e], LAVRENCIC Marko [e], MAVRIDIS Lazaros [f], NOVARINO Stefano [g], ZUB Ciprian-Ionuţ [h],*

[a] *Hochschule Karlsruhe, Germany*

[b] *Birzeit University, Palestine*

[c] *Czech Technical University in Prague, Czech Republik*

[d] *Budapest University of Technology and Economics, Hungary*

[e] *University of Ljubljana, Slovenia*

[f] *Aristotle University of Thessaloniki, Greece*

[g] *University of Genoa, Italy*

[h] *Politehnica University of Timisoara, Romania*


*CRISAN Andrei [a], HILDEBRAND Jörg [b]*

[a] *Politehnica University of Timisoara, Romania*

[b] *Juniorprofessur Simulation und Experiment, Bauhaus-Universität Weimar*

## Abstract

Within the framework of Project No. 4, *Numerical Analysis of Steel Frames*, two moment-resisting steel frames with reduced beam sections, RBS-S and RBS-L, were numerically analysed in ANSYS Workbench 14.5. Two different material and geometry models were used. The specimens were cyclically tested to ECCS loading protocols. Calibration of numerical models and sensitivity studies were carried out successfully. The numerical results and conclusions are summarized here too.

## Description, Motivation, Objectives

Moment resisting steel frames are often used in seismic areas due to their superior ductility and capacity to dissipate energy, which makes them a feasible solution as lateral load resisting systems. The seismic energy is primarily dissipated by beams undergoing plastic deformation in so called dissipative zones. In order to control the location of the plastic hinge formation, portions of the beam flanges are intentionally reduced at a specific distance from the column face. This concept of using reduced beam sections, RBS, (see **Figure 1**) has initially been proposed by Plumier (1990) and also experimental tests have been carried out by Dinu et al. (2013).

In particular short span-to-depth ratio L/h < 4 are not very common in the design of moment-resisting frames. For such beams, the shear stresses may become a controlling design factor as they can significantly influence the moment capacity. This is particularly important in areas of high seismicity where plastic hinges can occur. Therefore, the design of such structures generally requires additional experimental as well as numerical studies.
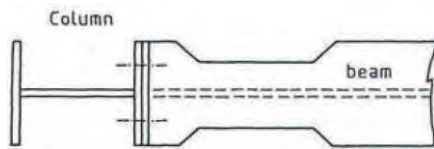
**Figure 1.** Reduced Beam Section (RBS) concept (Plumier, 1990)
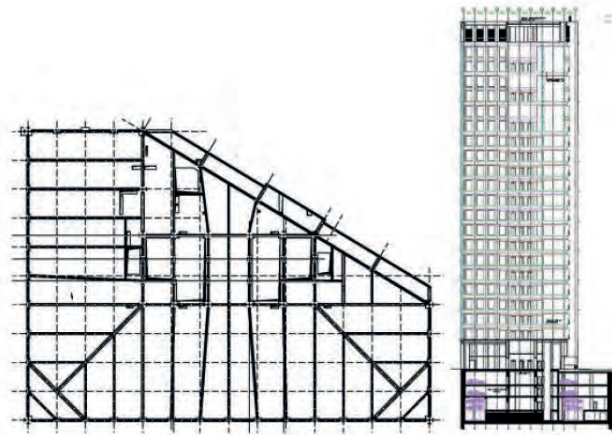


**Figure 2.** Plan and elevation of building (Dinu et al., 2013)

The objective of the Bauhaus summer school project was to carry out a numerical study of the short coupling beam behaviour using the ANSYS Finite Element Program by using different material laws and various dimensional parameters. The finite element models were calibrated using the experimental full scale tests by Dinu et al. (2013).

The project is connected with the design of an 18-story office building, located in Bucharest, Romania. The building height is 94 m, and the plan dimensions are 43,3m x 31,3m, (see **Figure 2**). The building site is located in a high seismic area, which is characterized by a design peak ground acceleration of 0.24g for a returning period of 100 years, and soft soil conditions, with $T_C$=1.6s.

Lateral force-resisting system consists of exterior steel framing with closely spaced columns and short beams. The central core is also made of steel framing with closely spaced columns and short beams. The ratio of beam length-to-beam height, L/h, varies from 3.2 to 7.4. In this given situation, some beams are below the general accepted inferior limit (L/h=4). The moment frame connections employee reduced beam section connections that are generally used for beams loaded mainly in bending.

For such beams, the shear stresses may become a controlling factor in the design, as the moment capacity is influenced by the presence of the shear. This is an important matter when such a beam is part of the seismic lateral force resisting system that is designed according to the dissipative concept. In this case, the contribution from the shear force affects the dissipation capacity and plastic mechanism.
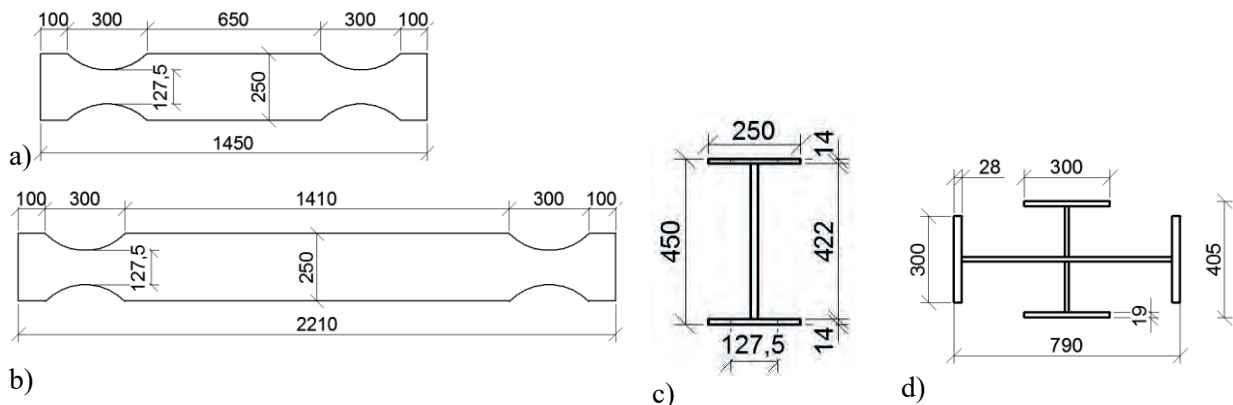


**Figure 3.** Geometry of elements: a) RBS-S; b) RBS-L; c) beam cross-section; d) cruciform cross-section of columns

Due to the fact that some beams have the ration L/h < 4 are not generally covered by the design codes (AISC 341-05), experimental and numerical test must be carried out in order to evaluate their behaviour.

## Experimental program

### Specimens and test setup

Within the experimental program two types of beams, which have the shortest *L/h* ratio, were selected for the experimental program:

> ➢ the first one, denoted *RBS-S*, has a clear length of 1450 mm and the lowest span-depth ratio, L/h = 3,20 (see **Figure 3**a).

> ➢ the second one, denoted *RBS-L*, has a clear length of 2210 mm and a corresponding span-depth ratio L/h = 4,90. The web and flange thicknesses for both beam types are 20 and 14 mm respectively (see **Figure 3**b).

The column has a cruciform cross-section made from two hot-rolled profiles (HEA800 and HEA400), see **Figure 3**d.

Beams and columns were both made from grade S355 steel. The base material characteristics were determined experimentally. The determined material parameters can be seen in **Table 1**.

Specimens were tested under a cyclic loading sequence taken from the ECCS recommendations. The experimental setup can be seen in **Figure 4**.

**Table 1.** Material parameters

| Section | Steel grade | Element | $f_y$ [N/mm²] | $f_u$ [N/mm²] | $A_u$ [%] |
|---------|-------------|---------|---------|---------|-------|
| HEA800 | S355 | Flange | 410.5 | 618.5 | 15.0 |
| | | Web | 479.0 | 671.2 | 13.0 |
| HEA400 | S355 | Flange | 428.0 | 592.0 | 15.1 |
| | | Web | 461.0 | 614.0 | 12.8 |
| Flat steel (15 mm) | S355 | Beam flange | 373.0 | 643 | 17.0 |
| Flat steel (20 mm) | S355 | Beam web | 403.0 | 599 | 16.5 |

## Results

Specimens with longer beams, RBS-L1 and RBS-L2, remained elastic until a drift of 30 mm, or 0.6 % of the storey height. Two failure modes were recorded. The first mode involved the fracture of the top beam flange-to-column flange welds, which afterwards propagated into the beam web. The second failure mode involved the fracture of the bottom flange due to the large tensile forces at ultimate load. Both failures occurred at interstorey drifts > 5 % of the storey height. The plastic behaviour was dominated by the buckling of the flange in compression and out-of-plane buckling of the web.
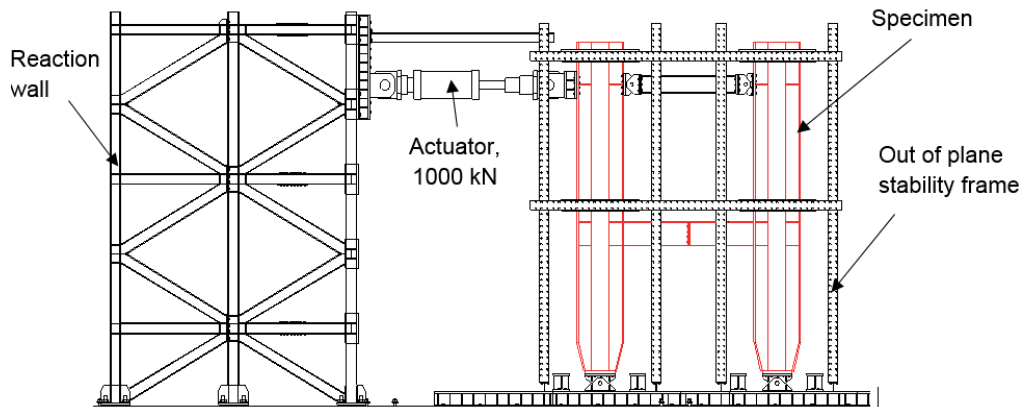
**Figure 4.** Experimental test setup

Specimens with shorter beams, RBS-S1 and RBS-S2, remained elastic until a drift of 25 mm, or 0.5 % of the storey height. The visible buckling of the flange in compression was first observed, followed by out-of-plane buckling of the web. Failure of the first short specimen, RBS-S1, involved fracture of the bottom flange due to the large tensile forces at ultimate load, followed by fracture of the beam web. The failure of the second specimen, RBS-S2, involved the fracture of the bolts at the splice connection. The plastic behaviour was dominated by the buckling of the flange in compression and shear buckling of the web.

The summary of experimental results can be seen in **Table 2**.

Owing to the large stiffness of the columns, the contribution of the column web panel can be neglected. The specimens exhibited good rotation capacity and stable hysteretic behaviour up to 5 % interstorey drift. This capacity supports the design of the structure which is based on a 2,5 % interstorey drift limitation at the ultimate limit state. The specimens showed reduced degradation in both strength and stiffness.

**Table 2.** Experimental test results

| Specimen | Failure mode | Observations |
|---|---|---|
| RBS-L1 | – cracks initiated in top flange welds, fracture propagated in web | – failure at interstorey drift of 5 % <br> – no slip at splice connection <br> – large dissipation capacity, reduced cyclic degradation |
| RBS-L2 | – failure due to fracture of flange in reduced area, then propagation in web | – failure at interstorey drift of 5 % <br> – no slip at splice connection <br> – large dissipation capacity, reduced cyclic degradation |
| RBS-L3 | – cracks initiated in bottom flange-to-column welds, fracture propagated in web | – failure at interstorey drift of 4.5 % <br> – no slip at splice connection <br> – large dissipation capacity, reduced cyclic degradation |
| RBS-S1 | – failure due to fracture of flange in reduced area, then propagation in web | – failure at interstorey drift of 5 % <br> – moderate slip at splice connection <br> – large dissipation capacity, reduced cyclic degradation |
| RBS-S2 | – failure due to fracture of bolts at beam splice connection | – failure at large interstorey drift <br> – large slip at splice connection <br> – large dissipation capacity, reduced cyclic degradation |
| RBS-S3 | – failure due to fracture of flange in reduced area, then propagation in web | – failure at interstorey drift of 5 % <br> – no slip at splice connection <br> – large dissipation capacity, reduced cyclic degradation |
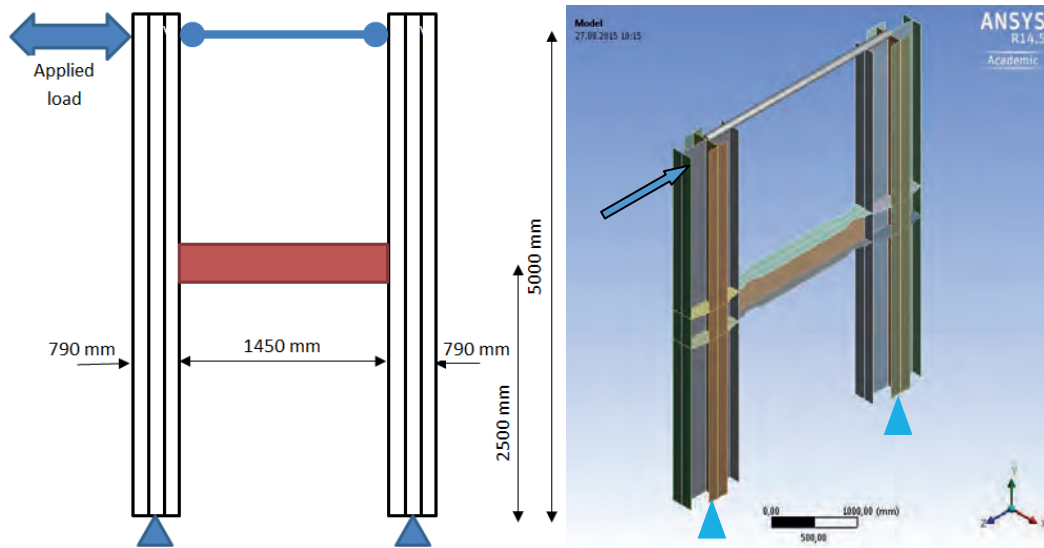
**Figure 5.** Ansys geometry model

# FEA modelling

In order to evaluate the experimental tests, it was created a numerical FEA model by using the finite element method based software ANSYS Workbench 14.5. In the following, the main steps of this numerical analysis will be described.

## Geometry

The already introduced steel structure consisted of two columns and a beam as connection between them, creating so an "H" shaped structure, as shown in **Figure 5**. In addition, there were introduced a steel rod connecting the tops of the columns, in order to have the same displacements.

The steel sections of the columns were HEA800 and HEA400 crossing each other, and type of steel S355. The beam between them were also an I-section having the width b = 250 mm and the height h = 450 mm. This beam is weakened by so called dog-bones with length of 300 mm and the width of the beam at the narrowest part is 127.5 mm. There were two cases analysed; the short and the long beam case, where the length of the short beam were 1450 mm and 2210 mm of the long beam.
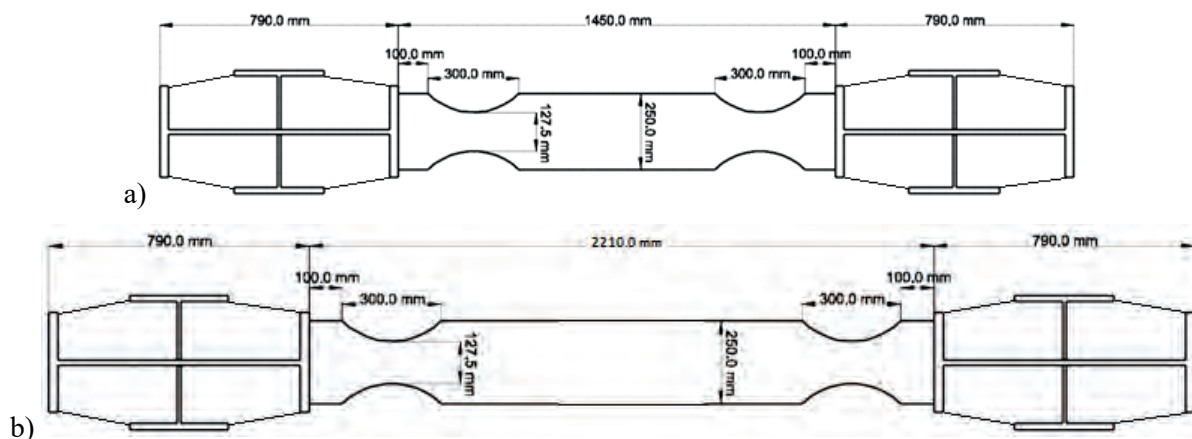


**Figure 6.** Top view of the geometry models: a) RBS-S; b) RBS-L

## Material model

For each model (RBS-S, BRS-L) there were performed two analyses in which the material law were varying. In the first analysis, a bilinear material law (elastic-perfectly plastic) were used. This material model did not performed well. In order to get more accurate results, in the second approach a nonlinear material model with kinematic hardening was used (Chaboche model with four nonlinear and one linear backstress). The input parameters for the Chaboche material model were taken from Budahazy and Dunay, 2013. The two material models are presented in **Figure 7**.

The yield stress was calculated from experimental results, using the ratio between the prescribed and real strength of the material ($f_{y,num}$ = 335 MPa and $f_{y,real}$ = 423 MPa). In addition, the material constants presented in **Table 3** were used to describe the kinematic behaviour.
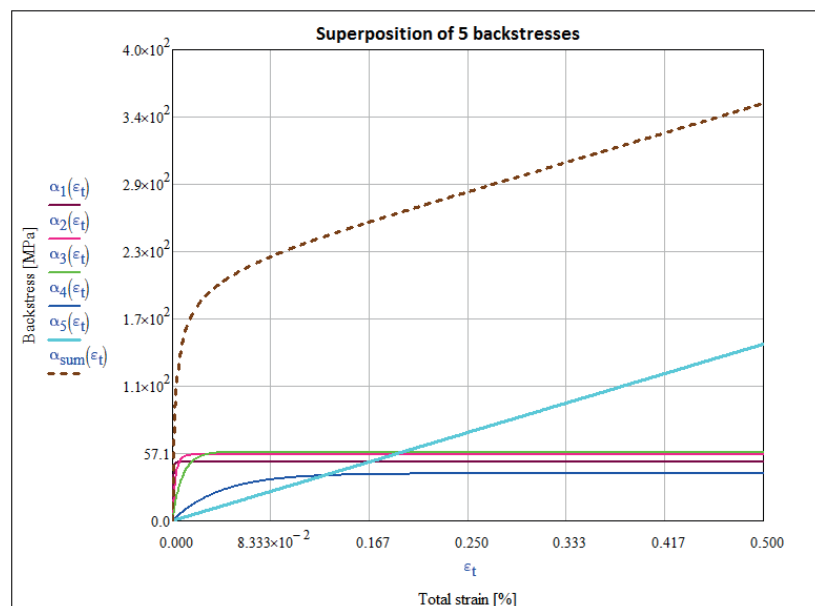
## Mesh

In the analysis, shell finite elements (SHELL181) were used, which made the calculation faster and simpler against using solid elements. Also, the option for automatic meshing of the model was used. Knowing from the experiments that the plasticization will occur in the beam, therefore the mesh for the beam was made finer in order for the results to be more accurate (structured mesh, quadrilaterals). Upper mesh size was limited to 40 mm.
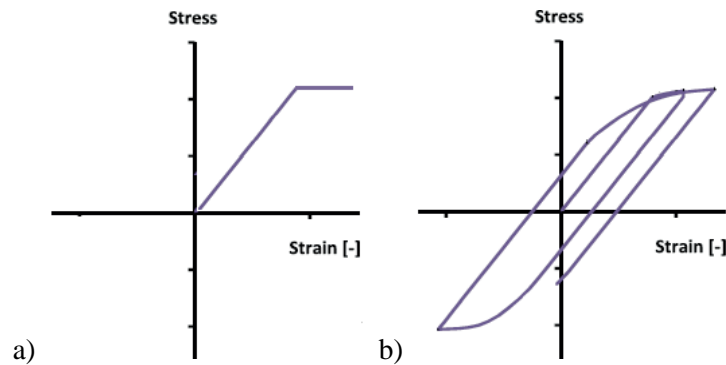


**Figure 7.** Material models: a) bilinear model; b) Chaboche model

**Table 3.** Chaboche parameters for kinematic hardening (Budahazy and Dunay, 2013)

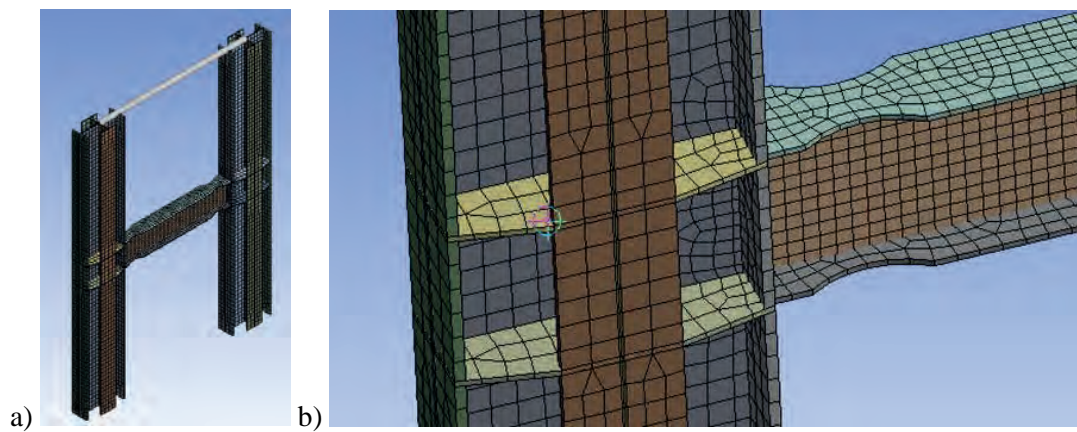| [MPa] | [/] |
|---|---|
| $C_1$= 75000 | $\gamma_1$= 1500 |
| $C_2$= 21000 | $\gamma_2$= 375 |
| $C_3$= 7000 | $\gamma_3$= 120 |
| $C_4$= 1100 | $\gamma_4$= 25 |
| $C_5$= 300 | $\gamma_5$= 0 |



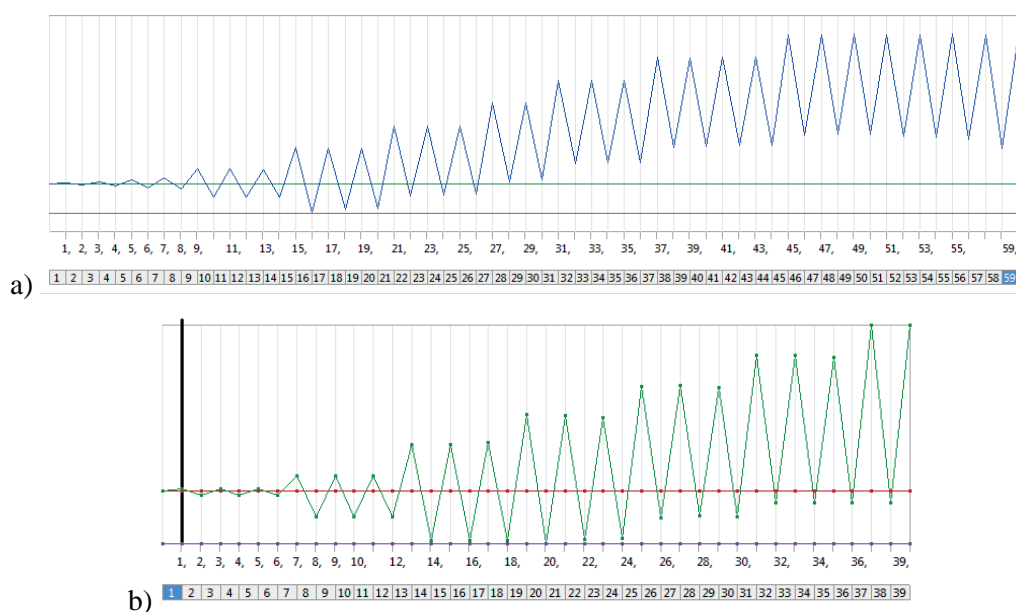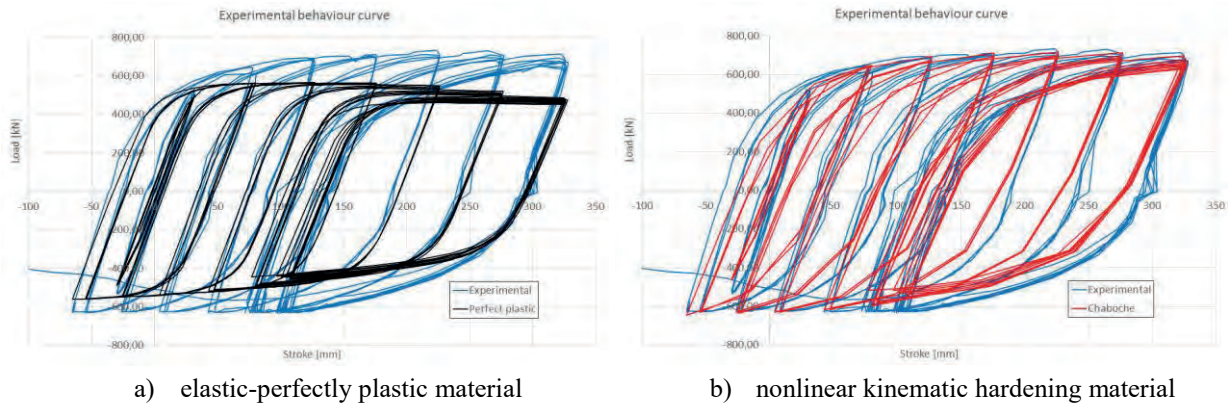**Figure 8.** Nonlinear kinematic hardening evolution laws
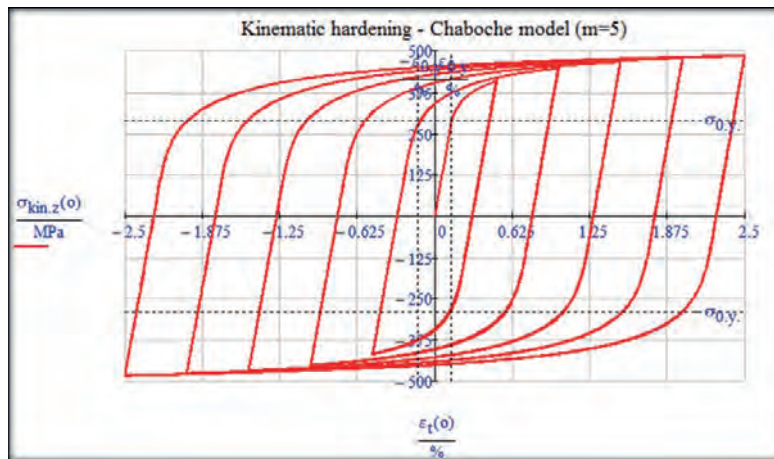
**Figure 9.** Theoretical cyclic behaviour of nonlinear kinematic hardening by using Chaboche model (input from **Table 3**)



a)          b)

**Figure 10.** a) Ansys mesh model. b) Mesh details



a)



b)

**Figure 11.** ECCS loading protocol for a) RBS-S and b) RBS-L

a)  elastic-perfectly plastic material      b)  nonlinear kinematic hardening material

**Figure 12.** Material calibration. FEM vs. experimental results

## Boundary conditions

The columns were modelled with hinged supports that allow rotation around X-axis. The steel rod (body-to-body) with diameter of 50 mm applied at the top of the columns was used to equalize the displacements in the Z direction.

In both examined cases (short and long beam) it was applied a cyclic loading according to the ECCS loading protocol, which is shown in **Figure 11**. The loading consisted of 59 steps for the short and 39 steps for the long beam. The load was applied at the top of the left column in Z direction.

## Results

The cyclic behaviour of the FEM models (RBS-S) having two different material laws are presented in **Figure 12**. The cyclic behaviour of the FEM model with bilinear material did not follow the experimental results. It was observed a loss in strength as the number and amplitude of cycles increased. The FEM model with Chaboche material followed the experimental results, so the calibration was done using this approach.

While the calibration was performed on RBS-S FEM model, the RBS-L FEM model was used as verification.

In both cases RBS-S and RBS-L FEM models it was observed that the external energy was dissipated only by the beams by undergoing plastic deformations in the reduced zones, while the columns remained elastic (see **Figure 13**).

The FEM results for the RBS-S case are presented in **Figure 14** .It was observed that: the interaction between the shear and normal stresses caused an inclination of the buckled shape in the web; all the plastic deformations occurred in the beams and concentrated in the reduced zones, while columns remained elastic. The cyclic behaviour of the RBS-S is presented in **Figure 15**.

The FEM results for the RBS-L case are presented in **Figure 17**. It was observed that: the influence of the normal stresses is greater than the influence of the shear stresses which leads to a bending behaviour; all the plastic deformations occurred in the beams and concentrated in the reduced zones, while columns remained elastic. The cyclic behaviour of the RBS-L is presented in **Figure 16**.
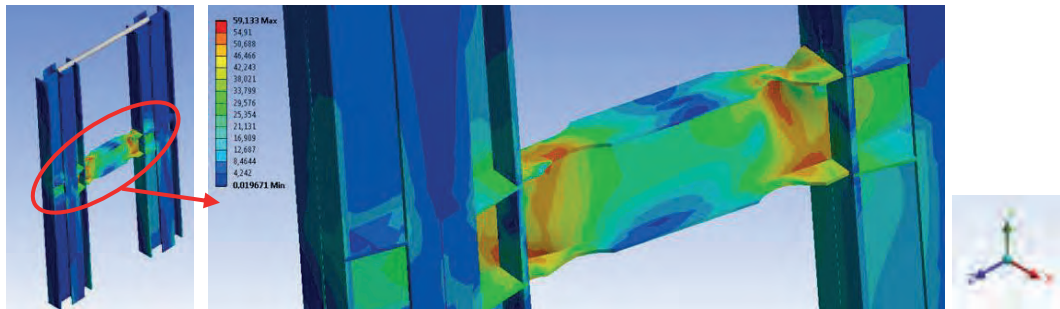
**Figure 13.** Dissipative dog-bone zones

# Numerical sensitivity study

The numerical model used for the parametric study was created in ANSYS software and the calibration and validation of the model were done to describe the static response of the experimental study.

Only the beam was considered in the geometric parameters study while the columns were not due to the elastic behaviour. The analysed geometric parameters are presented in Figure 18 and Table 4. The output parameters are presented in Table **5**.
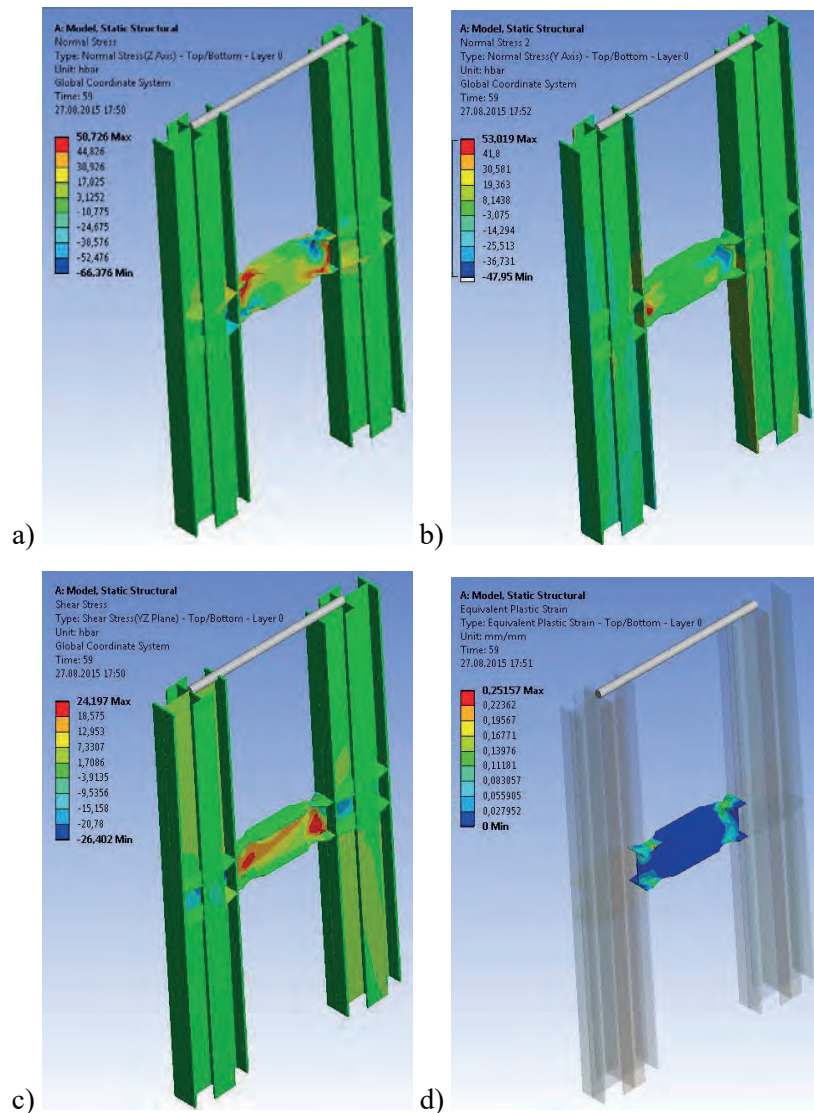


**Figure 14.** RBS-S FEM results: a) normal stress Z, b) normal stress Y, c) shear stress YZ, d) plastic deformation
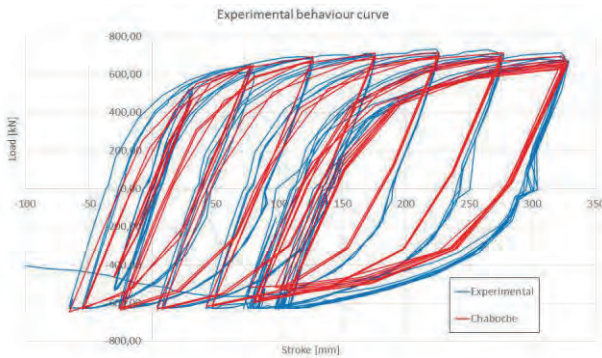
**Figure 15.** RBS-S FEM results: cyclic behaviour
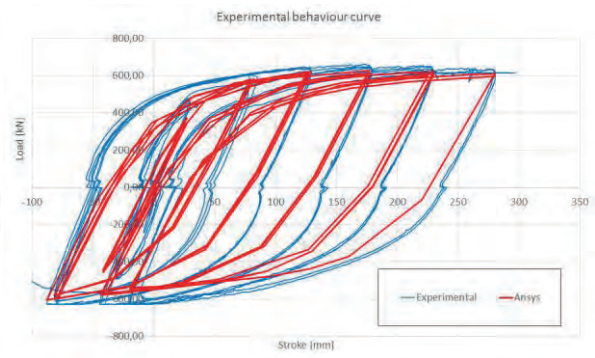


**Figure 16.** RBS-L FEM results: cyclic behaviour



a)



b)



c)



d)
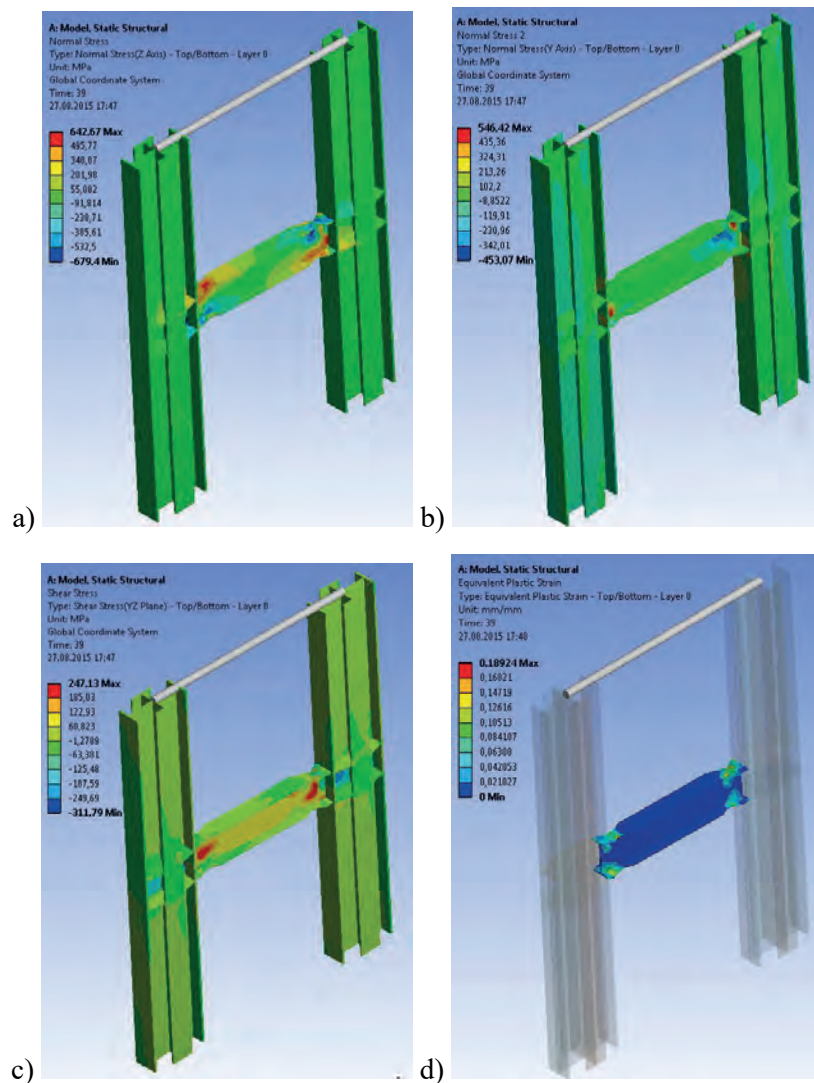
**Figure 17.** RBS-L FEM results: a) normal stress Z, b) normal stress Y, c) shear stress YZ, d) plastic deformation

The sensitivity study showed that the web height had a serious effect in the maximum force reaction about Z axis, meanwhile the dog-bone width, the web and flange thickness were less important. However, the web thickness had a significant role in case of the maximum normal and shear stresses as well (see **Figure 19**).

**Figure 18.** Geometric parameters used in the numerical sensitivity study

**Table 4.** Ansys input parameters for numerical sensitivity study

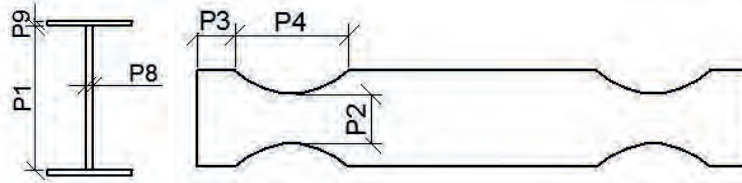| Geometric parameters for the beam | Lower limit (mm) | Upper limit(mm) |
|---|---|---|
| Web height – P1 | 300 | 600 |
| DogBone width – P2 | 120 | 200 |
| DogBone to Column distance – P3 | 70 | 130 |
| DogBone length – P4 | 270 | 330 |
| Web thickness – P8 | 15 | 25 |
| Flange thickness – P9 | 14 | 20 |

**Table 5.** Ansys output parameters for numerical sensitivity study

| Maximum force reaction about Z axis | P5 |
|---|---|
| Maximum normal stress | P6 |
| Maximum shear stress | P7 |

Related to the maximum normal and shear stresses, except the web thickness, web height, dog-bone width and flange thickness had secondary roles. Last but not least, it was clear that both of dog-bone length and the column to dog-bone distance have almost negligible effect. The results that have been reached from the parametric analysis were satisfactory due to the fact that the values of the coefficients of determination were almost equal to 1,0 (see **Figure 20**).
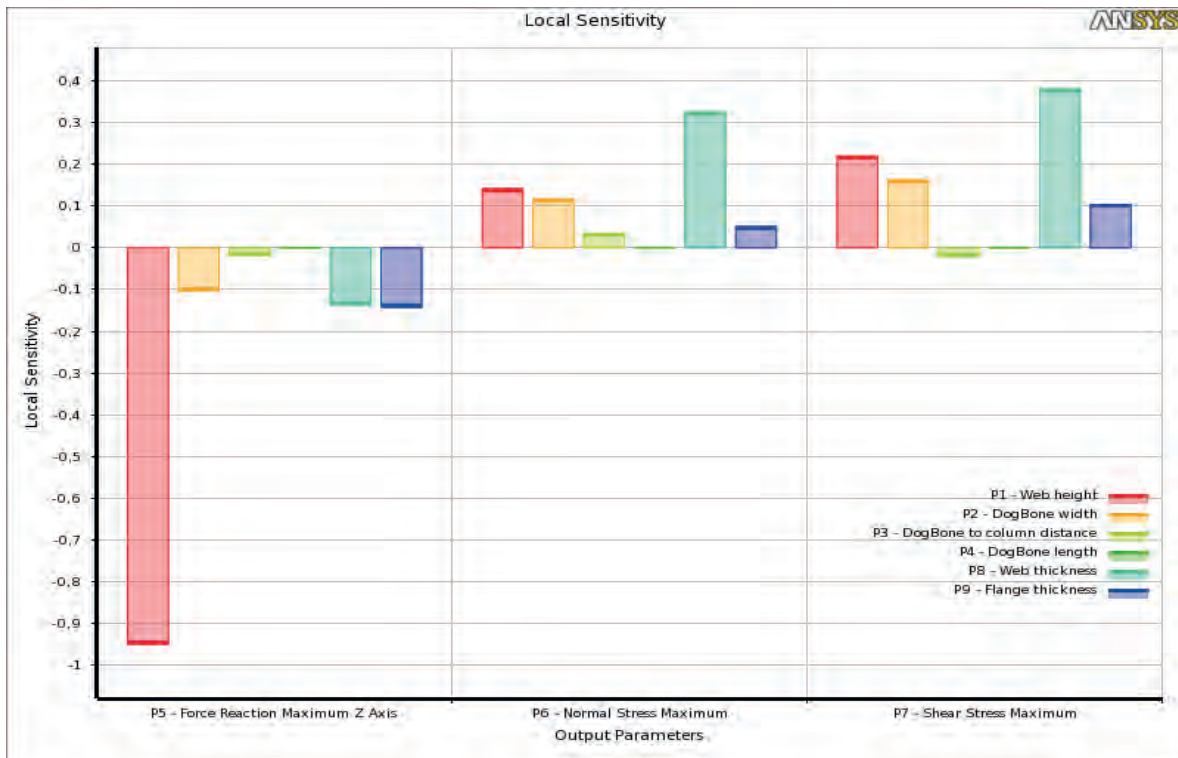


**Figure 19.** Sensitivity study results: Sensitivity of output to input parameters
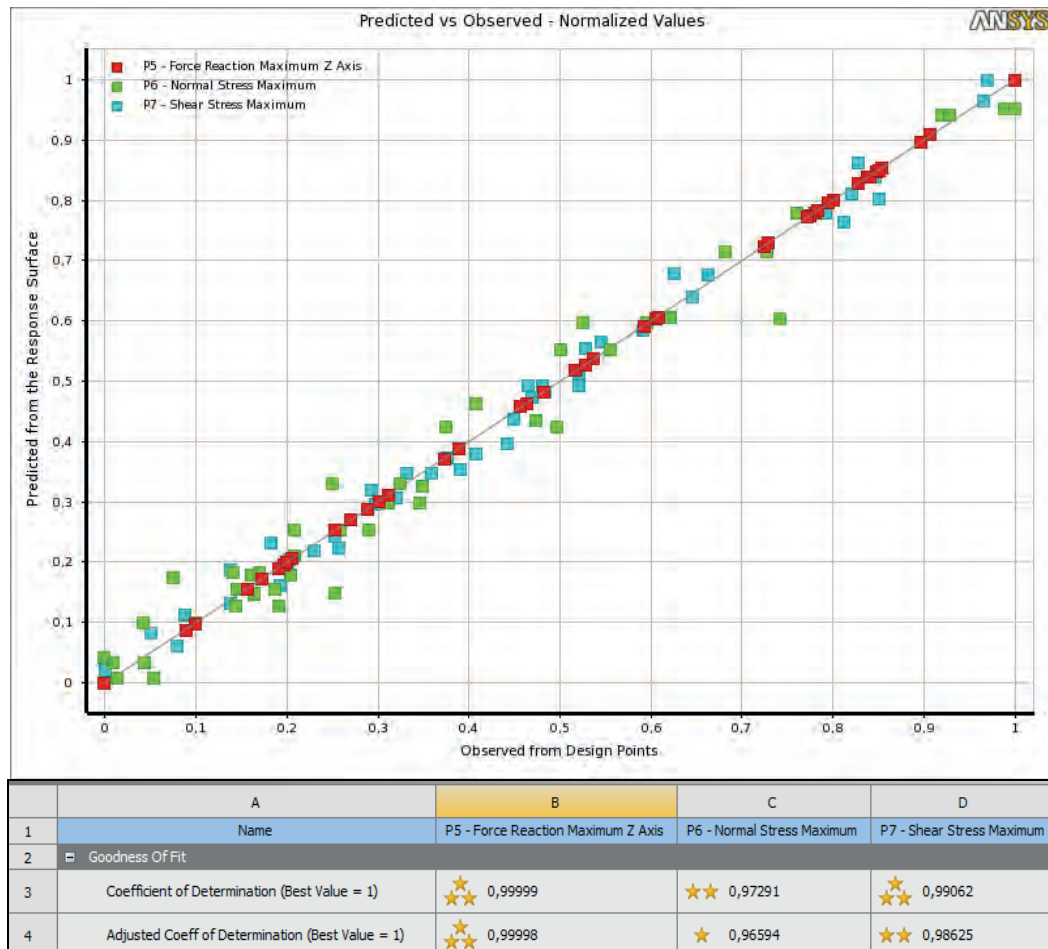
**Figure 20.** Sensitivity study results: coefficients of determination

## Conclusions

The main conclusions on the numerical evaluation of short coupling beams for moment-resisting steel frames in seismic areas can be summarized as follows:

- A numerical FEM model was successfully calibrated and validated against experimental data.
- Bilinear material model does not represent the real behaviour of the frame.
- Chaboche model takes into the account the hardening effect and the Baushinger effect.
- No plastic deformations were observed in the columns.
- Plastic deformations were concentrated in the RBS area.
- The sensitivity study presented the influences of the principal geometric dimensions of the connecting beam.

## References

Dinu, F., Dubina, D., Neagu, C., Vulcu, C., Both, I., Herban, S. (2013). Experimental and numerical evaluation of an RBS coupling beam for moment-resisting steel frames in seismic areas. *Steel Construction 6* (2013), **No. 1.**

Budahazy, V., Dunai, L. (2013). Parameter-refreshed Chaboche model for mild steel cyclic plasticity behaviour. *Periodica Politechnica Civil Engineering* (2013), **57/2**, pp. 139-153.

# Selected topics of Optimization in Civil Engineering

*ANIC Filip [a], BERNAGOZZI Giacomo [b], BILGIN Merve [c], DE SMEDT Maure [d], HOSSEINI Asefeh [e], LOPEZ Sebastián [f], TANHADOOST Amin [g],*

*[a] University Josip Juraj Strossmayer Osijek, Faculty of Civil Engineering, Croatia*

*[b] University of Bologna, Italy*

*[c] Middle East Technical University, Turkey*

*[d] KU Leuven, Belgium*

*[e] Isfahan University of Technology, Iran*

*[f] Escuela Colombiana de Ingenieria, Bogota, Colombia*

*[g] Sharif University of Technology, Iran*

*JAOUADI Zouhour, and LAHMER Tom*
*Junior Chair of Stochastics and Optimization, Bauhaus University Weimar*

## Abstract

This project is a part of the Bauhaus Summer School 2015 at Weimar about "Forecast Engineering: From past design to future decision". The project title 'Selected topics of optimization in Civil Engineering' shows the broad spectrum of possibilities in optimization. Different topics were therefore discussed, after a general overview of the theoretical aspects of optimization. This paper gives the results from these different topics.

## Introduction

Nowadays, design is performed by use of models and experiments. But it is important to construct a reliable model in order to predict the safety and serviceability of the structures. The quality of the model is strongly correlated with the knowledge of the material parameters. These parameters can sometimes be found in literature or due to laboratory testing. But in most complex cases, model calibration is needed in order to find the optimized model parameters. Also topology optimization is a subject that will be investigated through optimization techniques.

In general, optimization is the systematical choice of the best combination of admissible variables in a defined domain in the sense of minimizing a real valued function, namely the cost function. Different optimization schemes are developed and can be applied to common problems in Civil Engineering. [1]

## Theory of Optimization Techniques

There are four elements needed for an optimization problem:

1. A description of the problem and the corresponding model.
2. A function that can be minimized. This is called the cost function and assigns a value for each combination of admissible variables.
3. The variables to optimize. These are the parameters of the model.

4. A domain of admissible values for the different parameters. Sometimes, parameters are constrained by physical values, e.g. the Young's modulus E can never be negative.

In most calibration problems, the cost function is defined as the minimization of the distance between the measurements and the model outcome. This is expressed as the summed squared difference between both values. The model outcome depends on one or more parameters. If there are more measurements available than parameters to be identified, the cost function is non-linear. [1]

Different optimization schemes are available from literature, mostly iterative. They differ in calculation time and applicability, and have their own advantages and drawbacks. Some of these algorithms are further explained and implemented. Two main classes can be distinguished, depending on the differentiability of the cost function. If the cost function can be derived (either analytically or via a difference), the gradient and the Hessian can be used in the algorithm. If not, for example for noisy functions, other techniques must be used. [2, 3, 4, 5]

## Gradient and Newton Methods

Classical approaches in the field of non-linear optimization are Gradient and Newton-Methods. These methods are motivated by studying necessary and sufficient conditions of optimality. These class of optimizers are generally supported by mathematical analysis concerning convergence and convergence rates. In this course, the following methods are discussed:

– gradient methods with line-search strategies.
– the local Newton method, where also the Hessian is used to determine the step direction. As such, the step length is always optimal and the method is faster than the gradient methods.
– the so-called quasi-Newton method, where the Hessian matrix is approximated by a rank two update according to the BFGS approach. This allows to approximate Hessians and to use Newton directions in the optimizer instead of gradient directs, which depending on the topology of the optimizing problem may tend to zig-zagging leading to slow convergence.

Of course, there are also other optimization schemes or variants of the foregoing, which can be found in literature. [2]

## Direct Search Methods

It is not always possible to calculate gradients in a satisfying manner, mainly due to missing differentiability of the cost function or a contamination of the function with noise. In these cases it can be advisable to apply gradient free methods, so called direct search methods. A very effective and well-proven method is the algorithm according to Nelder-Mead, which bases on simplex. A simplex is the connection of (n+1) points in the parameter space, where n is the number of parameters which need to be identified. Now, the strategy is to replace always the vertice which has the largest value in the cost function. The replacement is done by reflecting this point to the centroid of all other points. A series of expansion and contraction approximates a kind of line search. After finding a new point, the vertices are sorted again and the vertice with the worst cost function value is again replaced. Being close to an optimum, the simplices start to shrink.

# The Topics

Optimization techniques can be used for a lot of applications. After the theoretical background, different topics are discussed. These selected topics of optimization in Civil Engineering will be further explained.

## Equation of motion

### *Description of the problem*

The first topic is an example of a basic civil engineering problem, which can be calibrated with different optimization techniques. The equation of motion describes the motion of a system as a function of time. It is a differential equation depending on the mass, the stiffness and the damping of the system. The one dimensional equation of motion is:

$$mu''(t) + cu'(t) + ku(t) = 0$$

with:

$u(t)$      Displacement of the system.
$u'(t)$      Velocity of the system. First derivative with respect to time.
$u''(t)$      Acceleration of the system. Second derivative with respect to time.
$m$      Mass of the system.
$c$      Damping of the system.
$k$      Stiffness of the system.

The solution of this equation for the following initial conditions

$$u(t = 0) = u_0 \ \text{ and } \ u'(t = 0) = 0$$

is known by literature:

$$u(t) = u_0 \cdot \exp(-\delta \cdot t) \cdot \cos(\omega \cdot t)$$

where

$$\delta = \frac{c}{2m} \ \text{and} \ \omega = \sqrt{\frac{k}{m} - \frac{c^2}{4m}}$$

For this example, five datasets with measurements of displacements in function of time are available. The objective is to optimize the values of the mass m, the damping c and the stiffness k, by minimizing the difference between the measurements and the outcome of the model. This results in the cost function, with $x$ the unknown parameters:

$$f(x) = \sum_{i=1}^{N} \left( u_{simulated}(t_i, x) - u_{measured}(t_i) \right)^2$$

Different optimization schemes are implemented in the computer program MATLAB and will be compared. The initial displacement $u_0$ is equal to the value 2, so that the other three parameters have to be optimized. For each optimization scheme, an initial value has to be chosen.

*Gradient method with line-search*

The optimization of the above mentioned Single Degree Of Freedom system is performed starting from its free damped vibration response. The parameters of the system are initially assumed as

$$u_0 = 2; \; m = 1; \; k = 1; \; c = 0,1$$

in order to simulate the measured data.

Only two parameters, which are the stiffness $k$ and the damping $c$, are firstly taken into account in the optimization. By minimizing the cost function, the gradient method manages to determine the values of the parameters which lead to an accurate fit into the measured data, as reported in Figure 1.

The optimal point is the minimum in the surface described by the cost function, as could be clearly individuated in the 3D plot of Figure 2.

The optimization of the three parameters, which characterize the system (i.e., mass, damping and stiffness) is subsequently taken into account. The contour plots of the cost function are obtained in Figure 3. In each of them, one parameter is fixed and equal to the exact value, while the other two are varying within a certain range. This also shows that an optimization of more than two parameters at the same time is not possible with the common methods.
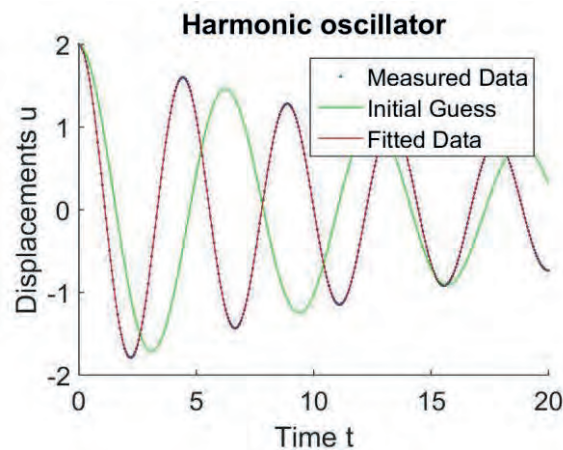


**Figure 1.** Optimization of the SDOF system by the gradient method.
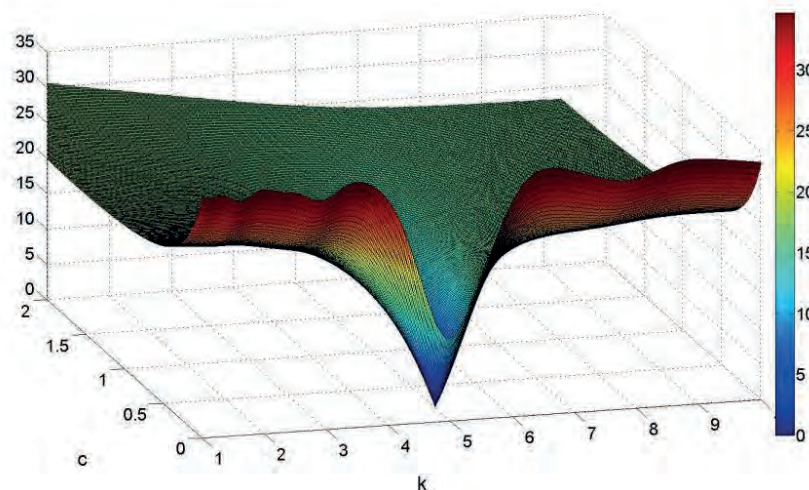


**Figure 2.** Surface of the cost function, depending on stiffness and damping.
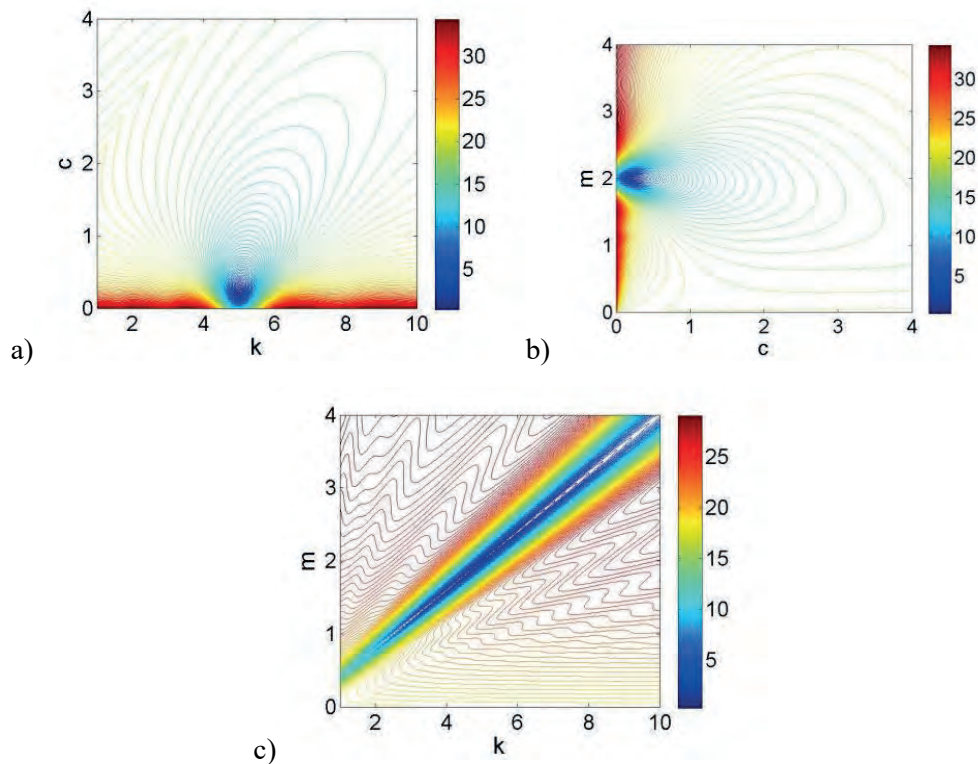
**Figure 3.** Contour plots of the cost function depending on: a) stiffness and damping; b) damping and mass; c) stiffness and mass.

It is worth noting that there is a linear trend in the contour plot that is related to the mass and the stiffness (Figure 3c). Therefore, it is difficult to find the most optimal value. When the damping is fixed, the solution of the stiffness and the mass may not be unique. This leads to the impossibility of adequately optimizing the three parameters ($m$, $c$, $k$) all together.

*Local Newton Method*

Instead of using the predefined MATLAB-algorithms, an optimization scheme can be implemented itself. This is done for the Local Newton Method, applied on the example of the equation of motion. The implementation uses the same framework as the other algorithms of previous example. The central idea of the Local Newton Method is to approach the cost function by the Taylor expansion to the second order. As such, the descent direction $d^k$ is determined by use of the gradient, but also the Hessian.

$$\nabla^2 f\left(x^k\right) \cdot d^k = -\nabla f(x^k)$$

$$x^{k+1} = x^k + d^k$$

The advantage of this method is the reduction in computational time. But the disadvantage is the local convergence. The initial value must be chosen close to the optimal value, so that the Hessian is positive definite. Otherwise, the Local Newton Method will not converge.

The Local Newton Method is implemented for optimizing the values of the stiffness and the damping. The mass m is fixed at value 2. After implementing this method, different tests are performed. First, the convergence is checked. It appears indeed that the algorithm does not work for all initial values.

For example, for the first dataset, the possible initial values must be chosen in the interval (determined by trial and error):

$$for\ the\ stiffness: 3{,}6\ \leq k \leq 4{,}4\ (optimal\ value = 4)$$

$$for\ the\ damping: 0{,}01 \leq c \leq 0{,}25\ (optimal\ value = 0{,}2)$$

The second test is the comparison with the previous optimization scheme. The calculation time can be computed with the MATLAB command 'tic toc'. For the initial values of stiffness equal to 4.4 and damping equal to 0.25, the Local Newton method needs 17 iterations or 2.58 seconds computational time. For the same initial values, the gradient method with line-search needs 38 iterations or 3.4 seconds computational time. In Figure 4, the value of the cost function and the norm of the gradient are plotted to the number of iterations. It is visible that the gradient method needs more iteration. The end of the iterations is determined by the norm of the gradient. In both cases, the tolerance is taken as $10^{-4}$.

Figure 5 shows that the gradient method goes fast to the neighbourhood of the optimal value, but needs a lot iterations around this point to reach it. The Local Newton Method on the other hand needs more iteration to go the neighbourhood, but then the optimal value is reached more quickly.
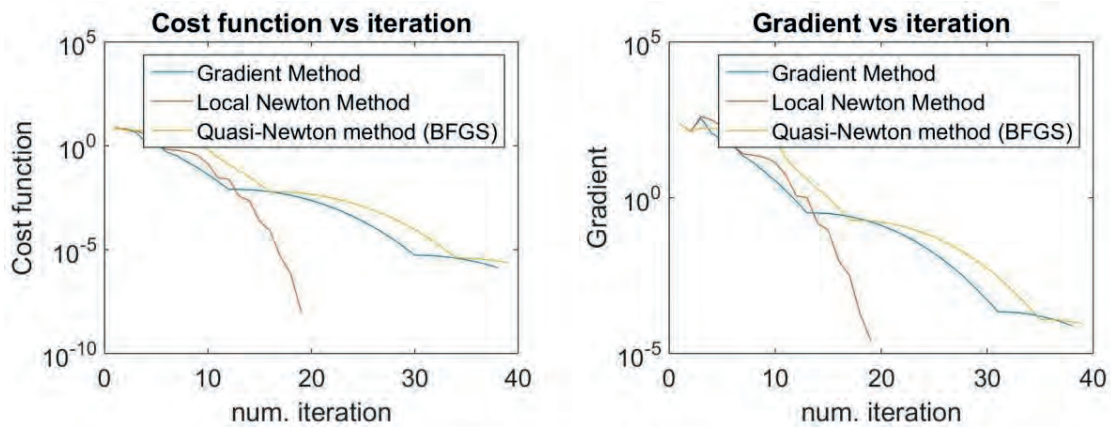


**Figure 4.** Comparison of the gradient method and the Local Newton method: (left) cost function; (right) gradient.
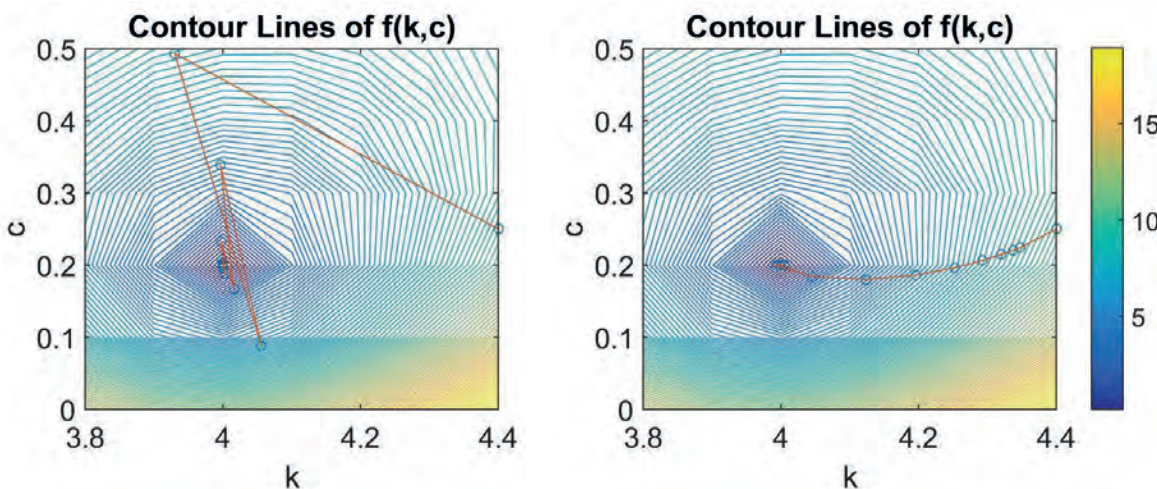


**Figure 5.** Comparison of the optimization by a) the gradient method; b) the Local Newton method.

This example shows indeed the reduction in computational time. For this simple calibration problem, the difference is not that large. But for more complex systems, it is important to consider the computational time. On the other hand, for a complex system, the calculation of the Hessian will require a lot of computational time. So there are examples for which the gradient method is faster. The Local Newton Method is therefore useful if there is a good estimation of the optimal value, so that convergence can be reached and the calculation of the Hessian is not too difficult.

A solution for this problem is to extend the Local Newton Method to the Global Newton Method. As such, the advantage of the gradient method and the Local Newton Method is combined. By starting with the first method, it is always possible to have convergence, even if the initial guess is far away from the optimal value. When the values come closer to the optimal value, the method switches to the Local Newton Method to have a smaller computational time.

### *Quasi-Newton Method – BFGS approach*

In the Local Newton Method, the Hessian needs to be calculated in each iteration step, which requires a large computational time. Therefore, the Quasi-Newton method is implemented. The Hessian is approximated by a rank two update, according to the BFGS approach (Broyden, Fletcher, Goldfarb, Shanno). This method is also compared to the gradient method with line-search on the example of the equation of motion.

It is expected that there is a reduction in the computational effort adopting the optimization through the Quasi-Newton method with BFGS update, which is a second order method, instead of using the gradient method, which is a first order one. Although, the initial values of the example used in the Local Newton Method does not confirm this expectation, see Figure 4. 39 iterations are needed, which is more than the 38 of the gradient method. So the performance of the Quasi-Newton method with BFGS approach depends also on the initial guess.

Figure 6 shows the optimization by the gradient method, compared to the Quasi-Newton method with BFGS update. The Quasi-Newton method goes smoother to the optimal value, but not as fast as the Local Newton Method (see Figure 5).

So, the Quasi-Newton method with BFGS update extends the Newton method and no exact computation of the Hessian of the cost function is needed. It is worth noting that all the methods belonging to the Newton class require a good initial guess that is not far from the optimal point to get convergence.
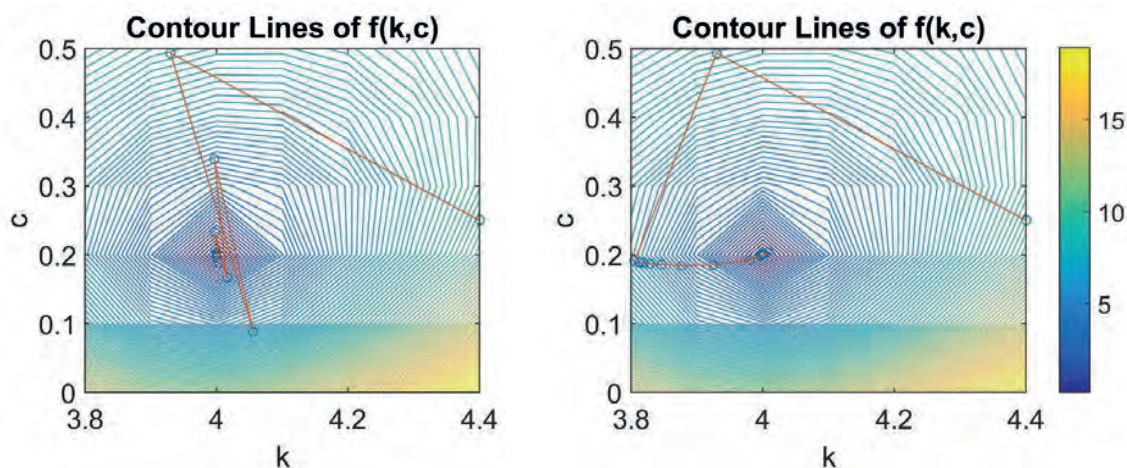


**Figure 6.** Comparison of the optimization by a) the gradient method; b) the Quasi-Newton (BFGS).

*Frequency domain*

In part 1.2, the problem of the not unique solution is explained by Figure 3c. Due to the linear trend in the contour plot, it is difficult to find the optimal values. A solution therefore can be found by considering the frequency response function of the system instead of the free vibration in time domain.

The optimization and the identification of the parameters of a SDOF damped system, performed in the frequency domain, starts from its receptance frequency response function (FRF). The equation of the FRF is recalled [6, 7]: it is a complex values function and its modulus and phase could be also computed.

$$H(\omega) = \frac{1}{k - \omega^2\, m + i\,\omega\,c}$$

$$|H(\omega)| = \frac{1}{\sqrt{(k - \omega^2 m)^2 + (\omega\, c)^2}}$$

$$\varphi(\omega) = tg^{-1}\left(\frac{-\,\omega\,c}{k - \omega^2\,m}\right)$$

The cost function for the optimization is firstly expressed only considering the measured and simulated modulus of the FRF, where $x=[k,c]$ or $x=[k,c,m]$.

$$f(x) = \sum \left(|H^{meas}| - |H^{sim}|\right)^2$$

The optimization is performed through both the steepest descent Gradient method and the Matlab implemented *fminunc* function [8], which is related to the extended Gradient method. The results are accurate, as noticeable in Figure 7, both for the two parameters and the three parameters optimization.

It is possible to state that the simultaneous identification of all the parameters ($m$, $c$, $k$) is possible starting from the FRF of the SDOF system. In fact a minimum is present in all the contour plots of the cost function (Figure 8). This result, obtained in the frequency domain, does not occur in the previous analysis in the time domain. The not-unique solution of the time domain is solved dye to the transformation to the frequency domain.

As expected, a different number of iterations is required for the two parameters optimization with respect to the three parameters one. The results obtained through the steepest descent Gradient method show that 84 iterations are required for $x=[k,c]$ while 1012 iterations for of $x=[k,c,m]$ (Figure 9).
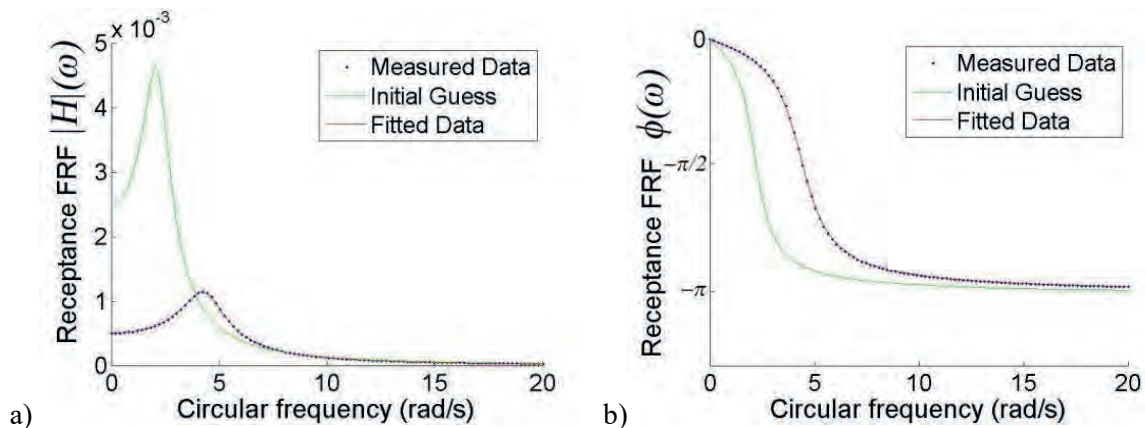


**Figure 7.** Optimization of the SDOF system through FRF: a) modulus; b) phase.
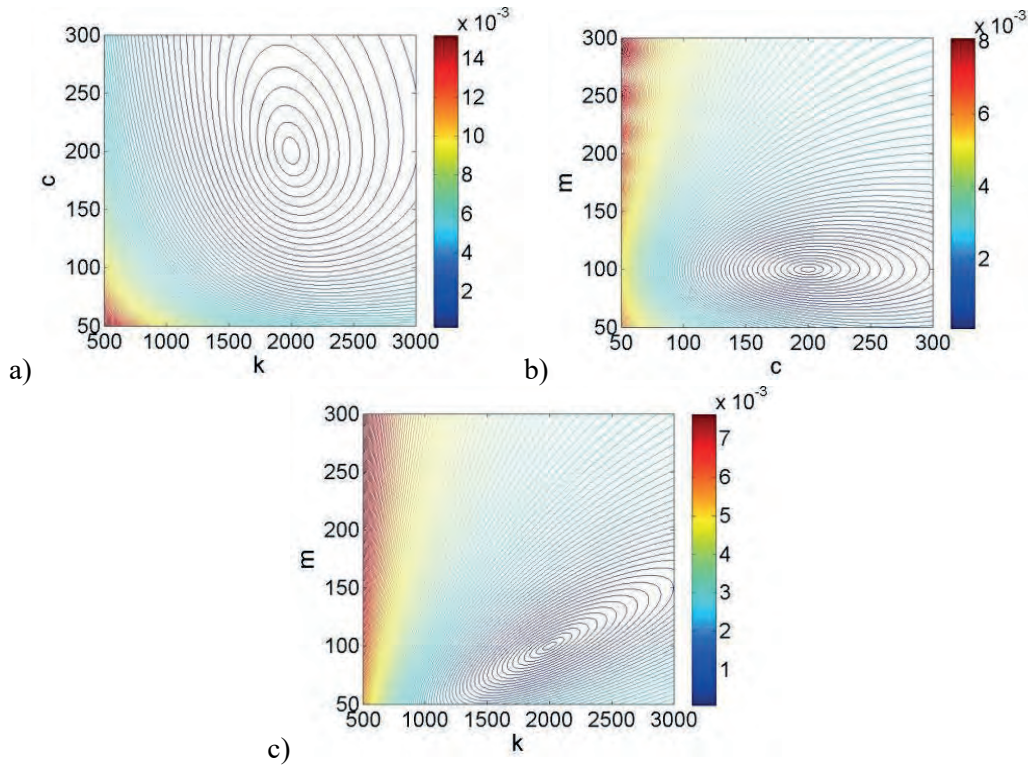
**Figure 8.** Contour plots of the cost function depending on: a) stiffness and damping; b) damping and mass; c) stiffness and mass.

A more extended cost function, which consider both the modulus and the phase of the FRF, is also investigated

$$f(x) = \frac{1}{\max(|H^{meas}|)} \sum (|H^{meas}| - |H^{sim}|)^2 + \frac{1}{\max(|\varphi^{meas}|)} \sum (\varphi^{meas} - \varphi^{sim})^2$$

where $x=[k,c]$ or $x=[k,c,m]$. Adopting this function instead of the cost function with only the modulus for the optimization leads to lower values in the residuals between the measured and the optimized data.
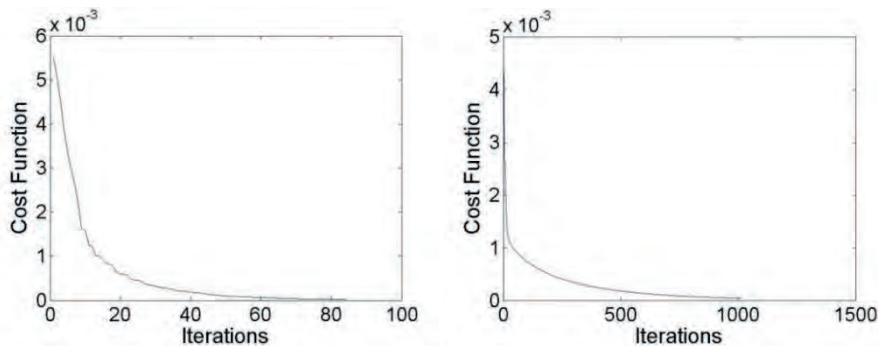


**Figure 9.** Cost function vs. iterations: a) k and c; b) k,c and m.

69

**Calibration of Engineering Structures**

After the topics about different optimization schemes applied on the equation of motion, some applications in structural engineering are made. In a first topic, a comparison is made between different objective functions. In the second one, the effect of noise on the measurements is investigated.

*Model updating of a RC plane frame*

A model updating [7] procedure is simulated and applied to a 4-storeys RC plane frame, which is assumed to be described by a 4-DOFs shear type model. Two different structural configurations, which are related to different distributions of the columns stiffness along the height of the frame, are considered. In the first case (Figure 10a) the elastic modulus ($E$) of the concrete is assumed to be constant at each floor. In the secon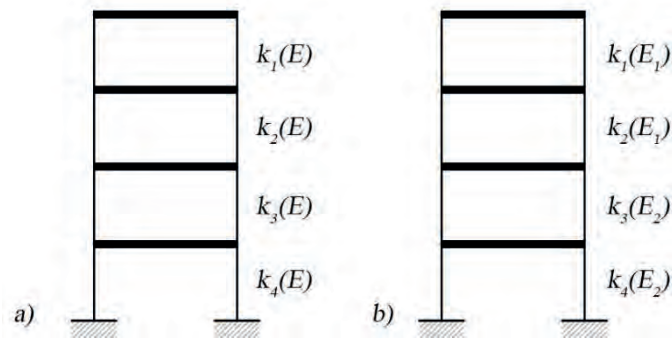d case (Figure 10b) the elastic modulus of the first two lower levels ($E_2$) is higher than the one related to the upper floors ($E_1$).



**Figure 10.** Shear type models of two frames with different distributions of the elastic modulus: a) one parameter - E; b) two parameters - $E_1$ and $E_2$.

The objective of the application is to study the performance of different cost functions that can be adopted in the model updating through optimization of the structure, starting from experimentally determined modal parameters [6,7] (i.e. natural circular frequencies and mode shapes). The optimization is performed with the Matlab implemented *fminsearch* function [4], which is related to the Nelder-Mead method. It is a very robust method since it does not require the computation of the gradient of the cost function.

In the model updating through optimization of the frame that is characterized by one elastic modulus, the cost function is assumed to be related to the differences between the measured and the simulated natural circular frequencies, where $i = 1.. n$ modes. The mode shapes are not considered since they are not modified by a global variation in the elastic modulus of the structure.

$$f(E) = \sum_{i=1}^{n} ( \omega_i^{meas} - \omega_i^{sim})^2$$

For this one parameter optimization, the optimal point is clearly shown by the cost function, as reported in Figure 11, and this easily leads to the exact determination of the elastic modulus of the concrete which is expressed in [N/m$^2$].
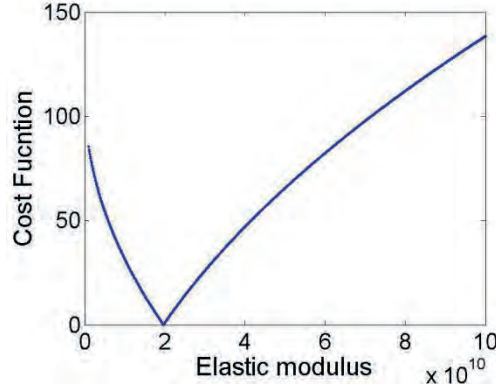
**Figure 11.** Cost function f(E) related to natural circular frequencies - first case.

In the second case, two parameters $E_1$ and $E_2$ are taken into account in the optimization procedure. Firstly, the cost function is assumed to be related to the natural circular frequencies, where $i=1.. n$ modes.

$$f(E_1,E_2) = \sum_{i=1}^{n} ( \omega_i^{meas} - \omega_i^{sim})^2$$

Secondly, the cost function is assembled as the difference between the measured and the simulated mode shapes, where $i=1.. n$ modes and $j=1.. m$ DOFs.

$$f(E_1,E_2) = \sum_{j=1}^{m}\sum_{i=1}^{n} ( \phi_{ij}^{meas} - \phi_{ij}^{sim})^2$$

Finally, the cost function is assumed to be related to both the natural circular frequencies and the mode shapes, where $i=1.. n$ modes and $j=1.. m$ DOFs.

$$f(E_1,E_2) = \frac{1}{max(\omega_i^{meas})}\sum_{i=1}^{n} ( \omega_i^{meas} - \omega_i^{sim})^2 + \frac{1}{max(\phi_{ij}^{meas})}\sum_{j=1}^{m}\sum_{i=1}^{n} ( \phi_{ij}^{meas} - \phi_{ij}^{sim})^2$$

Each of the three above mentioned cost functions is evaluated for a range of values related to the elastic moduli $E_1$ and $E_2$, which are expressed in [N/m$^2$].

The cost function that depends on the natural frequencies only (Figure 12a) leads to the possibilities of finding, through the optimization, a local minimum which is not the optimal point. In Figure 12b, the cost function related to the mode shapes only, shows that there is a linear trend in its contour plot and the optimization could not be an easy task. Only in the last case, when both the natural frequencies and the mode shapes are considered in the cost function, an unique and minimal solution is obtained, as clearly shown in Figure 12c.

This example shows that it is important to consider which cost function is chosen, otherwise bad or no results can be obtained.
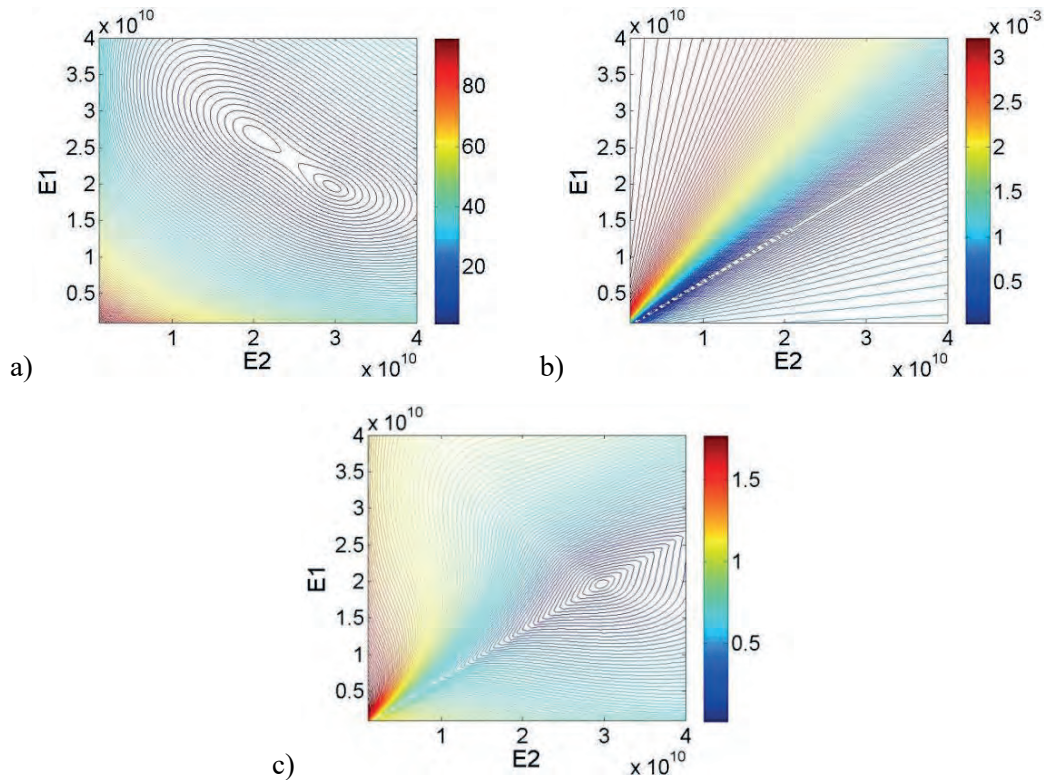
**Figure 12.** Second case - contour plots of the cost function f(E₁,E₂) depending on: a) natural circular frequencies; b) mode shapes; c) both.

## *Modal analysis optimization of a steel structure*

The objective of this topic was to investigate the power of different optimisation techniques using Matlab on a model made for a modal analysis. The optimisation techniques were as follows:

1. Multidimensional unconstrained nonlinear minimization, by Nelder-Mead direct search method

2. Scalar bounded nonlinear function minimization

The first method could implement as many unknowns as needed, the second one can implement only one parameter.

## *The general model*

The referred model was made using Calfem [9] via finite element method. The model consists of an column with steel section IPE100 and a beam with IPE80 section (see Figure13). The material characteristics needed for the modal function $f(x)$ are given in Table 1.

**Table 1**. Material properties.

| Data | Values |
|---|---|
| Elastic modulus | $x(1) = E = 3.0000 \cdot 10^{10} \ N/m^2$ |
| Density | $x(2) = \rho = 2500.0000 \ kg/m^3$ |
| IPE 100 area | $x(3) = A_v = 0.1030 \cdot 10^{-2} \ m^2$ |
| IPE 100 moment of inertia | $x(4) = I_v = 0.0171 \cdot 10^{-4} \ m4$ |
| IPE 80 area | $x(5) = A_h = 0.0764 \cdot 10^{-2} \ m^2$ |
| IPE 80 moment of inertia | $x(6) = I_h = 0.00801 \cdot 10^{-4} \ m4$ |

Furthermore, the eigenvalues and eigenvectors from the original file along with the properties from Table 1 are taken as a measurement data. However, to have more realistic results some random noise was incorporated in measured data as following:

$$\lambda = \lambda + c_v^{signal} \cdot \text{randn}$$

$$v = v + c_v^{signal} \cdot \text{randn}$$

where

$\lambda$ – is an eigenvalue

$v$ – is a eigenvector

$\sigma$ – is a standard deviation of the signal (default value approximated to. $c_v^{signal} = 0.07$)

randn – is a random number generator with normal distribution

Note that the randn was locked with one value, thus, the same value was used for each iteration. The difference can be seen in Figure 13c and Figure 13d.



a) The real structure

b) The FEM model setup

c) Normal first mode of vibration

d) First mode with artificial noise
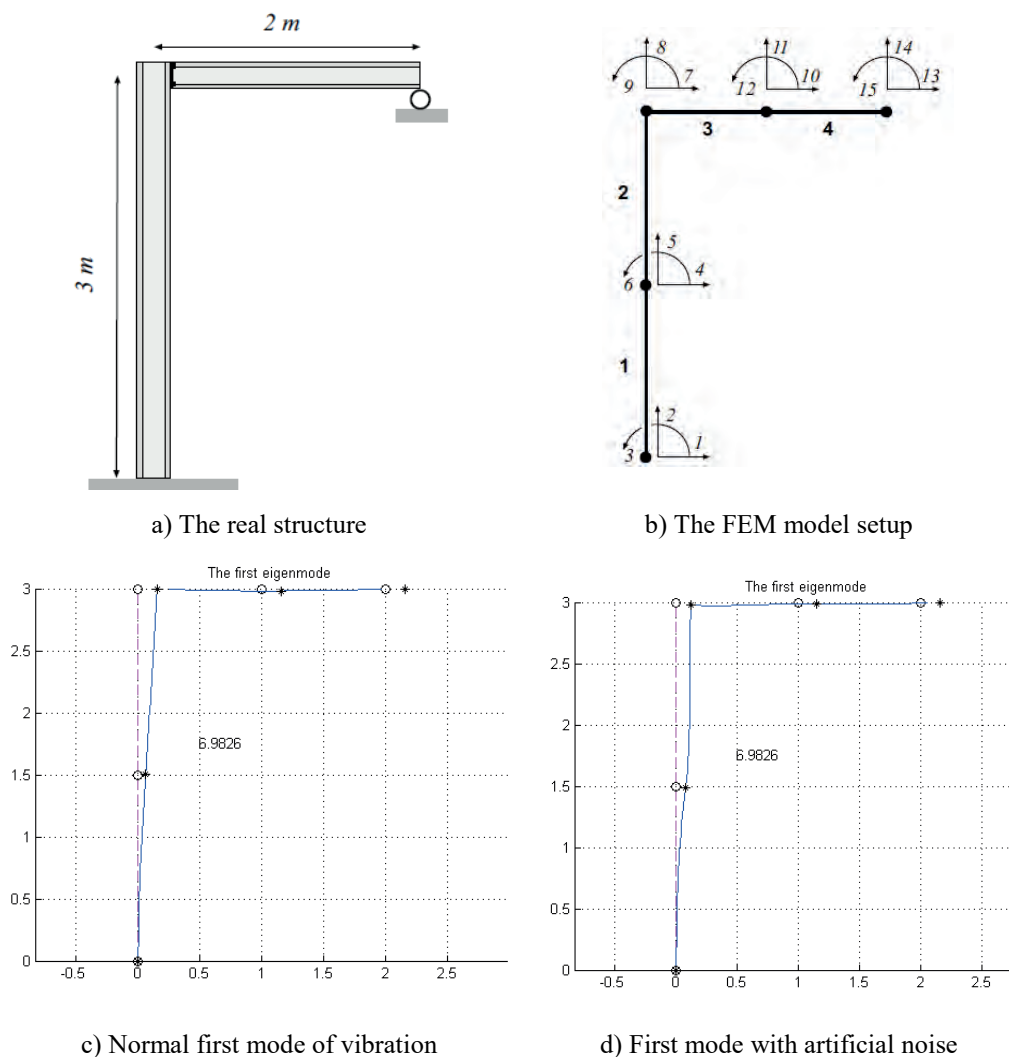
**Figure 13.** Observed model.

*The optimisation*

For the purpose of testing the power of the optimisation tools, 16 tests were made, 7 without noise and 9 with artificial noise. Additionally, with the scalar bounded nonlinear function minimization method more test were performed with variating signals coefficient of variation: $c_v^{sig} = \{0.07, 0.1, 0.2, 0.3\}$. Hence, the tests in Table 2 were made.

**Table 2.** The test models.

| Test | Unknowns and setup | Optim. method | Test | Unknowns and setup | Optim. method |
|------|--------------------|:---:|------|--------------------|:---:|
| 1 | $x(1)$ | 1 | 9 | $x(1,2,3,4,5)$ | 1 |
| 2 | $x(1)$ and noise | 1 | 10 | $x(1,2,3,4,5)$ with noise | 1 |
| 3 | $x(1,2)$ | 1 | 11 | $x(1,2,3,4,5,6)$ | 1 |
| 4 | $x(1,2)$ and noise | 1 | 12 | $x(1,2,3,4,5,6)$ and noise | 1 |
| 5 | $x(1,2,3)$ | 1 | 13 | $x(1)$ | 2 |
| 6 | $x(1,2,3)$ and noise | 1 | 14 | $x(1), c_v^{sig} = 0.1$ | 2 |
| 7 | $x(1,2,3,4)$ | 1 | 15 | $x(1), c_v^{sig} = 0.2$ | 2 |
| 8 | $x(1,2,3,4)$ and noise | 1 | 16 | $x(1), c_v^{sig} = 0.3$ | 2 |

The unknown values can be measured, expected and therefore, can be known. Hence, every characteristic has its own data distribution via standard deviations. Thus, for the purpose of the optimisation, the initial values were obtained by the following interval:

$$x(i) \in [x(i) - c_v(i) \cdot x(i), \; x(i) + c_v(i) \cdot x(i)]$$

Where the $x(i)$ is the unknown parameter of the $f(x)$ and $c_v$ is coefficient of variation. The starting point for the Nelder-Mead methods is the minimum value of the $x$ interval. The coefficient for each material was obtained and calculated from [10, 11, 12] Furthermore, the tolerance for all techniques was set to $10^{-10}$.

*The results*

Figure 14 gives some cost function plots of different tests. The results are shown in Table 3. The error was calculated as follows:

$$\Delta x(i) = 1 - \frac{x_{sim}(i)}{x_{meas}(i)} \cdot 100 \; [\%]$$

As Table 3 shows, the number of iterations is variable from test to test. The biggest number of iterations was observed in test 3, 4, 5 and 6. Hence, these are the problems with two and three unknown parameters. This may be due to the presence of the local minima as those observed in Figure 14b and Figure 14c. As the number of unknowns rises, the number of iterations get smaller. Thus, one can guess that those functions have less profound local minima. Test number 7 and 8, with four unknowns, have shown the maximum error difference (above 10%). On the other hand, logically, by having less parameters the error in difference was lower.
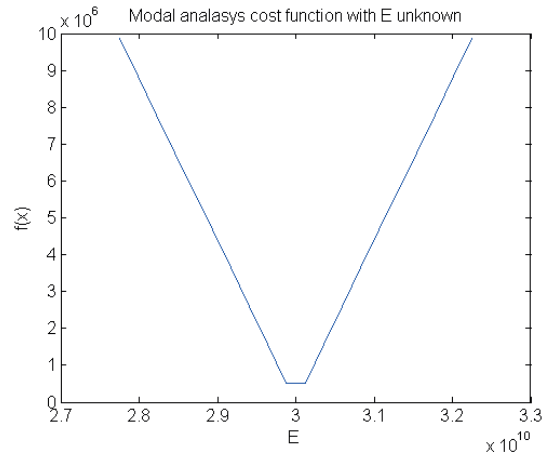
a) Cost function plot of the test no.1
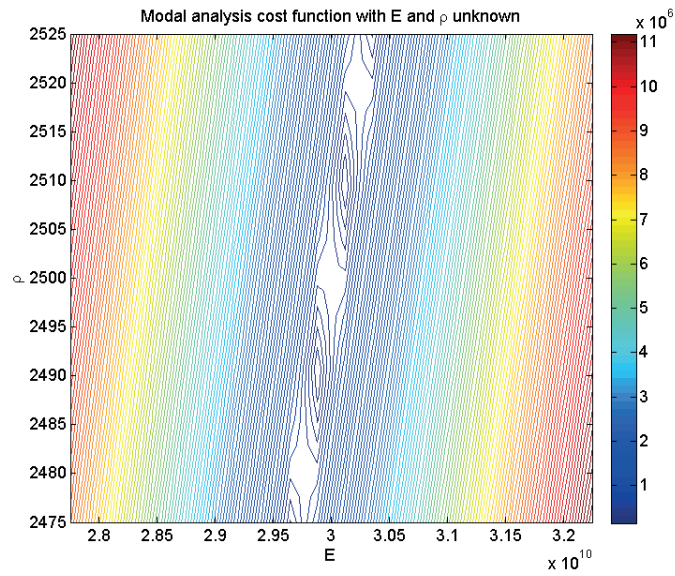


b) Cost function plot of test no. 3, the 2D projection
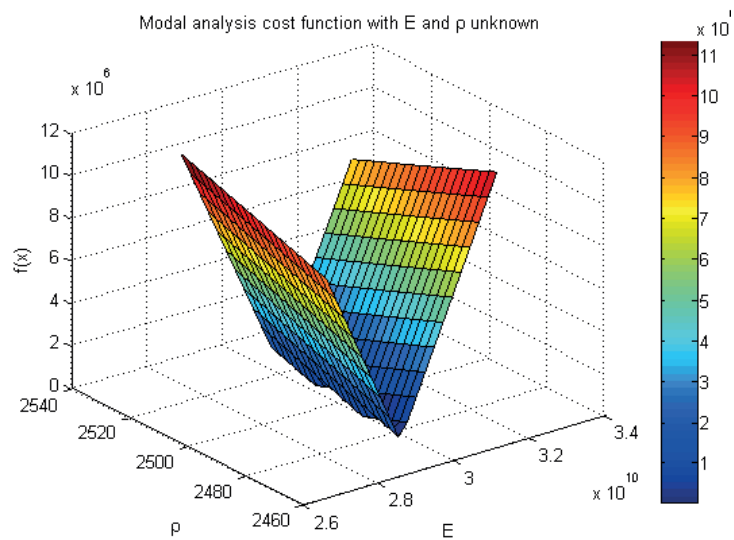


c) Cost function plot of test no. 3, the 3D projection

**Figure 14.** Cost function plots.

Furthermore, using the scalar bounded nonlinear function minimization has shown that having a single variable is more cost efficient method than the Nelder-Mead direct search method (regarding the number of iterations). In addition, adding and increasing the artificial signal did not show significant difference.

In summation, both methods have shown fast and accurate fitting of the simulated and measured data.

**Table 3.** The test results.

| Test no. | No. of iterations | $\Delta E$ (%) | $\Delta$rho (%) | $\Delta Av$ (%) | $\Delta Iv$ (%) | $\Delta Ah$ (%) | $\Delta Ih$ (%) |
|---|---|---|---|---|---|---|---|
| Multidimensional unconstrained nonlinear minimization, by Nelder-Mead direct search method | | | | | | | |
| 1 | 51 | 0,00 | / | / | / | / | / |
| 2 | 52 | 0,00 | / | / | / | / | / |
| 3 | 2592 | -7,50 | -1,00 | / | / | / | / |
| 4 | 3743 | 2,80 | 2,80 | / | / | / | / |
| 5 | 3888 | 3,52 | 3,52 | 0,00 | / | / | / |
| 6 | 2110 | 3,52 | 3,52 | 0,00 | / | / | / |
| 7 | 1889 | 11,97 | 11,97 | 0,00 | 0,00 | / | / |
| 8 | 1856 | 11,97 | 11,97 | 0,00 | 0,00 | / | / |
| 9 | 1756 | 2,37 | 2,37 | 0,00 | 0,00 | 0,00 | / |
| 10 | 1721 | 2,37 | 2,37 | 0,00 | 0,00 | 0,00 | / |
| 11 | 1549 | 5,93 | 5,93 | -1,65 | -1,65 | -1,65 | -1,65 |
| 12 | 1522 | 5,93 | 5,93 | -1,65 | -1,65 | -1,65 | -1,65 |
| Scalar bounded nonlinear function minimization | | | | | | | |
| 13 | 14 | 0,00 | / | / | / | / | / |
| Scalar bounded nonlinear function minimization with noise variations | | | | | | | |
| 14 | 14 | 0,00 | / | / | / | / | / |
| 15 | 13 | 0,00 | / | / | / | / | / |
| 16 | 13 | 0,00 | / | / | / | / | / |

## Working with real world data

In previous examples, only simulated data were used for the calibrations, eventually added with some noise. In this part, real measured data of the four point bending test of Steel Fiber Reinforced Concrete (SFRC) are used. Seven SFRC beams are tested in the laboratory of the University of Colombia (Escuela Colombiana de Ingenieria, ECI) at 2009 and the data registered are the deflection of the beam in the midspan ($\delta$) and the net applied force (P). The idea was to fit a mathematical function to this measurements, by finding the optimal parameters of the formula. Once a parametric equation exists, it is possible to derive characteristics as the maximum load at the moment of cracking.

Based on the characteristics of the tests results and the presence of noise on the measurements, the Nelder-Mead method was selected to calibrate an existing model. The model selected as a starting point was a model for compression strength in terms of axial stress for SFRC that resembles the shape

of the plots of the flexural tests results. Analysing the solutions led to a parametric equation as a first approach to correlate load and deflection for SFRC beams.

*Theoretical model*

The response of one of the measured SFRC beams during a bending test is shown in Figure 15. Nataraja et al [13] presents a model for the stress-strain curve of compression in SFRC with a similar behaviour as the load-deflection curves obtained in the tests. Figure 16 shows the graph with the experimental data used to fit the function that will be used to start the calibration process.
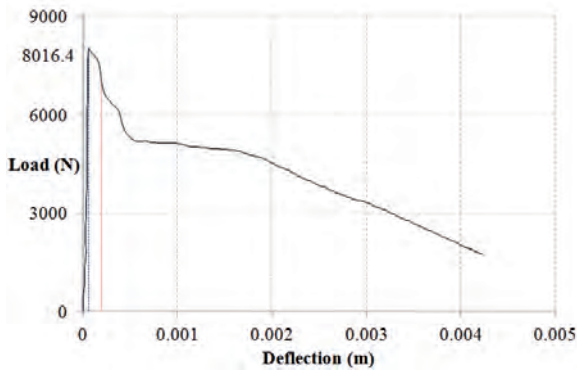


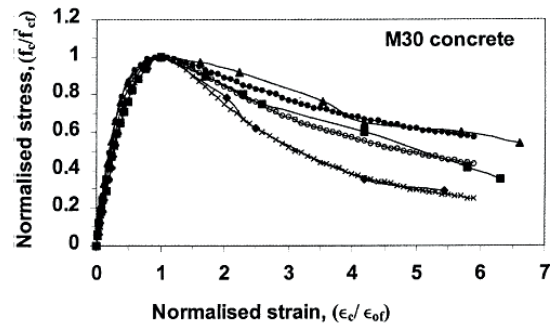**Figure 15.** Load-deflection curve for a SFRC beam.



**Figure 16.** Plot of the reference model [13].

The equation proposed by Natarja will be used as the mathematical function to calibrate the measurements and is equal to

$$\frac{f_c}{f'_{cf}} = \frac{\beta(\varepsilon_c / \varepsilon_{of})}{\beta - 1 + (\varepsilon_c / \varepsilon_{of})^\beta}$$

The variables in the equation are changed to have a function for the load P in terms of the deflection δ. The modified equation is:

$$P = \frac{\beta\delta}{\beta - 1 + \delta^\beta}$$

where

       P – is the total load applied to the beam (kN)
       δ – is the deflection in the mid span (mm)
       β – is a numeric parameters, function of the concrete matrix ultimate strength

*Calibration process*

Initially the mathematical formula was calibrated to the experimental results by implementing the Nelder-Mead method. First results showed an asymptote where $\beta - 1 + \delta^\beta = 0$. As negative loads have no physical meaning in this problem, the absolute value of the function is taken. Even though the initial guess for β was changed several times to avoid a possible local minimum, the obtained function did not resemble the beams behaviour correctly. To measure the sensibility of the model to the changes in β, two extreme values were selected and the obtained graphs were analysed. Figure 17a shows the results of calibrating the model using an initial guess $\beta_0 = 0.5$ and 17b for $\beta_0 = 7.0$.
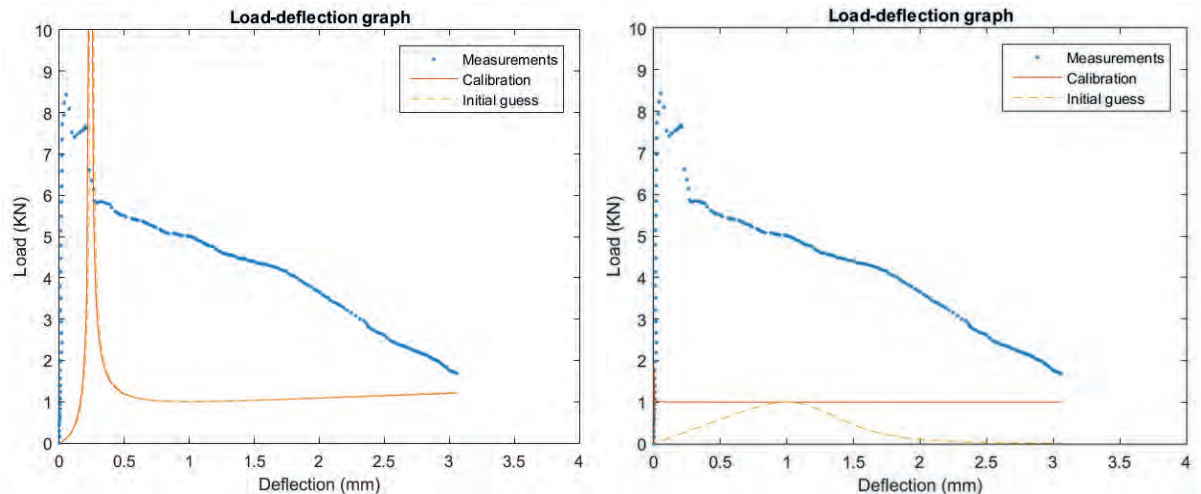
**Figure 17.** Calibration of the function with one parameter for initial guess a) 0.5 and b) 7.0.

As the result of the calibration is not satisfying, some changes has to be made. It is visible that the proposed function has not enough flexibility to fit correctly to the measurements. Therefore, flexibility is added by taking into account more parameters. Instead of only using one parameter $\beta$, the formula is extended to a three parameter equation ($\alpha$, $\beta$ and $\chi$ are numerical parameters to calibrate through the Nelder-Mead method):

$$P = \frac{\alpha\delta}{\beta - 1 + \delta^{\chi}}$$

The calibration with the new model was performed, with an initial value for all the parameters $\alpha$, $\beta$ and $\chi$ equal to 0.5. Nevertheless, the calibrated model did not accurately represent the laboratory test results. Figure 18a shows the results. Therefore, a second set of initial values was tested ($\alpha$=2.0, $\beta$=5.0 and $\chi$=7.0). This calibrated model is much better to represent the laboratory test results. Figure 18b shows the results.

It can be concluded that taking the absolute value and adding extra parameters has a beneficial effect on the results. It is not possible to make a good calibration if the model is not able to fit the measurements accurately. When working with real data, it is also more difficult to get a satisfying result.
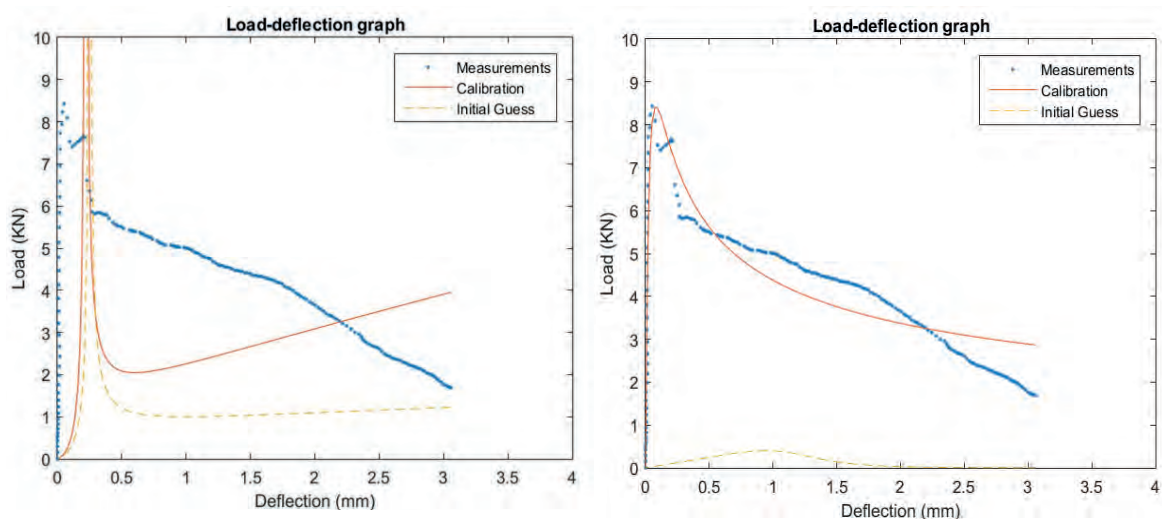


**Figure 18.** Calibration of the function with three parameters a) initial values all 0.5 b) initial values equal to $\alpha$=2.0, $\beta$=5.0 and $\chi$=7.0.

## *Results*

For a set of seven beam tests, Table 4 shows the values of the parameters α, β and χ. All the beams have the same amount of fibers (25 kg/m$^3$) and the difference between the specimens was the manageability of the concrete measured through the slump test and qualified as high, medium and low (two types of low slump mixes were tested, low 1 and low 3).

**Table 4.** Optimized parameters for a set of experimental results.

| Specimen | Manageability | Slump (mm) | α | β | χ |
|---|---|---|---|---|---|
| 1 | Medium | 75 | 4.427 | 1.012 | 1.386 |
| 2 | Medium | | 5.432 | 1.035 | 1.617 |
| 3 | High | 135 | 5.127 | 1.037 | 1.419 |
| 4 | Low1 | 3 | 1.908 | 1.042 | 2.349 |
| 5 | Low1 | | 2.244 | 1.018 | 1.901 |
| 6 | Low3 | 2.8 | 3.714 | 1.023 | 1.319 |
| 7 | Low3 | | 3.195 | 1.009 | 1.489 |
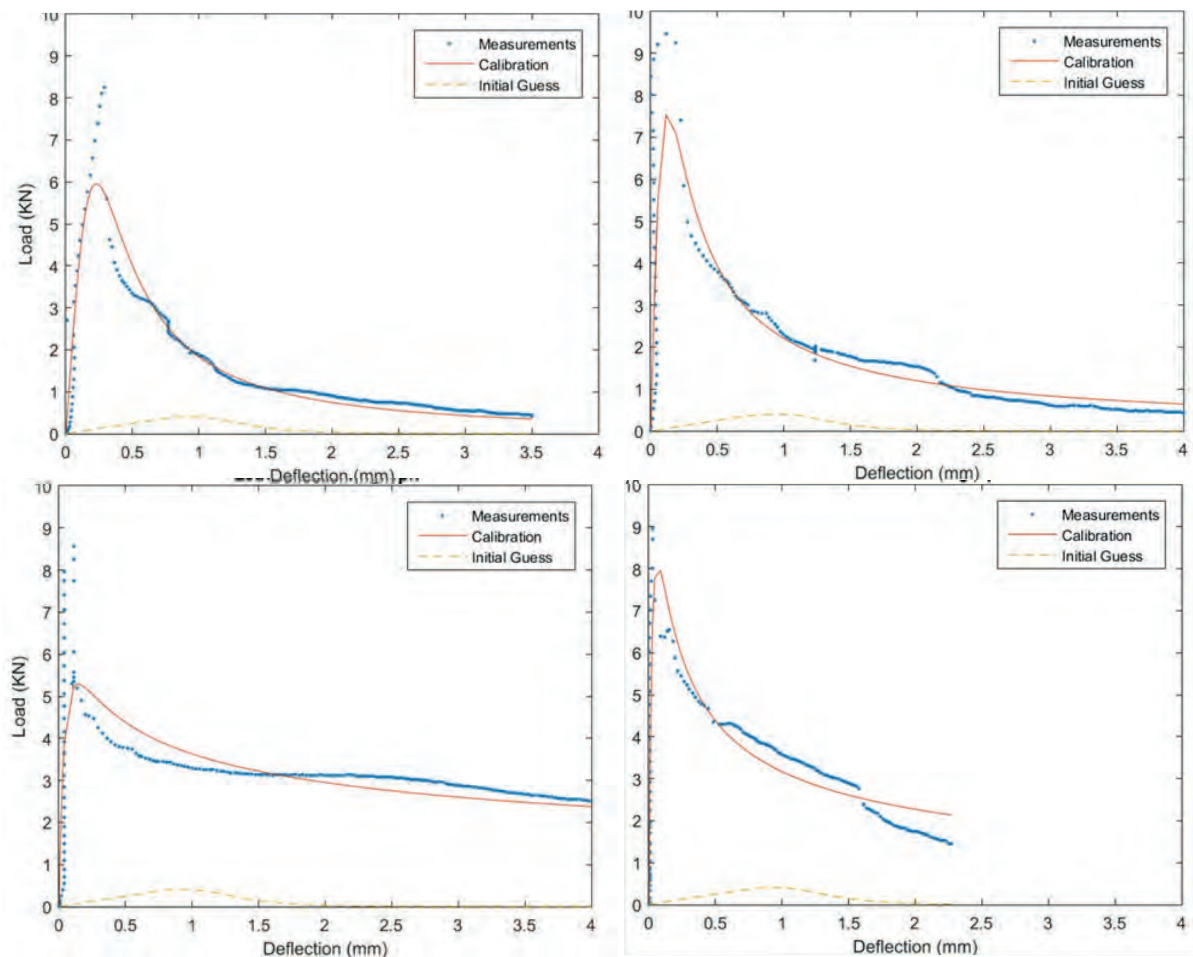


**Figure 19.** Plots of the calibrated models for specimen 4 to 7.
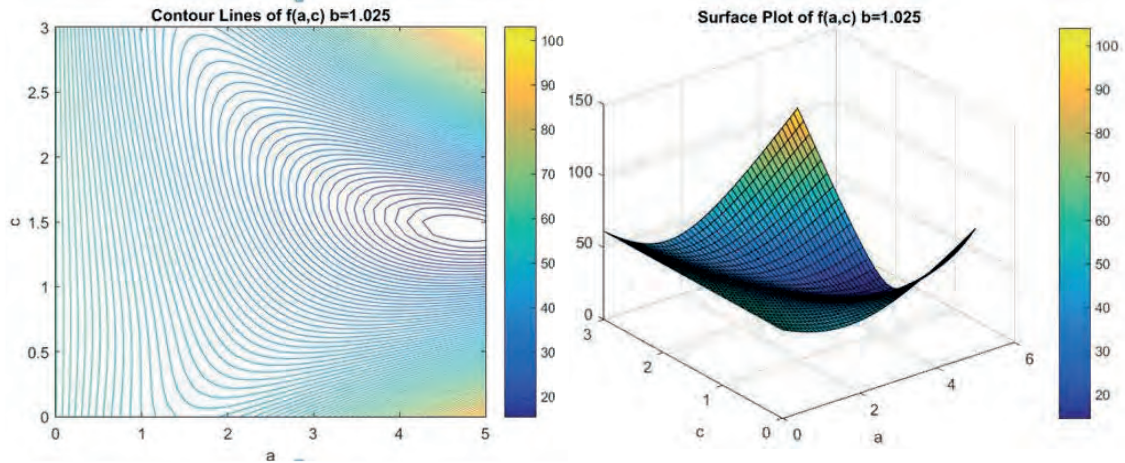
**Figure 20.** Contour lines and surface plot for specimen 1 with fixed β.

Figure 19 shows the measurements, calibration and initial guess for the specimens 4 to 7. The results of α and χ have an important variability, but β have a lower variation and it has an average value of 1.025. According to the obtained results, contour lines for α and χ were made with the average value of β as a fixed value. Figure 20 shows global minimum values in the contour lines and surface plot for specimen 1 in values of α and χ.

*Discussion*

By calibration, a mathematical formula is obtained for the load-deflection curve of the four point bending test of SFRC beams. With this formula, it is now possible to calculate the ultimate strength. Also the area below the curve can now be easily calculated by integrating the formula. These applications were much more difficult based on the measurements only.

Further research can be done by trying to find a relationship between the characteristics of the beams and the obtained optimal values of α, β and χ. As such, it can be possible to know the load-deflection curves for beams that are not measured. Of course, this will be a difficult task, since there are a lot of material properties that can have an influence.

The Nelter-Mead method can be used successfully to calibrate models based on real test results data. Nevertheless, a sensibility analysis must be done to guarantee that the selected parameters are the adequate. The initial guess and the flexibility of the model should be carefully evaluated.

**Topology Optimization**

After a lot of calibration examples, also topology optimization is considered. It is one of the structural optimization types and comparing to others, it is considered as the general one since it allows holes to be added.

*Formulation of the problem and the SIMP method*

The purpose of topology optimization is to find the optimal layout of a structure within a specified region. Many methods are used in topology optimization, like the heuristic methods (ESO/BESO),

SIMP method, simulated annealing methods and others. In this project, the SIMP method [14] is applied by using the codes top99 [15] and top3d [16].

The SIMP method is based on the power law approach, where the objective function is defined as the minimization of the compliance of the structure. The problem can be formulated as follows:

$$\min c(x) = U^T K U = \sum_{e=1}^{N} (x_e)^p U_e^T K_e U_e$$

$$Subject\ to:\ KU = F$$

$$\frac{V(x)}{V_0} = f$$

$$0 < x_{min} \le x \le 1$$

Where:

$U$ and $F$ are the global displacement and force vectors, respectively.

$K$ is the global stiffness matrix.

$U_e$ and $K_e$ are the element displacement vector and stiffness matrix, respectively.

$x_e$ is the vector of design variables.

$x_{min}$ is a vector of minimum relative densities (non-zero to avoid singularity).

$N = (n_{elx} \times n_{ely})$ is the number of elements used to discretize the design domain.

$p$ is the penalization power (typically $p = 3$).

$V(x)$ and $V_0$ are the material volume and the design domain volume, respectively.

$f$ (volfrac) is the prescribed volume fraction.

The SIMP method could be defined in the following steps:
- definition of the problem: the initial structure to be optimized, the applied loads, the boundary conditions and the design domain volume to be constructed.
- discretization of the structure using the Finite Element Method.
- calculation of the global compliance of the structure.
- sensitivity analysis of the compliance.
- application of the filters to avoid checkerboards in the optimized structure and to assure the mesh-independency.
- solving the problem by applying the Optimal Criteria method.

Two examples are implemented in this project to show the topology optimization process of homogeneous structures subjected to different loads.
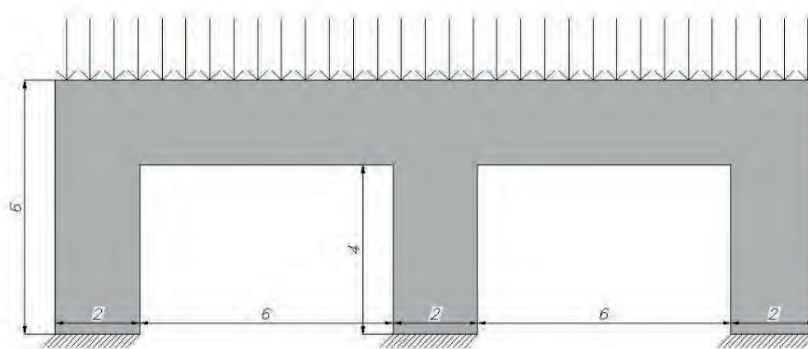


**Figure 21.** Full design domain.
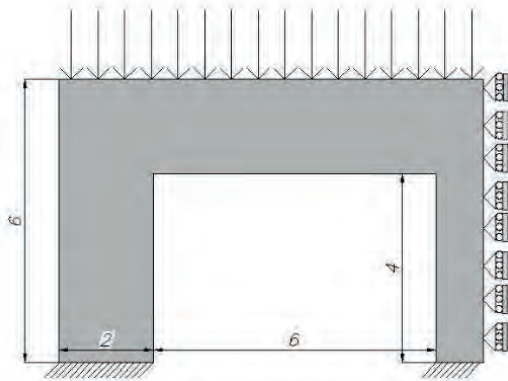
**Figure 22.** Half design domain with symmetry boundary conditions.



**Figure 23.** The optimal design.

*Example - Topology optimization of a bridge in 2D*

The first example was to find the optimal design of a symmetric bridge where the piers are fixed and only the traffic loads were considered. Due to the symmetry of the structure, the optimization process was conducted only on one half of the structure, while considering the boundary conditions, as shown in Figures 21 and 22.

The optimal design is assured after 150 iterations and reported in Figure 23. With less iterations, the results was not very accurate.

*Example - Topology optimization of a tower in 3D*

A 3D tower was optimized in this example, where the initial structure is only subjected to one eccentric load on the top (Figure 24a). The topology optimized design is shown in Figure 24b. The final design depends on the initial domain, the boundary conditions and the applied loads (magnitude and direction).
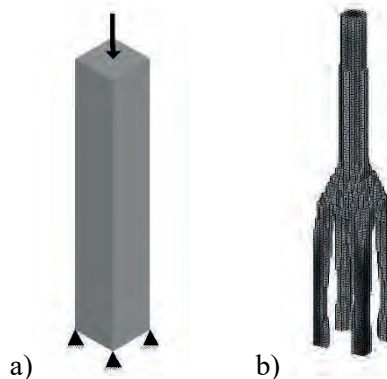


a)                              b)
**Figure 24.** a) initial design of a 3D tower; b) optimized design.

## Conclusions

It can be concluded that there exists a lot of different optimization techniques, which have all their own advantages and disadvantages. After a theoretical overview, some of the methods are implemented and used for Civil Engineering applications. Therefore, it can be shown that these techniques can be very useful in calibration and topology optimization. A bridge and a tower are optimized with this last method.

A lot of calibration examples were performed, with each their own topic. On the basic equation of motion, three methods are tested (gradient method with line-search, local Newton method and quasi-Newton method with BFGS approach). Their applicability depends on the type of the problem and the initial guess of the optimal point. Considering the FRF instead of the free vibration can give a solution for a non-unique optimal point in time domain.

Furthermore, the influence of different cost functions is investigated by a model updating of a RC plane frame. The effect of noise, on the other hand, is studied by a modal analysis optimization of a steel structure. At least, some calibration on real measured data is performed by determining the mathematical expression for a load-deflection curve of the four point bending test of steel fiber reinforced concrete beams.

# References

[1] Lahmer, T. and Jaouadi, Z. (2015). *Selected topics of Optimization in Civil Engineering, Weimar Summer Academy.* Lecture Notes.

[2] Kelley, C.T. (1999). *Iterative Methods for Optimization.* SIAM 1999.

[3] Bauhaus Summer School (2012). *Model Validation and Simulation, Project 5, Calibration of Numerical Models with Applications in Civil Engineering.*

[4] Bauhaus Summer School (2013). *Model Validation and Simulation, Project 1, System Identification. Model Updating and Simulation.*

[5] Bauhaus Summer School (2014). *Forecast Engineering, Project 5, Calibration of Engineering and Climate Models.*

[6] Ewins, D.J. (2000). *Modal testing: theory, practice and application*. Research Studies Press.

[7] Maia, N.M.M., Silva, J.M.M. (1997). *Theoretical and Experimental Modal Analysis*. Research Studies Press.

[8] MATLAB documentation, *The Language of Technical Computing*, MathWorks. http://it.mathworks.com/help/matlab/

[9] Dahlblom, O., Peterson, A. and Petersson H. (1986). *CALFEM — a program for computer-aided learning of the finite element method*, Engineering Computations, Vol. 3 Iss 2 pp. 155 – 160.

[10] Kala, Z., Melcher, J. and Puklický, L. (2009). *Material and geometrical characteristics of structural steels based on statistical analysis of metallurgical products*, Journal of Civil Engineering and Management, 15:3, 299-307.

[11] CIB Report no.115: *JSS Probabilistic model code Part 2 – Load models*. Rotterdam: CIB :2001.

[12] Hess, P.E., Bruchman, D., Assakkaf I.A. and Ayyub, B.M. (2008), *Uncertainties in Material Strength, Geometric and Load Variables*.

[13] Natarja, M.C., Dhang, N., Gupta, A.P. (1999). *Stress-strain curves for steel-fiber reinforced concrete under compression.* Cement & Concrete Composites, pp. 383-390.

[14] Bendsøe, M.P., Sigmund, O. (2003). *Topology optimization: theory, methods and applications*, Springer.

[15] Sigmund, O. (2001). *A 99 line topology optimization code written in Matlab.* Structural and Multidisciplinary Optimization, 21 (2): 120-127.

[16] Liu, K., and Andrés T. (2014). *An efficient 3D topology optimization code written in Matlab*, Structural and Multidisciplinary Optimization, 50 (6): 1175-1196.
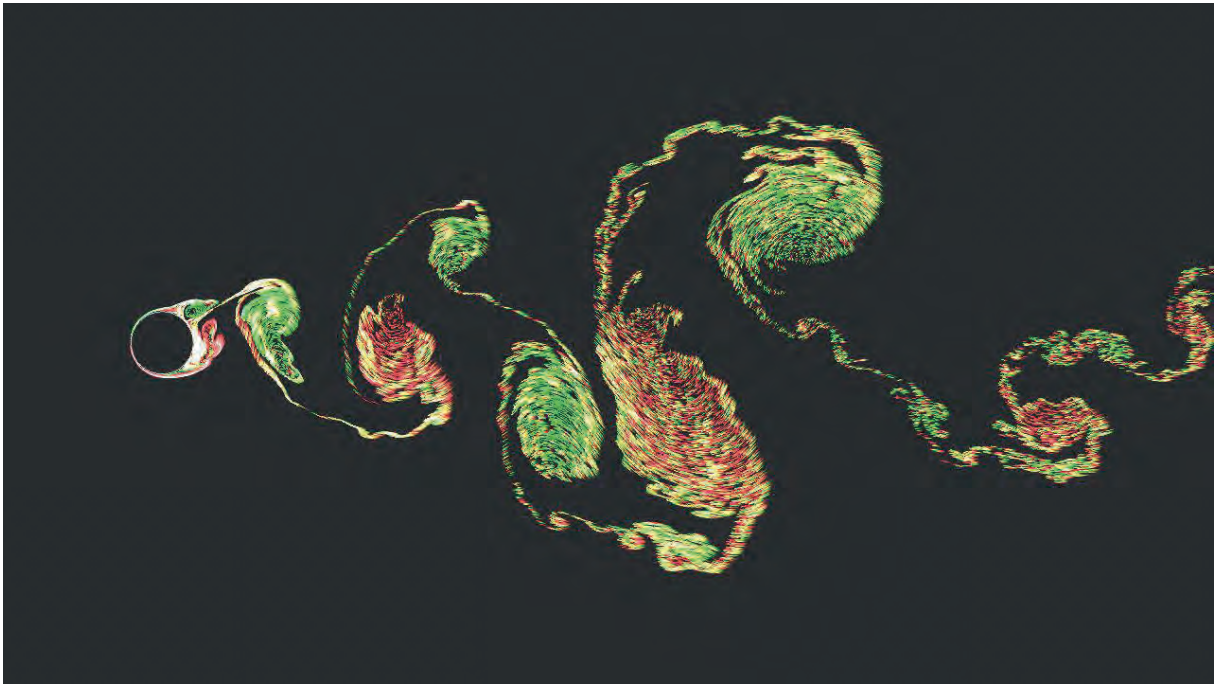
# Wind-induced vibrations of long-span bridges

*MORGENTHAL Guido*

*Chair of Modelling and Simulation of Structures, Bauhaus-Universität Weimar, Germany*

The project deals with the structural modelling and dynamic analysis of long-span cable-supported bridges under wind excitation. In 4 sub-groups the participants of the project are trained within the:

- Numerical modelling techniques for long-span cable-supported bridges;
- Simulation of dynamic structural behaviour;
- Models for Predicting Wind-induced Vibrations of Long-span Bridges;
- Numerical (CFD) analysis of bridge aerodynamics and dynamic response to wind;
- Optimising aerodynamic performance.

In the course the participants first looked at methods of modelling the structural behaviour of such bridges, specifically cable-stayed and suspension bridges, in commercial Finite Element software. The specific focus was on determining the dynamic properties, like natural frequencies and corresponding mode shapes. In the next step, various phenomena of dynamic wind excitation were introduced. These include turbulence-induced buffeting, vortex-induced vibrations and instabilities like flutter. A Computational Fluid Dynamics (CFD) software was introduced and applied to determine the aerodynamic properties of bridge decks. These results were used to assess the wind excitation phenomena using various analytical and numerical methods. Also fully coupled numerical fluid-structure interaction analyses were performed.

# Buffeting response of the Mersey Gateway Bridge Main Crossing

*LACHMANN Robert [a], KULTCHYTSKYY Artëm [b], KONARSKI Jakub [c]*

[a] *Faculty of Civil Engineering, Bauhaus-University, Weimar*

[b] *Department of building Construction, Donbas National Academy of Civil Engineering and Architecture, Kramatorsk, Ukraine*

[c] *Department of Structural Analysis and Dynamics, Faculty Architecture, Civil Engineering and Urban Planning, Brandenburg University of Technology, Cottbus-Senftenberg*

*Chair of Modelling and Simulation of Structures, Bauhaus-Universität Weimar, Germany*

## Abstract

The following paper deals with the problem of vibrations induced by turbulent flow. Therefore, the simulations were conducted using a CFD tool VXflow for stationary and modally excited deck. Results were compared in order to understand the effect of buffeting forces on the behaviour of the whole structure.

## General Description of Buffeting

Dynamic wind loads are of high importance for slender structures like towers and bridges. Vortex induced vibrations often prove to be governing loads for tall raising structures. Wind itself combined with poor design and lack of understanding of its phenomena often causes structure to behave unexpectedly, even leading in extreme cases to its collapse, e.g. Tacoma Narrows. While the self-induced response effect of vortex shedding (also known as vortex induced vibrations) and flutter are well investigated, they are just a mere approximation of reality due to neglecting approaching wind turbulence. If such turbulence is taken into account we are dealing with buffeting, a phenomenon of self-induced forces caused by turbulent wind. This problem has been wider explained in (Strømmen 2010, You-Lin 2014). The idea of that excitation is presented in "Fig. 1". Motivation of this paper is to document the effects of non-linear response of structure and fluctuating features in the approaching wind.

## Mersey Gateway Crossing

The bridge in question is Mersey Bridge Crossing located near Liverpool, England "Fig. 2". The crossing is planned to open in 2017. Total length of bridge is 2130m with main span length of 1000m. Geometric details of the bridge are depicted in "Fig. 4". Cross section will carry 3 lanes of traffic in each direction; its total width is 33m with height of 4.8m "Fig. 5".

# Finite Element Model

Due to its complicity bridge was analysed as a whole structure using commercial code SOFiSTiK "Fig. 3". In this paper only middle span at the stage of construction was considered, as wind tunnel measurements were conducted and comparison was possible to make (MGB 2014). Model was provided by supervisors and was used to conduct modal analysis and to determine frequencies associated with excitation of middle section. Results are presented in "Tab. 1".
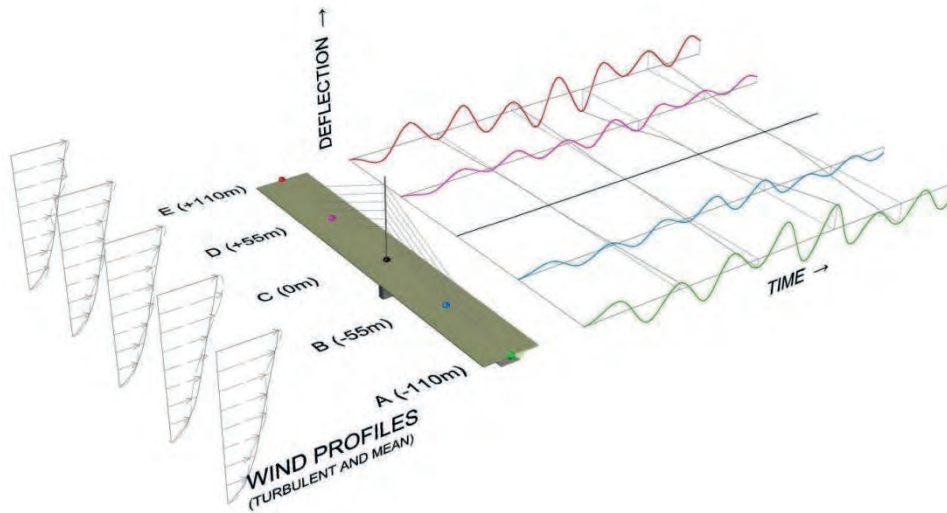


**Figure 1.** Schematic of pseudo-3D multi-slice simulation and slice locations



**Figure 2.** Bridge visualisation
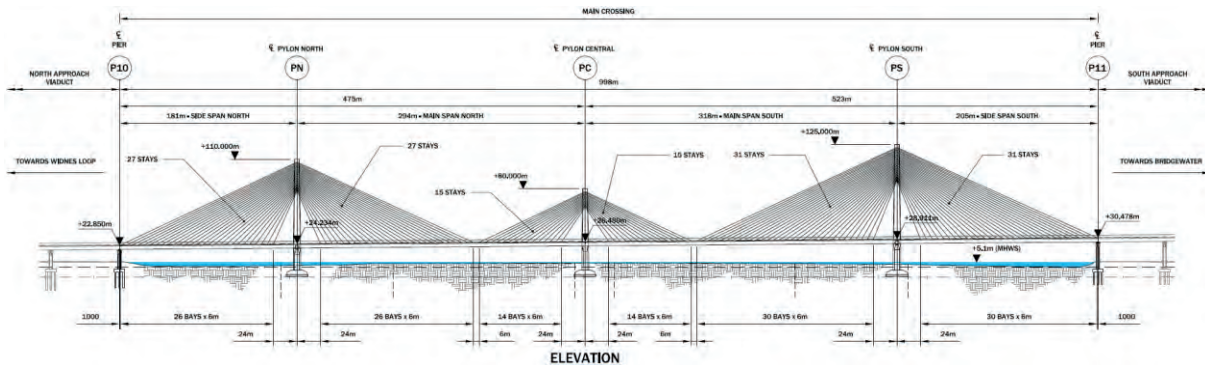(source: www.merseygateway.co.uk)



**Figure 3.** Finite element model in SOFiSTiK



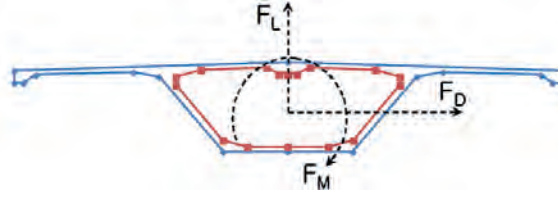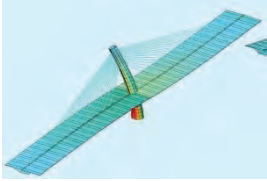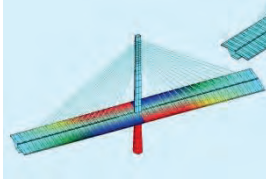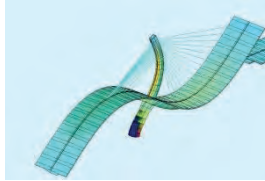**Figure 4.** Details of crossing (Morgenthal, 2015)
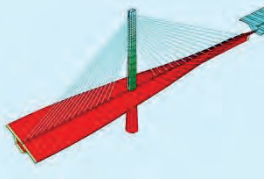
**Figure 5.** Dock cross section with acting forces

**Table 1.** Modes

| Mode 1 | Mode 2 | Mode 3 | Mode 4 |
|--------|--------|--------|--------|
|  |  |  |  |
| Vertical | Horizontal | Vertical | Rotational |
| 0.18 Hz | 0.19 Hz | 1.04 Hz | 1.67 Hz |

## Numerical Simulations

The Computational Fluid Dynamic (CFD) simulations were conducted using VXflow which is fundamentally based on Vortex Particle Method software (Morgenthal G. 2002). Due to limited time and resources only two simulations were made.

First of them will be referred to as "Static". This simulation was used to obtain time averaged values of lift, drag and moment coefficients $C_L$, $C_D$ and $C_M$, which, for different incident angle, can be used to find the buffeting forces on structure under vibration. The aerodynamic derivatives $A_i$ and $H_i$ of the bridge deck can be found by forced vibration simulations but the limitation of time schedule didn't allow doing so. These derivatives generally describe how much wind energy is transferred to structure movement. Aforementioned software is capable of directly delivering these values as well as phase shift and other aerodynamically important data.

Second simulation was conducted in "quasi-3D" using four parallel two-dimensional cases calculated simultaneously. Coupling between sections is performed using mode shape factors, damping and masses. Eigen mode shapes, which were determined using SOFiSTiK, were prescribed as normalized values in slice points locations "Fig. 1". Damping factor was calculated assuming value of 0.05 for highest and lowest frequencies and using Rayleigh equations to approximate value of damping for remaining modes.

Modal damping ratio is given by "Eq. 1":

$$\zeta_i = \frac{a_0}{2}\frac{1}{\omega_i} + \frac{a_1}{2}\omega_i \tag{1}$$

where $\zeta_i$ is the modal damping ratio for *i*-th mode, $\omega_i$ is frequency, $a_0$ and $a_1$ are coefficients, which can be determined using "Eq. 2" (assuming same damping ratio for mode *i* and *j*):

$$\begin{cases} a_0 = \zeta\, \frac{2\omega_i\omega_j}{\omega_i+\omega_j} \\ a_1 = \zeta\, \frac{2}{\omega_i+\omega_j} \end{cases} \tag{2}$$

Where *i* and *j* modes are in this example the lowest and the highest modes. Results for remaining damping factors are presented in "Fig. 6".
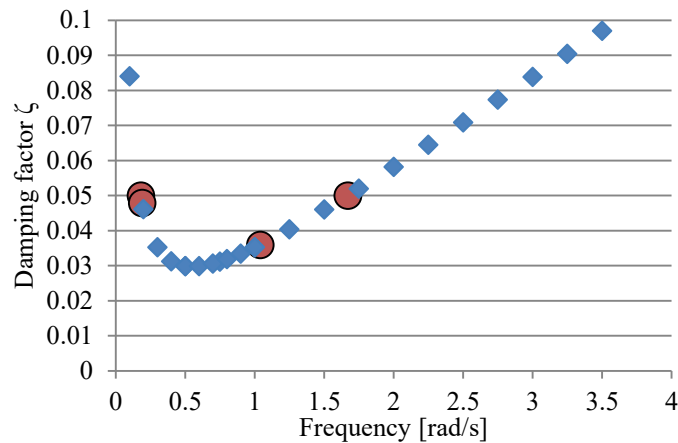
**Figure 6.** Damping factors - red dots for modes considered in this study

Modal masses were calculated using "Eq. 3" since the maximum modal displacement in SOFiSTiK is normalized by the modal mass:

$$M_{M,i} = 1/\sqrt{\delta_{max,i}} \qquad (3)$$

Where, $M_{M,i}$ is the modal mass and $\delta_{max,i}$ is the deflection for $i$-th mode. Values of deflections for every mode were obtained directly from FEM model. Additionally, the modal masses are calculated from the each modal shape to verify the results using "Eq. 3".

## Results

### Static simulation

Static calculation results were used to obtain drag, lift and moment coefficients $C_L$, $C_D$ and $C_M$ of deck that was not allowed to move. These values were used to validate the model and for further comparison. Coefficients were calculated using "Eq. 4" comparing all data to deck width. In "Tab. 2" results from CFD calculations are compared with results from wind tunnel test (MGB 2014). However, due to limited calculation time, which was little over 100s, obtained results are burdened with error, which was caused by too short averaging time.

$$\begin{cases} C_D = F_D/0,5 \cdot \rho \cdot U^2 \cdot B \\ C_L = F_L/0,5 \cdot \rho \cdot U^2 \cdot B \\ C_M = F_M/0,5 \cdot \rho \cdot U^2 \cdot B^2 \end{cases} \qquad (4)$$

Where $F_D$, $F_L$ and $F_M$ are total forces acting on section, U is approaching wind speed.

Differences between drag and lift coefficients are quite large, however wind tunnel tests were made with safety barrier made out of porous mesh and elastic model, while static CFD calculations forbid any section movement and safety barriers were not modelled at all. There is good comparison between values of moment coefficients. Also worth noting is fact, that lift coefficient is negative and quite substantial.

**Table 2.** Comparison between CFD and wind tunnel test (MGB 2014) for width B=33m

| Source | $C_D$ | $C_L$ | $C_M$ |
|--------|-------|-------|-------|
| CFD | 0.101 | -0.270 | 0.131 |
| Wind tunnel | 0.170 | -0.193 | 0.128 |

In "Fig. 7" results for $C_L$, $C_D$ and $C_M$ are presented with their averaged values. One can see that these results vary considerably with time, even with stationary deck. Instantaneous flow field is presented in "Fig. 8".
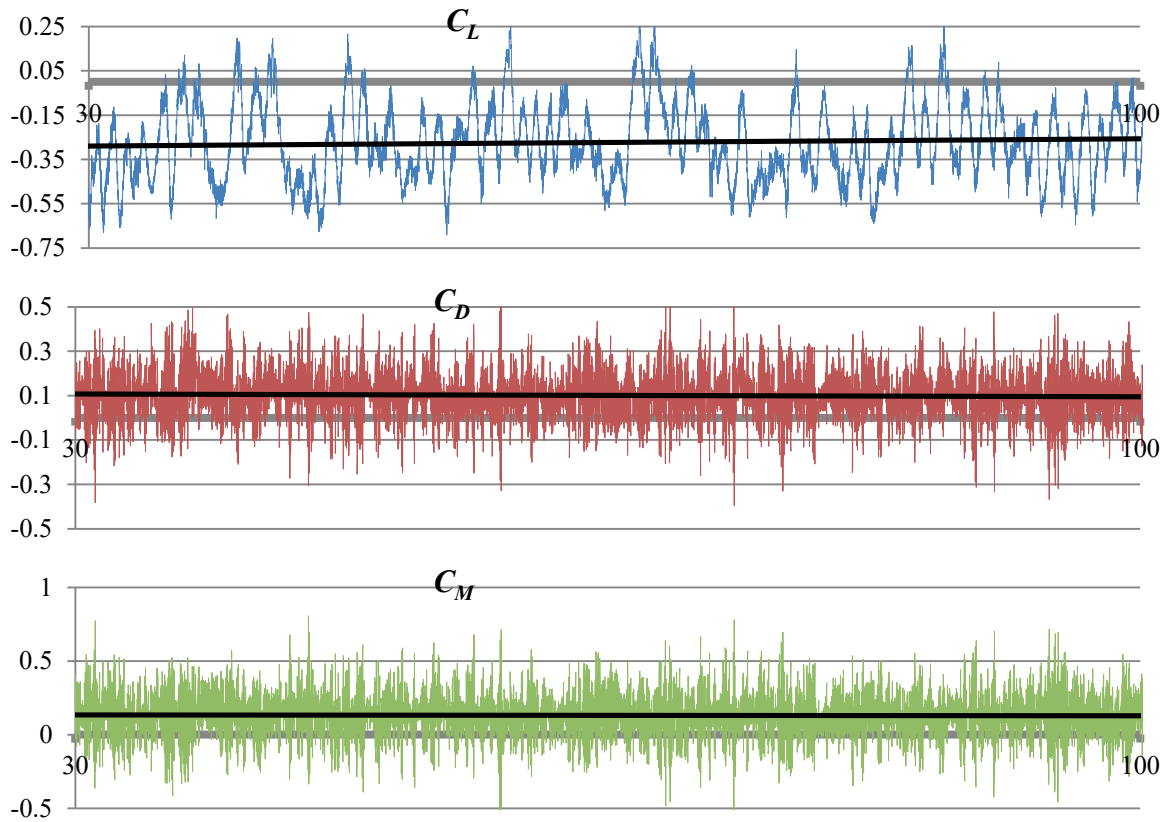


**Figure 7.** Results for static CFD simulation
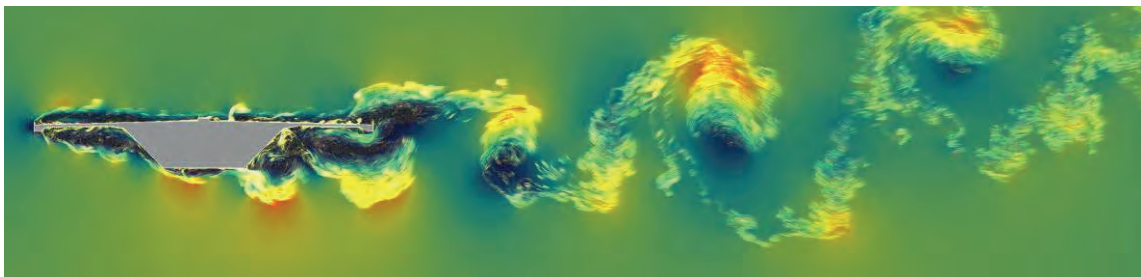


**Figure 8.** Instantaneous flow field

## Dynamic simulation

Dynamic simulations were carried out to find maximum displacements associated with modal excitations in quasi-3D using coupled slices. Due to limited time only 66 seconds of flow were modelled, which is only one tenth of what was necessary. Calculation planes were located at the ends of researched section and at halfway distance to pillar ("Fig. 1" points A, B, D and E).

In order to provide turbulent approaching wind a special generator was used, which provided same level of turbulence for each of the slices. Main idea behind generator is explained in "Fig. 9". In front of measured section on line *r-r'* entities are located. Their duty is to release particles with certain velocities $u_i$ and $v_i$, so that total vorticity of particle $\Gamma$ "Eq. 5" resembles that of a turbulent flow

($\sigma_u$=15%; $\sigma_w$=10%; $\sigma_v$=5%). Effect of this generator can be seen on the left in "Fig. 10", as it is disturbing flow in front of the section.
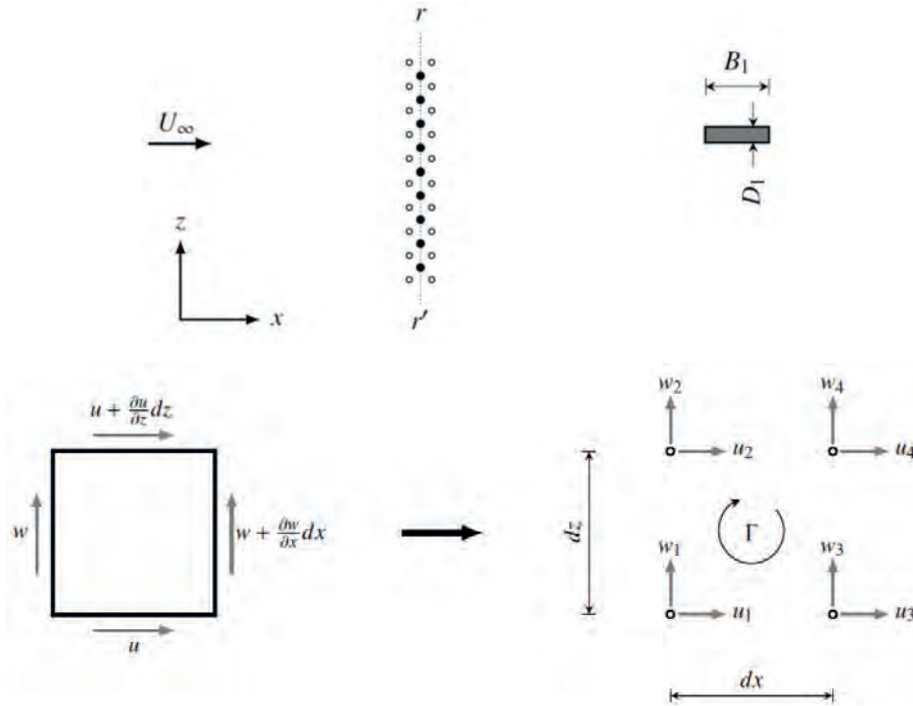


**Figure 9.** Modelling of statistically defined turbulence wind and transformation into vortex particles for turbulence modelling in VXflow simulation
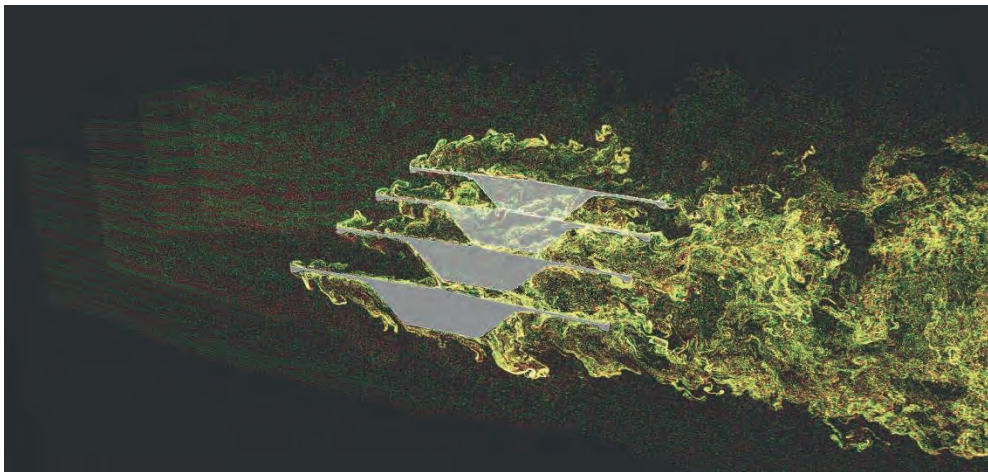


**Figure 10.** Turbulence generator and instantaneous flow patterns for all slices

$$\Gamma = \left( \left[ \frac{\left(\frac{u_2+u_4}{2}\right)-\left(\frac{u_1+u_3}{2}\right)}{\partial z} \right] - \left[ \frac{\left(\frac{w_2+w_4}{2}\right)-\left(\frac{w_1+w_3}{2}\right)}{\partial x} \right] \right) dzdx \qquad (5)$$

In "Fig. 11" displacements for all slices against time are presented. It can be seen that no constant pattern is present and sections move symmetrically with respect to pillar, which indicates movement according to first mode.
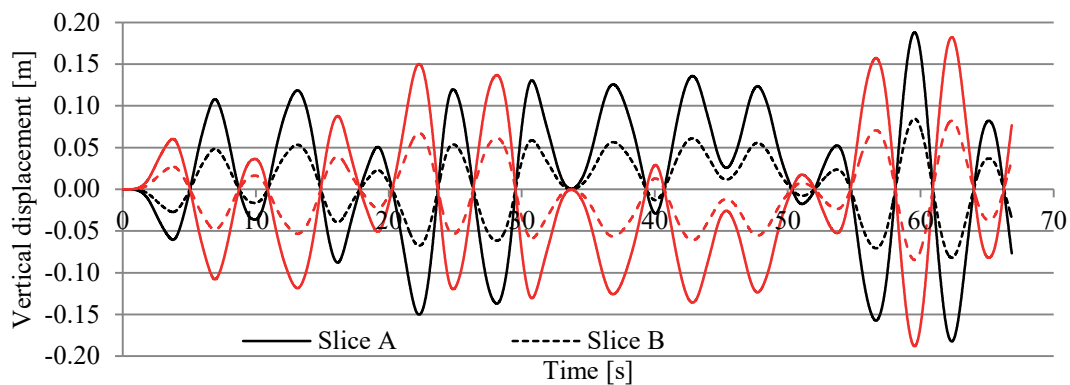
**Figure 11.** Vertical displacements in 4 slices for bridge axis

In "Fig. 12" vertical and torsional displacements for slice located at the end ("Fig. 1" point A) are presented as vertical movement of bridge deck corners. Edges are distinguished as left-windward and right-leeward. Results show that rotation according to mode four has big effect on total section movement. Horizontal displacements are on the verge of measurement error.
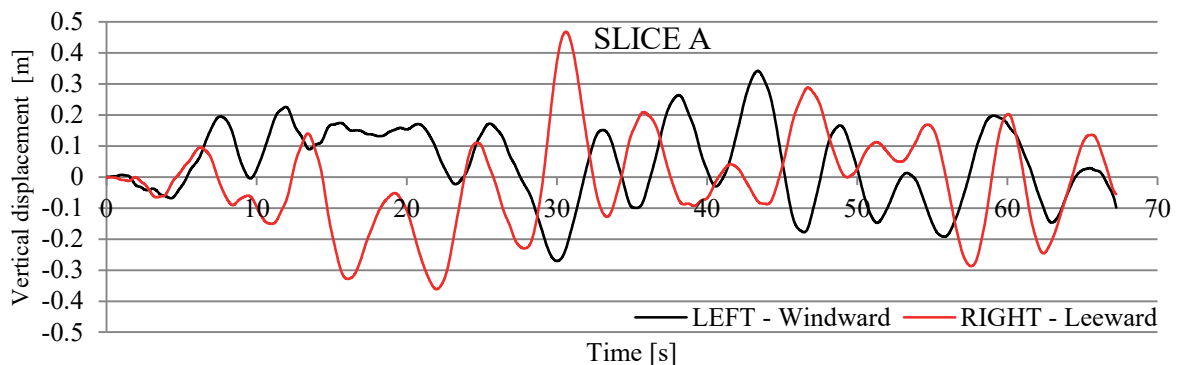


**Figure 12.** Displacements for slice A

## Conclusions

Calculations with static deck proved that an unsteady pressure field develops over deck causing lift coefficient to vary with time. Quasi-3D calculations showed that buffeting response of deck in turbulent wind has movement frequency of first mode with values of displacement varying for each subsequent shift. Calculations managed to capture the effects of non-linear response of structure and features in the approaching wind. This proves that buffeting excitation is not easy to describe and can cause forces and movements that are hard to predict.

## References

MGB (2014): *Mersey Gateway Bridge – Wind Tunnel Testing Interpretive Report.* Flint & Neill Ltd.

Strømmen E.N (2010): *Theory of Bridge Aerodynamics,* Springer.

Morgenthal G. (2002)*: Aerodynamic Analysis of Structures Using High-resolution Vortex Particle Methods, PhD thesis, University of Cambridge.*

You-Lin X. (2014). *Wind Effects on Cable-Supported Bridges, Wiley.*

Morgenthal G. (2015), *PROJECT 6: WIND-INDUCED VIBRATIONS OF LONG-SPAN BRIDGES,* Bauhaus Summer School 2015, course material.

# Flutter instability analysis of Lillebaelt suspension bridge in Denmark

*HOSOYA Akihiro [a], JINLIN Xia [b], PARODI Luca [c]*

*[a] Nagoya Institute of Technology*

*[b] Tongji University*

*[c] University of Genoa*

*Chair of Modelling and Simulation of Structures, Bauhaus-Universität Weimar, Germany*

## Abstract

Flutter is a phenomenon which is related to the self-excited oscillatory instability. Flutter mainly happens when the aerodynamic forces supply energy to the oscillating structure and the amplitude of the motion progressively increases. During the design stage of a bridge, it is important to verify at which critical wind speed the flutter would occur and to compare with Codes and Standards. In this study we analysed flutter performances of the Lillebaelt Bridge.

We computed the aerodynamic force coefficients and the aerodynamic derivatives using the CFD software VXflow. Afterwards Scanlan's aerodynamic derivatives have been used in the Flutter analysis in order to compute analytically the critical wind speed which causes flutter. On the other hand, we also have numerically simulated the fluid-structure interaction between the bridge and the wind flow. With this method we could also get the critical wind speed by simulating the. The results obtained in with the two methods match well in some aspects, but more simulation time is required to achieve a higher accuracy. The critical wind speed for flutter is higher than 90 m/s for the three different methods used.

## General insight

Flutter (see Figure 1) acts as a negative damping and it is developed for any wind speed above one threshold values, which is defined as the critical wind speed ($V_{cr}$).
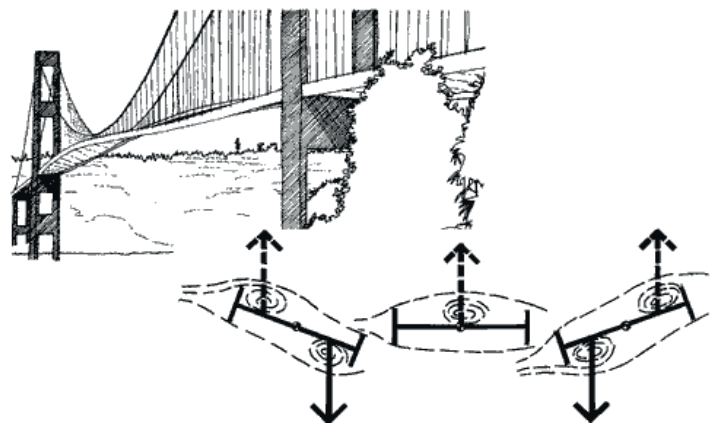


**Figure 1.** The flutter of Tacoma Bridge (source: www.wsdot.wa.gov)

The flutter phenomenon is an aeroelastic instability which involves the coupling of vibration modes, generally two (vertical motion and torsion). This is not a resonance problem, but a self-exited phenomenon initiated by dynamic wind actions over a structure. Flutter does not occur for the 1-DOF in translation but it may occur in case of torsion at certain angle of attack. This last case is named torsional flutter.

There are different flutter instability types depending on structural geometry and airflow characteristics. The oncoming different wind speeds have aeroelastic effects on the structure dynamic properties, i.e. damping and stiffness, and the structure might ultimately collapse its vibration amplitudes are too high. For bridge design, the identification of flutter mechanism is one of the main and important tasks. In case of wind sensitive bridges, normally flexible long-span ones, the critical wind speed must be provided. The flutter phenomenon can happen at any wind speed higher than the critical wind speed.

## Study cases

The Lillebaelt Bridge, showed in the Figure 2, has a total length of 1,700 m, with a central span of 600 m and two lateral spans of 240 m each. The total width of the bridge deck is 33 m.The bridge was constructed between 1965 and 1970 to connect the cities of Jylland and Fynn, in Denmark. It is one of the main traffic routes between Germany and Copenhagen and is, consequently, one of the most heavily trafficked bridges in Europe.

As a suspension bridge, its stiffness is not as strong as a cable-stayed or an arch bridge type. This bridge is also crossing the sea, which makes it vulnerable to wind actions hence we need to study the flutter performance in order to guarantee safety conditions.

## Dynamic characteristics

To calculate the dynamic characteristics of a bridge, we first need to model it through Finite Element software. In this research, we used SOFiSTiK, which is of common use in Germany.

Figures 3 and 4 show the model performed with the software and the fundamental mode shapes, 1st vertical and the 1st torsional. Table 1 present results of the dynamic analysis.



**Figure 2.** The layout of Lillebaelt Bridge (source: http://static.panoramio.com/)

**Table 1.** Dynamic characteristic of Lillebaelt Bridge

|  | Frequency(Hz) | Equivalent mass |
|---|---|---|
| 1st vertical mode | 0.156 | 11667[kg/m] |
| 1st torsional mode | 0.500 | 1017778[kgm$^2$/m] |



**Figure 3.** The Finite Element model of Lillebaelt Bridge
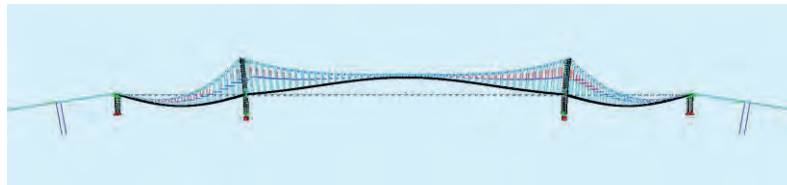


(a)  1$^{st}$ vertical mode shape
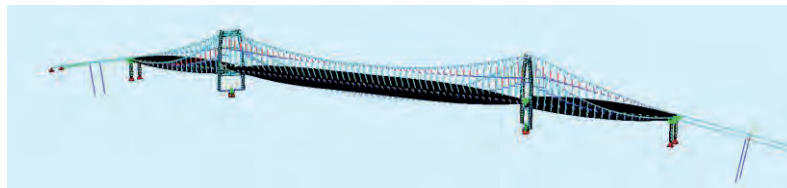


(b)  1$^{st}$ torsional mode shape

**Figure 4.** The shapes of fundamental modes

Usually, the frequency ratio of fundamental vertical and torsional mode is an important index for flutter prediction. We can see that the ratio of this bridge is f$_v$/f$_T$ =0.500/0.156= 3.205. This value is larger than 3, which indicates that the critical wind speed for flutter onset will not be very low.

## Static CFD-VXflow simulation

The computation of static wind force coefficients is important for analysing the static stability of the bridge in the wind flow. As basic parameters of a bridge deck cross-section, the definition of force coefficients follows:

$$C_L = \frac{F_L}{\frac{1}{2}\rho U^2 b} \quad (1) \qquad C_D = \frac{F_D}{\frac{1}{2}\rho U^2 b} \quad (2) \qquad C_M = \frac{FM}{\frac{1}{2}\rho U^2 b^2} \quad (3)$$

Where:

F$_L$ is the lift force (as shown in figure 5)     ρ is the air density
F$_D$ is the drag force     b is a section width
F$_M$ is the torsional moment     U is the free stream wind speed
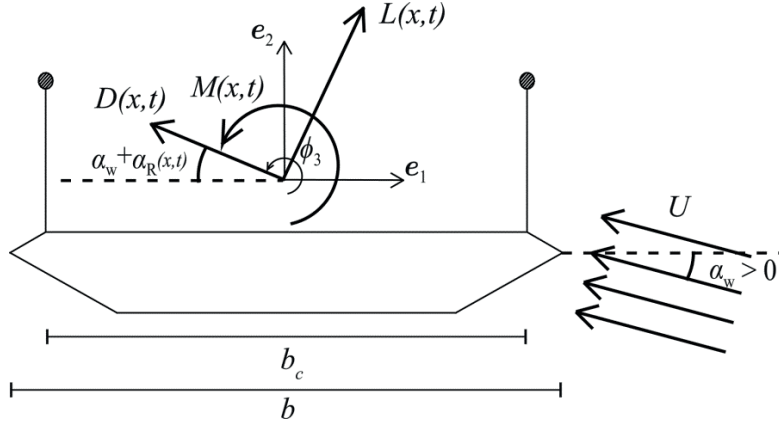
**Figure 5.** Static wind Force of bridge deck section

Force coefficients can be calculated through a static simulation with a CFD (Computational Fluid Dynamics) software.

**Table 2.** Force coefficients of the bridge deck

| Force coefficient | $C_D$ | $C_L$ | $C_M$ |
|---|---|---|---|
| Value | 0.016 | 0.416 | 0.000 |

We have just analysed the case of angle of attack equal to zero: α=0

## Flutter analytical analysis

### Theodorsen's Theory

From the basic principle of Potential Flow theory, Theodorsen (1931) showed that for thin airfoils and flat-plates in incompressible flow, the expressions for lift forces, $F_L$, and moments, $F_M$, are linear in displacement **h** and rotation, **α,** and their first- and second-order derivatives.

Theodorsen investigated the flutter phenomenon for aircraft wings and gave a very well known approach for flutter analysis. This approach is independent of the shape of the body, but on the other hand, it neglects the effects due to the simplification of the cross-section, as this theory is based on flat plate geometry.

According to Theodorsen, the theoretical expressions on a flat plate airfoil for sinusoidal oscillating lift $F_L$ (heave) and moment $F_M$ (pitch) are,

$$F_L = -\rho b^2 \left[ U_\infty \pi \dot{\alpha} + \pi \ddot{h} - \pi b a \ddot{\alpha} \right] - 2\pi \rho U_\infty b C \left[ U_\infty \alpha + \dot{h} + b(\tfrac{1}{2} - a)\dot{\alpha} \right] \qquad (4)$$

$$F_M = -\rho b^2 \left[ \pi \left( \frac{1}{2} - a \right) U_\infty b \dot{\alpha} + \pi b^2 \left( \frac{1}{8} + a^2 \right) \ddot{\alpha} - a\pi b \ddot{h} \right]$$

$$+ 2\rho U_\infty b^2 \pi (a + \tfrac{1}{2}) C \left[ U_\infty \alpha + \dot{h} + b\,(\tfrac{1}{2} - a)\dot{\alpha} \right] \qquad (5)$$

Where *C* is the Theodorsen's circulation function.
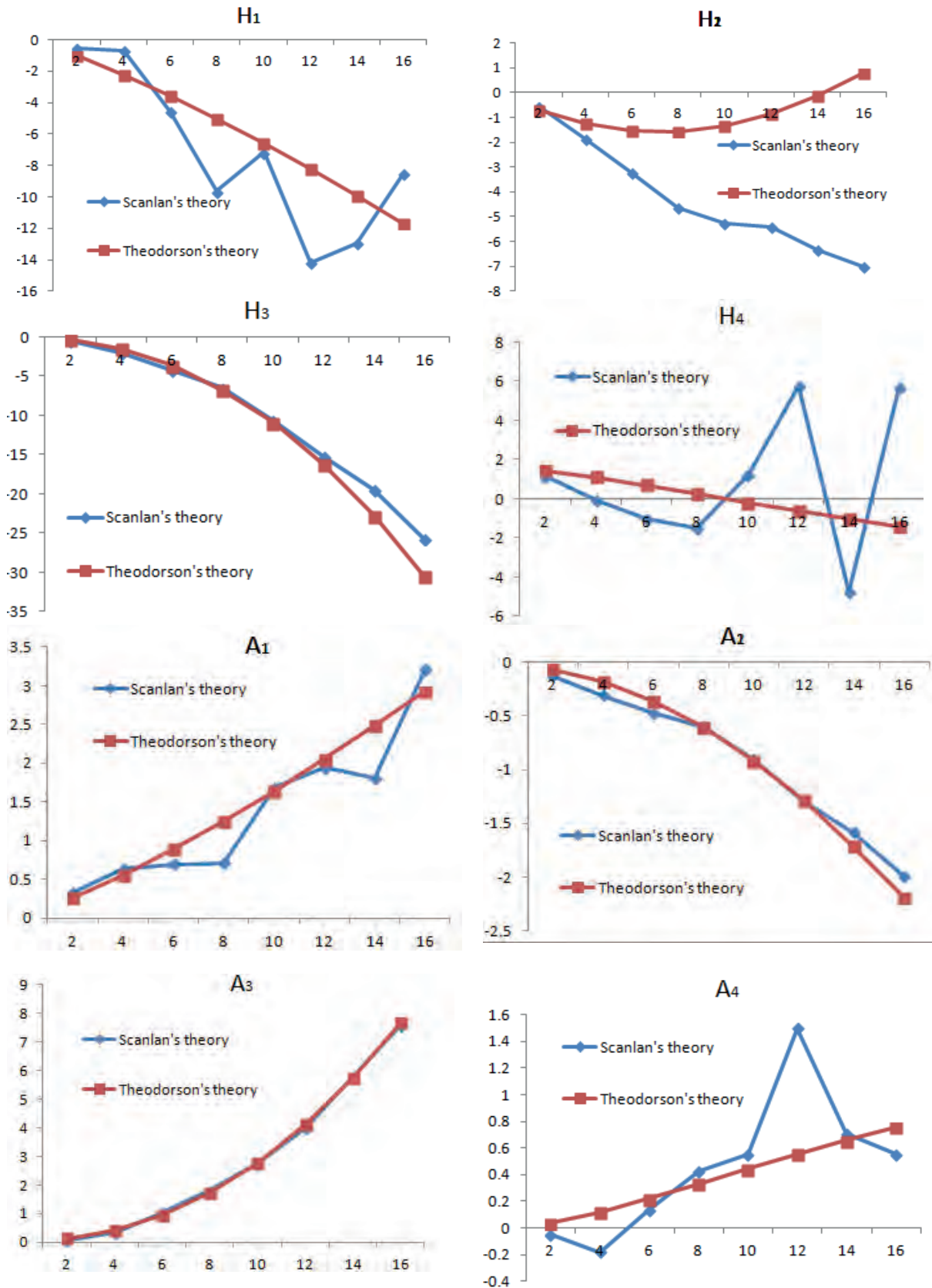
**Figure 6.** Flutter derivatives of bridge deck section. Comparison between Theodorsen's theory and Scanlan flutter derivatives obtained by numerical simulations (VXflow).

The system of differential equations can be written as follows,

$$
\begin{bmatrix} \dot{h} \\ \ddot{h} \\ \dot{\alpha} \\ \ddot{\alpha} \end{bmatrix} = \begin{bmatrix} 0 & 1 & 0 & 0 \\ a_{21} & a_{22} & a_{23} & a_{24} \\ 0 & 0 & 0 & 1 \\ a_{41} & a_{42} & a_{43} & a_{44} \end{bmatrix} \begin{bmatrix} h \\ \dot{h} \\ \alpha \\ \dot{\alpha} \end{bmatrix} \qquad (6)
$$

Simplifying to Eigenvalue Problem, it gives:     $[A - \lambda I] R e^{\lambda t} = 0$      (7)

By solving this Eigenvalue Problem, we can get the critical wind velocity and vibration frequency. Thus, the critical wind velocity is

$$U_{cr1} = 93 m/s \text{ (8)}$$

## Scanlan's Theory

For the aerodynamic forces on a bridge cross-section, Scanlan (1971) proposed a set of expressions. It assumes that the self-excited lift ($F_L$) and moment ($F_M$) for a bluff body may be treated as linear in displacement $h$ and rotation $\alpha$ and their first- and second-order derivatives.

The equations of motion are given as,

$$F_L = m\ddot{h} + 2m\xi_h\omega_h\dot{h} + m\omega_h^2 h \quad (9)$$

$$F_M = I\ddot{\alpha} + 2I\xi_\alpha\omega_\alpha\dot{\alpha} + I\omega_\alpha^2\alpha \quad (10)$$

The classical theoretical work has used complex number forms based on the representation of flutter oscillation. However, in wind engineering practice, real forms have been employed. Below, this a commonly used linearized form.

$$F_L = \frac{1}{2}\rho U_\infty^2 B \left[ KH_1 \frac{\dot{h}}{U_\infty} + KH_2 \frac{B\dot{\alpha}}{U_\infty} + K^2 H_3 \alpha + K^2 H_4 \frac{h}{B} \right] \quad (11)$$

$$F_M = \frac{1}{2}\rho U_\infty^2 B^2 \left[ KA_1 \frac{\dot{h}}{U_\infty} + KA_2 \frac{B\dot{\alpha}}{U_\infty} + K^2 A_3 \alpha + K^2 A_4 \frac{h}{B} \right] \quad (12)$$

Where $A_i$ and $H_i$ are the flutter derivatives, which are the functions of the reduced frequency, K. Figure 6 shows the flutter derivatives obtained from VXflow by forced vibration performance.

Using these flutter derivatives and combining Eqs. (9), (10), (11) and (12), we can also obtain a system of differential equation equivalent to Eq.(6). After computing the Scanlan's derivatives and solving the Eigenvalue problem, we obtained the followind critical wind velocity.

$$U_{cr2} = 103 \, m/s \qquad (13)$$

## Dynamic numerical simulation

We can also analyse the flutter phenomenon by simulating the fluid-structure interaction problem. We achieved this goal by performing 2D-simulations the VXflow software. The input is the cross-section geometry of the Lillabælt Bridge and its dynamic properties of frequency, stiffness, damping ratio and mode shapes.

In our research, we have simulated four cases with different wind speed, $U_\infty$= 85, 90, 95 and 100 m/s. According to the results, we can find that flutter will not happen for wind velocities under 90 m/s. In the case of 95 m/s, the cross-section starts experimenting flutter, as shown in Figure 7. This means that the critical wind speed is between 90 m/s and 95 m/s.
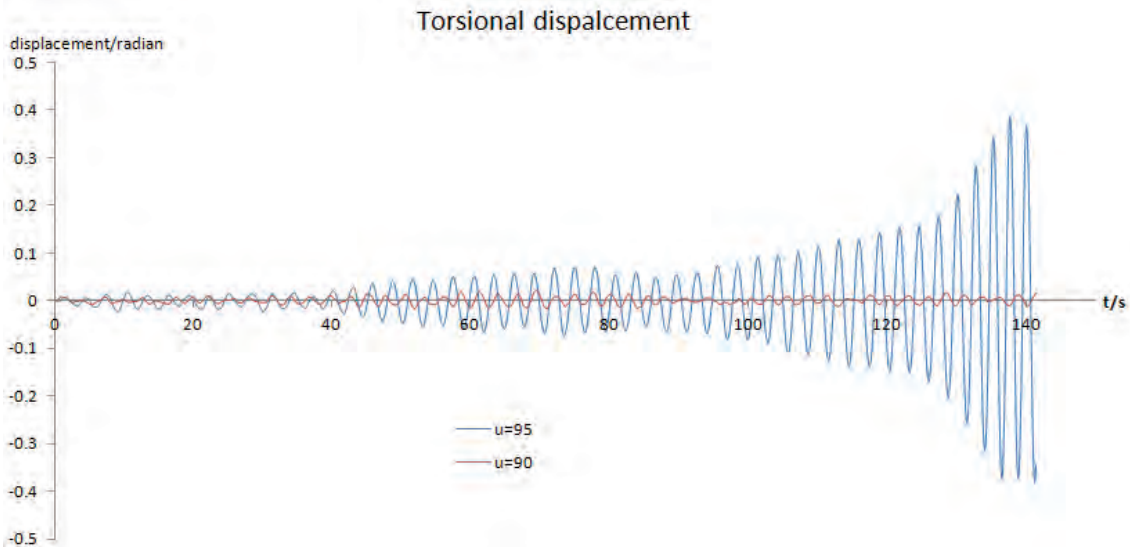
**Figure 7.** Torsional displacement from dynamic simulations of $U_\infty$= 90 m/s and 95 m/s

## Comparison and conclusion

In this paper, we analysed the Flutter phenomenon on Lillebælt Bridge. First, we computed the modes using a structural model created with SOFiSTIK. Afterwards, a static simulation has been carried out in order to identify the force coefficients. The critical wind speed for flutter has been estimated by using the Theodorsen's theory, Scanlan flutter derivatives. The velocity was finally compared with the one obtained by dynamic numerical simulations. Conclusions are summarized as follows:

(1) The frequency of the 1st vertical mode is 0.156 Hz, while the frequency of 1st torsional mode is 0.500 Hz.

(2) Using Theodorsen's theory, the critical wind speed is estimated around $U_\infty$ = 93 m/s.

(3) Using Scanlan flutter derivatives, the critical wind speed is set to 103 m/s. The obtained values were not smooth enough, so simulations should have been run longer to get more accuracy in prediction.

(4) According to the numerical method, the critical wind speed is between 90 and 95m/s, which match well with Theodorsen's theory.

**Table 3.** Comparison of critical wind speed

| Method | $U_{cr}$ (m/s) |
|---|---|
| Theodorsen's theory (analytical) | 93 |
| Scanlan's theory (analytical + numerical) | 103 |
| Numerical method (CFD software: VXflow) | 90-95 |

## References

Scanlan, R.H., Tomko, J.J. (1971). Airfoil and bridge deck flutter derivatives. Journal of Engineering Mechanics, ASCE 97(6):1171– 1737.

Theodorsen T. (1935). General theory of aerodynamic instability and the mechanism of flutter. NACA Report No. 496, US National Advisory Committee for Aeronautics, Langley, VA:1-23.

# Vortex Induced Vibrations on Long-Span Bridges: Case Study – Rio – Niterói Bridge

*CHANG Ying [a], VĂTĂMAN Adina [b]*

*[a] Tongji University, Shanghai*

*[b] Politechnics University of Timişoara, Romania*


*Chair of Modelling and Simulation of Structures, Bauhaus-Universität Weimar, Germany*

## Abstract

With the increase of bridge spans, study on wind-induced vibrations of these bridges has been a problem of great concern. When going around a bridge structure, wind will generate vortex shedding and flow separation, which give place to dynamic loads over the structure. Because of the slenderness applicability and low damping, long-span bridges become more sensitive to the action of wind, especially cable-stayed and suspension bridges. Aeroelastic problems often restrict the design of structure strength, rigidity and stability. Vortex-induced vibrations (VIV) occur with large amplitude on some important long-span bridges, such as Chinese Xihoumen Bridge, Danish Great Belt East Bridge approach spans, British Second Severn Bridge and Japanese Tokyo Bay Crossing Bridge. Therefore, it is significant to study the vortex-induced vibrations of long span bridges.

The present paper focuses on the study of the VIV on the Rio Niterói Bridge in Brazil, in order to establish the critical wind speed range at which this phenomenon occurs, the displacements produced and also to represent the behaviour of the bridge cross-section at VIV with regard to structural mass values.

## Introduction

The effects of wind interactions with civil structures are a very important criterion to be taken into consideration during design. If the structures are flexible and light, a significant dynamic response may result. Several dynamic interaction phenomena exist, for serviceability limit state (vortex induced vibrations), as well as for ultimate limit states (flutter, buffeting), requiring the modelling of fluid-structure interaction effects. Vortex-induced vibrations (VIV) represent an interaction between airflow and structure that is favoured by a uniform air stream with low turbulence and a regular wind speed.

The current report will be focused on the VIV on bridge sections, because they are a common aerodynamic problem on decks of line-like structures, resulting from the interaction of airflow with the cross section and the creation of two shear layers at the top and at the bottom of the cross section. The instability of the separating shear layers leads to vortex shedding, which is a periodic process because of the time varying pressure differences that create aerodynamic forces that excite the structure dynamically.

If the vortex shedding frequency ($f_v$) is close to the natural vibration frequency of the structure ($f_n$), there is a resonance phenomenon that occurs, i.e. synchronization between the two, also known as

lock-in. Since the vortex shedding frequency is linear with the wind speed, there is a critical resonant wind speed at which this can occur (Morgenthal et al, 2014).

For modelling and predicting the aerodynamic response of such structures, classic approaches include wind tunnel tests performed on small-scale section geometries and computational simulations with numerical algorithms. Full-scale analysis is hard to achieve because of the size, geometry, boundary conditions and high Reynolds numbers of such models. In this case, 2D models can be used, similar to wind tunnel tests, when the geometry is favourable, specifically in the aerodynamic assessment of line-like structures (towers, masts, bridges, etc.). A two dimensional Vortex Particle Method (VPM) is used, that takes into consideration only one vertical mode of vibration of the structure.

## Niterói Bridge Case Study

### General Description of the Bridge

The President Costa e Silva Bridge, also known as the Rio Niterói Bridge, is a box girder bridge crossing Guanabara Bay, connecting the two cities of Rio de Janeiro and Niterói. It is currently the longest prestressed concrete bridge in the southern hemisphere, and the sixth longest in the world. Construction began symbolically on 23 August 1968 in the presence of Queen Elizabeth II of the United Kingdom and Prince Philip, Duke of Edinburgh, alongside Mario Andreazza (Brazilian Minister of Transport) on their first, and thus far only, visit to Brazil. Actual works began on January 1969 and it was opened the 4th of March, 1974.
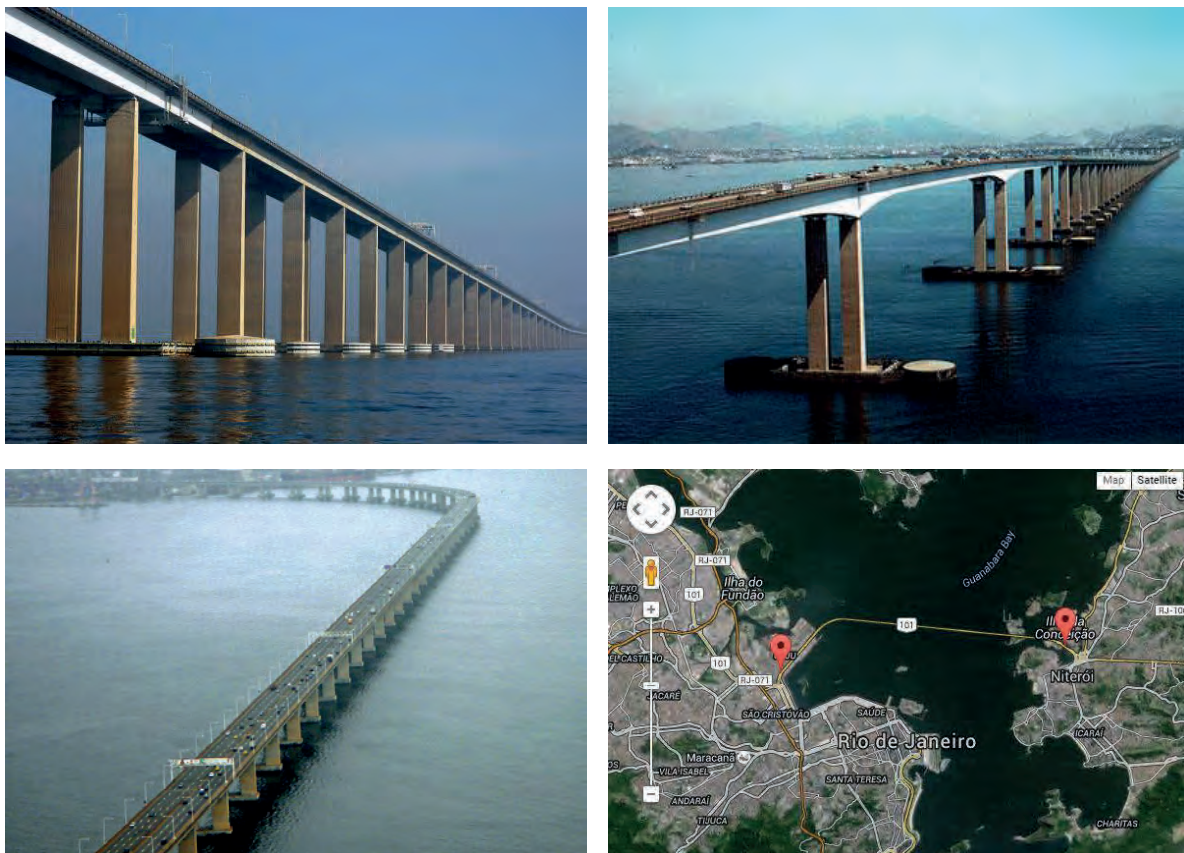


**Figure 1.** General Views of the Rio-Niterói Bridge (source: https://www.google.com/earth)

a)

b)
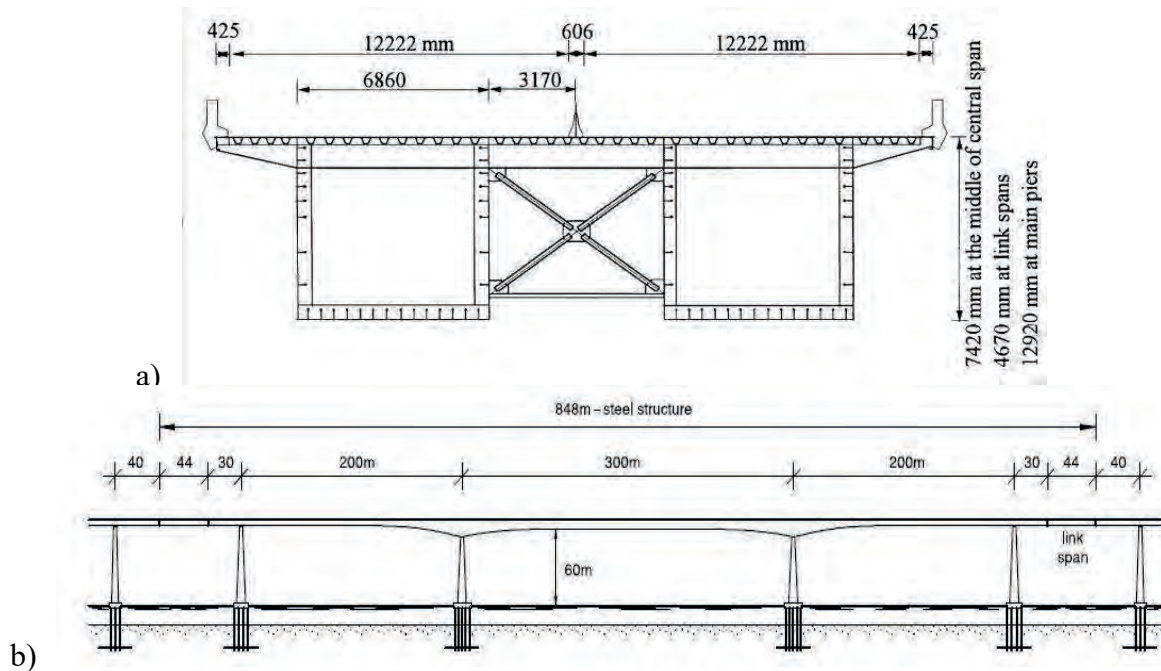
**Figure 2**. a) Cross-section dimensions of the midspan steel girder; b) Longitudinal dimensions of the main three steel spans and two steel links (Morgenthal, 2015)

## Geometry of the Bridge

The total length of the bridge is 13.3 km with twin steel girders connected by an orthotropic steel deck slab with a general structural solution in post-tensioned concrete, except for the three central spans (200m-300m-200m) and two lateral link spans, which have a steel structure reaching 848 m length. The height of the deck lies 65 m above water level, with a bridge depth-to-span ratio of 1:45 at midspan.

The cross-section of the bridge has a width of 25.90 m and a varying depth from 12.42 m to 7.42 m, from depth to midspan, with an added length from the barriers reaching 13.27m and 8.97m, respectively.

## Analysis of the Bridge

The Bridge was opened to traffic in March, 1974 with the first episode of vortex-induced vibrations taking place during a storm in 1980. This was just the first of many re-occurring episodes of oscillations of the lightly damped and remarkably long three continuous spans of the steel twin-box-girder bridge, because of the favourable conditions offered by the Guaranaba Bay with winds blowing transverse to the bridge longitudinal axis. When this occurs the bridge is closed to traffic for the sake of user's comfort and overall safety. However, sometimes because of inherent operational difficulties, the traffic barrier is closed too late and users are left frightened when crossing on the oscillating bridge (Battista, 2000).

## Static Analysis

When wind blows past bridges, the aerodynamic configurations of the decks directly determine the characteristics of the flow separation and the vortex formation, which is important for the occurrence

and development of vortex-induced vibrations. Besides the aerodynamic configurations, there are also other important factors that influence the behaviour of the cross section, as follows:

*Reynolds Number*

For incompressible fluid, both inertial and viscous forces are the two main parameters. The radio of inertial to viscous forces is defined as the Reynolds number, a dimensionless parameter. It has a significant impact on flow patterns. While the Reynolds number is overlooked at the beginning of wind-induced vibration study, many following experiments and practical engineering have proved that Reynolds number effects on bridge decks are closely related to the critical wind velocity, amplitude of vortex-induced vibration, validity of vibration suppression measures and the Strouhal number.

*Strouhal number*

The vortex-shedding frequency is related to the non-dimensional Strouhal number. The Strouhal number is defined as follows:

$$S_t = \frac{f_v D}{U} \qquad (1)$$

where    $f_v$ is the predominant frequency of vortex shedding

$U$ is the steady velocity of the flow

$D$ is the feature size of the structure (generally the projected size on the perpendicular plane to the airflow).

The Strouhal number is determined by both the section shape and the Reynolds number. If the Strouhal number is relatively large, the vortex-shedding frequency will approach to the first frequency of structures at a low flow speed, making vortex-induced vibration more likely to occur.

*Scruton number*

The Scruton number is a comprehensive parameter to reflect the mass and the damping of structures.

$$S_c = \frac{2\delta M}{\rho D^2} \quad \text{or} \quad S_c = \frac{2\delta I}{\rho D^2 B^2} \qquad (2, 3)$$

where    $M$ is the linear mass (for vertical modes)

$I$ is the linear mass inertia moment (for rotational modes)

$\xi$ is the damping ratio,

$\rho$ is the air density.

Damping and mass have a significant impact on the critical wind speed and in the amplitude of vibrations. VIV are more often to be observed in bridges that have relatively small damping and mass, because the bridges overcome less work done by damping force and inertial force during the vibration. Generally speaking, the smaller the Scruton number is, the more likely vortex-induced vibrations occur and the larger the lock-in regime is (Khalak, 1999).

In order to obtain a value of the Strouhal number to calculate the critical wind speed that produces VIVs on the Rio Niterói Bridge, firstly a static analysis was performed with the use of VXflow software. It is based on the Vortex Particle Method. A 2D-simulation model was performed by taking the cross section at the centre of the main span (300 m) as representative for the steel girder. The applied wind speed was 20 m/s, with a number of 100,000 time steps. The input of the geometry included 3 sections elements with their corresponding areas and coordinates (bridge section + 2 handrails). No angle of rotation for the cross section was specified, i.e. horizontal angle of incidence was studied.
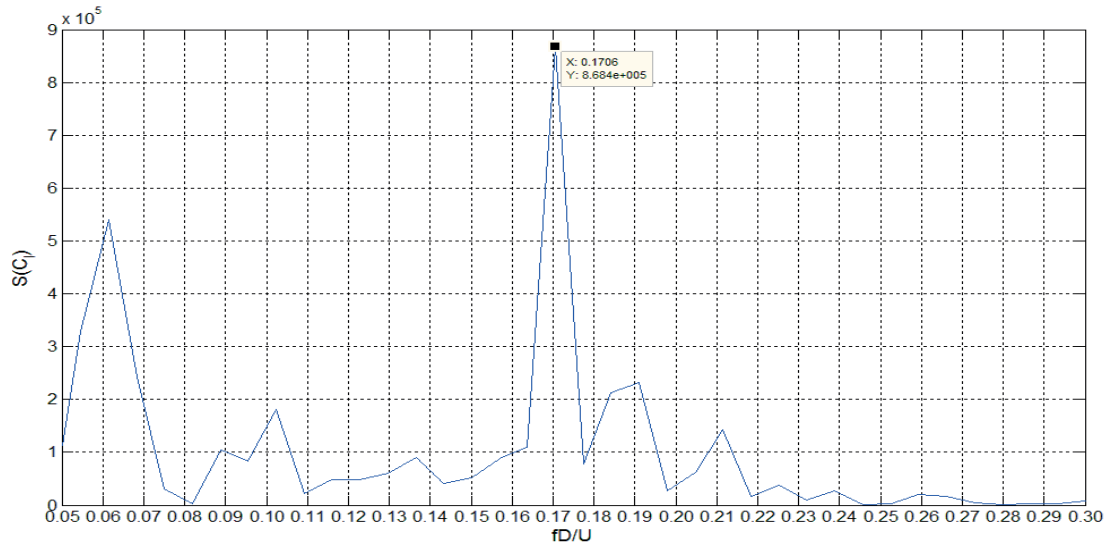
**Figure 3.** Fourier Analysis of Lift Coefficient
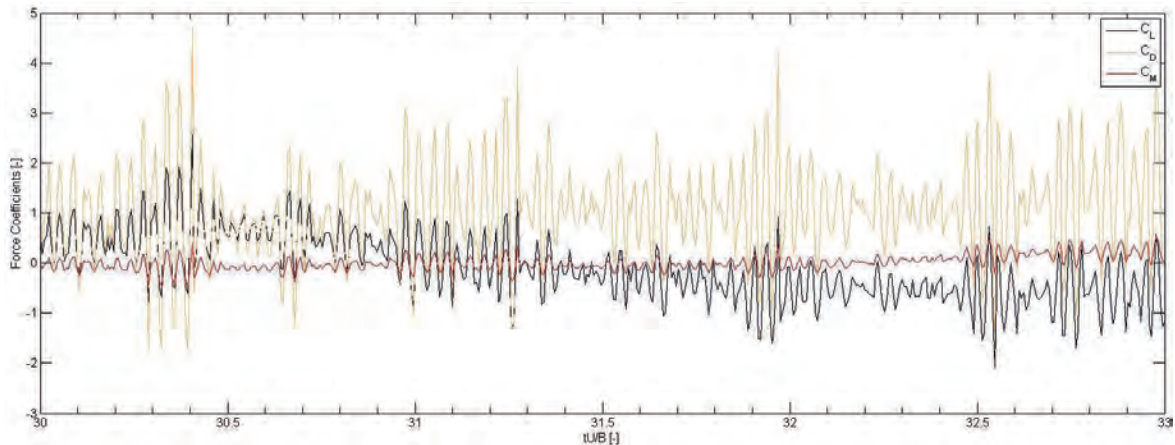


**Figure 4**. Lift, Drag and Moment Coefficients

The resulting Strouhal number was 0.1706, which combined with the natural frequency of the bridge $f_n = 0.32$ Hz and using the dimension D = 8.97 m, lead to the calculation of the critical wind speed $U_{cr} = 16.82$ m/s.

The interacting wind dynamic forces appear on the cross-section geometry as a result of the wind-structure interaction. They can be given as force coefficients related to lift ($C_L$), drag ($C_D$) and moment ($C_M$):

$$C_L = \frac{F_L}{\frac{1}{2}\rho U^2 B} \qquad C_D = \frac{F_D}{\frac{1}{2}\rho U^2 D} \qquad C_M = \frac{M}{\frac{1}{2}\rho U^2 B^2} \qquad (4,5,6)$$

In this case, the important one is the lift coefficient, due to the fact that VIVs only takes one vertical bending mode into consideration, because this is an uncoupled phenomenon. Vertical oscillations that will appear on the cross-section are due to the variance of pressure distribution on the upper and the lower cross-section surface along time.

103

## Dynamic Analysis

In the case of the dynamic analysis, the VXflow CFD code was also used with a similar input model as for the static analysis. The resulting critical wind speed of 16.82 m/s (from the static analysis) was taken into consideration and several dynamic simulations were run with different wind speeds between 13 m/s and 19 m/s, to capture the VIV occurrence.

One mode of vibration was used in all the dynamic models whilst taking into consideration the structural mass of $M_1$ = 11367 kg/m, a damping ratio $\xi$ = 0.01 and the same natural frequency of the structure $f_n$ = 0.32 Hz, resulting in 8 different dynamic analyses.

Also another set of similar 8 analyses have been performed with half the initial mass of the structure ($M_2$ = 5683.5 kg/m) in order to assess the importance of mass on the amplitude of the oscillations as a consequence of VIV.

A last model was created using double of the initial mass ($M_3$ = 22734 kg/m) and the wind speed of 16.5 m/s. This model was used to scale the root-mean square displacements ($y_{RMS}$) for the other wind speeds at the aforementioned mass.

For post-processing of the results the program Matlab was used, in order to obtain minimum and maximum displacement values and also the root-mean-square values ($y_{RMS}$), which were used to present the following diagrams. They offer a very clear view of the influence of mass, and wind speed on the amplitude of the oscillations.

Figure 5 present the three curves related to the three different masses M1, M2, M3 with resulting root-mean-square values of amplitude. As can be noticed the maximum values are present at a wind speed of 16 m/s for all three curves. This result is consistent with the initial presumption from the static analysis.
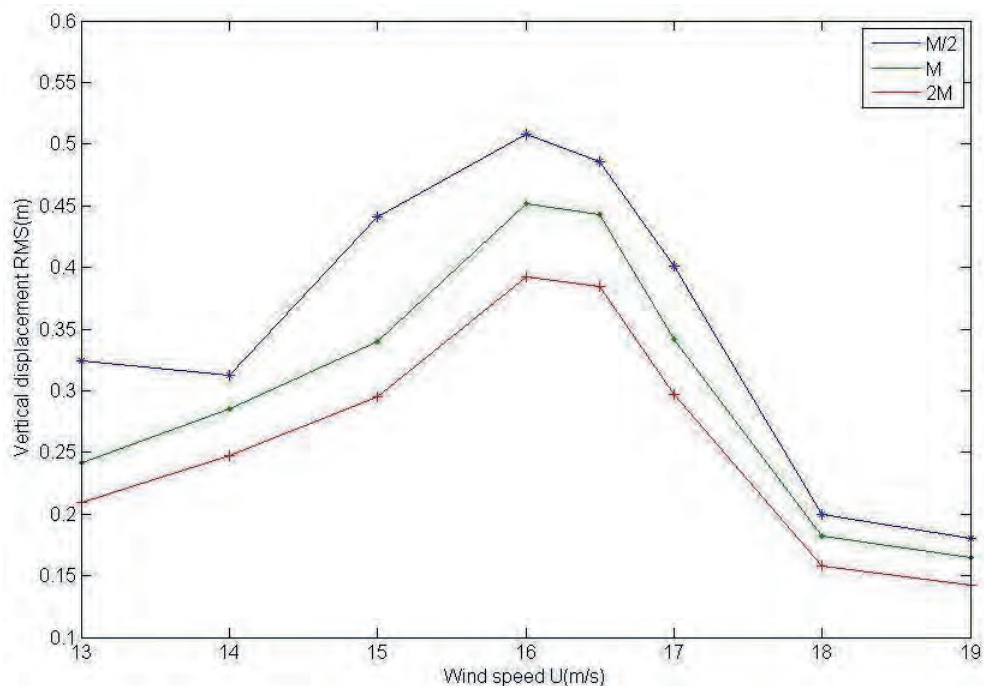


**Figure 5.** Comparative $y_{RMS}$-wind speed curves with regard to structural mass
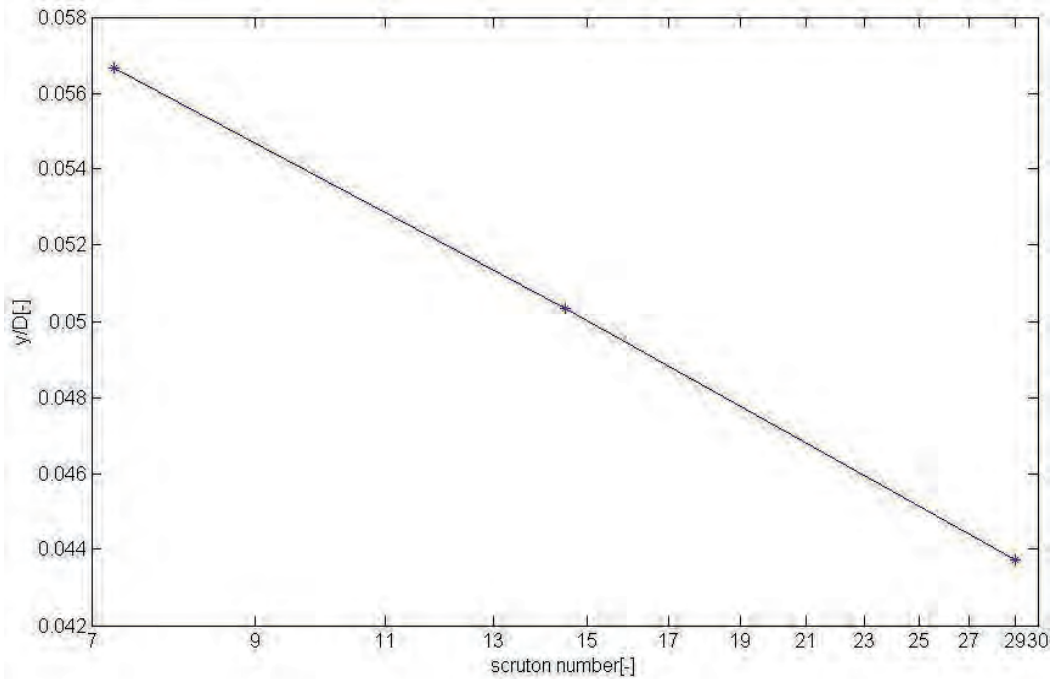
**Figure 6.** Variation of nondimensional RMS-Displacement with regard to Scruton number (M, ξ)
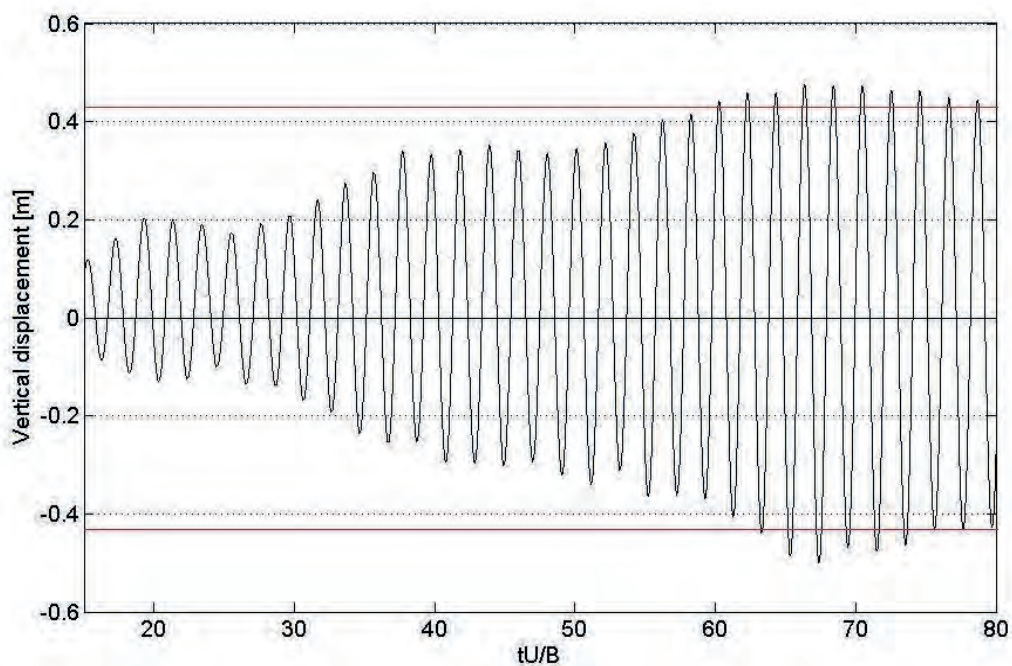


**Figure 7**. Time history of vertical displacement for U =16.5m/s

Usually in order to define its behaviour with regard to the Scruton number, a series of values have been used to define the curve, as shown in Figure 6. In this case we can observe a linear variation of the nondimensionalised root-mean square displacement values for a considered wind speed of 16.5 m/s.

# Conclusions

We have presented the aerodynamic phenomenon of vortex-induced vibrations (VIV), which has limited amplitude of displacements. However, this is important to evaluate its effects, since repeated incidents of VIV can lead to fatigue damage accumulation on structural elements. It also produces a reduction in travel comfort and safety levels, which is a very important reason why wind interactions need to be considered during design.

The case study is the Rio Niterói Bridge, which crosses the Guaranaba Bay between the cities of Rio de Janeiro and Niterói, in Brazil, and has a steel main span girder of 300 m. The static analysis revealed a critical wind speed of almost 16.5 m/s regarding VIV effects, which is not only concurrent with the results from the dynamic analyses, but also from the real-life observations of the Rio-Niterói Bridge. This means that around this value, the natural frequency of the bridge and the vortex shedding frequency lock-in to produce the vortex induced vibrations.

Structural mass is an important factor to take into consideration, because of the need for large dynamic forces to excite heavy structures. In the same idea, lighter structures also are prone to suffer higher amplitude oscillations, as expected.

Other important factors that need to be considered are the damping ratio of the structure, the cross-section geometry and the angle of attack on the wind-structure interaction.

# References

Batista R.C., Pfeil M.S. (2000): Reduction of vortex induced oscillations of Rio-Niterói Bridge by dynamic control devices. *Journal of Wind Engineering and Industrial Aerodynamics*, **84**: 273-288.

Khalak A., Williamson C.H.K. (1999): Motions, forces and mode transitions in vortex-induced vibrations at low mass damping. *Journal of Fluids and Structures*, **13**: 813-853.

Morgenthal G., Sánchez Corriols A., Bendig B. (2014): A GPU-accelerated pseudo-3D vortex method for aerodynamic analysis. *Journal of Wind Engineering and Industrial Aerodynamics*, **125**: 69-80.

Morgenthal G. (2015): PROJECT 6: WIND-INDUCED VIBRATIONS OF LONG-SPAN BRIDGES, Bauhaus Summer School 2015, course material.

*Presentation by the Participants* *(Photo: B. Proschak)*



*Participants at lecture class* *(Photo: B. Proschak)*

# Papers contributed by the participants

## 2015

Full papers are available at:

# On the influence of sensors placements in operational modal analysis of a medium-rise plan-symmetric frame structure: a simulation approach *

*BERNAGOZZI Giacomo, LANDI Luca, DIOTALLEVI Pier Paolo*
*Department DICAM, University of Bologna, Italy*

**Abstract.** Modal identification could be applied for the dynamic and the mechanical characterization of existing civil structures starting from the recordings of their accelerometric responses under unmeasured ambient vibrations. Referring to this promising technique, this work aims at evaluating the reliability of the output-only identification when applied to buildings instrumented with a number of sensors that is less than the number of the structural DOFs. Operational modal analysis, through NExT-ERA, is applied to RC plane frames, which only differ in the distribution of the columns stiffness, starting from their simulated responses when subjected to a white noise ground acceleration. Considering different subsets of these responses simulates various experimental setups in terms of complexity and costs that must be chosen in real applications. The results show the influence of the spatial distribution of the sensors on the identification of the first mode shapes, which are adequately expanded thought polynomial interpolation.

# Numerical solution of 2-D steady incompressible lid-driven cavity flow with three different numerical schemes *

*GHARAHJEH Siamak, ASHRAF Ammar*
*Middle East Technical University, Ankara, Turkey*

*SHIRAZI Ghorban Mahtabi*
*University of Zanjan, Zanjan, Iran*

**Abstract.** Numerical solution of 2-D steady incompressible lid-driven laminar cavity flow is presented. Three different numerical schemes are employed to make a comparison on the practicality of the methods. Alternating direction implicit (ADI) scheme for the vorticity stream function formulation, explicit and implicit scheme for primitive variable formulation of governing Navier-Stokes equations of flow were attempted. A fairly fine uniform grid was adopted for all the cases after a technical procedure was applied to come up with the proper mesh size that would make the solution roughly independent of mesh quality. The solutions obtained for different Reynolds numbers are presented and compared. Superiority of numerical approaches are investigated and compared to benchmark solutions available in the literature.

# Experimental research on the mechanical behaviour of Toyoura sand under low and normal confining pressure with monotonic and cyclic triaxial loading tests

*HOSOYA Akihiro, ZHANG Feng, GU Linlin, SHIRAI Yu*
*Nagoya Institute of Technology, Nagoya, Japan*

**Abstract.** In Japan, many element tests are conducted under normal and high confining pressure to evaluate the mechanical behavior of sandy ground during and after liquefaction, but few tests are conducted under low confining pressure (below 49kPa). In this paper, drained or undrained monotonic and cyclic undrained triaxial tests under the confining pressure of 5, 10, 20, 98kPa in different densities and stress ratios were conducted to illustrate the mechanical behavior of Toyoura sand. Meanwhile, very thin membrane whose thickness is 0.15mm has been used. The test results show that loose sand may behave like dense sand under low confining pressure in monotonic loading tests, so not only void ratio but also confining pressure are state variables that control the loose or dense state of sand.

# The application and parameter identification of an empirical non-linear model for vortex-induced force on rectangular sections

*JINLIN Xia, YAOJUN Ge*
*State Key Laboratory for Disaster Reduction in Civil Engineering, Tongji University, Shanghai, China*
*Department of Bridge Engineering, Tongji University, China*
*Key Laboratory for Wind Resistance Technology of Bridges of Ministry of Transport, Tongji University, Shanghai, China*

**Abstract.** Ehsan–Scanlan's empirical non-linear model is widely used to analyse the vortex-induced vibrations on frequently-used bridge decks. In this paper, the physical meanings of model's parameters ($Y_1$ and $\varepsilon$) as well as the dynamic performances of vortex-induced force were investigated at first, by some brief numerical calculations. Then, the relationship between reduced wind velocities and amplitudes of vortex-induced vibration on rectangular sections was demonstrated, which is a typical series of cross section. Afterwards, the parameters' characteristics of Ehsan–Scanlan's model on rectangular sections were discussed, and two fitting functions for the parameters were proposed, with simple forms. A least square fitting method based on the measured history of vortex-induced force was then established, to identify the undetermined parameters ($a, b, c, d, e, f$) of the fitting functions, using the empirical data on finite reduced wind velocities. With these undetermined parameters identified, the amplitudes of vortex-induced vibration on rectangular sections can be predicted, at any wind velocity of lock-in. Finally, a comparison of the amplitudes of vortex-induced vibration by experimental measurement and by numerical simulation was presented to verify the feasibility of this numerical method.

# Methods of Calculating Wind Loading of Cooling Towers *

*KONARSKI Jakub*

*Department of Structural Analysis and Dynamics, Faculty Architecture, Civil Engineering and Urban Planning, Brandenburg University of Technology, Cottbus-Senftenberg, Germany*

**Abstract.** Wind ribs on the surface of a cooling tower, their geometric dimensions and their spacing considerably affect both the pressure distribution around the circumference and the total wind load on the structure. Solving such problem using explicit rib modelling and direct numerical integration is extremely voluminous and time consuming, thus impractical. The purpose of this paper is to find a way to easily recreate the effect of ribs on values of pressure coefficient. Methods used consist of ribbed cylinder, cylinder with surface roughness and rotating cylinder. Comparison between two and three-dimensional models is shown. Various methods of correcting blockage effect are presented and studied. Acquired results are compared with each other, curves from German BTR code and full scale measurements.

# Statistical evaluation of the punching shear resistance of flat concrete slabs *

*KOZMA András*
*Budapest University of Technology and Economics*

**Abstract.** Punching shear failure is a complex phenomenon with brittle failure mode. Present design formula, proposed by Eurocode 2, for this failure mode is based on an empirical formulation for the prediction of shear strength of beams. The code uses the same partial factor for this failure mode as in the case of common design situations, which is may not be appropriate. Real experimental results were used for the calibration of the numerical results. Several nonlinear FEM simulations were carried out to determine realistic punching shear resistance of concrete slabs and these results were compared to the analytical approach. Based on this comparison the partial factor for the design formula was determined. The determined partial factor is higher than the actual one.

**Figure 1.** Punching failure of a flat slab from [*http://civildigital.com/punching-shear-punching-shear-flat-slabs/*]

# Analytical estimation of stiffness reinforcing ties in a crack in the model of discrete cracks deformation elements of reinforced concrete structures

*LEVIN V. M.*
*Donbas National Academy of Civil Engineering and Architecture, Ukraine*

*DMITRENKO E. A.*
*Institute of Airports, National Aviation University, Ukraine*

**Abstract.** The article presents the refined analytical technique for determining stiffness secant of reinforcing ties crossing crack $C_{sm}$ - essential parameters required for simulation of reinforced concrete structures by the model of discrete cracks through finite-elements method (FEM). Determination of secant stiffness of the reinforcing tie crosses a crack, depending on the existing effort $N_{sm}$ and movement $U_{sm}$ carried out by solving in mathematical packages a nonlinear boundary value problem consisting of four differential equations of the 1st order, representing the laws of deformation of concrete and reinforcement, as well as a clutch of reinforcement and concrete. The law adopted for the clutch is elastic-plastic, which is an approximation to the normal law of coupling by Kholmyanskiy [4], the work of steel reinforcement is represented by the elastic dependence (Hooke's law), concrete – by elastic-plastic dependence. The results clearly demonstrate a non-linear nature of the reinforcing tie work crosses a crack, which corresponds to the actual work of ties, but for greater authenticity need experimental confirmation.

# Experimental modeling of geosynthetic reinforcement - geogrids in noncohessive fill

*MARIĆ Dario, MINAŽEK Krunoslav, MULABDIĆ Mensur*
*Faculty of Civil Engineering, Osijek, Croatia*

**Abstract.** Geotechnical engineering recognizes the use of geosynthetic materials (geogrids, geotextiles or geocomposites) as a very effective way to produce soil reinforcement and stabilisation when they are used in construction of embankments or retaining walls. Using geogrids as reinforcement several positive effects can be achieved: reinforced composite made of soil fill with geogrid has an improved strength and stiffness so it can withstand higher loads and suffer smaller deformations, increasing the durability of the construction at the same time. All these effects are achieved due to soil – geogrid interaction. The main purpose of this article is to show how strong is influence of geogrids in noncohessive soil due to difference in wave velocity of longitudinal and/or transversal waves when geogrids are installed in soil and without them. Using wave velocity we are able to calculate Young's modulus for soil and establish stiffness of soil, considering reinforcement.

# Analytic and experimental evaluation of masonry walls externally reinforced with mortar and wire welded mesh applied to historical building walls

*LOPEZ Sebastián*
*Escuela Colombiana de Ingeniería, Julio Garavito. ECI*

**Abstract.** Colombian seismic provisions (NSR-10) had recently accepted a new system of externally reinforced masonry walls with welded wire mesh and mortar (W.W.M). Escuela Colombiana de Ingeniería Julio Garavito, with the objective of evaluate the response of full scale walls reinforced with this new reinforcement system for masonry structures like existing houses and historical buildings. Unreinforced masonry walls and reinforced masonry walls were tested; small specimens were used to evaluate the material properties; while in plane monotonic and dynamic lateral load were run in full scale walls. The article shows experimental results and their comparison with the values obtained by using the equations and recommendations of NSR-10 for walls typical of some historical buildings. Results demonstrate that calculations are conservative and safe; furthermore, the reinforcement technique increased the strength to in plane lateral loads between 4 to 8 times when was used by one or by two sides of the wall respectively.

# Seismic Performance Evaluation of a Steel Moment-resisting Frame using Local Damage Detection and Model Updating Techniques *

*NISHINO Hiromichi,*
*Department of Architecture and Architectural Engineering, Kyoto University*

*NAKASHIMA Masayoshi*
*Disaster Prevention Research Institute, Kyoto University*

**Abstract.** Knowledge of the extent and locations of earthquake-induced damage allows rapid damage assessments and safety evaluations for buildings. This paper proposes a method for estimating the residual capacity of earthquake-affected steel moment-resisting frames. A strain-based local damage evaluation method is applied to a series of shake table tests on a three-story steel frame. Identified damage is incorporated into a model-updating framework and the residual performance of the damaged model is estimated by a static non-linear pushover analysis.

# Application of 3D Micro Models for Seismic Resistance Forecast of Framed-Masonry Structures: Preliminary Activities *

*PENAVA Davorin, SIGMUND Vladimir, ANIĆ Filip, TRAJBER Domagoj, VIG Mirko*
*Josip Juraj Strossmayer University of Osijek, Faculty of Civil Engineering Osijek*

*KOŽAR Ivica*
University of Rijeka, Faculty of Civil Engineering

**Abstract.** Framed-masonry composites present the classical construction approach used in many earthquake prone countries worldwide. Unfortunately, the seismic resistance forecast of such structures remains difficult. One of the most important reasons for that is the lack of the appropriate material model that takes into account the orthotropic properties of the masonry wall and/or units such as hollow clay masonry units. A problem that extends on the previous is the high variation of the material properties of the masonry wall and its constituents. Therefore, this study is focused on the influence of the various strength deviations on the critical stress and strain outcome when hollow clay masonry units are used. We build spatial micro models of masonry walls and tested them under vertical and horizontal compression. The results have shown that the influence of the variation of masonry constituent properties is not negligible, which may significantly alter the stress and strain response of the structure.

# Reinforced concrete frames with masonry infills. Out of plane experimental investigation *

*PETRUS Cristian, STOIAN Valeriu, MOSOARCA Marius*
*Politehnica University of Timisoara, Faculty of Civil Engineering, Timisoara, Romania*

*ANSTASIADIS Anthimos*
*ASA Structural Consultants, Thessaloniki, Greece.*

**Abstract.** This paper presents a synthesis of the typical damages recorded in reinforced concrete frames and masonry infills after recent earthquakes. The behaviour and failure modes of the infill walls are of great importance, especially since no clear recommendations are provided in the current design codes for the performance of these types of walls. In the present time, masonry infill walls are considered to be non-structural building elements, while the seismic behaviour of reinforced concrete frame structures having these type of walls, indicated a structural behaviour of the infills. Several proposals for the improvement of the out-of-plane behaviour of infill walls are presented in this paper, together some experimental results of tests performed on a simple masonry wall. The investigation of these solutions can lead to the development of innovative systems of masonry infills, and can also provide viable consolidation measures for existing buildings.

# Influence of detailing of short links on seismic response of eccentrically braced frames *

*VĂTĂMAN Adina, GRECEA Daniel, CIUTINA Adrian*
*Politehnica University of Timişoara, Department of Steel Structures and Structural Mechanics*

**Abstract.** The Eccentrically Braced Frames represent highly dissipative seismic systems due to the formation of plastic hinges in link elements. In function of their length, they can work in shear (short), bending (long) and respectively combined bending and shear (intermediate links). Based on the ratio between the plastic bending and plastic shear resistances of the link element, and a minimum number of stiffeners on the link, the normative requirements do not differentiate between minimum/maximum required length of the link nor the increased number of stiffeners present on the link. The paper presents the performances of short steel link elements subjected to shear under the form of a parametrical study performed using Abaqus FEM tool. An initial FE model is calibrated based on an experimental test performed within the CEMSIG laboratory at Politehnica University for monotonic loading. In a second step the numerical analysis investigates three parameters that can affect the behaviour of such systems, whilst remaining in the range of short shear links: (i) use of compact/slender webs; (ii) influence of the number of web stiffeners and (iii) influence of link length. The results are presented under the forms of V-$\gamma$ response curves and judged in function of characteristic parameters.

# Probability of failure of an embankment dam due to slop instability and overtopping *

*ZHELYAZKOV Aleksandar, ANDREEV Stoyan*
*Risk Engineering Ltd.*

**Abstract.** The current paper analyses the probability of failure of an embankment dam due to slope instability and overtopping induced by flooding. The input data is as presented for the 2015 ICOLD Benchmark. Uncertainty is introduced by probabilistic values for the soil parameters. Probabilities for slope surface failure are computed with the Monte Carlo technique and the Taylor series method (First Order Second Moment Method) using a simple limit equilibrium method.

Sensitivity analysis is conducted assessing the significance of the assumptions made for the probability distributions of the soil parameters on the applicability of the Taylor series method. Recommendations are made for the reduction in uncertainty along with overall conclusions about the obtained results.

**Note:** Abstracts related to presentations by the participants are highlighted by '*'.

*Visit of the wind tunnel in part of the group work in Project No. 6 (Photo: B. Proschak)*


*Participants at project work (Photo: B. Proschak)*

*Summer course participants at the guided sightseeing tour in 2015* (Photo: H.-J. Nitzpon)



*Team building as part of the course activities in 2015* (Photo: B. Proschak)

# Bauhaus Summer School – Forecast Engineering 2016
## From Past Design to Future Decision

*ABRAHAMCZYK Lars, SCHWARZ Jochen*
*Earthquake Damage Analysis Center, Bauhaus-Universität Weimar, Germany*

## Guest lecturers and invited speakers

Nationally and internationally well-known and high-ranked scientist could be welcomed as guest speakers at the Engineering Summer Course at Bauhaus-Universität Weimar in 2016. The current state of research at the Project Partner's Universities as well as lecturers from other disciplines highlighted the future demands on Engineers to overcome future requirements on engineered structures.

- Introduction to Nonlinear Optimization with Applications in Engineering | *Prof. T. Lahmer (BUW)*
- Numerical and experimental assessment of the dynamic behaviour of Railway Bridges | *Dr. Diogo Ribeiro (ISEP, Portugal)*
- Design assisted by testing of Cold-formed Steel Structures | *Dr. A. Crisan (University of Timisora)*
- Wind flow modelling and climate analyses | *Dr. M.P. Repetto (University of Genoa)*
- Vision-based inspection of structures using unmanned aircraft systems | *Prof. V. Rodehorst (BUW)*
- Function Theoretic Methods in Elasticity | *Dr. S. Bock (BUW)*
- Natural Hazards & Climate Change: Future challenges for insurers and engineers | *Dr. T. Bistry (Deutsche Rück, Germany)*
- New Trends in Vibration-Sensor Developments | *Dr. H.-J. Nitzpon (SEMEX-EngCon, Germany)*
- New Trends in Engineering Seismology | *Prof. F. Cotton (GFZ Potsdam, Germany)*
- Numerical modelling of structures under fire conditions | *Prof. Dr. N. Lopes (Aveiro, Portugal)*

# Time Schedule

| | **Monday**<br>22. August | **Tuesday**<br>23. August | **Wednesday**<br>24. August | **Thursday**<br>25. August | **Friday**<br>26. August | **Sat. Sun.**<br>27./28. Aug. |
|---|---|---|---|---|---|---|
| **09:00 - 10:30** | Opening 2016 | Prof. T. Lahmer (BUW)<br><br>*Lecture Hall 6,* | Presentation by Participants<br><br>*Lecture Hall C* | Project work | Dr. M.P. Repetto (University of Genoa)<br><br>*Lecture Hall C* | Cultural events and program as part of the Bauhaus Summer School 2016 |
| **11:00 - 12:30** | Projects 1 & 2<br><br>*Lecture Hall 6,* | Dr. D. Ribeiro (ISEP, Portugal)<br><br>*Lecture Hall C* | Dr. A. Crisan (University of Timisora)<br><br>*Lecture Hall C* | *will be announced* | Prof. V. Rodehorst (BUW)<br><br>*Lecture Hall C* | |
| | Lunch | | | | | |
| **13:30 - 15:00** | Projects 3 & 4 | Project work<br><br>*will be announced* | Interdisciplinary experience exchange with specialised courses of Bauhaus Summer School **14:00 - 17:00** | Project work<br><br>*will be announced* | Project work<br><br>*Lecture Hall C* | |
| **15:30 - 17:00** | Projects 5 & 6<br><br>*Lecture Hall C* | | | | | |
| **17:30 - 19:00** | Icebreaker Party **17:30** | | Team Building (Sport challenges)<br><br>*"Falkenburg"* | | | |
| | Cultural events as part of the Bauhaus Summer School 2016 | | | | | |

| | **Monday**<br>29. August | **Tuesday**<br>30. August | **Wednesday**<br>31. August | **Thursday**<br>1. September | **Friday**<br>2. September | **Sat.**<br>3. Sept. |
|---|---|---|---|---|---|---|
| **09:00 - 10:30** | Dr. S. Bock (BUW)<br><br>*Lecture Hall C* | Presentation by Participants<br><br>*Lecture Hall C* | Prof. N. Lopes (Aveiro, Portugal)<br><br>*Lecture Hall C* | Project work | Presentation of project works & Closure | |
| **11:00 - 12:30** | Dr. T. Bistry (Deutsche Rück)<br><br>*Lecture Hall C* | Prof. F. Cotton (GFZ Potsdam)<br><br>*Lecture Hall C* | Prof. N. Lopes (Aveiro, Portugal)<br><br>*Lecture Hall C* | *will be announced* | *Lecture Hall C* | |
| | Lunch | | | | | |
| **13:30 - 15:00** | Dr. H.-J. Nitzpon (SEMEX-EngCon) | Project work | Excursion to Construction Sites **14:00 - 18:00** | Preparing of presentation | Preparation of final report | **05:00 - 10:00** Departure |
| **15:30 - 17:00** | Presentation by Participants<br><br>*Lecture Hall C* | | | *will be announced* | *will be announced* | |
| **17:30 - 19:00** | Sightseeing Weimar<br><br>*meeting point* | *will be announced* | | Food evening<br><br>*M18* | Farewell Party **18:00**<br><br>*Mensa* | |
| | Cultural events as part of the Bauhaus Summer School 2016 | | | | | |

119

# Excursion

A special highlight of the Engineering Course at the Bauhaus Summer School is the annual excursion to current construction sites or already finished outstanding engineering projects in Thuringia. In 2016 the participants could visit the bridge construction site "Ilmtalbrücke", which is part of the new state road B90N nearby Stadtilm.

The excursion was guided along and on the structure to highlight and impart knowledge about the special construction of engineering art in bridge design. Construction details of the "Ilmtalbrücke" are:

- Total length:          630 m
- Type:                  integral structure
- Height of the columns: 6 to 16m

- Construction costs:       ~ 11 Million
- Start of the construction: 01/2015
- Completion:               07/2017




*Impressions from the excursion to the bridge construction site "Ilmtalbrücke"* (Photos: N. Hallermann)



*Group picture from the participants of the excursion in 2016 (Photo: Ulrich Gawlas)*

# Project reports
# 2016

# A distributed-collaborative modal identification procedure for wireless structural health monitoring systems

*NASR Amro [a], DEHSHAHRI Fataneh [b], MICULAŞ Cristian Vasile [c], FICKER Kata [d], AZARI Sahar [a], ATTAULLAH Hamidullah [a]*

[a] *Bauhaus University Weimar, Germany*

[b] *Sharif University of Technology, Iran*

[c] *Technical University of Cluj-Napoca, Romania*

[d] *Budapest University of Technology and Economics, Hungary*

*DRAGOS Kosmas and SMARSLY Kay*
*Chair of Computing in Civil Engineering, Bauhaus University Weimar, Germany*

## Abstract

Structural health monitoring (SHM) has been increasingly employed to ensure public safety and integrity of the built environment. Wireless sensor networks, owing to their lower cost and ease of installation as compared to traditional cable-based systems, have been adopted to ensure the integrity of the structures. Due to the limited power resources of wireless sensor nodes, embedded algorithms are devised to exploit the inherent processing capabilities of the sensor nodes through on-board data processing, in an attempt to reduce the power-consuming wireless data transmission. In this paper, a wireless SHM system capable of distributed-collaborative modal identification is presented, using embedded algorithms. Modal identification in the proposed SHM system is based on the on-board selection of modal "candidate" peaks from the frequency spectra of acceleration response data from a monitored structure. The candidate peaks are sent to a central server, where the final peaks are selected and sent to the sensor nodes in order to retrieve the corresponding Fourier values for modal extraction. The wireless SHM system is validated through laboratory tests on a steel frame structure, showcasing the ability of the SHM system to yield accurate mode shapes regardless of the structural state. The SHM system has been designed and implemented within a summer school project at Bauhaus University Weimar.

## Introduction

Structural health monitoring (SHM) has been increasingly employed to ensure public safety and integrity of the built environment, such as buildings, bridges, pipelines, roads, and tunnels, which are exposed to operational and environmental loads over decades of service. Wireless sensor networks, owing to their lower cost and ease of installation as compared to traditional cable-based systems, are adopted to ensure the integrity of the structures. SHM is used in several engineering fields for conducting condition-based maintenance instead of conventional scheduled maintenance (Semperlotti, 2009). The rapid advancements in computer science and sensor technologies have paved the way for applying wireless sensor networks for SHM, offering easier and lower-cost installations, as opposed to traditional cable-based systems.

Due to the aforementioned benefits of wireless sensor networks, wireless sensor nodes have been increasingly adopted in SHM applications. However, the limited power autonomy and the restricted resources of wireless sensor nodes still pose non-negligible operational constraints. It has been reported that the most power-consuming operation of sensor nodes is due to wireless data transmission (Lei et al., 2010). As a result, embedded computing is employed in wireless SHM systems in an attempt to execute monitoring tasks on-board the sensor nodes and reduce data transmission.

Several approaches towards embedded models and embedded algorithms for wireless sensor nodes have been proposed. Zimmerman et al. (2008) have presented embedded algorithms for output-only system identification. The use of a linear quadratic regulation algorithm for structural control has been proposed by Wang et al. (2006) and Kane et al. (2014). Dragos and Smarsly (2015, 2016) have presented embedding numerical models into wireless sensor nodes for structural health monitoring and decentralized infrastructure health monitoring.

In this paper, a wireless SHM system with modal identification capabilities is presented. First, the mathematical background on modal identification is provided. Second, the architecture of the wireless SHM system is presented and the embedded algorithms are illustrated. Finally, laboratory tests for validation of the proposed SHM system are presented and an outlook on future research is given.

## Frequency domain decomposition

The extraction of mode shapes in this study is based on frequency domain decomposition (FDD) (Brincker et al., 2000). In FDD, first, the response time histories of all sets of collected acceleration response data (from all measured locations of the monitored structure) are transformed from the time domain into the frequency domain using the fast Fourier transform (FFT) (Cooley and Tukey, 1965). From the Fourier spectrum the highest peaks corresponding to resonant vibration, which are therefore indicative of modes of vibration, are then picked by a peak-picking algorithm. Then, the spectral density matrix, indicative of the power carried by each acceleration response data set, at the frequencies corresponding to the selected peaks is calculated using Eq. 1.

$$\mathbf{G}_{ij} = \sum_{i=1}^{r}\sum_{j=1}^{r} F_i \cdot \overline{F_j^*} \tag{1}$$

In Eq. 1, $\mathbf{G}$ is the spectral density matrix and $\mathbf{F}$ is the complex Fourier value, while $r$ is the number of acceleration response data sets. The overbar and the star denote complex conjugate. The relationship between the input spectral density matrix and the output spectral density matrix is shown in Eq. 2.

$$\mathbf{G}_y = \mathbf{H}(i\omega)\mathbf{G}_x\mathbf{H}(i\omega)^H \tag{2}$$

In Eq. 2, $\mathbf{G}_y$ is the output spectral density matrix, $\mathbf{G}_x$ is the input spectral density matrix, $\mathbf{H}$ is the frequency response function between the input and the output, $\omega$ is the eigenfrequency of the selected peak, while the superscript $H$ denotes complex conjugate and transpose (Hermitian). Assuming white noise excitation, the input spectral density matrix is constant. Therefore, according to Brincker et al., the singular value decomposition (SVD) of the output spectral density matrix yields a diagonal matrix holding the eigenvalues, and a left-singular matrix whose left-most vector, at an eigenfrequency corresponding to a resonant peak, is equivalent to the eigenvector of the structure, as shown in Eq. 3.

$$\mathbf{G}_y = \mathbf{U}\mathbf{S}\mathbf{U}^T \qquad \mathbf{U} = \begin{bmatrix} \mathbf{u}_{j1} & \mathrm{K} & \mathbf{u}_{jr} \end{bmatrix} \qquad \omega = \omega_p \Leftrightarrow \mathbf{u}_{j1} \cong \boldsymbol{\varphi}_p \tag{3}$$

where $\mathbf{U}$ is the left-singular matrix, $\mathbf{S}$ is the diagonal matrix holding the eigenvalues, $\mathbf{u}$ is the singular vector, $p$ is the index of the selected peak, and $\boldsymbol{\varphi}$ is the mode shape vector.

# A wireless SHM system for distributed-collaborative modal identification

A wireless SHM system to perform distributed-collaborative modal identification is presented. First, the overall SHM system is described. Then the implementation of the modal identification tasks in terms of embedded algorithms is illustrated.

## Description of the wireless SHM system

The wireless SHM system devised in this study consists of wireless sensor nodes, a gateway node, and a server (referred to as "base station"). In the proposed SHM system, modal identification is based on frequency domain decomposition. As shown in Eq. 1, to perform FDD, the Fourier values at peaks of the frequency spectrum corresponding to resonant response (i.e. "modal peaks") must be retrieved from all measured locations. As aforementioned, wireless transmission is particularly power-consuming; therefore, to reduce wireless transmission, parts of the FDD process are executed on board the sensor nodes. In particular, on each sensor node, the acceleration response data is transformed into the frequency domain on board, via an embedded FFT algorithm. Subsequently, the modal peaks are selected by an embedded peak-picking algorithm. To ensure accurate peak detection and to avoid false positive detections of peaks, a sufficiently large number of peaks are initially inquired. These so-called "candidate" peaks are then sent to the base station where, upon judging on the stability of the peaks, the final peaks are selected manually and sent back to the sensor nodes. Finally, the corresponding Fourier values are sent from the sensor nodes to the base station, where the extraction of the mode shapes is completed. A flowchart of the tasks executed by the wireless SHM system is shown in Figure 1.

## Embedded algorithms

To implement the tasks of the wireless SHM system, two types of applications are written in Java programming language. The "host application" handles the tasks of the base station and the "on-board" applications handle the tasks of the sensor nodes.
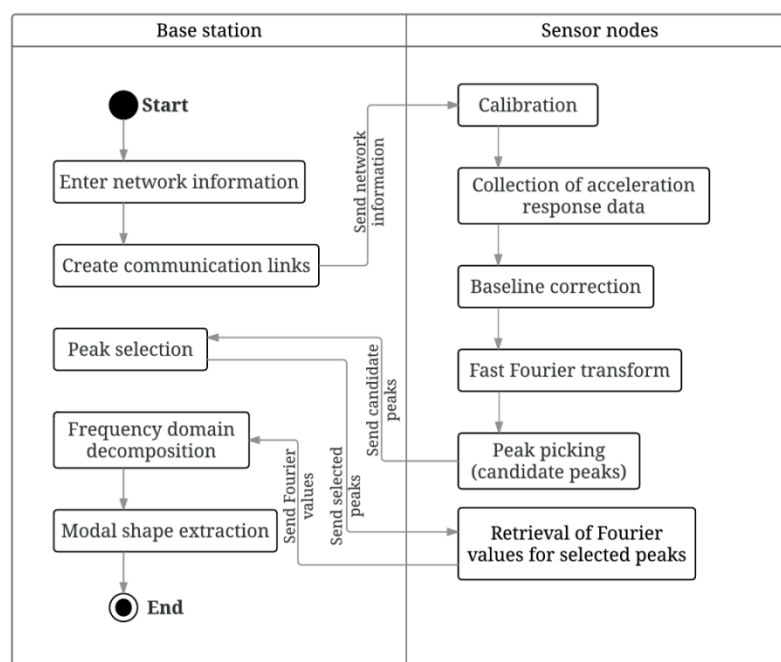


**Figure 1.** Activity diagram of the proposed wireless SHM system

In the host application, the base station is, first, initialized and the network parameters (i.e., number of sensor nodes, sampling rate, and number of peaks) are introduced. Wireless communication links are established based on the IEEE address of the sensor nodes, and the network parameters are transmitted over the air to the sensor nodes. Upon receiving the candidate modal peaks from the sensor nodes, the host application displays the respective indices of the peaks corresponding to the data series of the frequency spectra. Then, the final peaks are entered interactively into the host application and wirelessly communicated to the sensor nodes. Finally, upon receiving the complex Fourier values of the final peaks from the sensor nodes, the host application performs frequency domain decomposition to extract the mode shapes, employing Java classes from the JAMA library for matrix operations and singular value decomposition (JAMA, 2010).

In the on-board application, the wireless sensors nodes are, first, initialized and calibrated and wait to be triggered to start collecting acceleration response data. The sensor nodes are triggered once the acceleration exceeds a pre-defined threshold. Upon completion of acceleration response data sampling, baseline correction is performed to remove potential offsets. The wireless sensor nodes transform the collected acceleration response data into the frequency domain via an embedded FFT algorithm. Then, peak-picking is performed based on detecting the frequency with the maximum Fourier amplitude. After each peak detection, a part of the frequency spectrum of pre-defined range centered around the detected peak is removed and peak-picking is repeated until the specified number of peaks is detected. Finally, once the sensor nodes have received the final peaks from the base station, the real and imaginary parts of the corresponding Fourier values are packaged and sent to the base station.

## Validation tests

Laboratory tests for validation of the proposed wireless SHM system are devised using a frame structure. The tests are performed to showcase the ability of the SHM system to yield accurate mode shapes with minimal data traffic.

### Hardware used

The wireless sensor nodes and the base stations used in this study are Java-based Oracle SunSPOTs (Figure 2) (Oracle, 2010). The wireless sensor nodes support Java ME technology. The sensor nodes feature an Atmel AT91RM9200 computational core with a 32-bit processor executing at 400 MHz maximum internal clock speed. Peripheral interface units, such as USB port, programmable I/O controller and I2C bus, are included. The computational core has 4 MB flash memory and 512 kB RAM. For wireless communication, an integrated radio transceiver, the IEEE 802.15.4-compliant Texas Instruments (Chipcon) CC2420 single-chip transceiver is employed, operating on the 2.4 GHz unregulated industrial, scientific and medical (ISM) band. A rechargeable lithium-ion battery (3.7 V, 720 mAh) is provided for power supply. Each sensor node is equipped with a temperature sensor, a light sensor, and a three-axial 8-bit MMA7455L digital output accelerometer, able to sample at 125 and 250 Hz at a selectable range of ±2g, ±6g, or ±8g.

### Experimental setup

The validation tests are performed on a four-story laboratory steel frame structure. The structure consists of rectangular steel plates with 50 cm length, 25 cm width, and 0.75 mm thickness. As shown

in Figure 2, the height of each story is 23 cm. The plates rest on steel circular columns of 5 mm diameter fixed into a solid wooden blocks and rigidly connected to the plates. In the experimental setup of this study, one sensor node is placed at the center of each floor.
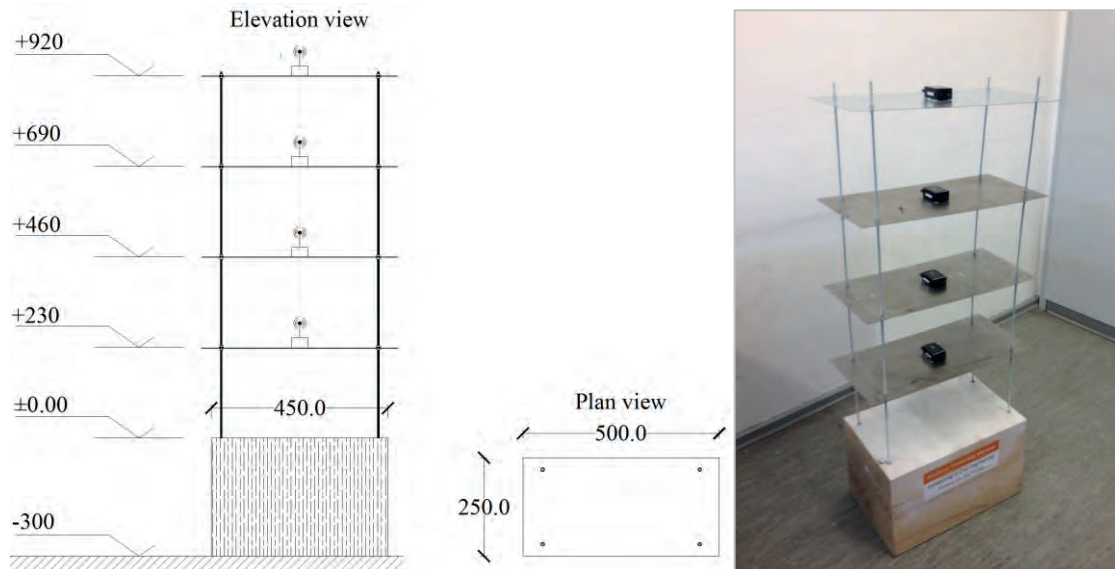


**Figure 2.** Schematic of the laboratory test structure and experimental setup

### Description of the validation tests

Upon initialization and calibration of the sensor nodes, the structure is deflected at the fourth floor. The pre-defined acceleration threshold of $\tau = 0.5$ g is exceeded, and acceleration response data is collected by each sensor node. Then, the collected acceleration response data is transformed into the frequency domain via the on-board FFT, and the peak-picking algorithm yields the candidate modal peaks. A total of 10 candidate peaks is chosen in this study. Next, the peaks are sent to the base station and the final peaks are selected and sent back to the sensor nodes. Finally, the sensor nodes send the complex Fourier values corresponding to the selected peaks to the base station, and the mode shapes are extracted through FDD.

To excite as many modes as possible, three groups of tests are performed, with varying excitation direction. More specifically, the structure is excited in the X direction, in the Y direction and in a random direction, while for verification purpose each test is repeated three times. In the first group of tests the structure is deflected in the X direction, in the second group of tests the structure is excited in the Y direction, and in the third group of tests the structure is excited in a random direction. To validate the applicability of the proposed SHM system regardless of the structural state, damage is introduced by loosening the plate-to-column connections of one side of the structure, and the same sets of tests are repeated. The selected peaks and their corresponding frequencies of all tests are shown in Table 1, Table 2, and Table 3.

## Results and discussion

In the laboratory tests, the fundamental (first) mode of vibration is successfully identified by the wireless SHM system in all tests. With respect to higher modes of vibration, in some tests the mode shapes are identifiable, whereas in other tests no stable mode shapes are extracted.

**Table 1.** Selected peaks for the first group of tests (excitation in X direction)

| Undamaged X direction | | | | | | Damaged X direction | | | | | |
|---|---|---|---|---|---|---|---|---|---|---|---|
| Test 1 | | Test 2 | | Test 3 | | Test 1 | | Test 2 | | Test 3 | |
| Peaks | $f$(Hz) | Peaks | $f$(Hz) | Peaks | $f$(Hz) | Peaks | $f$(Hz) | Peaks | $f$(Hz) | Peaks | $f$(Hz) |
| 1 | 2.32 | 1 | 2.32 | 1 | 2.32 | 1 | 1.53 | 1 | 1.59 | 1 | 1.53 |
| 2 | 7.45 | 2 | 7.32 | 2 | 7.39 | 2 | 4.46 | 2 | 7.93 | 2 | 4.46 |
| 3 | 18.37 | 3 | 18.43 | 3 | 18.62 | 3 | 7.87 | 3 | 4.52 | 3 | 7.87 |
| 4 | 20.63 | 4 | 19.65 | 4 | 19.90 | 4 | 18.92 | 4 | 19.10 | 4 | 19.04 |
| 5 | 32.29 | 5 | 29.05 | 5 | 29.79 | 5 | 42.72 | 5 | 42.05 | 5 | 42.54 |

**Table 2.** Selected peaks for the second group of tests (excitation in Y direction)

| Undamaged Y direction | | | | | | Damaged Y direction | | | | | |
|---|---|---|---|---|---|---|---|---|---|---|---|
| Test 1 | | Test 2 | | Test 3 | | Test 1 | | Test 2 | | Test 3 | |
| Peaks | f(Hz) | Peaks | f(Hz) | Peaks | f(Hz) | Peaks | $f$(Hz) | Peaks | $f$(Hz) | Peaks | $f$(Hz) |
| 1 | 2.87 | 1 | 2.81 | 1 | 2.81 | 1 | 1.83 | 1 | 1.83 | 1 | 1.83 |
| 2 | 8.00 | 2 | 8.48 | 2 | 6.65 | 2 | 2.08 | 2 | 5.43 | 2 | 5.49 |
| 3 | 16.97 | 3 | 18.01 | 3 | 8.06 | 3 | 7.26 | 3 | 7.26 | 3 | 7.32 |
| 4 | 19.65 | 4 | 19.84 | 4 | 18.25 | 4 | 9.09 | 4 | 9.16 | 4 | 9.22 |
| 5 | 31.13 | 5 | 30.21 | 5 | 31.25 | 5 | 27.16 | 5 | 18.80 | 5 | 30.82 |

**Table 3.** Selected peaks for the third group of tests (excitation in random directions)

| Undamaged random direction | | | | | | Damaged random direction | | | | | |
|---|---|---|---|---|---|---|---|---|---|---|---|
| Test 1 | | Test 2 | | Test 3 | | Test 1 | | Test 2 | | Test 3 | |
| Peaks | $f$(Hz) | Peaks | $f$(Hz) | Peaks | $f$(Hz) | Peaks | $f$(Hz) | Peaks | $f$(Hz) | Peaks | $f$(Hz) |
| 1 | 2.32 | 1 | 2.26 | 1 | 2.26 | 1 | 1.53 | 1 | 1.53 | 1 | 1.46 |
| 2 | 2.93 | 2 | 2.87 | 2 | 2.87 | 2 | 1.83 | 2 | 1.83 | 2 | 1.83 |
| 3 | 6.59 | 3 | 6.41 | 3 | 5.00 | 3 | 2.38 | 3 | 2.75 | 3 | 5.43 |
| 4 | 7.51 | 4 | 8.06 | 4 | 6.41 | 4 | 4.21 | 4 | 2.32 | 4 | 7.20 |
| 5 | 18.31 | 5 | 18.13 | 5 | 10.01 | 5 | 7.20 | 5 | 7.08 | 5 | 8.42 |
| 6 | 20.51 | 6 | 19.90 | 6 | 18.25 | 6 | 8.42 | 6 | 8.48 | n/a | n/a |
| 7 | 31.31 | 7 | 30.09 | 7 | 20.02 | 7 | 27.71 | 7 | 19.29 | n/a | n/a |

## Fundamental mode of vibration

The fundamental mode of vibration is accurately extracted. Despite the full elastic and inertial symmetry of the structure, which would yield equal eigenfrequencies in both directions, it is observed that the fundamental mode of vibration is translational in the X direction at a frequency of approximately $f_{1x,initial}$ = 2.24 Hz for the initial state and $f_{1x,damaged}$ = 1.51 Hz for the damaged state. The deviation of the eigenfrequencies between the X and the Y direction is attributed to structural imperfections. The mode shape coordinates for the fundamental mode at the initial state are summarized in Table 4; the coordinate distribution is similar in the damaged state. The X plane of the fundamental mode shape is plotted in Figure 3. The first mode shape in the Y direction is of similar pattern at approximately $f_{1y,initial}$ = 2.90 Hz.

**Table 4.** Coordinates of fundamental mode shape

| Story | First group of tests – excitation in X direction | | | | | |
|-------|--------|--------|--------|--------|--------|--------|
| | Test 1 | | Test 2 | | Test 3 | |
| | X | Y | X | Y | X | Y |
| 0 | 0.00 | 0.00 | 0.00 | 0.00 | 0.00 | 0.00 |
| 1 | 0.19 | 0.03 | 0.10 | 0.01 | 0.19 | 0.00 |
| 2 | 0.46 | 0.04 | 0.52 | 0.01 | 0.49 | 0.00 |
| 3 | 0.81 | 0.07 | 0.79 | 0.05 | 0.82 | 0.04 |
| 4 | 1.00 | 0.12 | 1.00 | 0.13 | 1.00 | 0.12 |
| $f$(Hz) | 2.30 | | 2.24 | | 2.24 | |

From the results of Table 4, it is observed that the extraction of the fundamental mode shape is consistent in all tests. Furthermore, the fundamental mode shape does not appear to be purely translational in the X direction as would be expected from the theory of structural dynamics, but there is non-negligible motion in the Y direction as well.
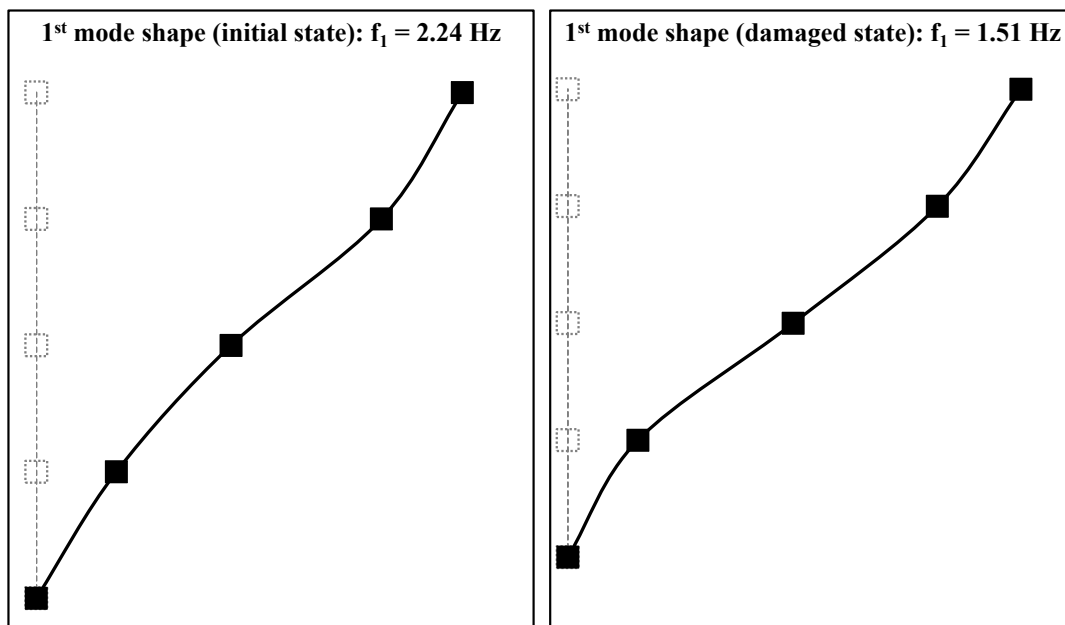


Figure 3. Fundamental mode shape (X plane)

**Higher modes of vibration**

Due to inaccuracies and to the interference of external factors in the measured acceleration response data, the results concerning the extraction of higher modes are not as consistent as in the fundamental mode. The extracted mode shapes of the second and third modes of vibration in the X direction are illustrated in Figure 4 and Figure 5.

As can be seen in Figure 4 and Figure 5, the second mode shape is characterized by one "nodal" point (zero crossing), while in the third mode shape there are two nodal points. Although these results are in accordance with the theory of structural dynamics, it cannot be directly assumed that the extracted mode shapes are the $2^{nd}$ and $3^{rd}$ purely translational modes, respectively, in the X direction. Rather, it is not unlikely that the extracted mode shapes resemble the X plane coordinates of torsional mode shapes lying between two successive translational mode shapes. In theory, the distinction of torsional mode shapes is possible by observing the existence of non-negligible motion in both horizontal

directions; however, as has been shown previously, some degree of directional coupling exists in the "purely" translational modes as well, as a result of structural imperfections.

Further investigation of the extracted mode shapes requires the use of more advanced methods for modal identification and/or the development of an elaborate numerical model of the structure.

The extraction of higher mode shapes is not consistent among all conducted tests, in terms of calculated modal coordinates. The reason for such inconsistencies may be primarily attributed to the lack of synchronization among the sensor nodes. In wireless sensor networks and particularly for modal identification, ensuring the synchronization among the sensor nodes is essential for the accurate processing of the collected acceleration response data. The lack of synchronization introduces a phase shift among the acceleration response data sets of different sensors, as shown in Figure 6. Since this phase shift is usually short compared to the fundamental period (inverse of fundamental frequency) of common civil engineering structures, it usually affects higher modes of vibration characterized by higher frequencies and, therefore, shorter periods (comparable to the phase shift itself).
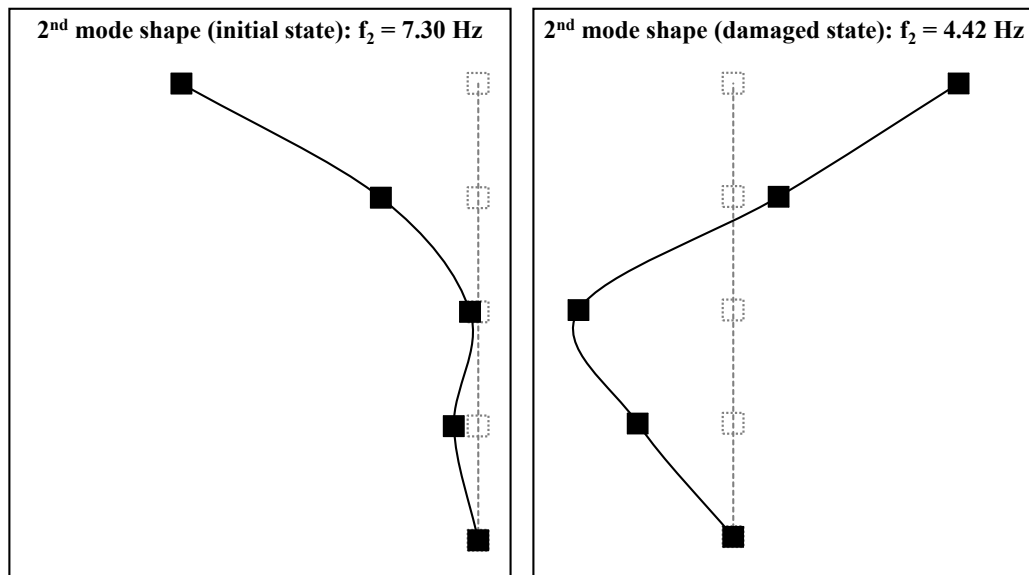


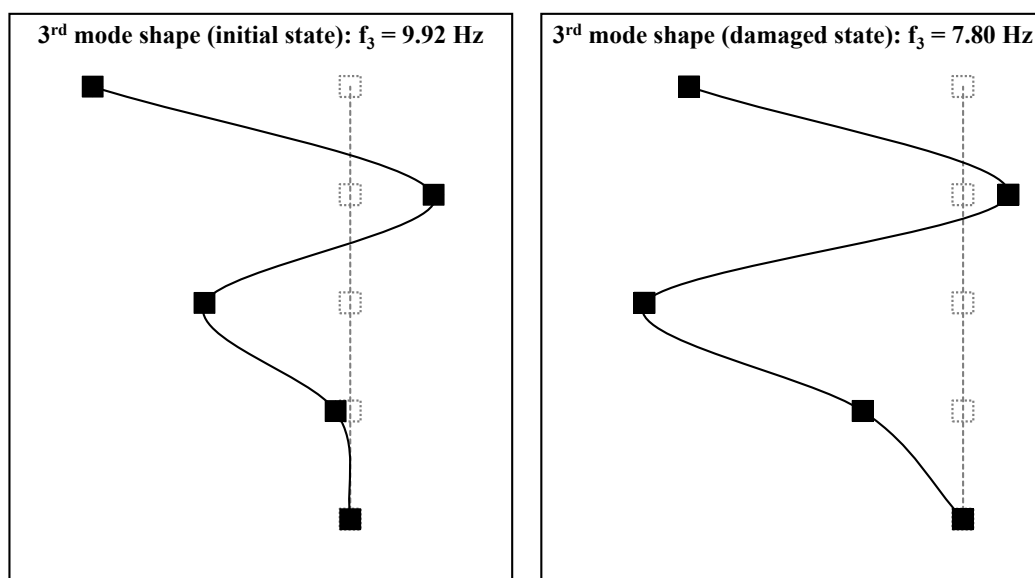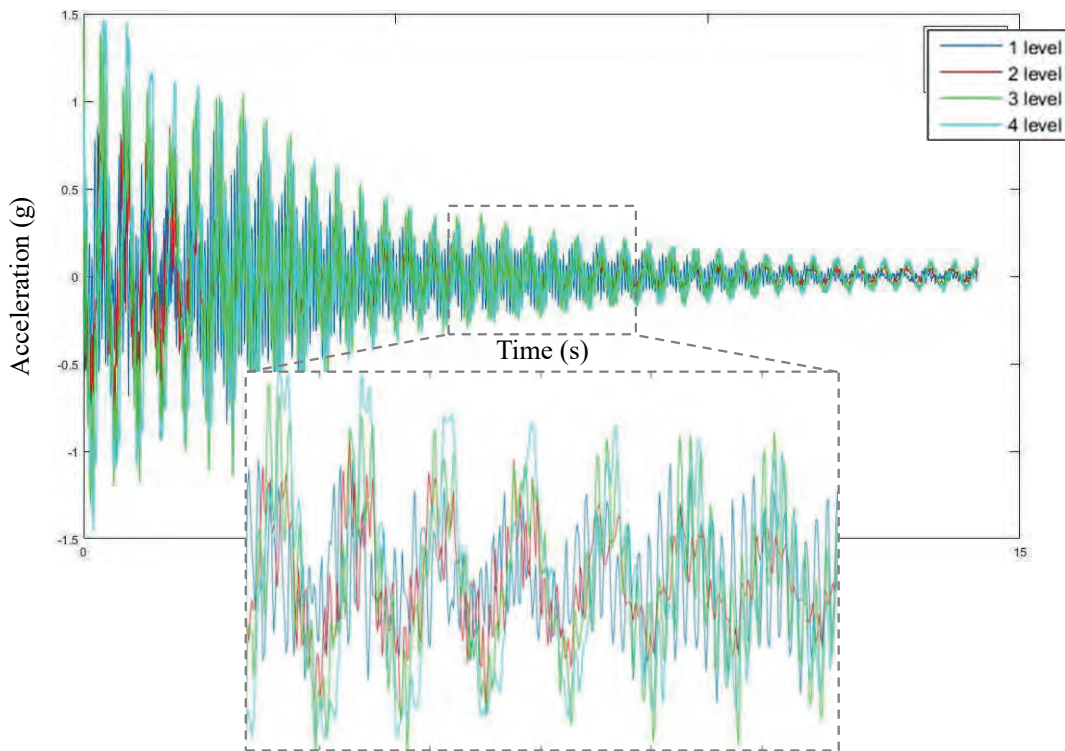**Figure 4.** Second mode shape in X direction



**Figure 5.** Third mode shape in X direction

129

**Figure 6.** Phase shift among the acceleration response data from different stories of the test structure

## Summary and conclusions

Due to the ease of installation and low costs of wireless sensor nodes compared to traditional cable-based systems, wireless sensor networks have been employed in several SHM applications. Since wireless sensor nodes are equipped with processing power, embedded computing is inherent to wireless sensor networks. Embedded computing, in the form of embedded algorithms, is used to reduce the wireless data traffic in wireless sensor networks, which is, however, particularly power-consuming and therefore requires resource-efficient algorithms. In this paper, a wireless SHM system able to perform modal identification using embedded computing has been presented. The identification of structural modes of vibration in the proposed SHM system is achieved distributed-collaboratively. Acceleration response data is first collected by the sensor nodes and transformed into the frequency domain via an embedded fast Fourier transform algorithm. Subsequently, the selection of the highest peaks of the frequency spectrum (peak-picking), corresponding to resonant response, is performed directly on the sensor nodes. To avoid inconsistencies and false peak detections in the peak-picking process, a sufficiently large number of "candidate" peaks is selected and sent to the base station (i.e. a remote server/host computer). Then, the final peaks are interactively selected based on the stability of the candidate peaks. The final peaks are sent to the sensor nodes to retrieve the corresponding Fourier values. The sensor nodes send the Fourier values to the base station, where modal extraction is completed by applying frequency domain decomposition.

The proposed SHM system has been validated in laboratory tests on a four-story frame structure. Three groups of tests, varying the direction of excitation (X-, Y-, and random-direction), have been conducted. One sensor nodes has been placed at the center of each story. Each test has been repeated three times for verification. The tests have yielded the fundamental (first) mode of vibration in both X and Y directions with satisfactory accuracy. However, while extracting higher modes of vibration has been possible, the results have not been characterized by the same level of consistency as in the

fundamental mode. The inconsistencies in the extraction of higher modes of vibration are attributed to a phase shift among the acceleration response data sets of different stories, which is comparable to the relatively shorter periods of higher modes.

In general, the results have shown that accurate modal identification can be conducted in wireless SHM systems in a distributed-collaborative manner. Future work may include methods for improving the synchronization among the acceleration response data sets to facilitate the extraction of higher modes, as well as ways to distinguish between translational and torsional modes.

## Acknowledgments

## References

Brincker, R., Andersen, P. and Zhang, L. (2000). "Modal identification from ambient responses using frequency domain decomposition". In Proc.: 18th International Modal Analysis Conference (IMAC), San Antonio, TX, USA, 07/02/2000.

Cooley, J. W. and Tukey, J. W. (1965). "An algorithm for the machine calculation of complex Fourier series". *Mathematics of Computation*, **19**(90): 297-301.

Dragos, K. and Smarsly, K. (2015). "Embedding numerical models into wireless sensor nodes for structural health monitoring". In Proc.: 10th International Workshop on Structural Health Monitoring (IWSHM), Stanford, CA, USA, 01/09/2015.

Dragos, K. and Smarsly, K. (2017). "Decentralized infrastructure health monitoring using embedded computing in wireless sensor networks". In: Sextos, A. & Manolis, G. D. (eds.). Dynamic Response of Infrastructure to Environmentally Induced Loads. S. 183-201, Cham, Switzerland: Springer International Publishing AG.

JAMA – A Java Matrix Package. Available at http://math.nist.gov/javanumerics/jama (Accessed: 30/08/2016).

Kane, M., Zhu, D., Hirose, M., Dong, X., Winter, B., Häckel, M., Lynch, J. P., Wang, Y. and Swartz, A. (2014). "Development of an extensible dual-core wireless sensing node for cyber-physical systems". In Proc.: SPIE, Sensors and Smart Structures Technologies for Civil, Mechanical, and Aerospace Systems, San Diego, CA, USA, 09/03/2014.

Lei, Y., Shen, W. A., Song, Y. and Wang, Y. (2010). "Intelligent wireless sensors with application to the identification of structural modal parameters and steel cable forces: from the lab to the field". *Advances in Civil Engineering* **2010**: 1-10.

Oracle Corp. (2010). Sun SPOT eDEMO Technical Datasheet, 8th edition. Sun Labs, CA, USA.

Semperlotti, F. (2009). "Structural Damage Detection Via Nonlinear System Identification and Structural Intensity Methods". Ph. D. Dissertation, The Pennsylvania State University, USA.

Wang, Y., Schwartz, A., Lynch, J. P., Law, K. H., Lu, K. C. and Loh, C. H. (2006). "Wireless feedback structural control with embedded computing". In Proc.: SPIE 11th International Symposium on Nondestructive Evaluation for Health Monitoring and Diagnostics, San Diego, CA, USA, 26/02/2006.

Zimmerman, A., Shiraishi, M., Schwartz, A. and Lynch, J. P. (2008). "Automated modal parameter estimation by parallel processing within wireless monitoring systems". *ASCE Journal of Infrastructure Systems*, **14**(1): 102-113.

# Machine Learning for Segment-based Change Detection in Very High-resolution Optical Satellite Imagery

BORRERO Maria Claudia [a], BUDAK Ezgi [b], ERKMEN Kadir Can [c], GHALANDARI Mohammadtaher [d]

[a] *Bauhaus-Universität Weimar*

[b] *Middle East Technical University*

[c] *Çankaya University*

[d] *Middle East Technical University*

KERSTEN Jens

*Chair of Computer Vision in Engineering, Bauhaus-University Weimar, Germany*

## Abstract

Remotely sensed imagery is a rich source of information and can contribute to various applications, for example land cover classification as well as rapid mapping for disaster and crisis management support. A central issue is the reliable detection of relevant changes based on images from two or more dates. In this paper, a segment-based change detection approach for *very high-resolution* (VHR) optical satellite imagery is presented and evaluated. The approach utilizes two well-known non-parametric machine-learning techniques: mean-shift clustering for segmentation and *support vector machines* (SVM) for classification. The final goal is to identify destroyed or damaged buildings and infrastructure after the heavy earthquake in L'Aquila, Italy on April 6, 2009. An accuracy assessment and a comparison of the results to those obtained by traditional pixel-based approaches demonstrates the superiority of the segment-based method. In order to further enhance the results, several additional features like contextual information and segment shapes could be integrated.

## Introduction

*Change detection* (CD) is the process of identifying differences in the state of an object or phenomenon by observing it at different times (Singh, 1989). Remote sensing is a powerful source of information to detect changes on the earth's surface through space-borne sensors (Ramachandra & Kumar, 2004). CD can provide a better understanding of the relationships and interactions between human and natural phenomena and can provide guidance in the management of the use of resources. Different temporal and spatial resolutions allow scientists to monitor and detect changes over a broad scale and help planners to obtain or maintain information on various phenomena, such as shifting agricultural patterns, crop stress, disaster monitoring, land use and land cover changes (Rogan & Chen, 2004). For spatial analyses and visualizations, e.g. measuring and mapping the land cover change between two or more points in time, a *geographic information system* (GIS) is a useful tool. It has the ability to incorporate various types of data into a CD platform (Lu et al., 2004). For example, the use of multiple layers, such as classified images, topographical maps, soil maps and hydrological maps, provides a greater ability to extract useful information about the changes over a particular area. Moreover, GIS can help to measure the trends in these changes by modeling the available data and using statistical and analytical functions. The benefit of GIS is the provision of different outputs in

different formats (e.g. maps or tables), which allows users to select the appropriate output for extracting the desired information.

Remotely sensed data and GIS are widely used for detecting land use and land cover changes. Many studies have attempted to use remotely sensed data and GIS to address land use CD e.g. (Brondizio et al., 1994; Kuemmerle et al., 2006; Pelorosso et al., 2009; Thapa & Murayama, 2009). A variety of procedures or methods of remote sensing technologies are used to detect land use and land cover changes. Some studies have actually utilized remote sensing techniques and others have integrated remotely sensed data with GIS data e.g. (Michalak, 1993; Weng, 2001; Rogan & Miller, 2007*)*. In addition, many studies have reviewed and summarized various CD techniques (Singh, 1989; Rogan & Chen, 2004; Mouat et al., 1993; Deer, 1995, Hussain et al., 2013).

Several different CD techniques for remotely sensed images have been developed which each comes in handy depending on the requirements and conditions. However, the selection of the most suitable method or algorithm for CD is not easy in practice (Lu et al., 2004). Researchers have made enormous efforts in developing CD methods including both the traditional pixel-based (Mas, 1999) and more recently, the object- or segment-based approaches (Araya & Hergarten, 2008).

In this work, an object-based approach is utilized in order to detect damaged and destroyed buildings based on two QuickBird satellite images, a pre-disaster scene from 2006 and a scene covering the same region acquired immediately after the earthquake in L'Aquila (Italy), April 2009. With a spatial resolution of 60 cm, pixel-based approaches are known to produce noisy results. Therefore, a mean-shift segmentation is utilized in order to group similar pixels in the first step. Instead of single pixels, all following analysis steps are using the image segments (super-pixels). With the goal of identifying destroyed and damaged buildings and infrastructure, the color and texture information of the super-pixels will be analyzed. For the classification of changes, *support vector machines* (SVM) are used in this work. This discriminative method is known to provide good results, even in case of only few available training samples. Compared to the supervised maximum-likelihood approach, no assumptions regarding the parametrization are introduced. Hence, several spectral classes can easily be grouped, which makes the CD faster and more user-friendly.

*Post-classification comparison* (PCC) and *multi-date direct comparison* (MDC) are two major CD methods. Whereas in PCC the changes are identified based on the land cover classification of the input images, the changes are directly classified in MDC by using a stack of multiple images as input. In this study, the PCC approach is used and compared to the pixel-based PCC and MDC results obtained in (Cerovecki et al., 2015).

## Pixel- vs. Object-based Analysis

Among various available CD strategies, in this study a segment-based approach is employed and compared with the results of traditional pixel-based strategies. Despite the fact that a segment-based analysis might be more complex to implement compared to pixel-based approaches, it is known to be more suitable for the analysis and classification of VHR satellite data and therefore is able to yield more accurate results (Blaschke, 2010). Pixel-based approaches were successfully used for the analysis of low and medium resolution imagery up to a ground sampling distance of 30 meters. Each pixel represents the mean reflected light from a $30 \times 30$ m area of the surface, which is suitable for detecting general classes, like vegetation, water and settlement areas. A higher spatial resolution enables analyses that are more detailed but in turn, the data is also larger and more complex. The

higher the spatial resolution, the higher the intra-class variations and the lower the inter-class similarities. For example, with VHR data, we are able to identify rooftops. However, the spectral variations of pixels within this class can be very high, since rooftops often consist of several different additional materials, like windows and solar panels. In order to handle these high variations, spatially adjacent pixels are grouped to non-overlapping segments for example based on a homogeneity criterion or more complex methods, as the multi-scale approach proposed in (Blaschke & Strobl, 2001). Instead of single pixels, these image segments are then used for further analysis. Whereas for each pixels the spectral information is available, for each image segment it is likely to retrieve additional features such as the mean spectral values and higher moments, shape, size, radius as well as texture. Furthermore, for land cover and land use applications, contextual relations between the segments can be integrated into the analysis. However, it has to be noted that the accuracy of segment-based analysis methods strongly depends on the quality of the segmentation.

## Datasets and Software

Two QuickBird scenes covering the city of L'Aquila, Italy, acquired on September 4, 2006 (Figure 1) and April 8, 2009 (DigitalGlobe, 2009) are used in this study. The pan-sharpened scenes have a ground sampling distance of 0.6 m, cover an area of 25 km² and consist of four spectral bands (R = red, G = green, B = blue and NIR = near infrared).



**Figure 1.** Input pre-disaster QuickBird scene (DigitalGlobe, 2006).

For detecting the changes in the images QGIS software (QGIS, 2015), previously known as "Quantum GIS", was used. QGIS is a cross-platform and open-source desktop GIS application that provides data viewing, editing, analysis and mapping capabilities. It allows creating maps with many layers using different map projections. Several raster formats are supported and the software can perform georeferencing of images (Treglia, 2015).

# Change Detection Workflow

In this study, a segment-based CD workflow is proposed. It consists of the following main steps: Pre-processing, mean-shift image segmentation, image classification using SVMs, CD and accuracy assessment. Since a PCC approach for CD is used, the first three steps are applied on both pre-scene and post-scene individually and the obtained classification results are used in PCC. The complete workflow (Figure 2) is described in the following.
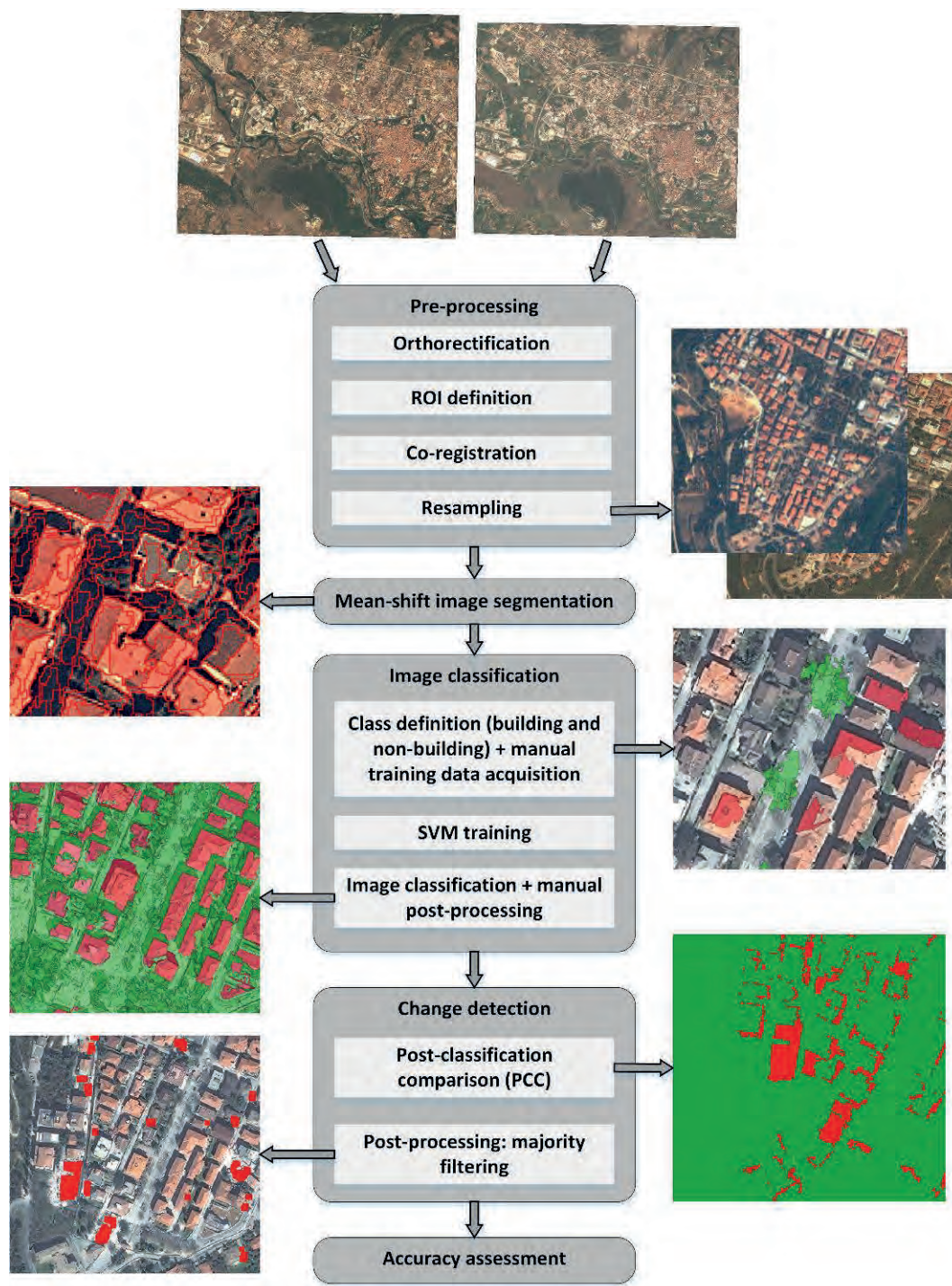


**Figure 2.** Change detection workflow.

## Pre-processing

The topographical variations of the earth's surface as well as the tilt of the satellite sensor affect the position on which objects are mapped in satellite images. The more topographically diverse the landscape, the more distortion inherent to the image. As image distortions are an inevitable source of errors especially in CD, they have to be removed or reduced as much as possible. Hence, the first step is orthorectification (Figure 3), which describes the process of removing perspective distortions for each image pixel individually (GIS dictionary, 2015).

For each differential rectified destination pixel (4) on the discreet grid in Figure 3, the corresponding elevation data point (1) of the terrain is projected into the image plane (3) using the exterior orientation of the sensor (2). The color values of the new pixel in (4) are interpolated from the sub-pixel position in (3) using the neighboring color values (resampling). In this study, the ASTER global digital elevation model (GDEM) V2 available at (ASTER, 2015) with a ground sampling distance of 30 m was used.

In order to reduce the computational loads and the complexity of CD for this study, a *region of interest* (ROI) is defined in the orthorectified images (Figure 4). All further processing steps are applied on this sub-image.
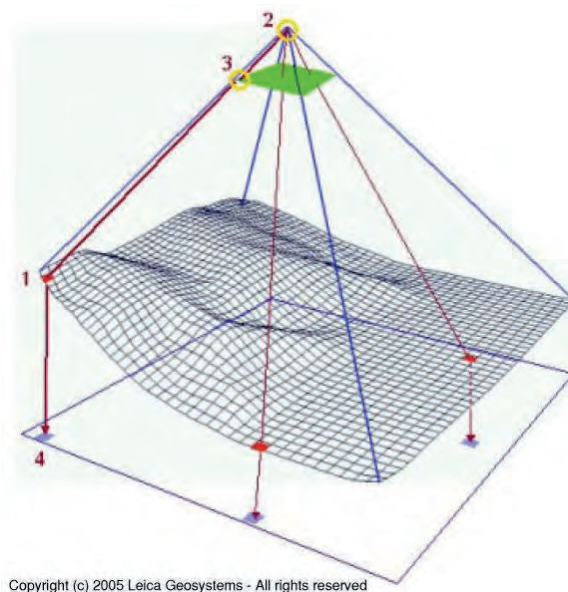
**Figure 3.** Orthorectification process.

Whereas pixel displacements due to sensor orientation and topography are removed by the orthorectification step, it is still possible that the two scenes do not exhibit perfect overlay due to inaccuracies of the provided satellite metadata. Therefore, a further image-to-image- or co-registration is required, which geometrically transforms one of the images to have perfect overlay with the second one. Similar to the orthorectification, this step has a crucial value since the CD results depend on the registration quality. A four-parameter 2D-Helmert transform is used for this step, where at least two corresponding points have to be identified manually in the two scenes in order to estimate the transformation parameters (two translations, one rotation and a scale factor). The best matching accuracy can be achieved by providing a higher number of corresponding points covering the entire image area.
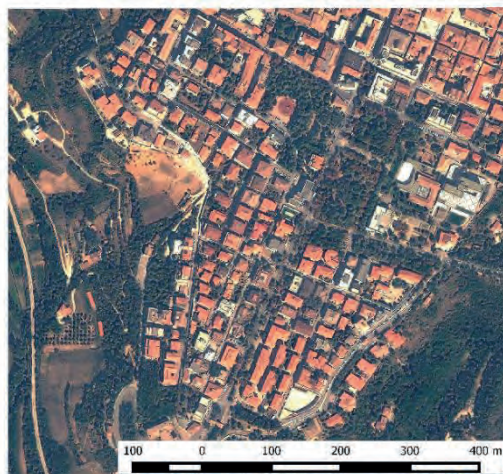
**Figure 4.** Defined ROI.

Since no detailed information regarding the objects on top of the earth's surface, for example buildings, are incorporated into the orthorectification step, the rooftops and other objects usually still are displaced in the images according the sensor pose and the height of the object. Hence, it is crucial to use corresponding points located on the ground for the registration. A Helmert transformation in QGIS software can be applied easily with the „Georeferencer" plugin.

In order to enable comparisons and analyses down to the pixel-level, the spatially transformed image is finally resampled with respect to the reference image using a nearest neighbor interpolation. After this step, both scenes have exactly the same spatial resolution and pixel positions.

## Mean-shift Image Segmentation

Subdividing an image into non-overlapping segments can generally be done by grouping spatially adjacent pixels. By assigning different labels on groups of pixels, they are categorized into sets (segments) which helps to utilize their characteristics for further analyses. Hence, image segmentation can be seen as a first step in image understanding, since it aims on finding boundaries of semantic objects or object parts. In this paper, the non-parametric mean-shift algorithm is used. A pixel of a color image (R, G, B) can be mapped to a point in a corresponding 3D-feature space. Mapping all pixels of an image into this space, we are interested in identifying the local maxima of this density. The mean-shift algorithm starts at every pixel location in the feature space and iteratively computes the centroid of the local neighborhood of feature space points around the current position. A local maximum is found when the centroid does not move anymore while iterating. All starting pixels (feature space points) which converge to the same maximum centroid are spatially adjacent and will be part of the same image segment. A preliminary edge-aware smoothing helps to reduce the number of local maxima and therefore bigger segments can be obtained.

The mean-shift algorithm is valuable in many aspects. It is general, application-independent, robust against outliers and model-free, i.e., no assumptions regarding the prior shape (spherical, elliptical, etc.) of data clusters and also the number of clusters have not to be introduced. Furthermore, it uses just a single parameter, which defines the radius for the centroid computation (window size) in the feature space domain. However, selecting this parameter may not be trivial since it directly affects the size and number of output segments. It has to be noted that this method also does not scales well with respect to the number of feature space dimensions.

**Image Classification using Machine Learning**

Machine learning is studied and investigated in detail under the umbrella of pattern recognition and artificial intelligence. Based on exploration and algorithm construction, machine learning enables making predictions on data. The logic behind these algorithms is simulation of data models as predictions or decisions, which is different from static linearization. Machine learning and computational statistics are tied with each other for estimating predictions using computers. The application of machine learning is in a broad range of computing tasks where objectives of design and programming of algorithms is supposed to be infeasible. Image analysis, search engines and computer vision are some particular examples in this field.

As a member of machine learning methods, SVMs can be used to analyze data for classification and regression analysis. In terms of classification, an SVM finds an optimal feature space hyperplane, which can be used as a decision boundary between two or more classes. This requires a set of labelled training data inputs that are fed to a training algorithm. The simplest form of SVMs are linear binary classifiers where a linear decision boundary is estimated and two labels are possible. In parameter estimation (quadratic optimization problem), the margin between the positive and negative training samples is maximized, which helps to avoid overfitting.

For more complex classification tasks, i.e., where a linear function does not meet the requirements, a so-called kernel trick can be used. The idea behind is the assumption that the input space can always be mapped into a higher dimensional feature space where the training set is linearly separable. Instead of explicitly computing this transform, a corresponding kernel function is used, which in turn leads to non-linear decision boundaries in the original feature space.

In this study, the two input images are classified into two classes of interest: *building* and *non-building*. For each class, a set of approximately 70 image segments are provided for training. Furthermore, an 8-dimensional feature space (mean and standard deviation of the input channels R, G, B and NIR) is used. For further information on how to apply mean-shift segmentation and SVM image classification in QGIS, the reader is kindly referred to (Fehrmann, 2016).

**Change Detection**

After the single images are classified individually according to the defined classes, the changes of interest can easily be obtained by simply searching for the corresponding changes of the thematic classes. This process is known as PCC. In Figure 5 exemplary results of classification and PCC are shown.

In the pre-scene, a container is present and in the post-scene more artificial objects are visible (Figure 5, left and center). All changes from non-artificial classes to artificial objects are marked in red in the CD result (Figure 5, right). Since the container was already present in the pre-scene, it is not detected as changed. The quality of CD obviously depends on the accuracy of geometric co-registration as well as the quality of the classification results. Due to some outliers as result of the used pixel-based classification and CD in this example, majority filtering is utilized in order to decrease the false positive ratio.
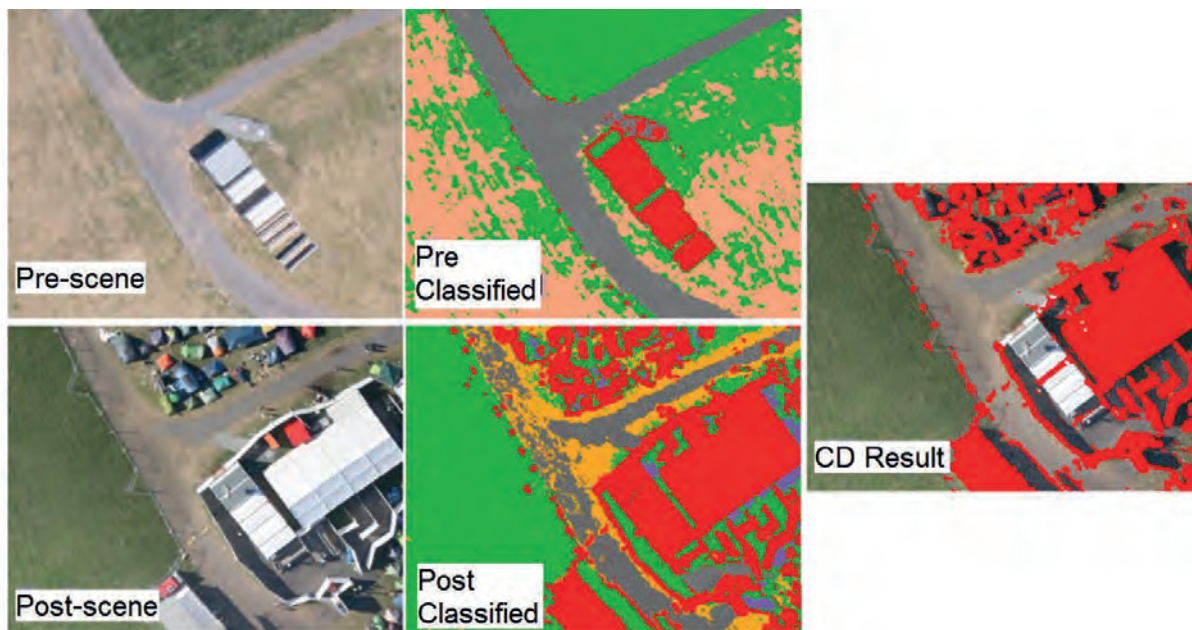
**Figure 5.** Detection of changes in PCC: artificial structures in the pre and post scenes (red, center images) and the corresponding changes w.r.t. this class (red, right image).

## Post-processing

Classifying VHR image pixels individually often leads to salt-and-pepper noise, which can be reduced by applying morphological operators or majority filtering. In segment-based approaches this noise is expected to be reduced. However, if the introduced features and the classifier itself are not able to achieve a separation of the defined classes due to spectral similarities, misclassifications are likely to occur. Therefore, the result labels of obviously misclassified image segments are corrected manually in a post-processing step for this study.

# Results and Discussion

In this paper, the proposed workflow (Figure 2) is applied in order to detect damaged and destroyed buildings after the earthquake in L'Aquila, Italy, on April 6, 2009. After the pre-processing of both input images, a nearly perfect co-registration was achieved. Thanks to nearly identical sensor configurations, acquisition times and seasons, also the rooftops and the shadows were almost identical. This clearly helps to avoid false positives in PCC.

## Segmentation and SVM Image Classification

According to the tutorial described in (Fehrmann, 2016), the mean-shift segmentation was applied on the co-registered and resampled images. Using the parameters suggested in the tutorial lead to quite reasonable and useful segmentations.

Since our aim is to identify the destroyed and damaged buildings, only two classes of interest, *building* and *non-building*, are defined. Instead of manually digitizing image segments for the SVM training, already existing segments can be labelled (Figure 6). This drastically reduces the manual workload compared to pixel-based supervised approaches.

**Figure 6.** Example of post-scene training areas: buildings (red) and non-buildings (green).

In Figure 7, the SVM classification result obtained with the training data from Figure 6 is shown. Even though segment-based results visually tend to be very accurate, some misclassifications could be identified. Hence, a post-processing was conducted in which misclassified labels were corrected manually. In order to restrict the manual interaction to a minimum, a maximum of five minutes was allowed for this step.



**Figure 7.** Example SVM classification result: buildings (red) and non-buildings (green).

## Detected Changes

The aim is to detect changes that represent damaged and collapsed buildings. As explained above, the SVM classifier is not able to perfectly separate the classes *building* and *non-building* due to spectral similarities, which could not be resolved with the used features. Furthermore, the quality of CD is affected by changes, which happened over time but are not a result of the disaster itself. Without additional information, this ambiguity cannot be resolved and its impact is getting higher the larger the time period between the acquisitions is. Another source for confusions is the shift of the rooftop positions due to different sensor poses also depending on the position of the buildings as well as their height. The resulting (but in this study quite thin) linear changes erroneously detected at building borders are reduced using a majority filter.

For the PCC itself a simple comparison of pixel values from two images was performed with the help of a self-implemented MATLAB script. The changes from segments of the class *building* in the pre-scene to *non-building* in the post-scene are shown in Figure 8 (marked in red).

Due to some inaccuracies and problems in separating spectral classes, also the final CD result contains some wrong detections. In Figure 9, examples for correct and incorrect classifications of changes are shown.

These visual examples indicate that there is room for improvements in several stages of the processing. Due to the nature of segment-based analysis, misclassifications tend to have a larger impact to the final result compared to pixel-based approaches, simply because of the bigger size of the image segments. In pixel-based analysis, erroneous pixels can be filtered in a relatively easier manner.

This is a bit more complicated in segment-based analysis. Even though the theory how to achieve a filtering of image segments is quite clear, it was not possible to implement this in QGIS within the study period. The CD results presented here may therefore serve as a support for the identification and localization of destroyed infrastructure in large satellite images by visual analysts.

## Accuracy Assessment

Due to limitations in time, the *accuracy assessment* (AA) was only performed for CD and not for the single classification results individually. Similar to the manual labeling done in the SVM training step, an additional set of test segments has to be defined for this task. In order to get reliable AA results, these regions should not be used in the training procedure. In particular, this strategy helps to discover overfitting behavior of the used classifier. Furthermore, the percentage of tested segments for each class should be similar to the number of segments actually representing this class in the image.



**Figure 8.** Changes detected usıng PCC method.



**Figure 9.** Left: Correctly classified changes (red). Right: Not correctly classified changes (red).

**Table 1.** Accuracy assessment results for the proposed segment-based PCC approach (2016) compared to the pixel-based results obtained in (Cerovecki, et al., 2015) using PCC and MDC.

| Accuracy | Class | 2015 (PCC) | 2015 (MDC) | 2016 (PCC) |
|---|---|---|---|---|
| OA [%] | All | 94.20 | 96.57 | **98.35** |
| PA [%] | Changed | 61.54 | 63.96 | **76.22** |
| | Unchanged | 97.24 | 99.60 | **100.00** |
| UA [%] | Changed | 67.53 | 93.77 | **100.00** |
| | Unchanged | 96.44 | 96.74 | **98.26** |

According to that, approximately 500 test segments were manually defined in this study, whereas the number of changed segments was significantly lower than the non-changed segments.

Based on the known class memberships of the test segments as well as the predicted class label from the CD analysis, a square 2×2 confusion matrix can be obtained. Usually, the rows of this matrix represent the true test instances, whereas the columns are related to the predicted changes using the SVM. A perfect classifier would result in a diagonal confusion matrix. The more incorrect predictions we observe, the more and higher off-diagonal elements can be observed. The *overall accuracy* (OA) can be derived by counting all correctly classified CD test segments and dividing this sum by the total number of all test segments. In order to derive more detailed class-related information, the user's and producer's accuracy can be computed for each class. The *producer's accuracy* (PA) refers to the probability that a certain land cover of an area on the ground is classified as such, while the *user's accuracy* (UA) refers to the probability that a segment labeled as a certain land cover in the map is really this class. The obtained overall accuracy of the detected changes in this study is 98.35 %, which shows a significant improvement compared to the results obtained in (Cerovecki, et al., 2015, Table 1). In this preceding study, a pixel-based PCC as well as a MDC were compared.

The results in Table 1 show that 76.22 % of all reference segments could correctly be detected as changed and 100% of all reference segments classified as changed were reference segments from that class. This clearly indicates that false positive detections occur (see also Figure 9). Because of this, it can be pointed out that this method should be used to highlight potentially destroyed areas as part of a decision support workflow.

## Conclusion and Outlook

In this study, a segment-based CD workflow using non-parametric machine learning methods for segmentation and classification is proposed and evaluated in the context of detecting destroyed buildings in VHR satellite images. A segment-based approach is chosen since it is known to be better suited than traditional pixel-based methods for the analysis of VHR satellite imagery. The obtained results and experiences demonstrate that the quality of the results directly depends on various components: (1) An accurate orthorectification and image co-registration is essential for CD. (2) Since man-made objects are not captured in DEMs used for orthorectification, the sensor configuration, acquisition time and season should be nearly identical in order to ensure the same displacements of high buildings as well as similar shadow arrangements. (3) The accuracy of land cover classification and detected changes strongly depends on the quality of image segmentation. In general, an over-

segmentation yields better results than under-segmentations, since in the latter case potential objects of interest and other adjacent objects are merged to bigger segments, which makes the classification of the objects of interest impossible. On the other hand, features like the standard deviation of pixels computed from very small segments tend to be significantly less descriptive. Hence, a balanced segment size has to be found. (4) SVMs implemented in QGIS are user-friendly and easy to use. The non-parametric approach allows defining arbitrary thematic classes without taking into account their spectral distribution in the feature space domain. (5) The used features for land cover classification in this study were not able to perfectly distinguish between the classes due to spectral similarities. Hence, using further segment-related features, like texture and shape parameters, as well as the incorporation of contextual information, for example the expected position of shadows from buildings, would further increase the detection accuracies. (6) If the images for comparison have a very long time delay (several years), it might be very difficult to distinguish between changes over time (e.g. new or stripped down buildings) and those changes we are interested in (e.g. buildings that are partially or completely destroyed by external forces).

The proposed workflow fails in some cases where spectral ambiguities could not be resolved. Hence, the incorporation of additional features is strongly recommended for future works. In general, the results of the CD accuracy assessment indicate that the segment-based approach produces better results than pixel-based approaches for the used dataset. Since in MDC no individual land cover classification of the pre- and post-scene is required and the results from 2015 are better than for PCC, it should be investigated with the segment-based approach in future works.

Overall, it can be concluded that although CD based on machine learning methods requires some experiences in choosing parameters and training data, the proposed workflow is significantly less time consuming and requires less domain knowledge than traditional supervised classification approaches. The proposed workflow has shown to be a good indicator for the most likely areas suspicious of experiencing change. While it can be quite tedious to identify such changes in very large satellite images manually, the result of analysis narrows this quest down to a practical level in terms of decision support.

## References

Araya, Y.H., Hergarten, C. (2008). A comparison of pixel and object-based land cover classification: a case study of the Asmara region, Eritrea. In: *WIT Transactions on the Built Environment, Geo-Environment and Landscape Evolution III,* **100**, pp. 233-243.

ASTER (2015). http://gdem.ersdac.jspacesystems.or.jp/, accessed August 10, 2015.

Blaschke, T. (2010). Object based image analysis for remote sensing. *ISPRS Journal of Photogrammetry and Remote Sensing*, **65**, pp. 2-16.

Blaschke, T., Strobl, J. (2001). What's wrong with pixels? Some recent developments interfacing remote sensing and GIS. GIS, **14**(6), pp. 12-17.

Brondizio, E.S., Moran, E.F., Mausel, P., Wu, Y. (1994). Land Use Change in the Amazon Estuary: Patterns of Caboclo Settlement and Landscape Management. *Human Ecology*, **22** (3), 249-278.

Cerovecki, A., Gharahjeh, S., Harirchian, E., Ilin, D., Khotnikova, K., Kersten, J. (2015). Evaluation of Change Detection Techniques using Very High Resolution Optical Satellite Imagery. Technical Report, Summer School 2015, Bauhaus-Universität Weimar.

Deer, P. (1995). Digital Change Detection Techniques in Remote Sensing. *DSTO-TR-0169, Technical Report*.

DigitalGlobe (2006). QuickBird scene 054594261010_01_P001, Level S2AS, DigitalGlobe, Longmont, Colorado, 09/04/2006.

DigitalGlobe (2009). QuickBird scene 054594261020_01_P001, Level S2AS, DigitalGlobe, Longmont, Colorado, 04/08/2009.

Fehrmann, L. (2016). AWF-Wiki for forest inventory and remote sensing, Universität Goettingen. http://wiki.awf.forst.uni-goettingen.de/wiki/index.php/Object-based_classification_%28Tutorial% 29, accessed August 1, 2016.

GISdictionary (2015).http://support.esri.com/en/knowledgebase/GISDictionary/term/orthorectification accessed August 28, 2015.

Kuemmerle, T., Radeloff. V. C., Perzanowski, K., Hostert, P. (2006). Cross-Border Comparison of Land Cover and Landscape Pattern in Eastern Europe Using a Hybrid Classification Technique. *Remote Sensing of Environment*, **103** (4), pp. 449-464.

Lu, D., Mausel, P., Brondízio, E., Moran, E. (2004). Change Detection Techniques. *International Journal of Remote Sensing*, **25** (12), pp. 2365-2401.

Mas, J. F. (1999). Monitoring land-cover changes: a comparison of change detection techniques. *International Journal of Remote Sensing,* **20**, pp. 139-152.

Hussain, M., Chen, D., Cheng, A., Wie, H., Stanley, D. (2013). Change detection from remotely sensed images: From pixel-based to object-based approaches. *ISPRS Journal of Photogrammetry and Remote Sensing,* **80,** pp. 91–106.

Michalak, W. Z. (1993). GIS in Land Use Change Analysis: Integration of Remotely Sensed Data into GIS. *Applied Geography*, **13** (1), pp. 28-44.

Mouat, D. A., Mahin, G. G., Lancaster, J. (1993). Remote Sensing Techniques in the Analysis of Change Detection. *Geocarto International*, **8** (2), pp. 39-50.

Pelorosso, R., Leone, A., Boccia, L. (2009). Land Cover and Land Use Change in the Italian Central Apennines: A Comparison of Assessment Methods. *Applied Geography*, **29** (1), pp. 35-48.

QGIS (2015). http://www.qgis.org/en/site/, accessed at October 1, 2015.

Ramachandra, T., Kumar, U. (2004). Geographic Resources Decision Support System for Land Use, Land Cover Dynamics Analysis. *Proceedings of the FOSS/GRASS Users Conference*, Bangkok, Thailand.

Rogan, J., Chen D. (2004). Remote Sensing Technology for Mapping and Monitoring Land-Cover and Land-Use Change. *Progress in Planning*, **61** (4), pp. 301-325.

Rogan, J., Miller, J. (2007). Integrating GIS and Remotely Sensed Data for Mapping Forest Disturbance and Change. In*: M. A. Wulder and S. E. Franklin, Eds., Understanding Forest Disturbance and Spatial Pattern: Remote Sensing and GIS Approaches*, pp. 133-171.

Singh, A. (1989). Review Article Digital Change Detection Techniques Using Remotely-Sensed Data. *International Journal of Remote Sensing,* **10 (**6), pp. 989-1003.

Thapa, R. B., Murayama, Y. (2009). Urban Mapping, Accuracy, & Image Classification: A Comparison of Multiple Approaches in Tsukuba City, Japan. *Applied Geography*, **29** (1), pp. 135-144.

Treglia, M. L. (2015). An Introduction to GIS using QGIS (v. 2.6.1). http://mltconsecol.github.io/QGIS-Tutorial/QGIS-Tutorial/Treglia_OSOS%20Notes_V1.01.pdf, accessed August 28, 2015.

Weng, Q. (2001). A Remote Sensing GIS Evaluation of Urban Expansion and Its Impact on Surface Temperature in the Zhujiang Delta, China. *International Journal of  Remote Sensing*, **22** (10), pp. 1999-2014.

# Evaluation of Existing RC Structures under Multiple Extreme Impacts

*GANTAR Uroš[a], HABIJANIĆ Helena-Ena[b], NASHI Haruki[c], JANKOVIC Gabrijela[a], JOZINOVIĆ Magdalena[b], MUKHTAR Rabiya[d], QDEIMAT Malik[e], PEREIRA ABRIGO Danitza Giannina[f], VILCEANU Victor[g]*

[a] *University of Ljubljana, Faculty of Civil and Geodetic Engineering, Slovenia*

[b] *Josip Juraj Strossmayer University of Osijek, Faculty of Civil Engineering Osijek, Croatia*

[c] *Nagoya Institute of Technology, Nagoya, Japan*

[d] *University College London,UK*

[e] *Birzeit University, Faculty of Engineering and Information Technology, Palestine*

[f] *Universidad del Bio Bio, Concepcion, Chile*

[g] *Technical University of Civil Engineering, Bucharest*


*ABRAHAMCZYK Lars, SCHWARZ Jochen*
*Earthquake Damage Analysis Center, Bauhaus-Universität Weimar, Germany*

## Abstract

Seismic response of reinforced concrete (RC) structures with unreinforced masonry infill walls differs with the response of bare RC frames, so it is important to include infill walls for reliable results. In part of the summer school project the conducted case study was divided in three parts:

First part was investigation of different methods for modelling bare RC frames. Two different approaches were examined. Fiber section modelling offers high accuracy in computation and simulation of actual structure but it is time consuming and modelling is more complex. Modelling of plastic hinges is more widely used in practice because of its simplicity and sufficient accuracy.

In the second part, a parametric study of strut elements for masonry infill panels was conducted. In total fifteen in the literature proposed equations for the determination of the equivalent strut width and two equations for the strut hinge were evaluated. The trilinear degrading model provides an accurate description of nonlinear structural behavior. In the end, six models were analyzed using Perform-3D software.

The last part dealt with nonlinear time history analysis, where the focus was on the effect of the after-shock on the structure. In addition, the impact of tsunami was investigated. With the use of Perform-3D software, nonlinear behavior of bare RC frame was evaluated.

## Frame modelling

### Description of the structure

The RC frame which was modelled in our research is a four story building with three bays, which is designed for gravity loads [1]. Vertical loads considered in design: self-weight of the slab, transverse beams, finishing, infill walls and the quasi permanent static load. Elevation view of the frame is shown in the Figure 1.
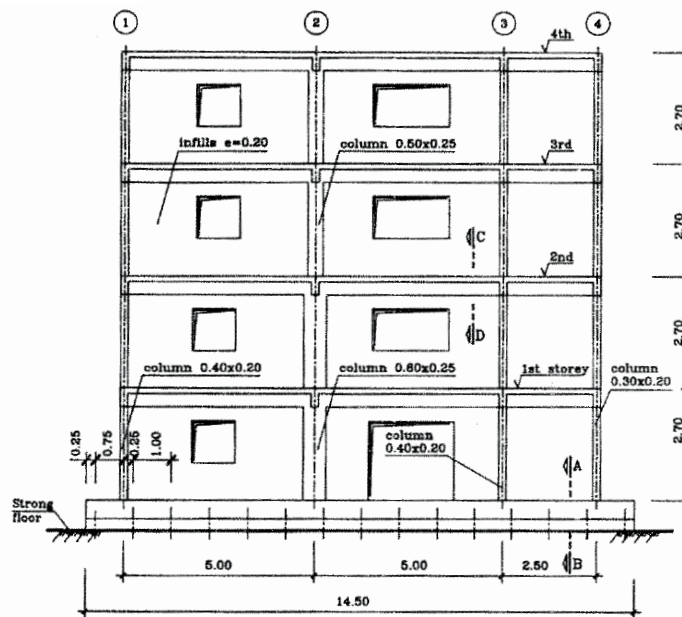
**Figure 1.** Elevation of the frame according to [1]

The frame is consisted of four stories with each 2.70 m height and three bays with 5.0 m span for two bays and 2.5 m span for the last bay. The system of the slab used is two way slabs (0.15 m thick and with 0.50 m deep beams). As it is shown on Figure 1, only column 2 is working on its stronger axis. This column plays a dominant role in the response of the frame and is therefore referred as "strong" column. Materials used in structure are concrete C16/20 and steel FeB22k (Italian standards). Bricks are 40×20×15 cm, horizontally perforated with 50% voids. (cf. [1, 2])

## Objectives of the project

- Learning PERFORM-3D software to model and analyze 2D and 3D frames;
- Modeling 2D RC frame using fiber section method and Plastic Hinge Method on PERFORM 3D software;
- Modeling of infill walls based on different proposed equations and to perform pushover analysis;
- Making a comparison between the capacity of the frame with and without modeling of the infill walls;
- To perform a time history analysis on the 2D frame under extreme impacts (main-shocks and after-shocks);
- Modeling of the forces acting on the structures due to a Tsunami event.

## Overview about PERFORM-3D

PERFORM-3D [3] is a typical Windows program (Figure 2). You can move around the program by clicking on buttons and folder tabs; select items by clicking on a drawing of the structure or by choosing from drop-down lists; and enter data by typing into text boxes.

PERFORM-3D has powerful capabilities for inelastic analysis, but it is not intended for general purpose nonlinear analysis. If you have no idea how your structure will behave when it becomes inelastic in a strong earthquake, PERFORM-3D can probably help you to identify the weak points, and hence can guide you in improving the design. However, software is not intended for design by analysis, where the engineer expects the analysis to determine exactly how a structure will behave.
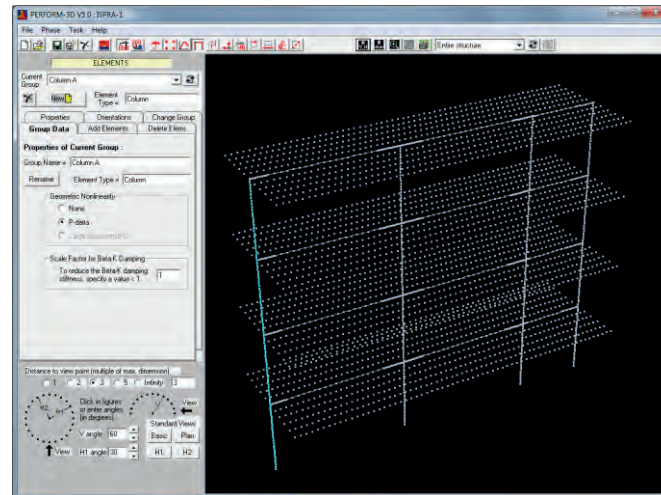
**Figure 2.** PERFORM-3D window

# Analysis of RC frame using plastic hinges

There are a lot of ways to model inelastic element. Elements could be modelled using chord rotation models that consider the member as a whole, and essentially require specifying relationship between end moment and end rotation. One way of modelling elements using this approach is to use plastic hinges. It is the best model for elements where inelastic behavior is limited to specific locations. It is also useful in situations when element can form hinges near mid-span as well as at its ends.

## Rigid-plastic hinge concept

A moment plastic hinge is literally a hinge, closely analogous to a rusty hinge that rotates only after enough moment has been applied to overcome the friction between the hinge pin and the casing. Figure 3 shows a hinge and a possible moment-rotation relationship. The hinge is initially rigid, and begins to rotate at the yield moment.

## Rotation and curvature hinges

There are "rotation" and "curvature" hinge components. A rotation hinge is a rigid-plastic hinge, exactly as in Figure 3. A curvature hinge is essentially the same, but in the action-deformation relationship the deformation is curvature rather than hinge rotation. Concept for a curvature hinge is shown in Figure 4.
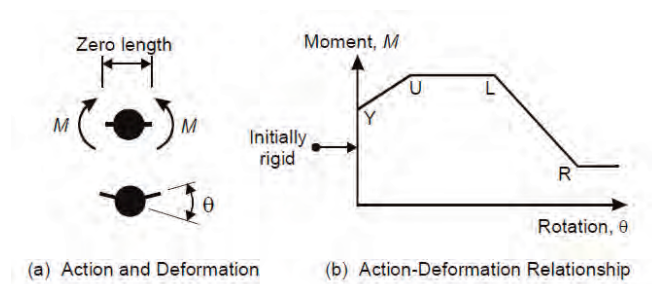


**Figure 3.** Hinge element
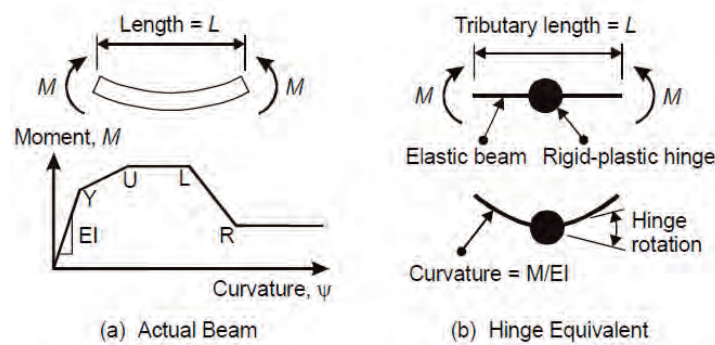
**Figure 4.** Curvature hinge

Advantages of using this approach in modelling constructions are that it is easy to use, and it provides sufficient accuracy in computations for practical problems. Disadvantage is that this approach is not sufficient to capture more realistic behavior as compared to fiber section modeling.

## Analysis of RC frame using fibers

Applicability of frame elements, using fibers subjected to uniaxial normal stress states is limited to those cases in which shear and torsional forces are not determinant on their behavior and ultimate capacity.

There are two main approaches:
- lumped-plasticity modeling
- distributed-inelasticity modeling (fiber beam-column elements)

The fiber approach fits perfectly within the Euler-Bernoulli beam theory and caters for the accurate description of response of slender flexure-dominated members and full structures.

The advantages of using fiber cross section are:
- providing high accuracy in computation
- more realistic simulation of actual structure behavior
- confinement reinforcement is also taken into account
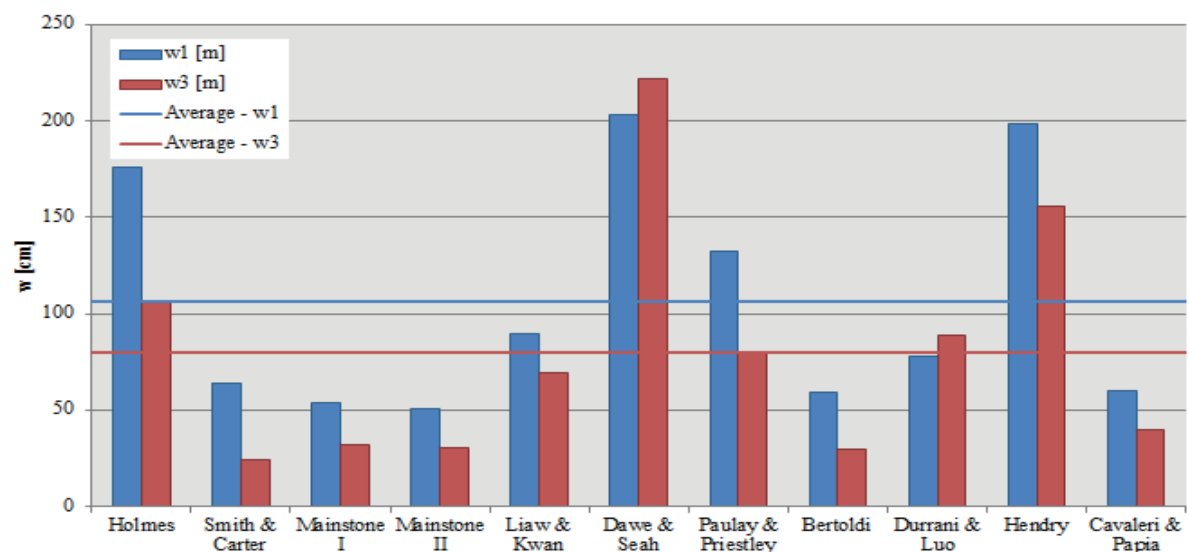


**Figure 5.** Different approaches for equivalent strut width
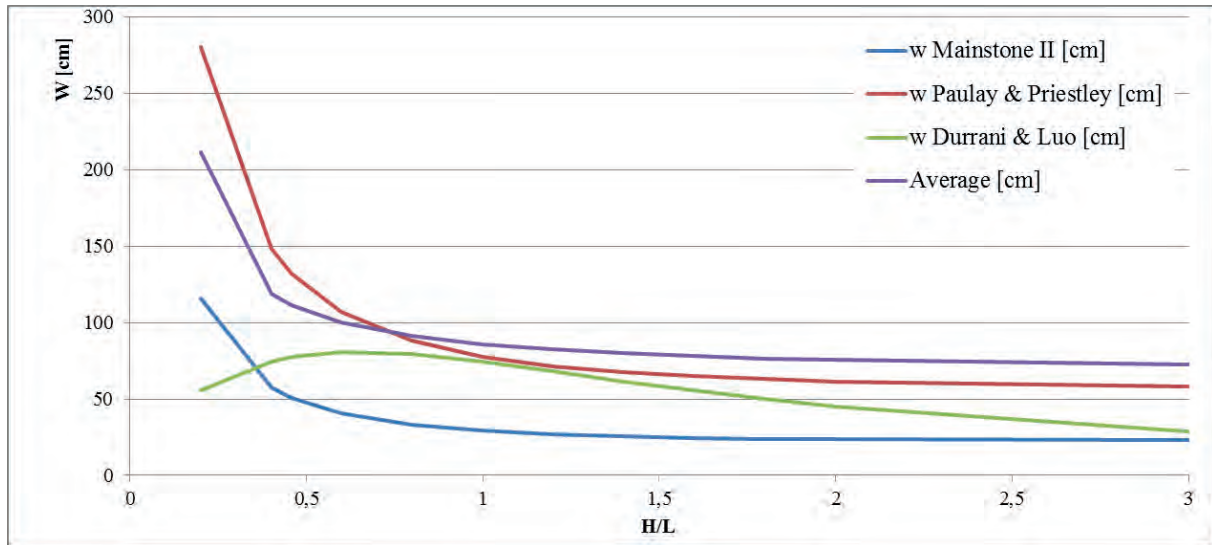
**Figure 6.** Approaches for equivalent strut width proposed by Mainstone II, Paulay and Priestley and Durrani and Luo compared with average value

## Infill models

There are many possibilities for modelling masonry infill panel. In this paper, there will be presented approaches for equivalent strut model with assigned force–displacement envelope. Fifteen equations for strut width were investigated (Figure 5) and aim was to select three of them which are representative (Figure 6). In future work, only those three approaches will be presented.

Mainstone II [5] (equation 1) provides good results which are lower than average values. Paulay and Priestley [6] (equation 2) approach behaves well in ratios H/L>0.5 but in lower ratios it is not so efficient because it gives too high values of width. Approach proposed by Durrani and Luo [7] (equations 3, 4 and 5) gives values of equivalent strut width which are closest to average ones. (cf. [8])

Mainstone II: $\qquad w = 0.175\, d \cdot (\lambda_1 \cdot H')^{-0.4}$ (1)

Paulay & Priestley: $\qquad w = \dfrac{d}{4}$ (2)

Durrani & Luo: $\qquad w = \gamma\, d\, \sin 2\Theta$ (3)

$$\gamma = 0.32 \sqrt{\sin 2\Theta} \left( \frac{H'^4 E_2\, t}{m\, E_1\, I_1\, H} \right)^{-0.1}$$ (4)

$$m = 6 \left( 1 + \frac{6\, E_1\, I_{11}\, H'}{\pi\, E_1\, I_1\, L} \right)^{-0.1}$$ (5)

Nomenclature:

w - strut width, d - diagonal length of the infill wall, t - thickness of the infill wall, θ – angle of inclination by strut, H' - height of the RC frame, H - height of the infill wall, L - length of the infill wall, $I_1$ - moment of inertia of column, $I_{11}$ - moment of inertia of beam, $E_1$ - modulus of elasticity of concrete, $E_2$ - modulus of elasticity of masonry, $\lambda_1$ - infill wall to column stiffness parameter, $\lambda_2$ - infill wall to beam stiffness parameter, γ - Poisson coefficient
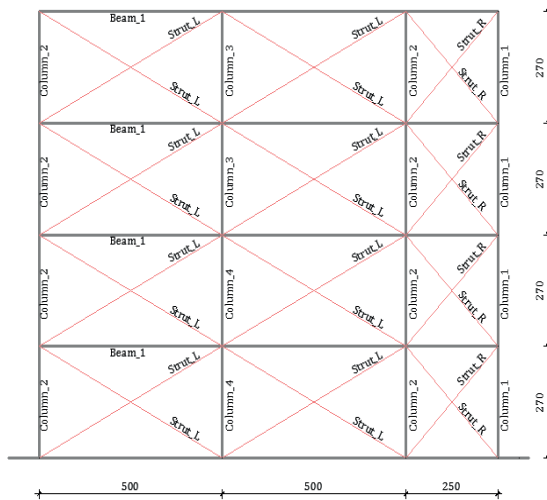
| Structural element | width(cm) | hight(cm) |
|---|---|---|
| Column_1 | 30 | 20 |
| Column_2 | 40 | 20 |
| Column_3 | 50 | 25 |
| Column_4 | 60 | 25 |
| Beam_1 | 20 | 50 |

| | |
|---|---|
| H (cm) | 220 |
| H´ (cm) | 270 |
| t (cm) | 15 |
| $E_1$ (kN/cm$^2$) | 2900 |
| $E_2$ (kN/cm$^2$) | 450 |

**Figure 7.** Model and parameters used in analysis

**Table 1.** The parameters defining the equivalent strut

| | | $L_w$ (m) | $b_w$ (m) | d (m) | Θ (rad) | I (cm$^4$) | $\lambda_1$ | $\lambda_2$ |
|---|---|---|---|---|---|---|---|---|
| Mainstone II | Strut_La | 4,55 | 0,51 | 5,05 | 0,450 | 45885,42 | 0,014579 | 0,009988 |
| | Strut_Ra | 2,15 | 0,28 | 3,08 | 0,797 | 23333,33 | 0,018348 | 0,010614 |
| Paulay & Priestley | Strut_Lb | 4,55 | 1,26 | 5,05 | 0,450 | 45885,42 | 0,014579 | 0,009988 |
| | Strut_Rb | 2,15 | 0,77 | 3,08 | 0,797 | 23333,33 | 0,018348 | 0,010614 |
| Durrani & Luo | Strut_Lc | 4,55 | 0,85 | 5,05 | 0,450 | 45885,42 | 0,014579 | 0,009988 |
| | Strut_Rc | 2,15 | 0,74 | 3,08 | 0,797 | 23333,33 | 0,018348 | 0,010614 |

**Force–displacement envelope proposed by Panagiotakos and Fardis [9]**
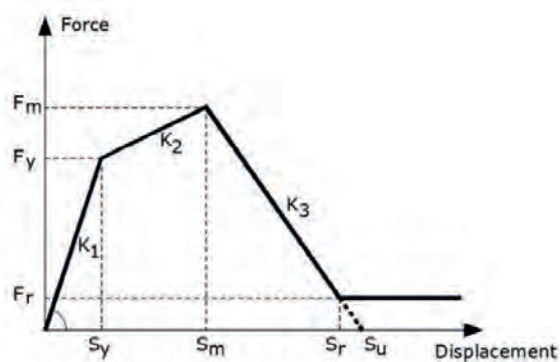


**Figure 8.** The Force–Displacement relationship proposed by Panagiotakos and Fardis [9] for the equivalent strut

Input parameters for Strut_La:

$G_w = 50 \, kN/cm^2 = 500 \, 000 \, kN/m^2$
[Tomaževic, 2009.]
$t_w = 0,15 \, m$
$L_w = 4,55 \, m$
$H_w = 2,20 \, m$
$f_{tp} = 0,020 \, kN/cm^2 = 200 \, kN/m^2$
[Tomaževic, 2009.]
$E_m = 450 \, kN/cm^2 = 4 \, 500 \, 000 \, kN/m^2$
[Tomaževic, 2009.]
$b_w = 0,51 \, m$
$d = 5,05 \, m$

**Table 2.** The parameters defining the different branches of the curve proposed by Panagiotakos and Fardis [9]

|  | Mainstone II | | Paulay&Priestley | | Durrani&Luo | |
|---|---|---|---|---|---|---|
|  | Strut_La | Strut_Ra | Strut_Lb | Strut_Rb | Strut_Lc | Strut_Rc |
| $F_r$ (kN) | 0.00 | 0.00 | 0.00 | 0.00 | 0.00 | 0,00 |
| $F_y$ (kN) | 136.50 | 64.50 | 136.50 | 64.50 | 136.50 | 64.50 |
| $F_m$ (kN) | 177.45 | 83.85 | 177.45 | 83.85 | 177.45 | 83.85 |
| $K_1$ (kN/m) | 155'113.64 | 73'295.45 | 155'113.64 | 73'295.45 | 155'113.64 | 73'295.45 |
| $K_2$ (kN/m) | 68'281.24 | 62'282.09 | 168'750.00 | 168'750.00 | 113'542.64 | 161'419.19 |
| $K_3$ (kN/m) | 15'511.36 | 7'329.55 | 15'511.36 | 7'329.55 | 15'511.36 | 7'329.55 |
| $S_y$ (m) | 0.000880 | 0.000880 | 0.000880 | 0.000880 | 0.000880 | 0.000880 |
| $S_m$ (m) | 0.001480 | 0.001191 | 0.001123 | 0.000995 | 0.001241 | 0.001000 |
| $S_r$ (m) | 0.007399 | 0.005953 | 0.005613 | 0.004973 | 0.006203 | 0.004999 |

## Force–displacement envelope proposed by Žarnić & Gostič [10]
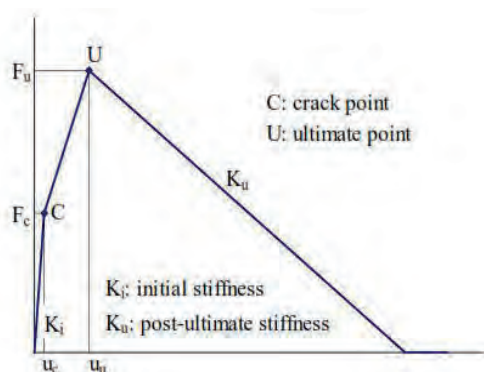


**Figure 9.** Tri-linear force-deformation envelope proposed by Žarnić & Gostič [10]

Input parameters for Strut_La:

$E_p = 450 \, kN/cm^2 = 4\,500\,000 \, kN/m^2$
[Tomaževič, 2009.]
$W_{ef} = 0{,}51 \, m$
$t_p = 0{,}15 \, m$
$h_p = 2{,}20 \, m$
$d = 5{,}05 \, m$
$$\varphi_d = arc \tan\frac{h_p}{l_p} = arc \tan\frac{2{,}20}{4{,}50} = 0{,}45 \, rad$$
$l_p = 4{,}55 \, m$
$f_{tp} = 0{,}020 \, kN/cm^2 = 200 \, kN/m^2$
[Tomaževič, 2009.]

**Table 3.** The parameters defining the different branches of the curve proposed by Žarnić & Gostič [10]

|  | Mainstone II | | Paulay&Priestley | | Durrani&Luo | |
|---|---|---|---|---|---|---|
|  | Strut_La | Strut_Ra | Strut_Lb | Strut_Rb | Strut_Lc | Strut_Rc |
| $F_{u,h}$ (kN) | 143.17 | 87.80 | 143.17 | 87.80 | 143.17 | 87.80 |
| $F_u$ (kN) | 159.03 | 125.62 | 159.03 | 125.62 | 159.03 | 125.62 |
| $F_c$ (kN) | 79.51 | 62.81 | 79.51 | 62.81 | 79.51 | 62.81 |
| $K_{i,h}$ (kN/m) | 55'342.76 | 30'425.25 | 136'773.88 | 82'435.60 | 92'027.66 | 78'854.45 |
| $C_I$ | 3.98 | 1.88 | 3.98 | 1.88 | 3.98 | 1.88 |
| $K_i$ (kN/m) | 68'281.24 | 62'282.09 | 168'750.00 | 168'750.00 | 113'542.64 | 161'419.19 |
| $K_u$ (kN/m) | 6'828.12 | 6'228.21 | 16'875.00 | 16'875.00 | 11'354.26 | 16'141.92 |
| $u_c$ (m) | 0.001165 | 0.001008 | 0.000471 | 0.000372 | 0.000700 | 0.000389 |
| $u_u$ (m) | 0.011000 | 0.011000 | 0.011000 | 0.011000 | 0.011000 | 0.011000 |
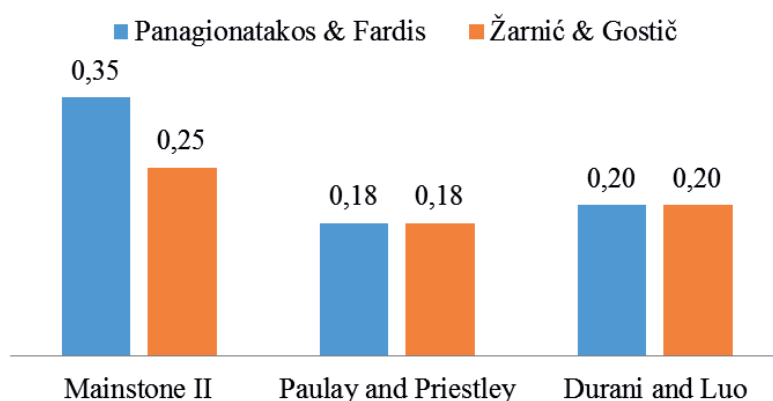
**Figure 10.** First modal period T(s)

# The discussion of results

In PERFORM-3D modal analysis and pushover analysis were carried out for RC frame with the equivalent strut. The equivalent strut was modelled with all defined parameters for different approaches for hinge model. The result of modal analysis was the period which is directly related to the width of the strut. If the strut width is larger, the building has more stiffness and it results in lower period of the structure. Like it is shown in Figure 10, Mainstone II proposed smaller values for width of the strut and it resulted with the highest period. Also, the modal period of the structure without infill (bare frame) is 0.7349 seconds which is about double of the period which we get from taking into account the masonry infill with least dimensions, i.e. approach by Mainstone II.

# Multiple extreme impacts

In this section the impact of multiple extreme events on the structures will be discussed. First, the impact of strong earthquakes with damaging after-shocks is considered, and in second part some observations and discussion about severe tsunamis are presented.

### Earthquakes with strong after-shocks

A good example of multiple extreme impacts is the structure from Turkey (Figure 11), which has suffered minor damages during the main-shock of Van earthquake on October 2011 and was collapsed several days later during the after-shock.



(a)  (b)

**Figure 11.** Building in Turkey: (a) After the main-shock, October 2011 and (b) collapsed building due to the after-shock, November 2011

[http://earthquake-report.com/2011/11/09/aftershock-near-van-turkey-creates-more-destruction-and-human-misery]
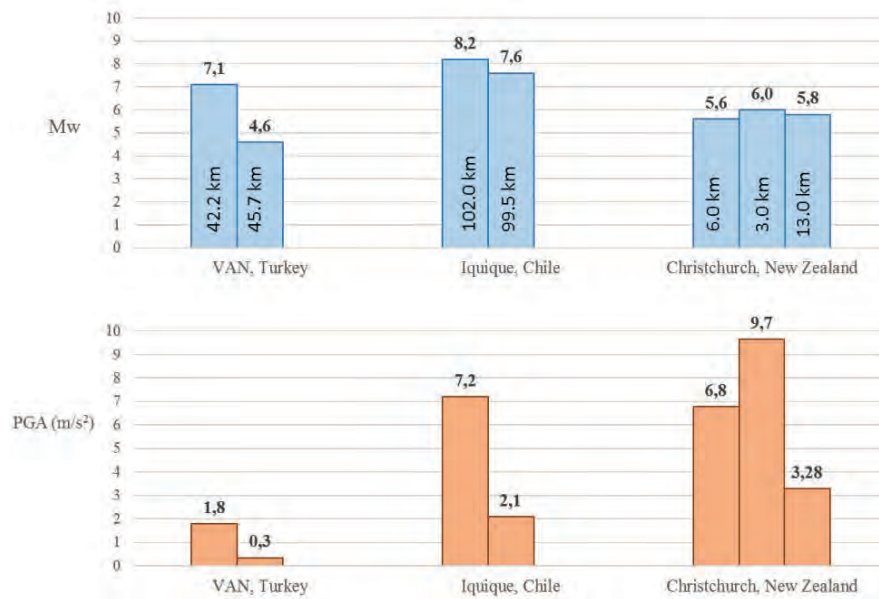
**Figure 12.** Moment magnitudes and distance of the station from the earthquake epicenter (up) and the peak ground acceleration from all recorded earthquake shocks (bottom)

Therefore, for our study, three earthquakes with strong after-shocks have been discussed: Van from Turkey, Chile and New Zealand earthquakes. The records of the main- and after-shocks are from the same station, for each earthquake respectively. As it can be seen in Figure 12 the moment magnitudes of all earthquakes are relatively high. The measured peak ground acceleration (PGA) is also high but here we should note that the value depends on the distance from the station and the direct comparison should not be done. In later study we have assumed that the studied building is located next to the station where the time histories have been measured. The main-shock and following after-shocks have been put together to create time histories, which were used in the study (Figure 13).
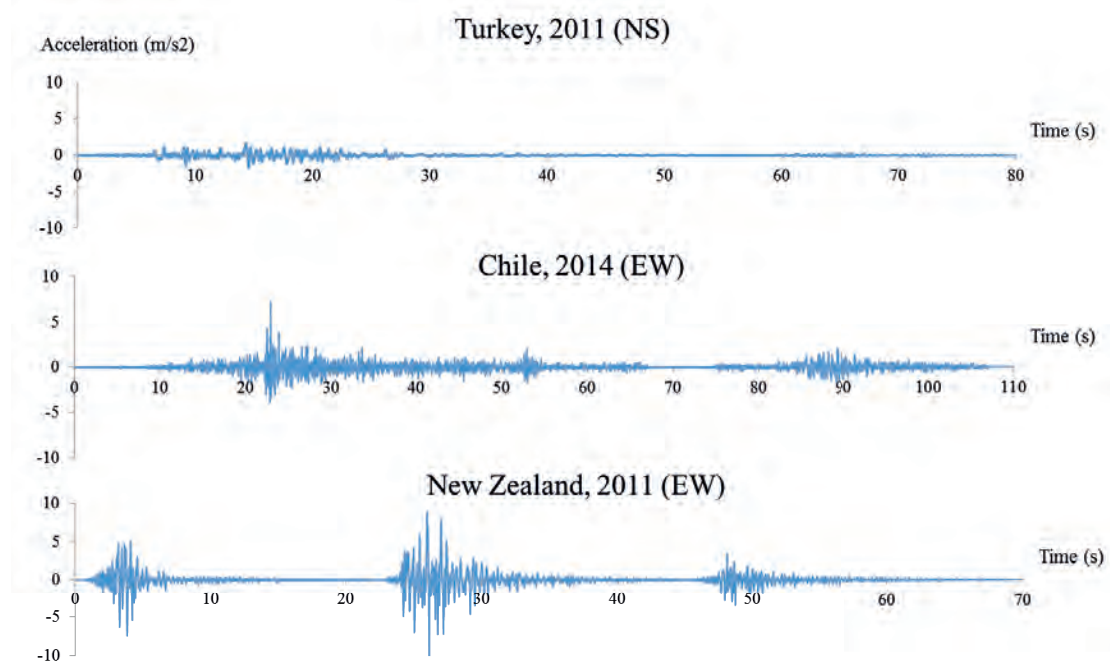


**Figure 13.** Time histories of all three observed earthquakes (main- and after-shocks)

Following results are representing the time history analysis of the structure using the New Zealand earthquake. Also the other two time histories have been considered, and some results and conclusions regarding the Chile earthquake have been done and are presented at the end of this section.

The comparison between the response spectra of each shock and the elastic site spectrum from the code (Figure 14) reveals that response spectra of the first and second shock are above the spectrum according to the code. The high magnitude and PGA that has been recorded during aforementioned earthquake was not expected. Therefore, these observations suggest further revision and improvements of the code.

Propagation of deformation in steel reinforcement was observed during the time history analysis, which can be seen at Figure 14. First yielding occurred at the bottom of the inner column, and after the second shock the yielding propagated through all the columns of the structure. The damages after the main-shock are much smaller than after the second shock. It can be mentioned, that achieved results are comparable with the data from experimental investigation. Ultimate steel deformation had not been reached during the chosen time history analysis in any of the elements so the failure of the structure did not occur. The reason for this might be in the definition of the material behavior, where the hysteretic behavior which would take into account the strength degradation of the material was not modelled. Similar conclusion has been done while observing the drifts of the building, where no residual drifts has been recorded. This is opened question for further investigation.

Nevertheless, we observed the building drift at the top of the frame. At the Figure 15 the red line indicates the limit when the first yielding of the reinforcement is achieved, and the green line presents the value of the building drift at which the concrete starts to spall. From this analysis, it is possible to conclude that the spalling of the cover concrete starts later due to the after-shock. As already indicated before (Figure 14), the first yielding of the steel reinforcement is reached after first 3 seconds.

The structure analyzed using the time history from Chile earthquake suffered more damages and higher drifts during the main shock. In this case the first shock was higher than the after-shock but again it should be noted that the degradation of the material was not taken into account.
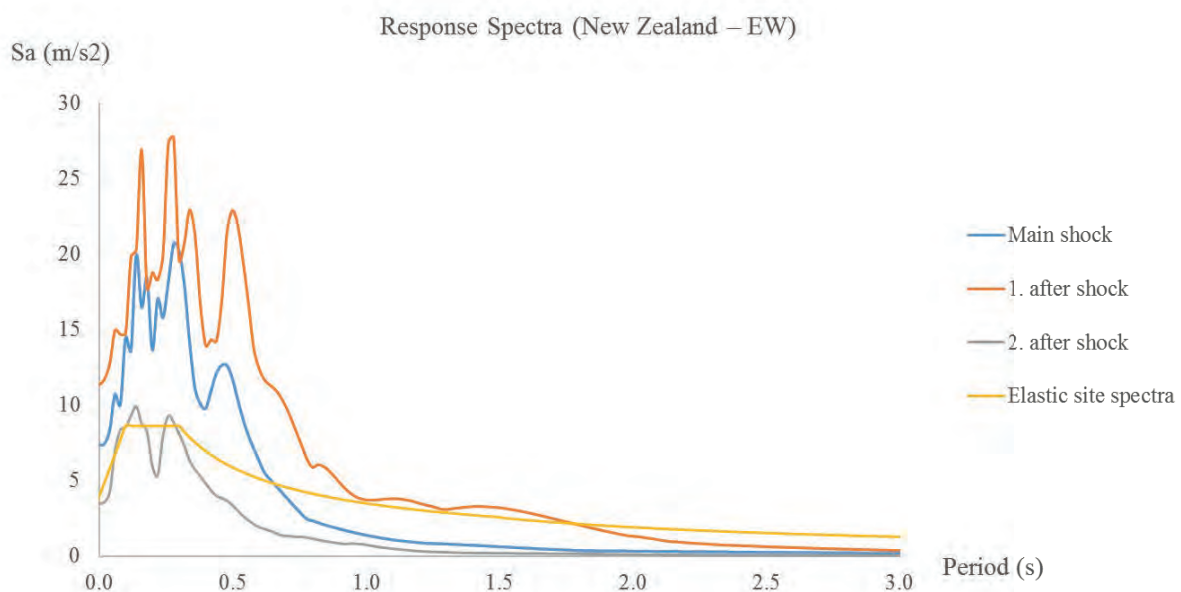


**Figure 14.** Time histories of all three observed earthquakes (main- and after-shocks)

first yielding (T = 3 s)          after main shock (T = 10 s)          after 1. after shock (T = 35 s)
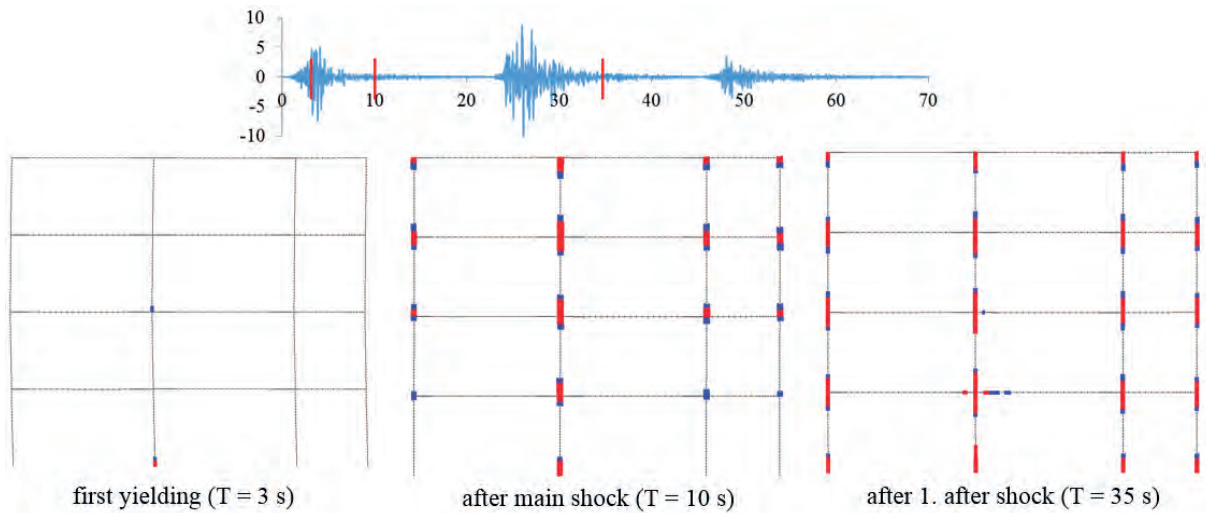
**Figure 15.** Yield deformation in steel reinforcement at three stages of the time history analysis
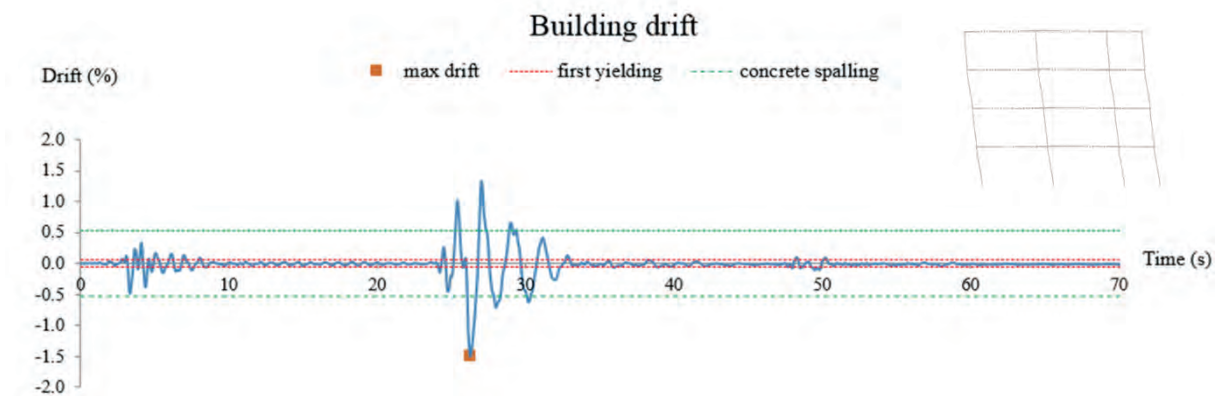


**Figure 16.** Drift at the top of the building

## Impact of Tsunami

Another extreme impact that can produce severe damages to buildings is tsunami. These are ocean waves triggered by geological processes, commonly earthquakes. The impact generated by these waves on structures has a strong character that can produce economical and life losses. One recent event in Japan (Figure 17a) shows us the destructive power of a tsunami. The forces to assess the impact of tsunami are various and more complex to evaluate than in the case of earthquakes or floods. For our study case, a masonry infill wall is considered to be subjected to impulsive force with the purpose of finding the critical flow velocity for the wall failure. Based on the geometry and parameters for masonry wall described above in this paper and the regulations from FEMA P646 regarding the assessment of impulsive forces due to tsunami, the comparison is made. The out of plane capacity of the infill was computed using the equation 6 given by FEMA 356:

$$P_{Out-of-plane} = \frac{4 \cdot M_{eq}}{d} = 26.2 \; kN \qquad (6)$$

where $M_{eq}$ is the equivalent out of plane moment and d is the diagonal of the strut.

The flow is assumed to be uniform with its resultant force acting at the centroid of the projected area in the direction of the flow. The impulsive force was taken from FEMA P646 with the following equation:

**Figure 17.** (a) Impact of tsunami (Tohoku 2011, Japan) , (b) Impulsive force acting on the centroid of the masonry infill

[http://es.portalmie.com/wp-content/uploads/2017/03/xtsunami.jpg.pagespeed.ic_.mLrlM1krFq.jpg]

$$F_I = 0.75 \cdot C_D \cdot \rho_S \cdot A_p \cdot u^2 \tag{7}$$

where $C_D$ represents the drag coefficient, $\rho_S$ is fluid density including sediment, $A_p$ - projected area of the body and u is the flow velocity at the location of the structure.

By setting the flow velocity as a variable parameter, the analysis showed that the out of plane capacity is exceeded for a speed of 2 m/s, which is a moderate wave speed. As a reference from literature, at 3 m/s they start to be more damaging, stressing the fact that a masonry infill wall should be carefully considered in the analysis in case of a tsunami impact.

## Conclusion

There were several tasks to be analyzed using the software PERFORM 3D. A reinforced concrete frame was studied using fiber section and plastic hinges modelling. The analysis and observations showed that the fiber section modelling gives a closer simulation to the actual structural behavior due its cross-section optimization (introducing the confined concrete in the analysis) but it is time consuming, whereas the plastic hinge is a faster method and can be defined according to available design codes. By using a nonlinear time history analysis of New Zealand earthquakes (main-shock and after-shocks) on the RC frame, the results showed that the after-shock had more destructive power compared with the main one, therefore structural analysis of buildings under subsequent earthquakes should be considered in the future. For masonry infill, more experimental validation is required to determine the most appropriate approach since it has impact on structural behavior. Given the available geometry and parameters of the infill, the out of plane capacity was compared with the impulsive force due to tsunami impact. The result showed that at a moderate flow velocity the wall would fail and may cause additional damage to the structure.

As an overview of this study, using the available international codes only one major event is designed (i.e. earthquake, flooding, tsunami) but the question still stands for the case of multiple events. Given the complexity of assessing the state of the structure after a tsunami impact while it was previously subjected to earthquake, this paper covered theoretical and design issues of low-story buildings under multiple extreme impacts, but future work should be done to cover these aspects with a certain level of accuracy.

# References

[1] Pinho, R., Elanshai, A.S. (2000): Dynamic collapse testing of a full-scale four stores RC frame. *ISET Journal of Earthquake Technology*. Paper No 406, **Vol. 37**(4), pp 143-163.

[2] Pinto, A., Varum, H., Molina, J. (2002): Experimental assessment and retrofit of full scale models of existing RC frames. *In: Proceedings of the 12th European Conference on Earthquake Engineering*. Elsevier Science Ltd, London.

[3] Computers and Structures, Inc.1995 University Avenue (2006): PERFORM COMPONENTS AND ELEMENTS FOR PERFORM-3D AND PERFORM-COLLAPSE. pp 6-6 - 6-7

[4] Petragneli, M., Pingo, P.E., Ciampi, V. (1999): Fiber element for cyclic bending and shear of RC structures. I: Theory. *Journal of Engineering Mechanics,* **Vol. 125**(9).

[5] Mainstone, RJ. (1971): On the stiffness and strength of infilled frames. *In: Proc. Inst Civil Eng.*, Suppl (IV) – London 1971, Paper 7360, pp: 57–89.

[6] Paulay, T, Priestley, MJN. (1992): Seismic design of reinforced concrete and masonry buildings. New York: John Wiley & Sons; 1992.

[7] Durrani, AJ, Luo YH. (1994): Seismic retrofit of flat-slab buildings with masonry infills. *In: Proceeding from the NCEER workshop on seismic response of masonry infills*. Report NCEER-94-0004. March 1, 1994. p. 1/3–8.

[8] Uva, G., Raffaele, D., Porco, F., Fiore, A. (2012): On the role of equivalent strut models in the seismic assessment of infilled RC buildings. *Engineering Structures* **42**, 83-94.

[9] Panagiotakos, T.B., Fardis, M.N. (2006): Seismic response of infilled RC frames structures. *Eleventh World Conference on Earthquake Engineering*, Paper No. 225

[10] Žarnić, R., Gostič, S. (1997): Masonry infilled frames as an effective structural sub-assemblage, *Seismic Design Methodologies for the Next Generation of Codes*, Fajfar & Krawinkler (eds), Balkema, Rotterdam, 335-346.

[11] Tomaževič, M. (2009): Shear resistance of masonry walls and Eurocode 6: Shear versus tensile strength of Masonry. *Materials and Structures*.

[12] Faifar, P., Dolšek, M., Zarnic, R., Gostic, A. (2001): Towards European integration in seismic design and upgrading of building structures EUROQUAKE: Development of numerical methodologies for infilled frames. *Final report*. INCO – Copernicus Project No. IC15-CT97-0203.

[13] CSN, Centro Sismológico Nacional, Universidad de Chile. *http://www.sismologia.cl/seismo.html*

[14] Lagos, M., Gutiérrez, D. (2005) Simulación del tsunami de 1960 en un estuario del centro-sur de Chile, Revista de Geografía Norte Grande, **33**: 5-18.

[15] McVerry, G.A., Gerstenberger, M.C., Rhoades, D.A., Stirling, M.W. (2012) Design Spectra for the Reconstruction of Christchurch. 15 *WCEE*, Lisboa 2012.

[16] NZS 1170.5 Supp 1:2004. New Zealand Standard. Structural Design Actions. Part 5: Earthquake actions – New Zealand Commentary.

[17] SHOA. (1995) Maremotos en la costa de Chile. Valparaíso, Chile. Servicio Hidrográfico y Oceanográfico de la Armada de Chile (SHOA). 2ª edición, 48 p.

[18] Strong-motion virtual data center (VDC). *http://www.strongmotioncenter.org/vdc/scripts/default.plx*

[19] Federal Emergency Management Agency FEMA (2000): Prestandard and commentary for the seismic rehabilitation of buildings (**FEMA 356**). Federal Emergency Management Agency and National Institute of Building Sciences, Washington D.C. 2000.

[20] Federal Emergency Management Agency FEMA (2008): Guidelines for Design of Structures for Vertical Evacuation from Tsunamis (**FEMA P646**). Federal Emergency Management Agency and National Institute of Building Sciences, Washington D.C. 2008.

# Numerical analysis of steel frames

*AHMED Aqueel [a], DONINI Luca [b], PUCA Vittorio [b], SHOPSKI Martin [c], TRANDAFIR Alexandru [d]*

*[a] Faculty of Civil Engineering, Bauhaus-University, Weimar, Germany*

*[b] Università degli Studi di Genova, Italy*

*[c] University of Architecture, Civil Engineering and Geodesy – Sofia, Bulgaria*

*[d] Technical University of Civil Engineering Bucharest, Romania*

*CRISAN Andrei Nicolae [a], KRAUS Matthias [b]*

*[a] CMMC Department, Politehnica University Timisoara, Romania*

*[b] Chair of Steel and Hybrid Construction, Bauhaus-Universität Weimar*

## Abstract

The project is connected with the design of an 18-story office building, located in Bucharest, Romania. The building height is 94 m, and the plan dimensions are 43,3m x 31,3m. The building site is located in a high seismic area, which is characterized by a design peak ground acceleration 0.24g for a returning period of 100 years, and soft soil conditions, with TC=1.6 s. Lateral force-resisting system consists of exterior steel framing with closely spaced columns and short beams. The moment frame connections employee reduced beam section connections that are generally used for beams loaded mainly in bending. By using the FEM-simulation-program ANSYS© the experimental data could be verified. During the analysis different material law were compared for finding the best way to reflect the real behaviour of the construction.

## Introduction to FEM

The complexity of numerical and FE models has advanced to the point where human understanding is of little use as a validation tool. Moreover, the interdisciplinary use of finite element methods to solve different complex models rise the need of accurate and reliable rules for the quantification of principal model parameters, the evaluation of individual partial models, their coupling as well as the overall model. In order to produce reliable results, any given model has to be verified and validated. In practice, validation is often blended with verification, especially when measurement data is available for the system being modelled.

In order to achieve a high quality FE model, there are a series of parameters to be considered and monitored. For the case of homogeneous models, the validation and calibration can be done relatively easy and a high quality model is usually obtained. For the case of complex models, composed of multiple sub models with different requirements regarding the geometric detail, mesh density and overall quality, the correct evaluation can become a difficult procedure.

Model verification is intended to ensure that the model does what it is intended to do. Adding supplementary output in order to check for eventual hidden errors, step-by-step analysis of the model, the use of simplified models, testing for extreme values are few of the model verification techniques that can be used to asses complex models.

Validation is the task of demonstrating that the model is a reasonable representation of the actual structural system and it reproduces the system behaviour with enough fidelity to satisfy analysis objectives. A complex model is usually composed of more sub models representing different parts of the system at different levels of abstraction. As a result, the complex model may have different levels of validity for different sub models, parts of the system across the full spectrum of system behaviour.

During the validation process different attributes are usually included: precision, repeatability, reproducibility, curve fitting and its range.

# General description of the research project

## Building geometry

The project is connected with the design of an 18-story office building, located in Bucharest, Romania. The building height is 94 m, and the plan dimensions are 43,3m x 31,3m (Figure 1).

Lateral force-resisting system consists of exterior steel framing with closely spaced columns and short beams. The central core is also made of steel framing with closely spaced columns and short beams. The ratio of beam length-to-beam height, L/h, varies from 3.2 to 7.4, which results in seven different types of beams. Some beams are below the general accepted inferior limit (L/h=4). The 82 moment frame connections employee reduced beam section connections that are generally used for beams loaded mainly in bending (Figure 2).
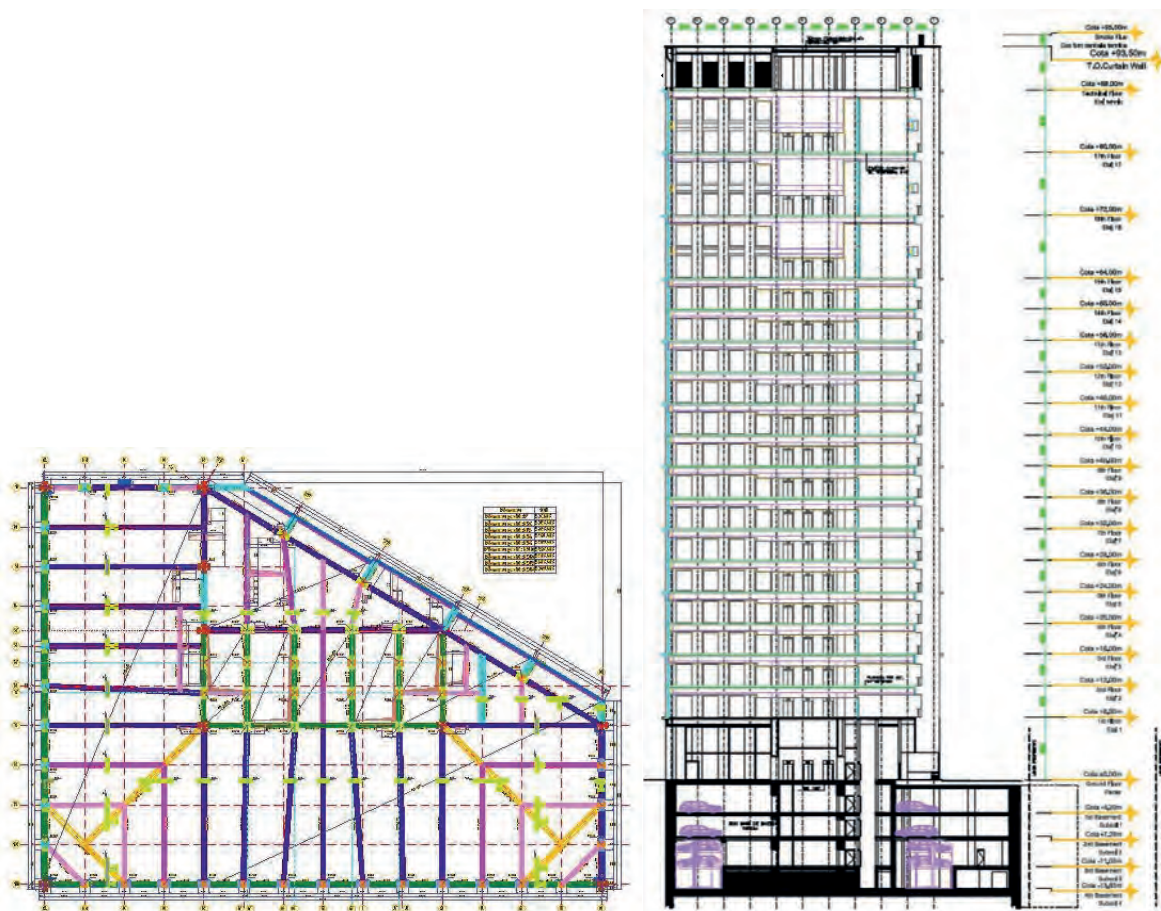


**Figure 1.** Plan layout and elevation of the building.
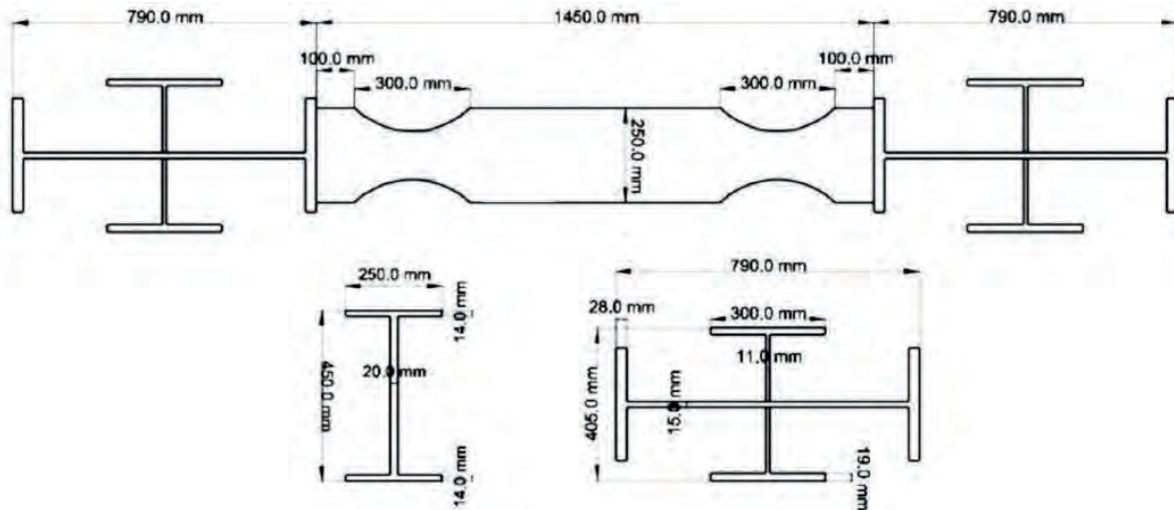
**Figure 2.** Moment frame with short beam – beam and column details.

Circular radius cuts in both top and bottom flanges of the beam were used to reduce the flange area. For current experimental program, two types of beams, which have the shortest L/h ratio, have been selected. The first beam, denoted as RBS-S, has a clear length of 1450 mm, and the lowest span over height ratio, L/h=3.2. The second type, denoted as RBS L, has a clear length of 2210 mm, and a corresponding span over height ratio L/h of 4.9. The columns have a cruciform cross-section made from two hot-rolled profiles of HEA800 and HEA400 section (Dinu et. al., 2013).

Beams with span-to-depth ratios shorter than four are not very common in the design of moment resisting frames. For such beams, the shear stresses may become a controlling factor in the design, as the moment capacity is influenced by the presence of the shear. This is an important matter when such a beam is part of the seismic lateral force resisting system that is designed according to the dissipative concept. In this case, the contribution from the shear force affects the dissipation capacity and plastic mechanism. Both beams and columns are made from S355 grade steel.

## Seismicity of Romania

The earthquake risk on Romania is one of the highest in Europe, and seismic hazard for almost half of the territory of Romania is determined by the Vrancea seismic region, which is situated beneath the southern Carpathian Arc. The region is characterized by a high rate of occurrence of large earthquakes in a narrow focal volume at depth from 70 km to 160 km (e.g, Wenzel et al., 1999).
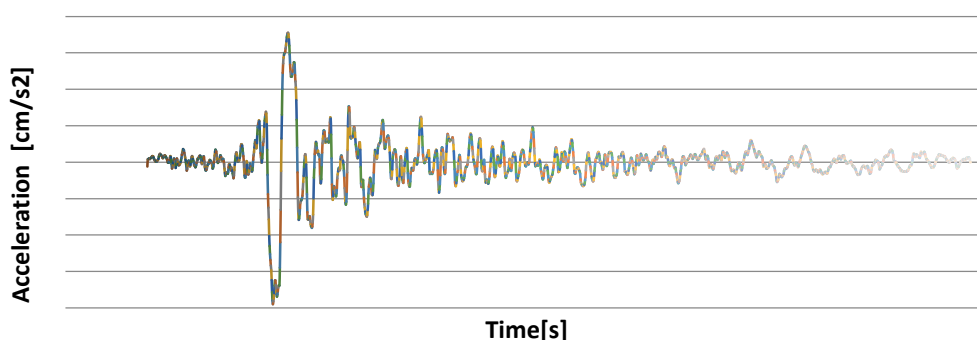


**Figure 3.** Vrancea 1977, Incerc-Bucuresti Accelerogram (N-S direction).
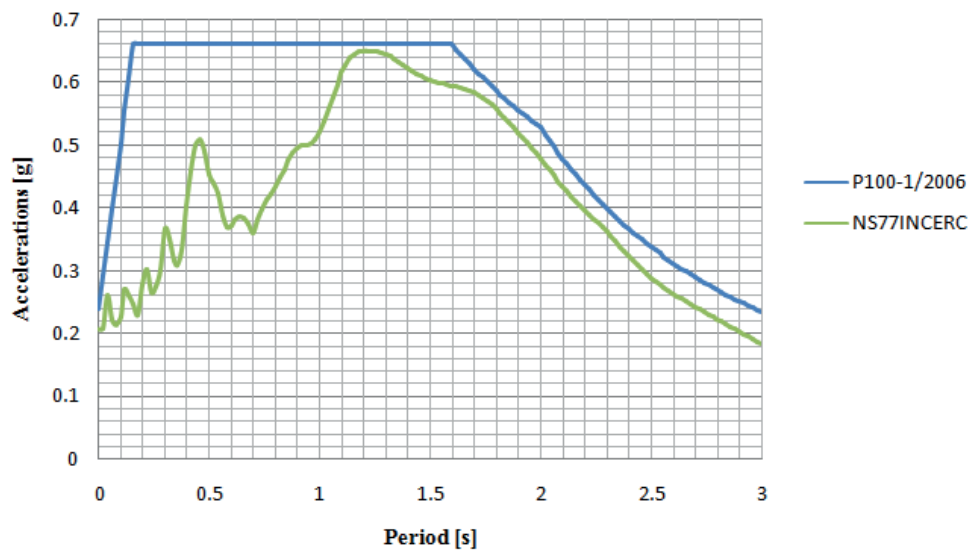
**Figure 4.** Response Spectrum.

Besides the Vrancea area, several zones of shallow seismicity located within and outside territory of Romania are considered as seismically dangerous. The accelerogram (Figure 3) was recorded during the earthquake from Vrancea in 1977, component N-S, at INCERC Bucharest. This is the most severe, with PGA=0.2g. In Figure 4 is presented a comparison between design spectrum according to P100/2006 and the response spectrum of Vrancea 77 N-S accelerogram.

The building site is located in a high seismic area, which is characterized by a design peak ground acceleration 0.24g for a returning period of 100 years, and soft soil conditions, with TC=1,6 s.

### Experimental test setup and test protocol

Specimens were tested under cyclic loading. The cyclic loading sequence was taken from the ECCS Recommendations. The yielding displacement is then used for establishing the cyclic loading. In order to reduce the number of tests, the monotonic test was replaced by the pushover curve obtained numerically using the general-purpose finite element analysis program ABAQUS. For the FE model, the measured material properties were used.

In Table 1 and Table 2 are presented the experimental results for uniaxial tension tests for the hot rolled profiles and flat steel plates.

**Table 1.** Material properties of rolled profiles (Columns) – Dinu et. al., 2013

| Section | Steel grade | Element | $f_y$ [N/mm²] | $f_u$ [N/mm²] | $A_u$ [%] |
|---------|-------------|---------|---------------|---------------|-----------|
| HEA80 | S355 | Flange | 410.5 | 618.5 | 15.0 |
| | | Web | 479.0 | 671.2 | 13.0 |
| HEA400 | S355 | Flange | 428.0 | 592.0 | 15.1 |
| | | Web | 461.0 | 614.0 | 12.8 |

**Table 2.** Material properties of flat steel (Beam) – Dinu et. al., 2013

| Section | Steel grade | Element | $f_y$ [N/mm²] | $f_u$ [N/mm²] | $A_u$ [%] |
|---------|-------------|---------|---------------|---------------|-----------|
| 14mm | S355 | Beam flange | 373.0 | 643.0 | 17.0 |
| 20mm | S355 | Beam web | 403.0 | 599.0 | 16.5 |
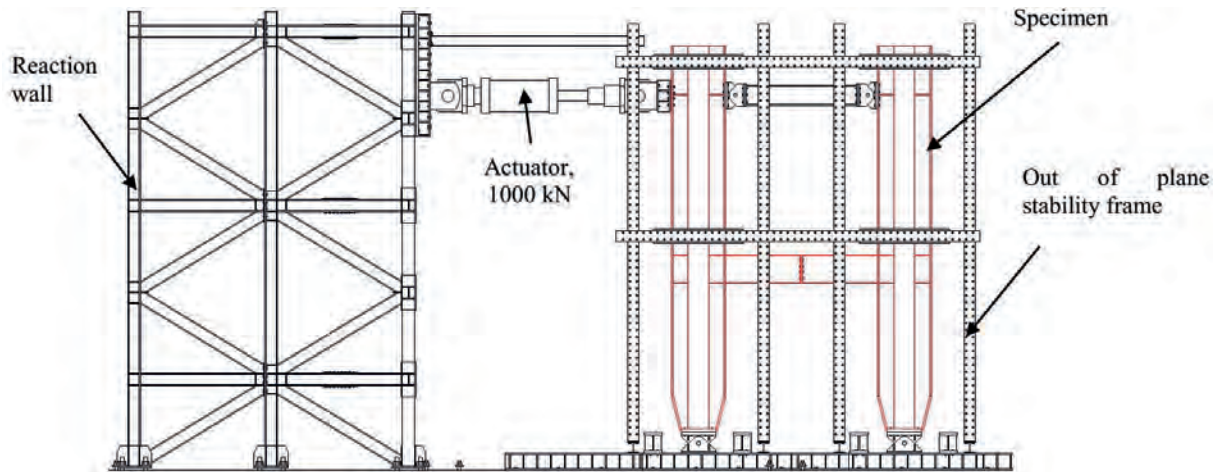
**Figure 5.** Experimental test setup (Dinu et. al., 2013).

It can be observed that the experimentally measured yield strength and tensile stress of the plates and profiles were larger than the nominal values. The highest increase has been recorded for the hot rolled sections, being lower for plates. In Figure 5 is presented the experimental setup.

Further, in Figure 6 is presented the loading protocol. Due to physical limitations, an asymmetric loading protocol was selected.

## Experimental test results

In Figure 7 are presented the experimental test results for the RSB-S3 coupling beam and the observed failure mode (Dinu et. al., 2013).
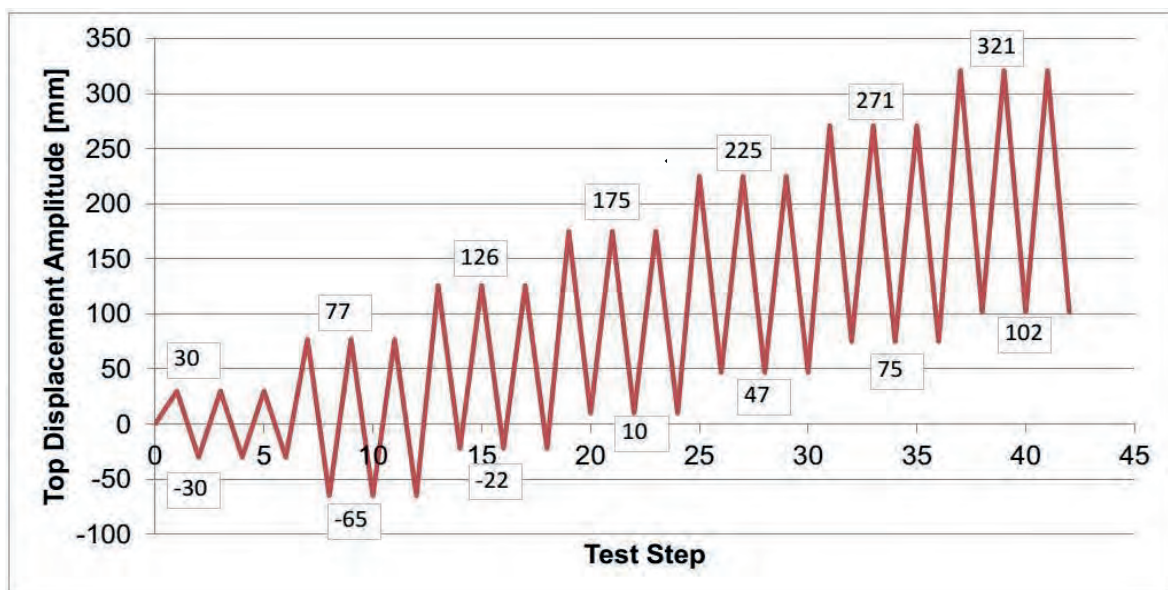


**Figure 6.** Experimental test loading protocol.
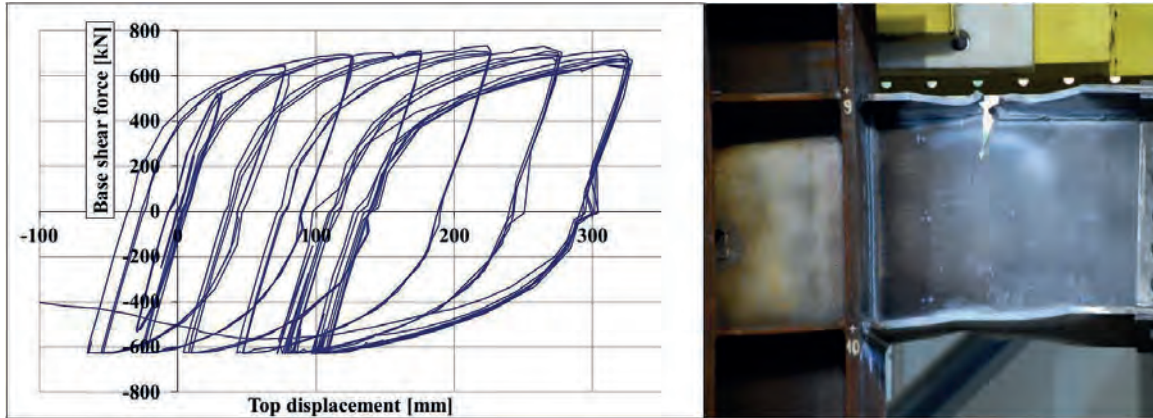
**Figure 7.** Experimental test results and failure mode.

# Numerical model calibration and validation

Based on the experimental test results presented in previous chapter, Ansys WorkBench R16.2 Academic commercial finite element software package was used to create a calibrated and validated numerical model.
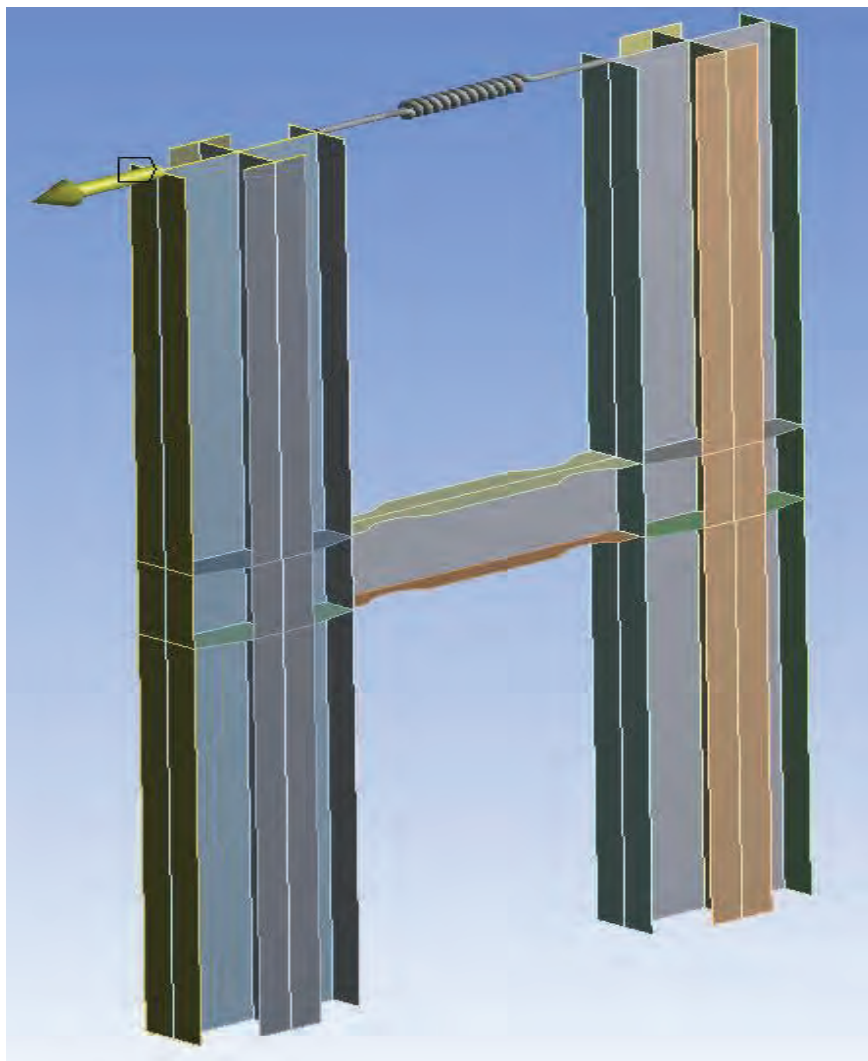


**Figure 8.** FE model geometry.

163

In order to be able to conduct a successful sensitivity analysis, the numerical model has to have the following characteristics:

- Successfully replicate the experimental test results with high accuracy;
- Simple model in order to better control the input parameters, but complex enough in order to model the observed structural behavior.

## FE model

For this model, the calibration consists, in fact, in finding the suitable material behavior law to be used in analysis. A complete model was created using shell elements, as presented in Figure 8.

At the bottom, the supports were modelled using Remote Displacement constraints. The translation was blocked on X, Y and Z together with the rotation about Y and Z, while the rotation about the X axis was left free in order to simulate a pinned connection.

The connection beam at the top was considered using a Beam Body-Body connection. Frictionless support was used to model the rigid diaphragm behaviour of the subsystem. The displacement was applied at the top left column and it was introduced using a 59 time steps static analysis.

## Meshing

In this analysis, the method used for the mesh was Multizone Quad along with face sizing. The size of an element was 25 mm. (Figure 9)
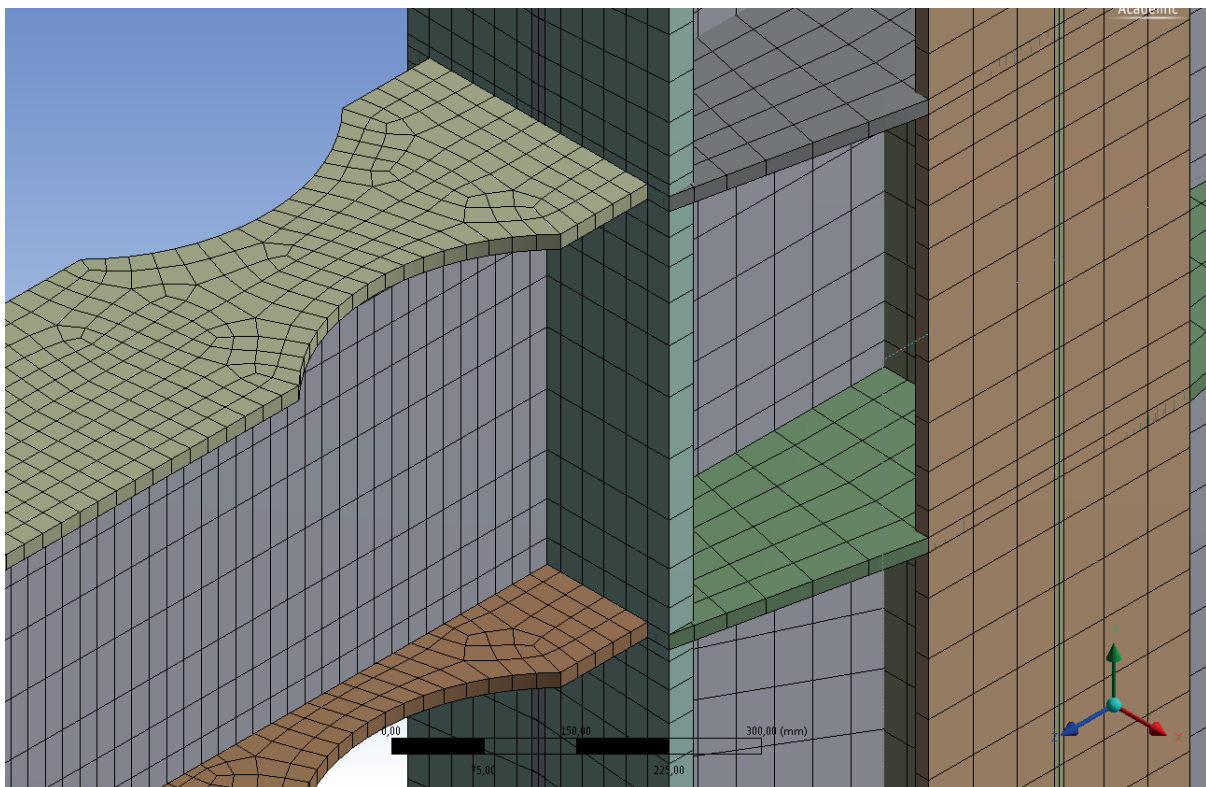


**Figure 9.** FE model mesh.

**Material calibration**

Different types of material behaviour were considered, according to EN1993-1-5 provisions:

- Elastic – Perfect Plastic;
- Isotropic hardening with a modulus of E/1000;
- Kinematic hardening modulus of E/1000;
- Chaboche model;

It must be mentioned that, for monotonic loads, the isometric hardening models with above given properties offer a good approximation, while material models with kinematic hardening are the simplest way to model cyclic loadings. Using ANSYS WorkBench capabilities, different material models were considered using isotopic or kinematic plasticity. The results of these analyses are presented in the following figures.

It can be observed that the case of cyclic loading none of these models is appropriate to simulate the behaviour obtained following the experimental tests. A more sophisticated approach was considered the Chaboche material model. For this material model, the parameters were taken from Budaházy and Dunai (2013).
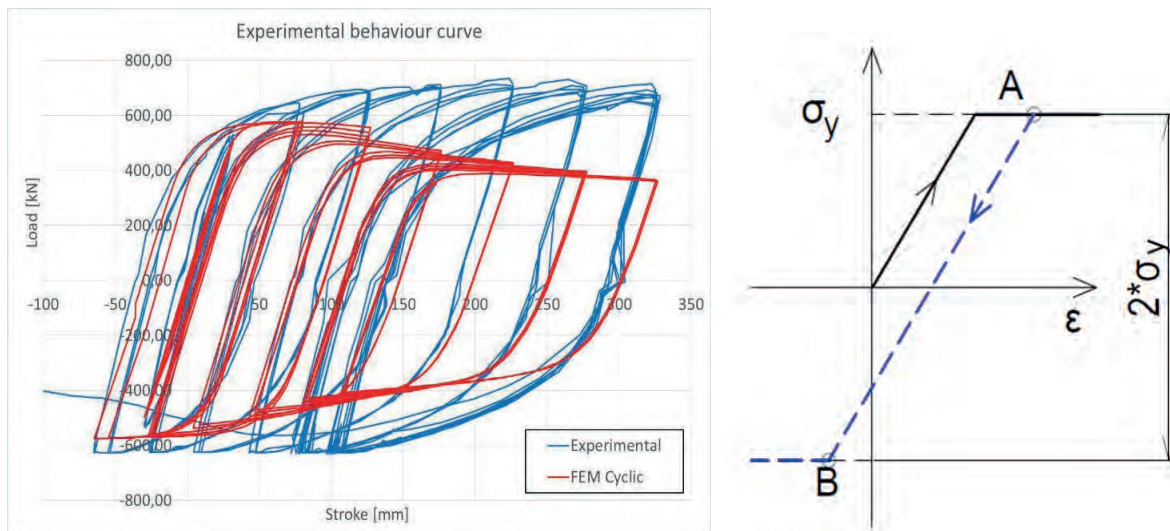


**Figure 10.** Hysteresis curve (left) and material law (right): Elastic – Perfect Plastic.
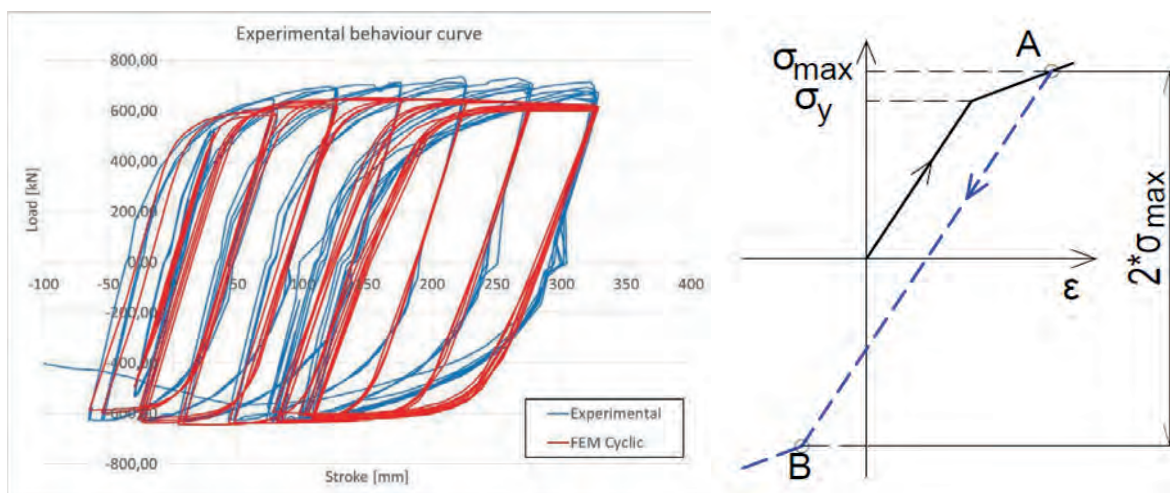


**Figure 11.** Hysteresis curve (left) and material law (right): Isotropic Hardening.
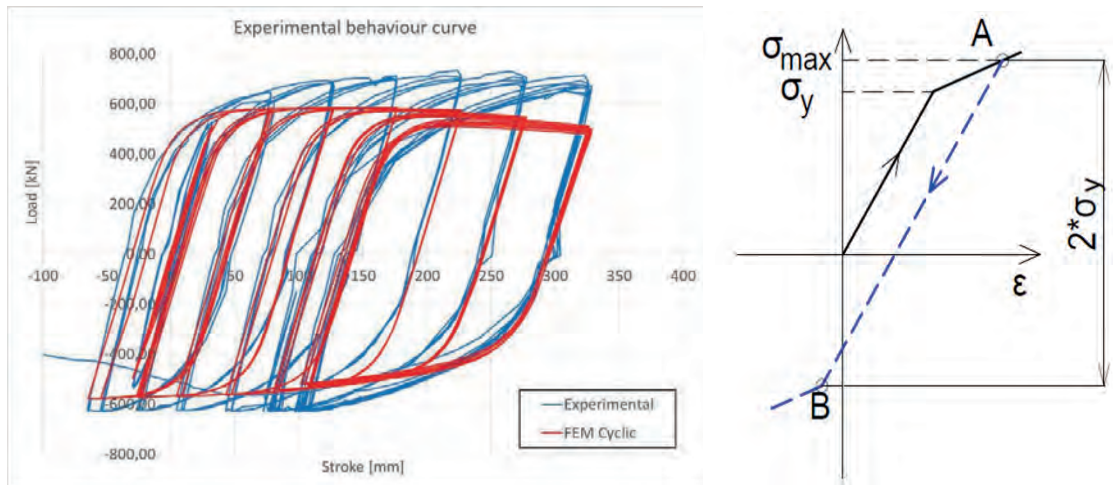
**Figure 12.** Hysteresis curve (left) and material law (right): Kinematic Hardening.

The obtained von Mises stresses are plotted in Figure 14, while the equivalent plastic strain plot is presented in Figure15 for maximum displacement. It can be observed that the maximum stresses are concentrated in the reduced area of the beam. Furthermore, no plastic deformations were found in the column. These observations are in accordance with the test results.
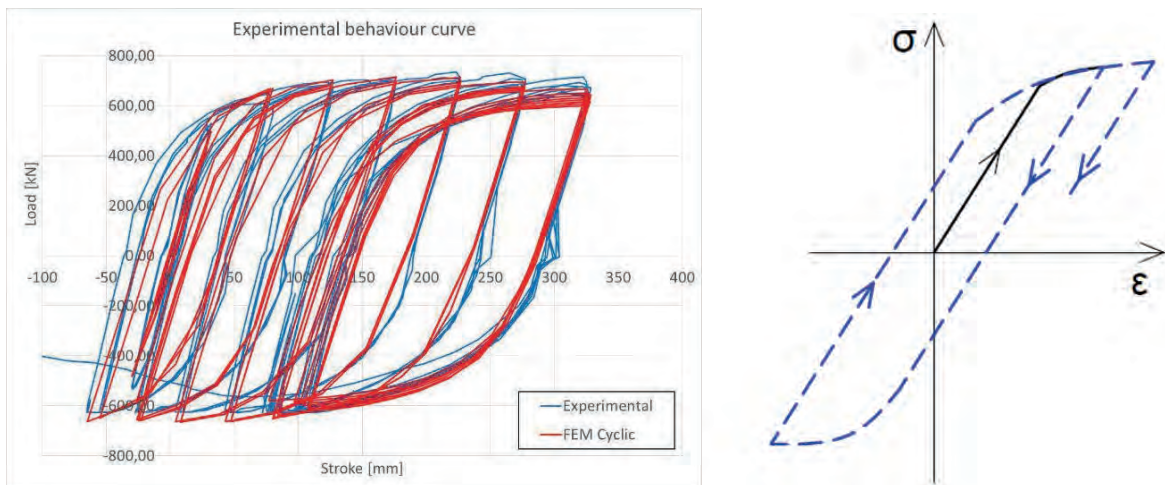


**Figure 13.** Hysteresis curve (left) and material law (right): Chaboche.
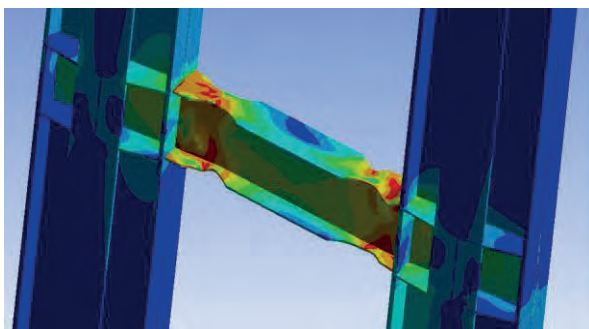


**Figure 14.** von Mises stresses.
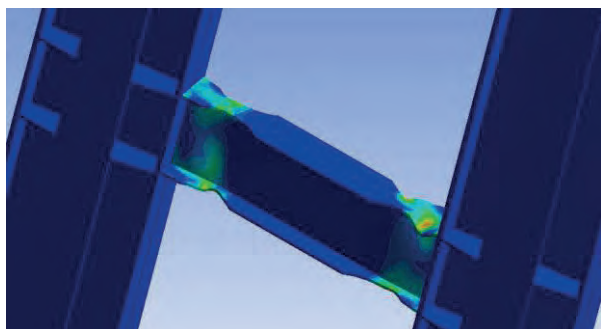


**Figure 15.** Plastic strain plot.

166

## Validation of the long beam specimen
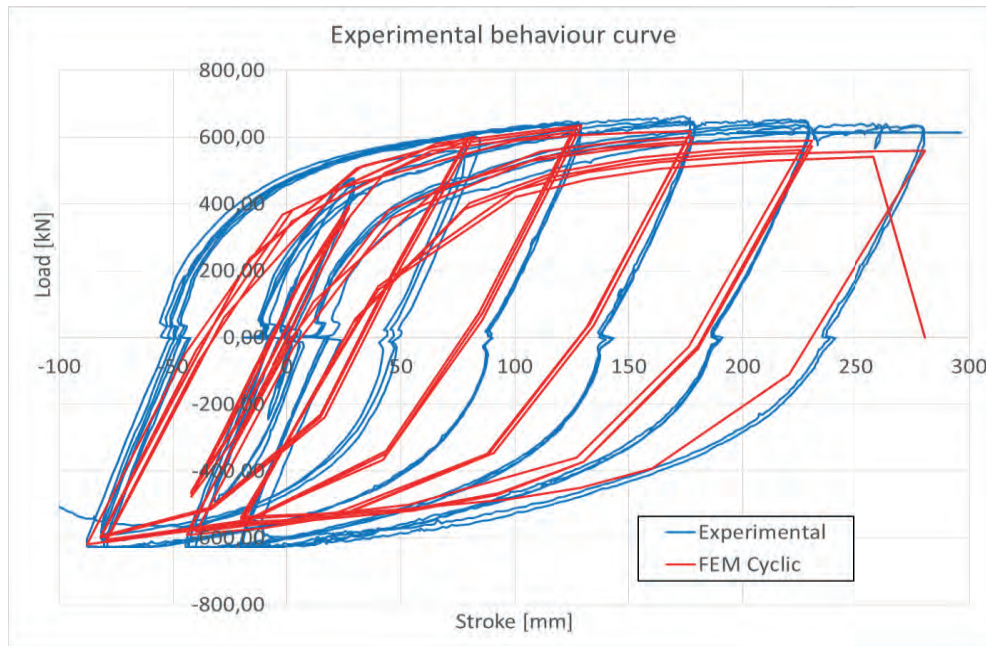


**Figure 16.** Hysteresis curve: RBS – L (length = 2210 mm).

## Parametric study

For steel structures, the uncertainty for material behaviour and geometry is usually limited. Even so, considering the experimental test results for the material properties, the S355 steel used for beam web was found to have the yield stress of 403 MPa (+13.5%), while for steel properties used in the beam flanges, the yield stress was found to be 373 MPa (+5%). According to norms, the Young modulus for steel has different values in Europe, USA and Japan.

From the geometric point of view, the width and thickness of flat steel used to create the welded beam profile influence the normal to shear stress ratio. The dog bone dimensions (depth and length) can influence the overall behaviour of the assembly. The software has the option to perform a parametric study, meaning that different samples are analysed and the results are plotted in terms of correlation and sensitivity charts.

On this line, using the calibrated reduced model, a parametric study was performed with respect to the following parameters:

Input parameters

   a.  Dog-bone depth   (30mm – 70mm)
   b.  Dog-bone length  (150mm – 350mm)
   c.  Flange thickness  (10mm – 30mm)
   d.  Web thickness    (10mm – 30mm)
   e.  Overall beam height   (350mm – 550mm)
   f.  Beam length      (800mm – 2500mm)

Output parameters

   a.  Maximum plastic strain
   b.  Maximum shear stress in the web of the beam
   c.  Equivalent maximum stress in the beam
   d.  Equivalent maximum stress in the flange
   e.  Force reaction

In order to be able to consider a higher number of samples for the sensitivity study, the computational time was reduced even more. For this, a monotonic analysis was defined. The monotonic analysis can successfully characterize the response of the structure.
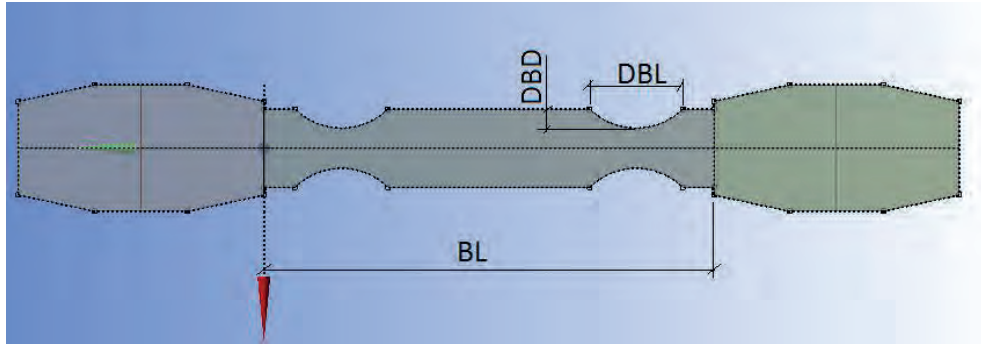
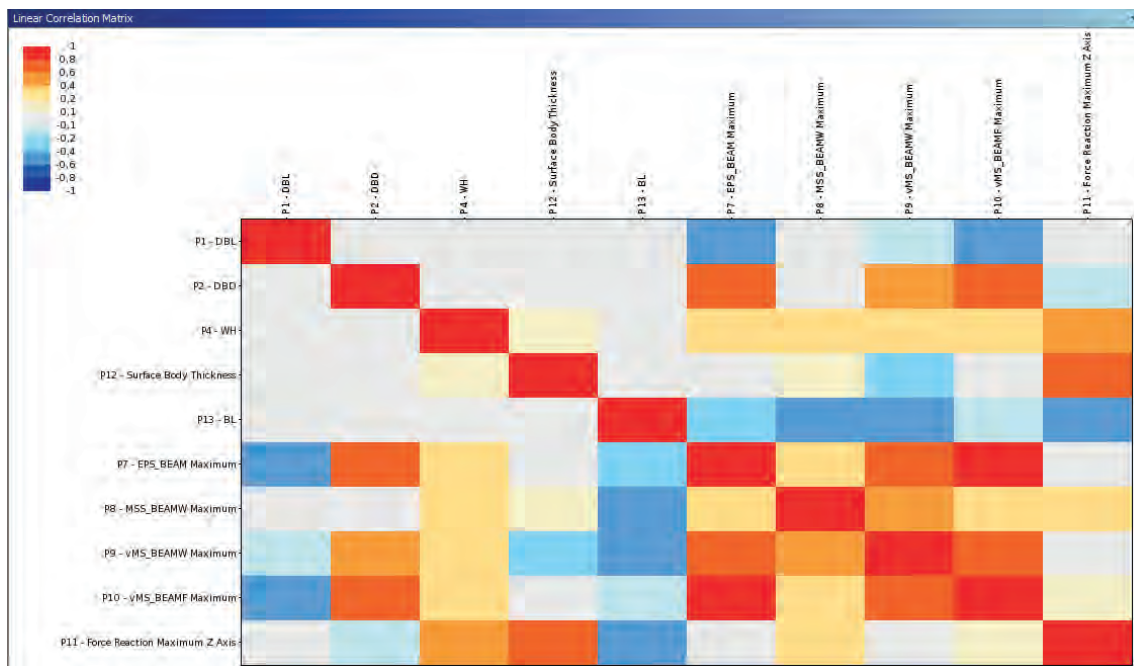**Figure 17.** Parameters definition



**Figure 18.** Correlation matrix

# Concluding remarks

A numerical (FEM) model has been developed and calibrated with the results from the experimental test. The hysteretic loops obtained by using different material models have been compared to the experimental one. The Chaboche model shows the best results and is most appropriate for this task.

Considering the results of the sensitivity study the following remarks can be made:

The beam length and the beam web thickness are important parameters to be considered in design of short coupling beams. The former changes the shear force in the critical cross section and the latter changes the cross-section area taking the shear stresses. In Figure 20 it can be observed that for the case of plastic deformations, the web thickness is the most important parameter.

Due to the fact that the beam flange width was reduced to change the location of the plastic hinge, the geometry of the dog-bone has become more important than the beam overall dimensions. The role of initial beam dimensions is to ensure the over-strength for the beam to column connection in accordance with the P100-1/2013 (or EUROCODE 8) provisions.

Having the calibrated model and the geometry, we can perform further numerical analyses that can aid the design and optimization the structure.
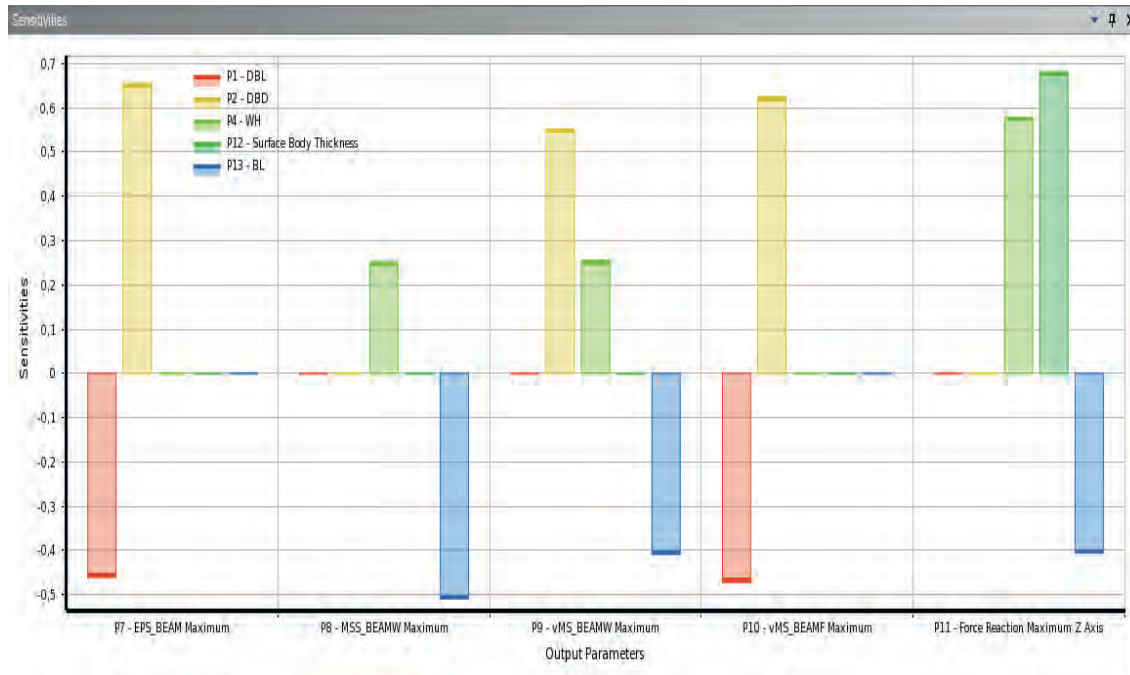
**Figure 19.** Sensitivity test

# References

ANSYS Release 16.2 documentation, Theory reference for ANSYS and ANSYS Workbench R16.2, ANSYS Inc., Canonsburg, Pennsylvania, USA, 2012

Budaházy V., Dunai L. (2013). Parameter-refreshed Chaboche model for mild steel cyclic plasticity behaviour, Periodica Polytechnica, *Civil Engineering* 57/2 p.139–155

Dinu F., Dubina D., Neagu C., Vulcu C., Both I, Herban S., Marcu  D. (2013). Experimental and numerical evaluation of an RBS coupling beam for moment-resisting steel frames in seismic areas, *Steel Construction*, Vol. 6 (1), p. 27–33

Dubina D., Dinu F., Stratan A., Marcu D., Voica F., Demeyere J. (2012), Proiectarea asistata de experiment a structurilor complexe, In: Proceedings of the 22th AICPS National Conference; Bucharest, Romania, 19 pp.

Eurocode 3 (2002). *Design of steel structures – Part 1-1: General rules and rules for buildings*. European Committee for Standardization

Eurocode 3 (2002). *Design of steel structures – Part 1-5: Plated structural elements*. European Committee for Standardization

Eurocode 8 (2004). *Design of structures for earthquake resistance.* European Committee for Standardization.

Federal Emergency Management Agency (2000). *FEMA 356: Prestandard and commentary for the seismic rehabilitation of buildings*. Federal Emergency Management Agency

P100-2013 (2013). *Romanian Seismic Design Code-Part I: Design Provision for Buildings*. Technical University of Civil Engineering Bucharest

Sokolov V., Wenzel F., Mohindra R., Grecu B., Radulian M. (2007). Probabilistic seismic hazard assessment for Romania considering intermediate-depth (Vrancea) and shallow (crustal) seismicity, *International Symposium on Strong Vrancea Earthquakes and Risk* Mitigation, Bucharest, Romania, 16pp

# Advanced modelling techniques for structures under cyclic and fatigue loads

*SHAMS Abdelrahman Emad[a], SIGAUAN Andreea[b], SILVA António[c], ALENCAR Guilherme[c], SITIKHU Prakash[d]*

*[a] German University in Cairo, Egypt*

*[b] Politehnica University of Timisoara, Romania*

*[c] Faculty of Engineering of the University of Porto, Portugal*

*[d] Bauhaus-Universität Weimar, Faculty of Civil Engineering, Germany*

*KÖNKE C., TAHIR A.M., BEINERSDORF H., RASCHE S.*

*Institute of Structural Mechanics, Bauhaus University Weimar, Germany*

*Materialforschungs- und Prüfanstalt an der Bauhaus-Universität Weimar, Germany*

## Introduction

This project was based on the study of the fatigue behaviour of a high pressure manifold (see Figure 1), which is a commonly used component in the automotive industry. Instead of modelling the entire component, only a representative part of the critical hole intersection region was considered, as shown in Figure 2 and Figure 3.

For this project work, the following tasks were devised:

- **Modelling of the specimen (circular disk with cross-drilled holes)**, in order to learn the basic numerical modelling and analysis procedures of ANSYS Workbench;
- **Investigate the influence of mesh and specimen typology on the maximum stresses**, by testing different mesh resolutions, as well as the different geometries of both the specimen and the cross holes;
- **Study initial stressing and residual stress conditions**, thus showing how induced residual stresses inside the specimen affect the fatigue strength;
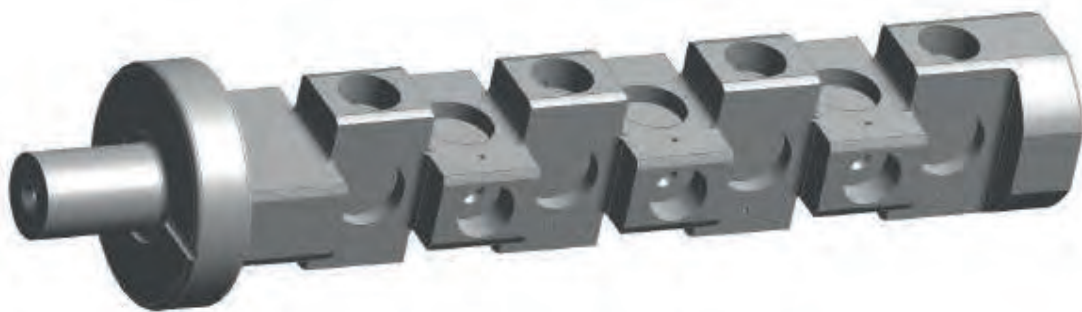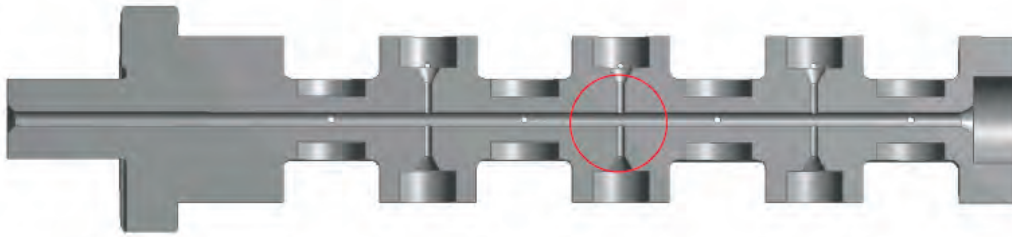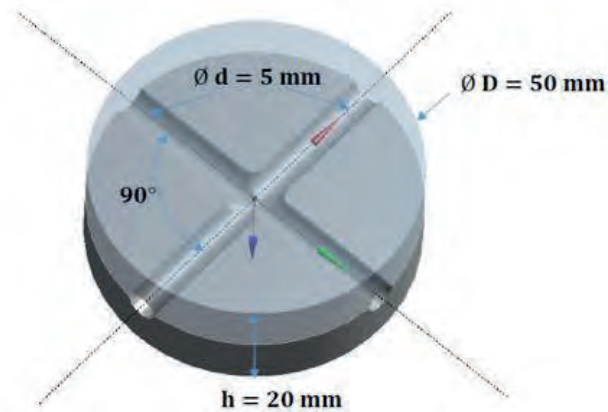- **Examine the effects of cyclic load pressure with variable averaged stress and stress amplitude**.



**Figure 1**. 3D model of a manifold

**Figure 2.** Critical hole intersection of manifold



**Figure 3.** Considered disk model

# Numerical modelling

In this project the ANSYS Workbench software was used to define the numerical model of the specimen, as well as to analyse its behaviour under internal pressure conditions. Different modelling aspects were considered, such as the definition of the material properties of the specimen, its geometry, loading and the required output of the analyses. Each aspect may be defined from the model tree of the software (see Figure 4).

One important aspect to consider in the modelling of the steel disk was the symmetry planes of the piece, which (if considered in the numerical model) allow for a reduction in the computational time, or even for more detailed meshing strategies without the compromise of the available calculation resources. As such, only a portion of the specimen was ultimately modelled in ANSYS, as shown in Figure 5. It is important to note that these symmetry planes automatically act as boundary conditions of the model in the ANSYS software. The only applied load was a normal uniform pressure at the whole surface.
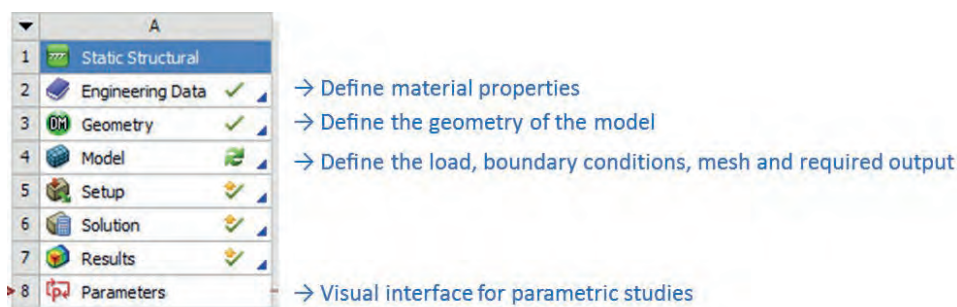


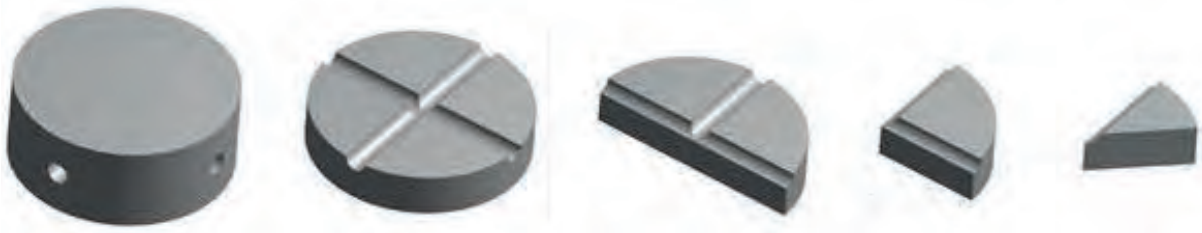**Figure 4.** ANSYS Workbench model tree

**Figure 5.** Symmetries of the specimen

## Sensitivity study

In the context of this project, a number of sensitivity studies were carried out, namely in terms of the best mesh refinement strategy, the influence of the hole intersection geometry ("smoothing" of the intersection edges), and, finally, the influence of specimen geometry (disk thickness-to-hole ratio). All analysis were carried-out with linear elastic material behaviour.

Regarding the mesh refinement, two approaches were evaluated. The first (Figure 6) consisted on the definition of the finite element size in the model. Dimensions between 8mm and 0.4mm were considered, with ranges in the total number of elements from 71 to 315 000, respectively. The influence of the element size (and the respective total number of elements) was evaluated by comparing the ratio between the maximum von Mises stresses in the model and the applied normal pressure (100MPa), defined as the stress concentration factor, k.

Analysis of the results shown in the previous figure allow concluding that a reduced number of elements is not able to accurately capture the behaviour of the specimen, as the difference between the obtained values of k. For the coarsest mesh (8mm element size), the peak von Mises stress was about 60% of the real value (estimated as 4.76 with the most refined mesh). This difference tends to decrease as the number of elements grows, reaching values close to the exact value at around 25 000 elements (1mm element size).
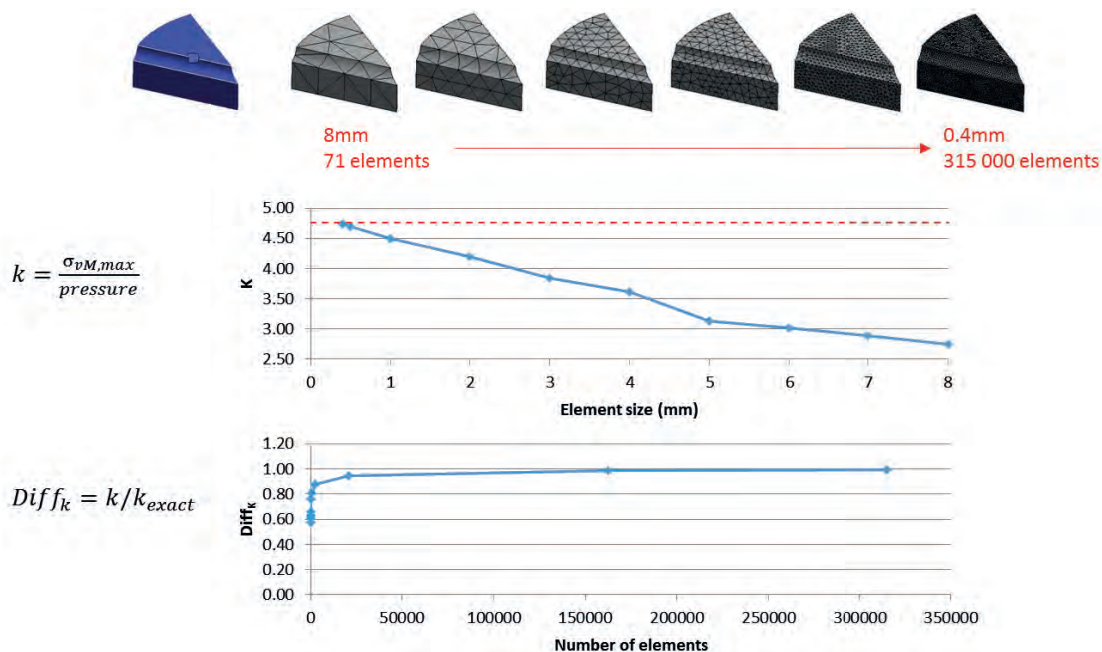


**Figure 6.** Sensitivity study of the mesh refinement (global element size)
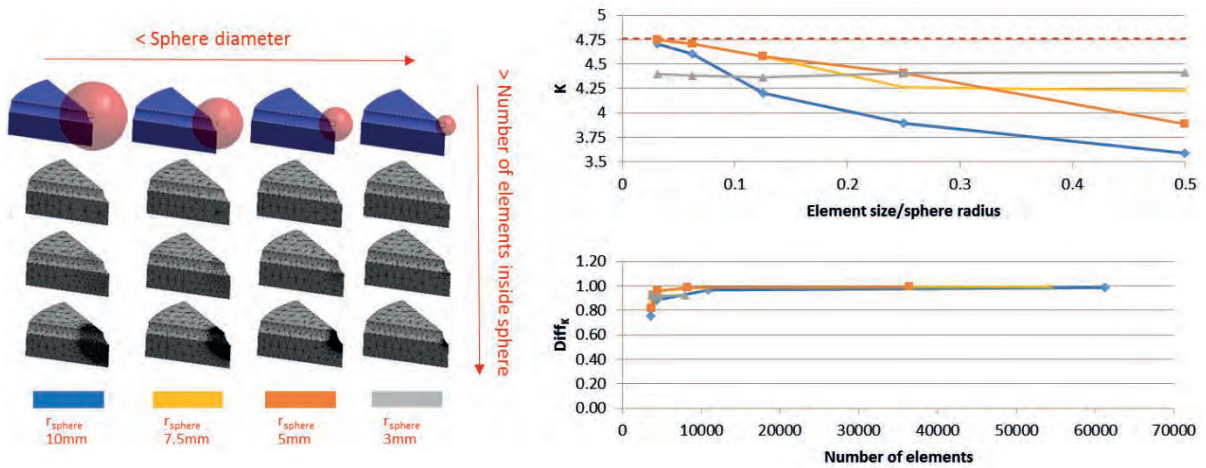
**Figure 7.** Sensitivity study of the mesh refinement (default mesh + sphere)

It is important to note that whilst an increase in the number of elements (≈150 000 and ≈300 000 for 0.5mm and 0.4mm elements, respectively) leads to more accurate values of k (as the ratio between the obtained value and the exact values tends to 1.0), this is achieved by a substantial increase in the computational cost of the model. However, the results clearly indicate that this does not benefit the quality of the numerical results, as they remain almost the same.

The second mesh refinement approach was more elaborate. Basically, define a more refined mesh in the region of the model where the peak stresses will occur, whilst the remaining model was meshed with the default mesh from ANSYS. This meshing strategy was attained with the definition of a sphere (centred at the point of interception between all symmetry planes). Multiple values of both the radius of the sphere and the size of the finite elements inside that sphere were considered (cf. Figure 7).
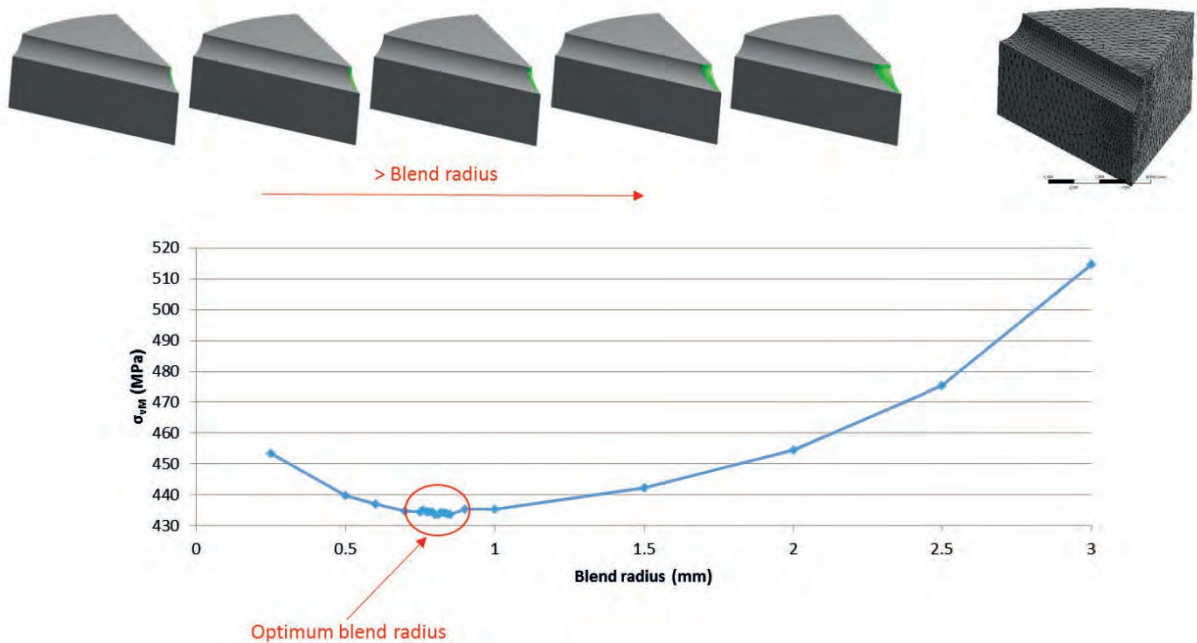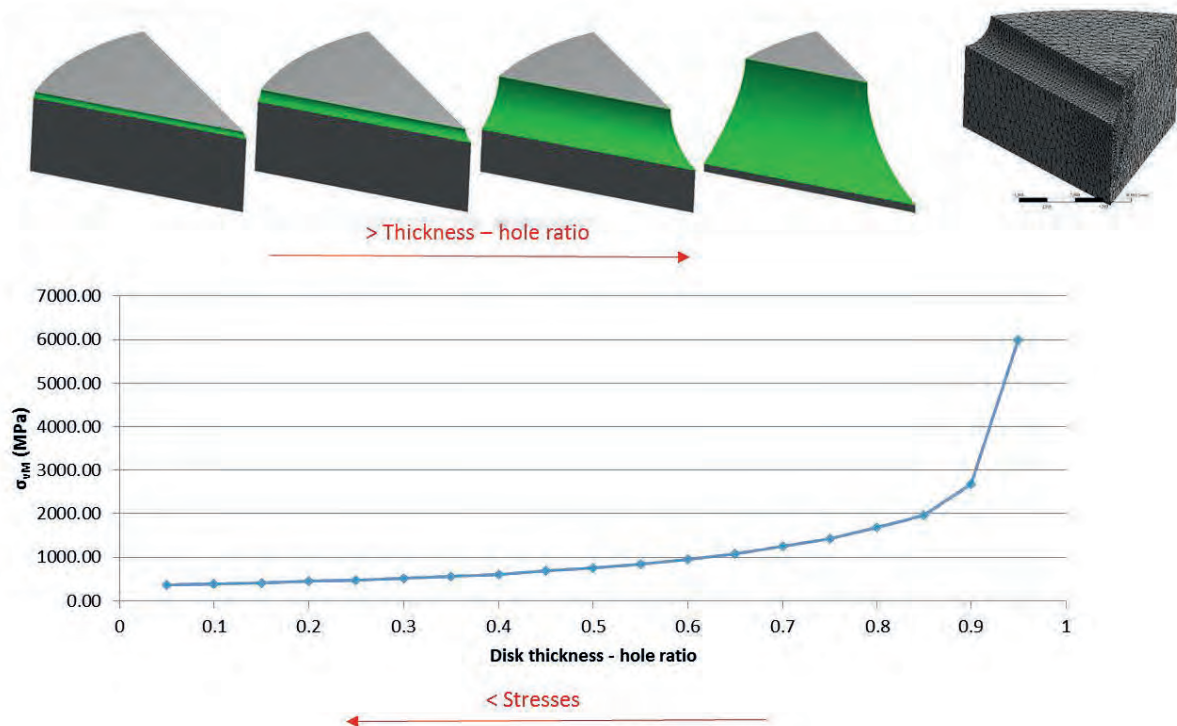


**Figure 8.** Sensitivity study of the blend radius

**Figure 9.** Sensitivity study of the specimen geometry

As one may infer from the previous, the numerical models were able to accurately represent the behaviour of the specimen (values of k close to the exact value) for a minimum total number of elements close to 10 000. Thus, by concentrating the mesh refinement to the area surrounding the critical region (specimen tip), the computational cost of the model is reduced, in comparison to a scenario in which the full model is mesh with a high degree of detail. It is important to note that for a higher number of elements could be used (> 10 000), but, as shown in Figure 7, the added computation time cost would not benefit the results.

Moving on to the influence of the intersection geometry, namely the radius of the "smoothing"/blending of the intersection edges, multiple values were evaluated. Their effect on the behaviour of the specimen was evaluated by comparing the evolution of the global peak von Mises stress in function of the blend radius, as shown in Figure 8.

Analysis of the results shown in the previous figure allow concluding about the importance of "smoothing" the hole intersection edges, as the peak stresses may be lowered (or increased) in comparison to the base scenario (no blending). The numerical results showed that it is possible to reduce the critical stress in the specimen from 476MPa to close to 430MPa, simply by modifying the edges of the hole intersection. The optimum blend radius was found to be around 0.8mm. For higher values, the maximum stress increases, even surpassing the value of the base scenario for radius higher than ≈2.5mm. This roughly equates to the radius of the hole in the base scenario, meaning that if the radius of the blend is higher than the radius of the hole itself, the critical stresses will be the highest.

The final sensitivity study carried-out concerned the influence of the specimen geometry, namely by changing the disk thickness-to-hole ratio (keeping the thickness and changing the hole radius). Hole diameters between 5% and 95% of the disk thickness were considered, as shown in Figure 9.

As shown in Figure 9, the peak stress in the specimen was lowest for the minimum hole radius considered. As the hole increases in dimensions, so does this stress. In comparison to the minimal

hole, stresses were approximately doubled for a scenario in which the hole occupies half the disk thickness. For higher values, the increase follows an almost exponential distribution, reaching values almost 10 times the initial value for the largest hole dimensions.

## Initial stressing and residual stress

Besides the parametric study performed in the previous sections to reduce the stress concentration factor at the crack-tip, the effect of introducing residual stresses on the component is also discussed on this section. The process of change the stress state of a mechanical component is also called Autofrettage. Basically, Autofrettage is a metal fabrication technique in which a pressure vessel is subjected to enormous pressure, causing internal portions of the part to yield plastically, resulting in internal compressive residual stresses once the pressure is released. The goal of Autofrettage is to increase the durability of the final product.
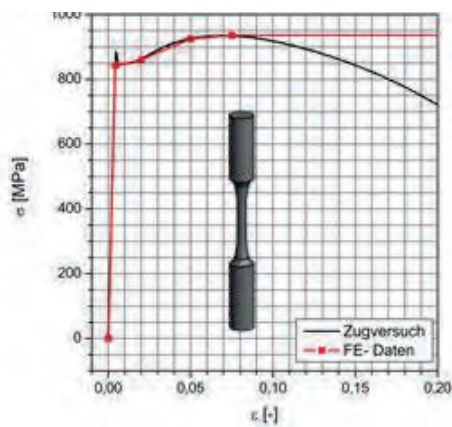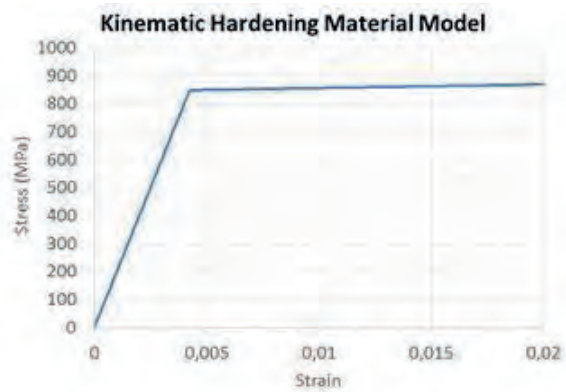


**Figure 10.** Tensile test (material 42CrMo4)
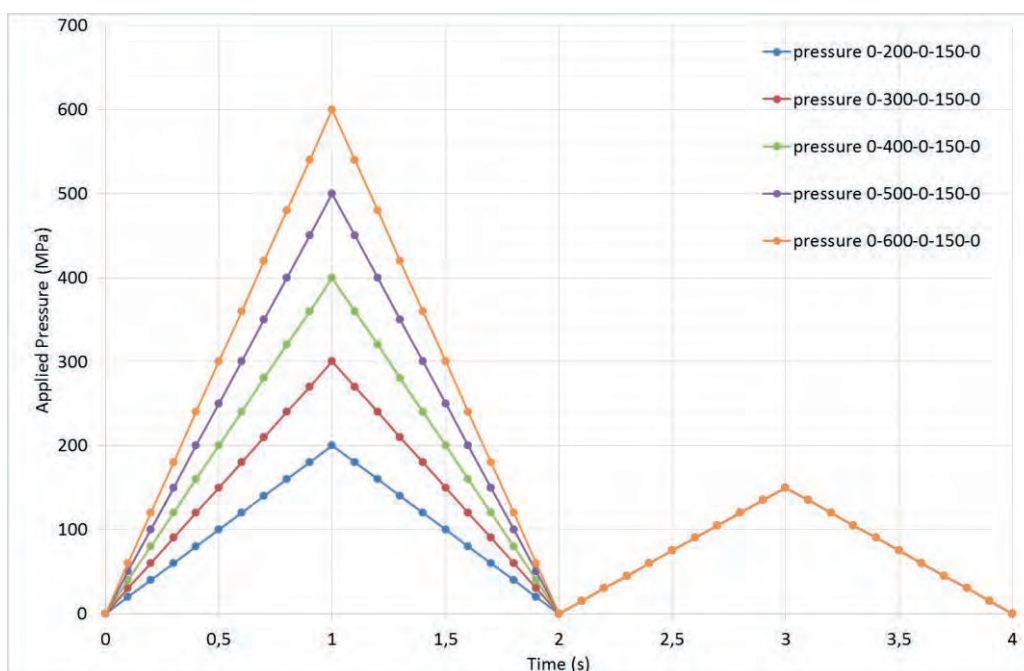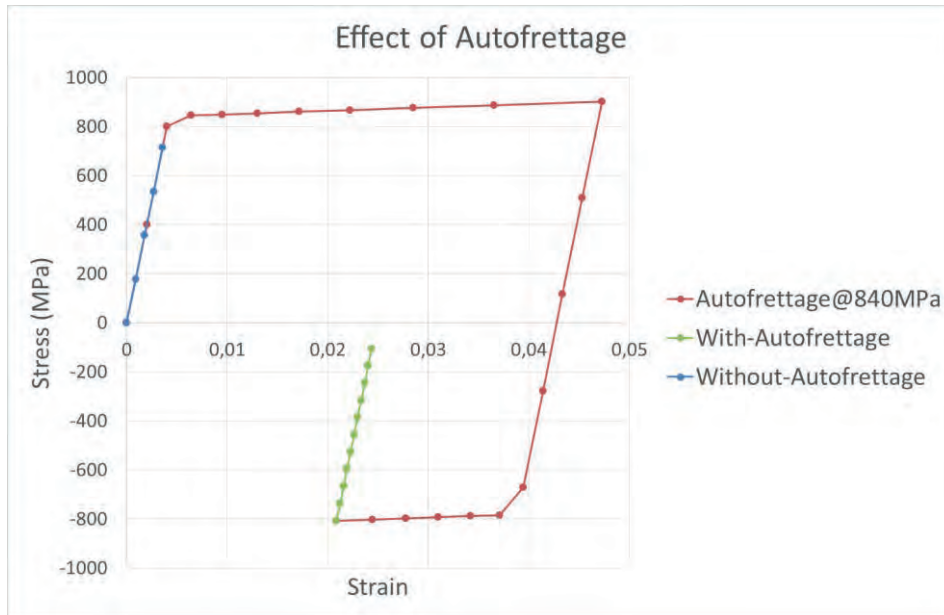
**Figure 11.** Simplified bilinear model



**Figure 12.** Different load cycles that were applied to the components

**Figure 13.** Typical stress-strain response for Autofrettage process at the crack-tip

The Autofrettage process can be simulated in numerical studies by performing non-linear material analyses. Thus, it was applied different load cycles in the component (Figure 11), by using the Bilinear Kinematic Hardening Model, which is a simplified model of the Elasto-plastic behaviour that was observed on experimental tests (Figure 12) of the same material used for the component (42CrMo4).

The loads cycle were applied in such a way that the first peak varies from 200MPa to 600MPa in steps of 100 MPa. This first cycle is also called the Autofrettage cycle, which is responsible to plastify the region of interest. At this first cycle, the path followed in the stress strain curve is represented by blue (still in elastic regime) and then by the red line, which corresponds to the plastification caused by the Autofrettage. Therefore, during this phase the crack-tip is supposed to reach the yield stress of the material (840MPa). Then, for the second cycle, the region of interest which is most prone to develop cracks is already plastified, and now it remains only in the elastic regime.
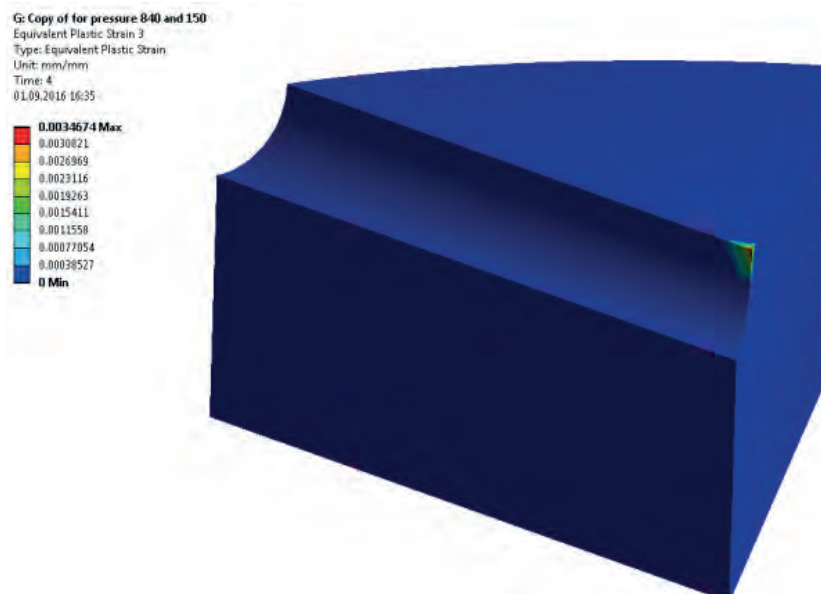


**Figure 14.** Typical plastic strains at the crack-tip
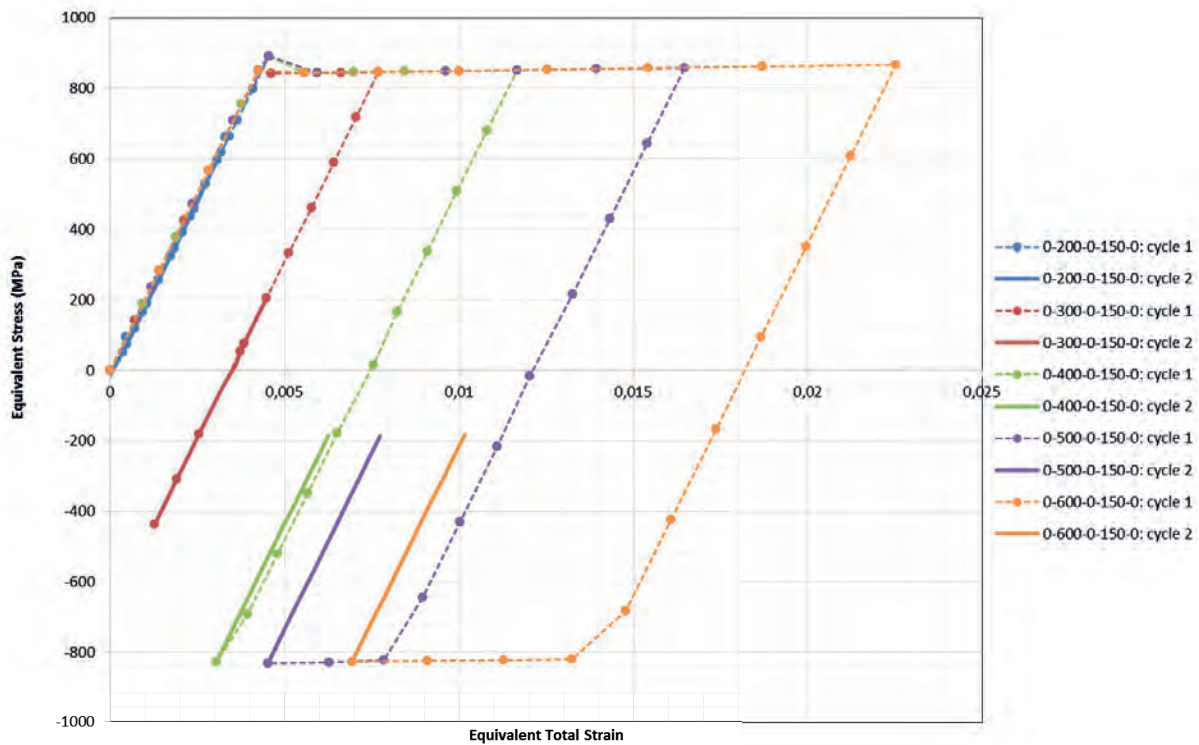
**Figure 15.** Typical plastic strains at the crack-tip

The final mean stress is the most important parameter in this kind of process. The process is executed in such a way that the final mean stress released on the material be negative, i.e. a compressive stress. As can be seen in Figure 14, which shows the plastic strains developed on the whole body, only the crack-tip was plastified during this analyses.

For the different load cycles applied in the numerical analyses, Figure 15 shows the different stress-strain responses obtained. In this Figure, is possible to observe that the first applied load cycles (in blue, 0-200-0-150MPa) remains only in the elastic regime. The load cycle in red releases at the end of the analysis a mean stress in tension, which is not desirable. The remaining applied load cycles reaches the yield stress, releasing at the end of the analysis a negative mean stress with almost the same value.
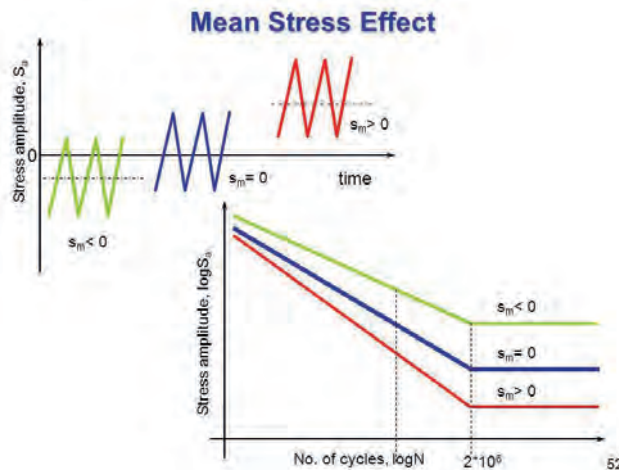


**Figure 16.** Mean stress effect on the Wöhler Curve (increase of the number of cycles required to the fatigue failure)

177

**Table 1.** Main load characteristics of each applied pressure cycle

| First cycle | Max Stress [MPa] | Min Stress [MPa] | Mean Stress [MPa] | Stress Amplitude [MPa] | R |
|---|---|---|---|---|---|
| 200 | 663,76 | -16,06 | 323,85 | 339,91 | -0,02 |
| 300 | 204,75 | -437,08 | -116,17 | 320,92 | -0,47 |
| 400 | -185,07 | -827,02 | -506,05 | 320,98 | 0,22 |
| 500 | -186,92 | -829,95 | -508,44 | 321,52 | 0,23 |
| 600 | -181,56 | -826,34 | -503,95 | 322,39 | 0,22 |

The influence of the mean stress on the fatigue life can be seen in Figure 16. For negative mean stresses, it is possible to obtain a greater fatigue life. This can be seen in the fact that, for the same constant stress amplitude, it is possible to obtain a greater number of cycles up to failure, as shown in the Wöhler curve (stress amplitude against number of cycles up to fatigue failure). Also, Table 1 shows the main parameters that have to be evaluated in a fatigue analysis in terms of stress response. The most important aspect to be evaluated in the Autofrettage process is the mean stress. As can be seen, the increase of the value of the first load cycle results in lower mean stresses, from a tensile mean stress of 323,85MPa to a compressive mean stress of -503,95MPa.

## Conclusion

During this project, a part of mechanical component was modelled employing the Finite Element Method, which was possible by using the ANSYS Workbench Software. Also, time-dependent analyses were performed with material non-linearity, in order to evaluate the stress-strain curves at the crack-tip in the context of the Autofrettage process. Thus, the main conclusions of this study are presented below:

- During the numerical analyses, it was possible to observe the importance of the symmetries adopted in the modelling strategy. It was noted that the computational time was much lower for finite element models with symmetry, without affecting the accuracy of the results, comparing the stress concentration factors that were obtained for the full model in previous works;

- Also, the strategy adopted for the mesh refinement only at the crack-tip revealed to be very useful. Once again, it implied on reduction of the computational time;

- It was performed a parametric study by applying a "smoothing" radius on the holes intersection, by changing the thickness-to-hole ratio and also by varying the hole diameter. All these parameters revealed to influence the stress concentration factor at the crack-tip. The parametric study conducted to an optimized typology of the component in terms of reducing the stress concentration at the crack-tip, which increases the fatigue strength of the component;

- Finally, the Autofrettage process that was conducted allows for an increase on the fatigue life of the component. Different loads cycles were applied to study the influence of varying the intensity of the first load cycle peak. The residual compressive stress introduced by the pressure cycles applied to the component at the final steps increases the fatigue life, mainly due to the fact that the probability of have fatigue cracks on regions of high compressive stresses is very low. Indicators of the best Autofrettage pressure cycle were shown (0-400MPa -0-150MPa).

# Vortex Induced Vibrations on Long-Span Bridges

CONTESTABILE Carlo [a], KENÉZ Ágnes [b], PIERINO Sonia [c],

[a] Università degli studi di Genova, Italy

[b] Budapest University of Technology and Economics, Hungary

[c] Università degli studi di Genova, Italy


*Chair of Modelling and Simulation of Structures, Bauhaus-Universität Weimar, Germany*

## Abstract

The phenomena of the vortex-induced vibrations have been investigated numerically applying the vortex particle method. The shape of the cross-section has large influence on the flow and on the vibration as well, therefore different geometry were tested. The optimization of the shape was performed, and the goal of the optimization was to reduce the maximal and the mean squared displacement of the structure.

## Introduction

Vortex-induced vibrations may occur on slender structures such as chimneys, towers and bridge decks. This study is focused on long-span bridges, therefore the phenomenon is represented by the following example.

Alconétar Viaduct which is a deck arch bridge was built in 2016. The main span of the bridge 234 m, the rise is 42.5 m and the span of the arch is 220 m. The arches were rotated around the horizontal axis in the construction phase. After the first parallel span was closed, the arch started to oscillate from a 20 km/h wind which generates lift forces acting on the structure, and push the arch up and down. On the other hand, when the wind speed increases above 30 km/h, the problem disappeared. The problem was resolved by welding metal flaps or deflectors along the edge of the arch ribs.[2]



**Figure 1.**     General View of Alconétar Bridge (left), vortex-induced motion of the bridge (right) [3, 4]

This phenomenon is the so called vortex-induced vibration (VIV) are motions induced on bodies interacting with an external fluid flow, and these motions result in periodical irregularities on this flow as well. Since the vortices are not generated symmetrically around the body, different lift forces arise on each side of the body, which leading to motion transverse to the flow.

The phenomenon of lock-in happens when the vortex shedding frequency becomes close to a natural frequency of vibration of the structure. The vortex induced vibration is not instability and not destructive, it is a self-limiting phenomenon. (differently from what would be expected in a case of resonance). [1] A full analytical description of the phenomenon is still not available, and the procedures used to determine vortex-induced vibrations of structures are still rough. [1]

The Strouhal number relates the frequency of shedding to the velocity of the flow and a characteristic dimension of the body:

$$St = \frac{f_v\,D}{U} \tag{1}$$

where

 fv : vortex shedding frequency of a body at rest (Strouhal frequency)

 D : the diameter of the circular cylinder

 U : the velocity of the ambient flow.

The phenomena have been investigated numerically applying the vortex particles method. The influence of the shape of the cross-section on the flow was studied.

First, static analysis was carried out to calculate the Strouhal number and determine the critical velocity for each case. After that the dynamic analysis were carried out (Figure 2) and the maximum and the root mean square of the displacements were calculated.
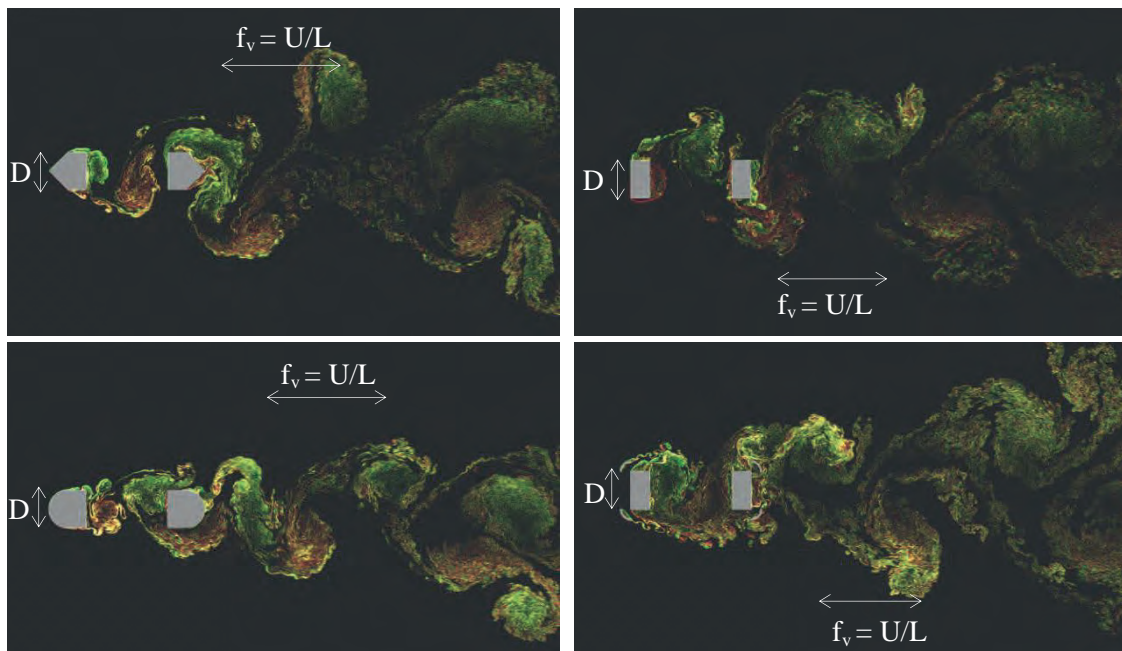


**Figure 2.**   Generated vortices

As we can see in Figure 3, the largest maximum displacement belongs to the 14 m/s wind speed, which is the critical velocity.

The goal of the study is to find the minimum value of the maximum and root mean square (RMS) displacement of the body. The optimized cross-section shape was the so-called semi-circle attached to the rectangular, because the maximum displacement was the smallest in that case. On the other hand, lower critical velocity belongs to this case, which can be unsafe and fatigue analysis should be carried out. (Figure 4).
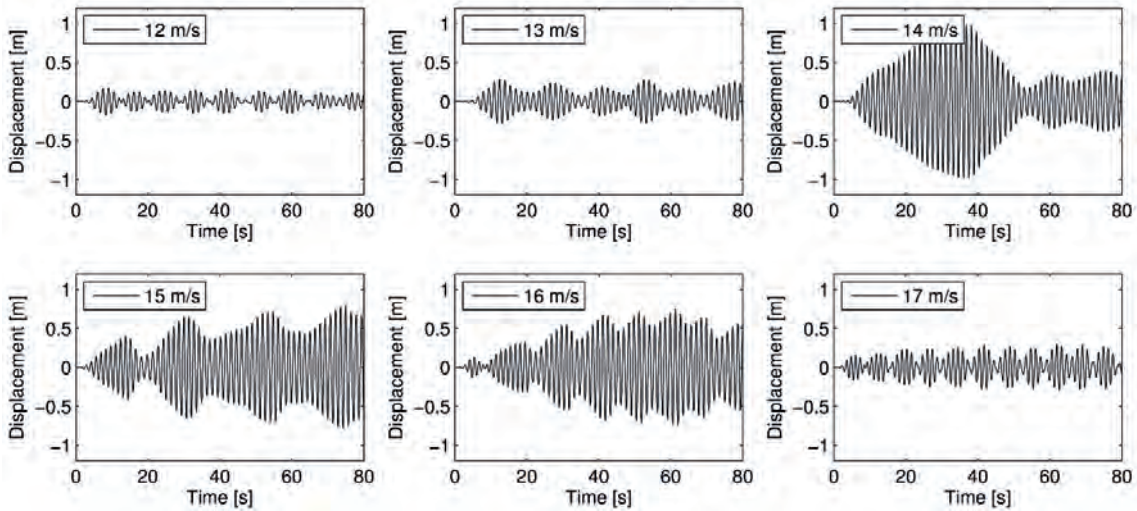
**Figure 3.**     Time history function of the double rectangular cross-section
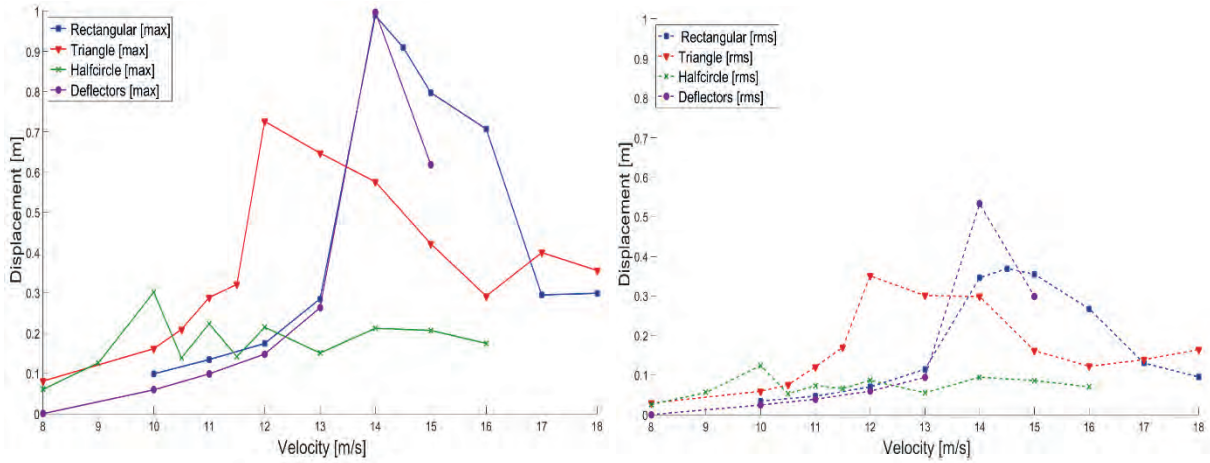


**Figure 4.**     Maximum and RMS displacements is depicted as a function of the wind velocity
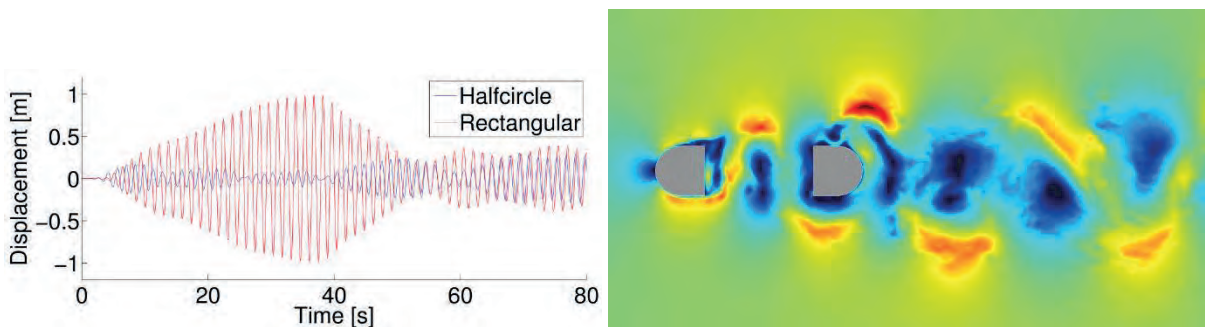


**Figure 5.**     Time history function (left) and the velocity field (right) of the semi-circle cross-section

The velocity field can be seen in Figure 5, the blue colour indicates the lowest value of the velocity and the red indicates the highest velocity.

# Conclusions

The vortex induced vibration is not instability and not destructive, it is a self-limiting phenomenon, so the maximum displacement of the structure is not infinity. The shape of the cross-section has large influence on the flow and on the vibration as well, the optimized shape was the so-called 'semi-circle' case.

If the amplitude of the stresses passes the threshold the fatigue analysis has to be carried out. In the other hand the comfort of the passengers is important as well, the vibration perception should be minimized.

We should mention that the effect of the tuned mass damping can be studied as well, and moveable flaps can be installed on the structure to reach a favourable phenomenon.

# References

[1] Wikipedia, Vortex-induced vibration.
    https://en.wikipedia.org/wiki/Vortex-induced_vibration, 09.01.2016.

[2] Tajo River Bridge.
    http://www.highestbridges.com/wiki/index.php%3Ftitle%3DTajo_River_Bridge, 09.01.2016.

[3] Wikipedia, Arcos de Alconétar - Río Tajo, 09.01.2016.

[4] Morgenthal G. (2016). PROJECT 6: WIND-INDUCED VIBRATIONS OF LONG-SPAN BRIDGES, Bauhaus Summer School 2016, course material.

[5] Svend Ole Hansen (2007). Vortex-induced vibrations of structures, Structural Engineers World Congress 2007, Bangalore, India http://www.eurocodes.fi/1991/1991-1-4/background/Hansen_2007.pdf, 09.01.2016.

*Conduction of wind tunnel experiments in part of the group work in Project No. 6 (Photo: B. Proschak)*

# Flutter Phenomenon of Long-Span Bridges

*IVANOVIĆ Nikola[a], LUČIĆ Sanda[b], ŠPIRIĆ Stefan[a]*

[a] *University of Belgrade, Serbia*

[b] *University of Josip Juraj Strossmayer of Osijek, Croatia*


*Chair of Modelling and Simulation of Structures, Bauhaus-Universität Weimar, Germany*

## Abstract

This paper showcases the analysis of the flutter phenomenon of Lillebælt (Little Belt) suspension bridge in Denmark. Total length of the bridge is 1700 m, with the largest span 600 m long. Three different methods were used in order to obtain the critical wind velocity: fully analytical method, forced vibrations method and fully coupled CFD simulation. Various wind speeds were used: from 70 m/s to 100 m/s, increasing by 5 m/s, in order for the divergent response of the structure to be manifested. Simulations were performed using software VXFlow.

## Introduction

The flutter phenomenon was first observed in 1940, when the Tacoma Narrows Bridge collapsed soon after opening. The bridge itself was designed to sustain wind loads produced by wind velocities higher than the one which caused this previously unknown type of instability. This phenomenon is defined as the divergent response of a structure which is the result of coupling of vertical and torsional degrees of freedom, in which case the motion of the structure further increases the internal forces. Term „flutter" is usually mentioned in the context of coupled degrees of freedom; however, flutter can form in only one oscillation mode, usually the torsional mode. The assumption of which modes will couple is not as straightforward as it may seem to be; coupling depends on both the mode shape and the differences between the natural frequencies of the torsional and bending modes. When the torsional and bending modes are coupled, the structure vibrates with a frequency which is close to the mean frequency of the modes included in the coupling. For the purpose of analysing the flutter phenomenon, Lillebælt suspension bridge in Denmark was used as a model.
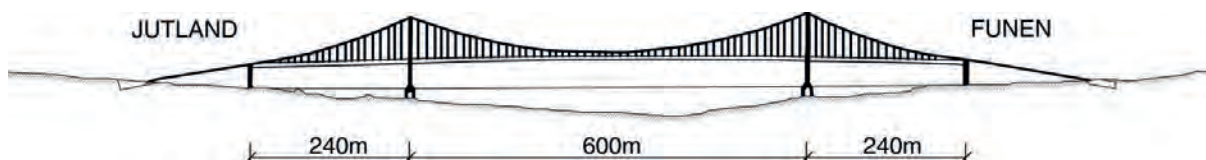


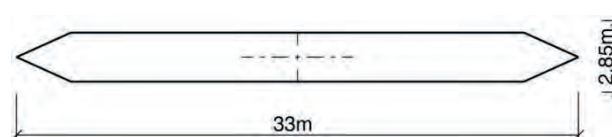**Figure 1.** Bridge dimensions [3]



**Figure 2.** Bridge deck [3]

# Reference object

The analysed object was the Lillebælt (Little Belt) suspension bridge in Denmark. Most important dimensions of the bridge can be seen in the figures 1 and 2 below. A numerical model in SOFiSTIK was used to obtain the eigenmode shapes and frequency values. First bending mode occurs at frequency value of 0.156 Hz while the corresponding value for first torsional mode is 0.5 Hz.

# Analysis methods

Various methods can be used for the purpose of obtaining the critical wind velocity. Methods used in this analysis are: a) fully analytical method based on the potential flow theory, b) forced vibrations method and c) fully coupled CFD simulation. Method a) uses Theodorsen's approach, which is applicable only for flat plates, but can be used in some cases as an indicator. In this method both the structural and aerodynamical models are analytical. Method b) involves the application of the forced vibrations with defined period and amplitude. In this method, the structural model is numerical while the aerodynamical model is analytical. Shown in Figure 3 are the aerodynamic derivatives used in the analysis. Method c) uses vortex particle method, in which the particles, defined as calculation points, are being produced as the wind flow interacts with the model. In this method, both the structural and aerodynamical models are numerical.
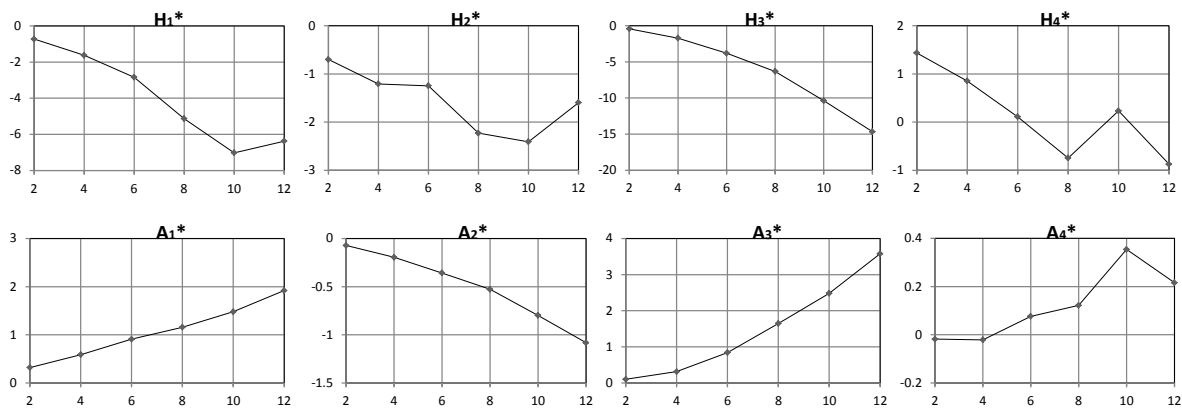


**Figure 3.** Aerodynamic derivatives

# Results

The main aim of the analysis was to determine values of critical velocities which will cause the aeroelastic instability phenomenon known as flutter. Different approaches provided different results, as shown in Table 1.

It can be concluded that the obtained values of critical velocities are not so different for the analysed model, but these values could be substantially different, which depends not only on the cross-section shape, but also on the geometrical characteristics of the structure, in general. Shown in Figure 4is the response of the structure which is represented by one cross-section.

**Table 1.** Critical wind velocity values

| Analysis method | Critical wind velocity [m/s] |
|---|---|
| Theodorsen | 94 |
| Scanlan | 101 |
| Fully Coupled CFD | 98 |
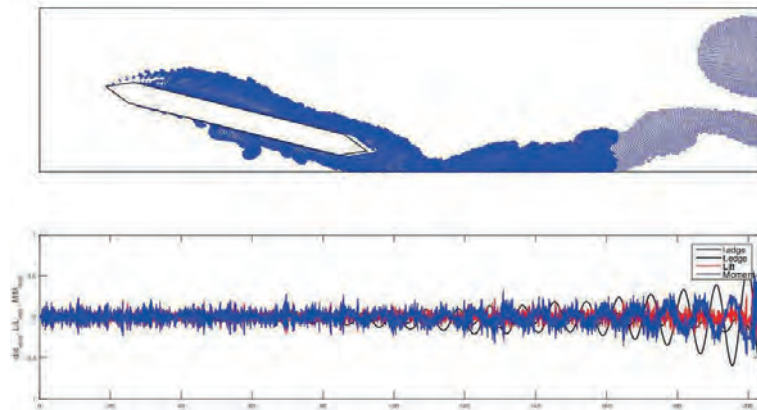
**Figure 4.** Divergent response of the single-slice model

The model of the bridge, represented by twelve adjacent cross-sections excited to flutter, is shown in Figure 5.



**Figure 5.** Divergent response of the multi-slice model

# Conclusions

Because of the destructive character of flutter instability, this is the first phenomenon that should be accounted for when designing a bridge. Usually, the shape and the material of the cross-section can be estimated according to the span-length. The wind velocity measurements can provide the maximum wind velocity for a certain return period, which is then multiplied by a safety factor. Engineers task is to ensure, using the given analysis methods, that the flutter will not form for that wind speed. This type of phenomenon is extremely destructive, because the collapse is inevitable after a certain limit defined by the critical wind velocity. However, the flutter effect is excluded at the beginning of the design of long-span bridges, so it does not represent a problem for a fully functional bridge. Even though greater problems for bridges are vortex induced vibrations and buffeting effect, it is mandatory to take flutter into consideration while designing these structures.

# References

[1]   Scanlan R.H., Simiu, E. (1996). *Wind effects on structures,* John Wiley & Sons, Inc., New York

[2]   Strømmen E. (2010). *Theory of Wind Aerodynamics,* Springer-Verlag Berlin Heidelberg

[3]   Morgenthal G. (2016), PROJECT 6: WIND-INDUCED VIBRATIONS OF LONG-SPAN BRIDGES, Bauhaus Summer School 2016, course material.

*Visit of the BUW laboratories and conduction of experiments in part of project No. 3* (Photo: B. Proschak)



*Participants at project work* (Photo: B. Proschak)

# Papers contributed
# by the participants

# 2016

Full papers are available at:

# Fatigue of lean duplex welded details after post-weld treatments

*COOLS Thomas, ROSSI Barbara*
*TC Construction, Department of Civil Engineering, KU Leuven*

**Abstract.** Duplex stainless steel combines high mechanical properties and excellent corrosion resistance. In recent years, the application of lean duplex has progressed, the effective utilisation of which is however often limited by the fatigue strength of critical welded details. The fatigue resistance of duplex welded details was yet scarcely investigated. In this project, this topic will be studied through experimental investigations comprising the determination of fatigue strength of full penetration single V butt welds and T fillet welds. As-welded details and details submitted to post-weld treatments (PWT) will be studied. Last, one duplex longitudinal stringer welded to a cross girder will be studied under fatigue. A geometrically and materially non-linear finite element model, calibrated against this last test, will be used to calculate the structural stress at the weld toe position and to assess the load bearing capacity and fatigue behaviour, based on currently accepted design rules, to give directions for improvement.

# Earthquake resistance of clay block masonry *

*GULJAŠ Ivica, PENAVA Davorin, KRAUS Ivan, HABIJANIĆ Helena-Ena, JOZINOVIĆ Magdalena*
*Josip Juraj Strossmayer University of Osijek, Croatia*

*KOŽAR, Ivica*
*University of Rijeka, Croatia*

**Abstract.** In design of structural masonry in compliance with EN 1998-1 and EN 1996-1-1 provisions, the earthquake resistance is considered as shear resistance. Therefore it relies on adhesion developed between the masonry units and mortar bed joints. The shear resistance is determined equally regardless of the group of masonry units from which masonry is constructed from. However, in construction of clay block masonry, during placement of masonry units and mortar, intrusion of mortar into clay block voids occurs. For this reason, the failure of masonry in shear occurs when masonry unit tensile strength is exceeded, instead of sliding over the mortar bed joints. This paper gives the results of experimental investigation on clay block masonry shear resistance in direction of mortar head joints and bed joints. For the purpose of design for earthquake resistance of structural clay block masonry, mathematical expressions were recommended which take into account the clay block masonry unit and mortar joint interlocking.

# Numerical lateral-torsional buckling analysis of an aluminium alloy channel section beam

*IVANOVIC, Nikola*
*Master's student, Faculty of Civil Engineering, University of Belgrade*

**Abstract.** The research paper focuses on lateral-torsional buckling analysis of an aluminium alloy channel section beam. Analysed members are simply supported beams, with span lengths of 1.5 m, 2m and 2.5 m, loaded with linear loading, which is applied on the top flange, perpendicular to the major axis of inertia. Two load positions were analysed: in the direction towards the centroid of the cross-section and in the middle of the top flange. Numerical analysis was conducted using the commercial finite elements software Abaqus. Results obtained from the finite elements software are then compared to the results calculated using the expression available in the European standard for aluminium structures design EN 1999-1-1: Eurocode 9.

# Evaluation on Seismic Enhancement Effect of Ground Improvement for Existing Box Culvert

*KHERADI Hamayoon, NISHI Haruki, IWAI Hiromasa, ZHANG Feng*
*Nagoya Institute of Technology, Nagoya, Japan*

**Abstract.** The collapse of Daikai station of Kobe subway during the 1995 Hyogoken-Nanbu earthquake exhibited that underground structures are also at high risk of earthquake with shallow overburden. In this paper, in order to find an optimum ground-improvement pattern for rectangular-shaped box culvert constructed in soft ground that does not meet the present seismic requirement, numerical analysis with nonlinear 3D dynamic finite element analysis are conducted. Different patterns of the ground improvement for the rectangular-shaped box culvert constructed with cut-and-cover method are investigated and finally an optimum ground-improvement pattern is proposed by the numerical analysis. In the numerical analysis, the structural and physical quantities of the box culvert considered are taken from the Daikai station. Additionally, in the 2D/3D dynamic analyses, the ground is composed of Toyoura sand, typical clean sand, and its nonlinear mechanical behavior is described by Cyclic Mobility model. Validity of the proposed numerical method is firstly confirmed with 1g shaking table test and then the numerical analyses are conducted to find the optimum pattern for the ground improvement.

# An overview of past and future research activities on the seismic behaviour of the cladding systems in RC prefabricated buildings *

*JANKOVIČ Gabrijela, ISAKOVIĆ Tatjana, ZOUBEK Blaž*
*University of Ljubljana, Faculty of Civil and Geodetic Engineering, Ljubljana, Slovenia*

**Abstract.** Cladding-to-structure connections have been traditionally designed for out-of-plane action only. However, as demonstrated in recent strong earthquakes, the complex response due to the in-plane action may lead to the failure of the connections. Therefore, extensive experimental and numerical research program has been undertaken. Main results obtained at the University of Ljubljana as well as the on-going research plans are presented in the paper.

# Vibrations in buildings induced by small-scale turbines for urban wind harvesting: a case study *

*LUČIĆ Sanda, KRAUS Ivan*
*Josip Juraj Strossmayer University of Osijek*

**Abstract.** Vibrations induced by machinery, traffic and other stochastic frequency-rich sources may cause deformations and cracks on both structural and non-structural elements but also fatigue related problems. Moreover, vibrations in buildings may cause discomfort for people and animals. On the other hand, wind turbines may often be found in urban areas surrounded by buildings or placed a top of a building. Although the turbines support green engineering and production of clean energy, they also produce vibrations that may negatively influence the behaviour of both structures and living beings. This paper aims to investigate effects of vibrations generated by small-scale wind turbines placed on buildings in urban areas. A platform for this research is a soil-structure-wind turbine system, where the structures selected for this case study are typical buildings that can be found in city of Osijek. The aim of this research is to set the stage for a small-scale wind turbine that will harvest green energy in Osijek in near future. Numerical analysis was performed using software Ashes 1.2 and SAP2000, while program SeismoSignal was employed for interpretation of analysis results. Parametric analysis provides results in the light of displacement response spectrums and acceleration response spectrums taken from characteristic structural elements on different floors compared with code-based thresholds. In addition, parametric study provides transfer functions calculated by dividing output (structural vibration) and input (vibration of the top of the turbine) signals pointing out amplified frequencies by structural members.

# Road to Resilience – Factors to be considered for improvement in structural response to earthquakes – Case of Reinforced Concrete Moment Frame *

*MUKHTAR Rabiya*
*University College London, UK*

**Abstract.** For the design of structures, there is a drastic shift from rigorous building code-specified procedure to Performance Based Design (PBD). PBD offers relatively flexible and customized design of buildings such that code-specified performance criteria are met in an alternative way without following the prescriptive clauses of code. The ultimate performance objective of building-code and PBD currently in practice is "life safety" during the extreme scenario earthquake considered in design. This paper discusses the emerging concepts being developed by earthquake engineering community to enhance "during and post-disaster performance" of structures so that the ultimate performance objective may not be limited to "life safety" but also minimize damage and swift recovery of building functionality. For this purpose, comparison of "Guidelines for Performance-based Seismic Design of Tall Buildings" developed by Pacific Earthquake Engineering Research Centre (PEER) is done with "REDi Rating System" developed by Arup. Further, the case of reinforced concrete moment frame is presented for which 3D finite element analysis is conducted using code-specified equivalent static lateral force procedure, response spectrum procedure and non-linear push over analysis. The results of code-specified equivalent static lateral analysis and response spectrum are compared in terms of lateral displacements and inter-story drift ratios. The results of non-linear analysis are utilized for damage assessment of the structure using "Performance Assessment Calculation Tool "(PACT) in accordance with "Seismic Assessment of Buildings, Methodology and Implementation" (FEMA P-58).

# Experimental assessment of the flexural behaviour of rubberized concrete-filled steel tubes *

*SILVA António, CASTRO José Miguel*
*Department of Civil Engineering, Faculty of Engineering, University of Porto*

*JIANG, Yadong*
*Department of Civil Engineering, Faculty of Engineering, University of Porto*
*Istituto Universitario di Studi Superiori di Pavia, Italy*

**Abstract.** This paper describes an experimental campaign in which a total of 36 concrete-filled steel tube specimens were tested under flexural loading. The test campaign was conceived with a number of parameters in mind, namely rubberized and standard concrete infills, cross-section type and slenderness, aggregate replacement ratio, axial load level and lateral loading type. A special device was developed as part of an innovative testing setup, aimed at reducing both the cost and preparation time of the specimens. The members were tested under both monotonic and cyclic lateral loading, with different levels of applied axial loading. The test results show that the bending behaviour of CFST elements is highly dependent on the steel tube properties and that the type of infill does not have a significant influence on the flexural behaviour of the member. It was also found that Eurocode 4 is conservative in predicting the flexural capacity of the specimens.

# Plastic failure mechanisms of eccentrically loaded thin-walled cold-formed steel members *

*ŠPIRIĆ, Stefan*
*Faculty of Civil Engineering, University of Belgrade*

*UNGUREANU, Viorel*
*Department of Steel Structures and Structural Mechanics, Civil Engineering Faculty, Politehnica University of Timisoara*

**Abstract.** Thin-walled cold-formed (TWCF) steel structures are usually made of class 4 sections which are prematurely susceptible to local or distortional buckling in the elastic range. As such, local plate buckling and cross-section distortion need to be a paramount part of member design, while also keeping the design method simple enough for the engineer. Failure of these members in compression and bending is always initiated by local-global interactive buckling of plastic-elastic type, and this interaction manifests as a plastic failure mechanism. This fact can be used to develop an alternative method for determination of ultimate strength of these members which would be based on the analysis of these plastic failure mechanisms.

# Improving the Seismic Response of a Reinforced Concrete Building Using Buckling Restrained Braces

*TRANDAFIR, Alexandru*
*Technical University of Civil Engineering Bucharest*

**Abstract.** In the last years BRB were used in existing structures and in new ones as primary lateral force resisting elements. Retrofit of existing buildings in seismic areas can be made by using buckling restrained braces (BRBs), because they have the ability to sustain large inelastic deformations without important loss of strength. Therefore dynamic nonlinear analysis was performed on a reinforced concrete structure, with buckling restrained braces included. Computation was made for one recorded accelerogram. The aim of the study was to highlight the advantages and disadvantages of using BRBs together with a moment-resisting frame structural system for improving the seismic response of buildings. Parameters like displacements and stresses were carefully evaluated and then some comparatively studies were made in order to establish the efficiency of the buckling restrained braces.

# Effectiveness of Tuned Liquid Dampers for an Oscillating Bridge Deck portion during lifting phase *

*VÎLCEANU, Victor*
*Technical University of Civil Engineering, Bucharest*

**Abstract.** Flutter instability of bridge decks due to wind forces is one of the major problems that can be encountered during lifting phase. To counteract this, three solutions are possible: (i) by changing the stiffness of the deck section by modifying its geometry, (ii) by changing the aerodynamic properties of the deck or (iii) by adding damping to the model. While the second solution (ii) was previously explored for a real case at Third Bosphorus Bridge, the present paper investigates the latter by implementing an unconventional technique namely Tuned Liquid Dampers (TLD). Using a scaled model (1:100), an experimental study in the Wind Tunnel (WT) was conducted with the purpose of testing the efficiency of TLDs by varying parameters such as height or position of the water tanks which provides the maximum critical wind speed.

**Note:** Abstracts related to presentations by the participants are highlighted by '*'.